DRAFT VERSION AUGUST 1, 2024
Typeset using LaTeX **twocolumn** style in AASTeX631

Broad-Line Region Characterization in Dozens of Active Galactic Nuclei Using Small-Aperture Telescopes

CATALINA SOBRINO FIGAREDO,[1,2] DORON CHELOUCHE,[1,2] MARTIN HAAS,[3] SHAI KASPI,[4] SWAYAMTRUPTA PANDA,[5,6,*] MARTIN W. OCHMANN,[3,7] SHAY ZUCKER,[8] ROLF CHINI,[3,9,10] MALTE A. PROBST,[7] WOLFRAM KOLLATSCHNY,[7] AND MIGUEL MURPHY[9]

[1]*Department of Physics, Faculty of Natural Sciences, University of Haifa, Haifa 3498838, Israel*
[2]*Haifa Research Center for Theoretical Physics and Astrophysics, University of Haifa, Haifa 3498838, Israel*
[3]*Ruhr University Bochum, Faculty of Physics and Astronomy, Astronomical Institute (AIRUB), 44780 Bochum, Germany*
[4]*School of Physics and Astronomy and Wise Observatory, Raymond and Beverly Sackler Faculty of Exact Sciences, Tel-Aviv University, Tel-Aviv 6997801, Israel*
[5]*Laboratório Nacional de Astrofísica, MCTI, Rua dos Estados Unidos, 154, Bairro das Nações, Itajubá, MG 37501-591, Brazil*
[6]*International Gemini Observatory/NSF NOIRLab, Casilla 603, La Serena, Chile*
[7]*Institut für Astrophysik und Geophysik, Universität Göttingen, Friedrich-Hund Platz 1, D-37077 Göttingen, Germany*
[8]*Department of Geosciences, Raymond and Beverly Sackler Faculty of Exact Sciences, Tel Aviv University, Tel Aviv 6997801, Israel*
[9]*Universidad Católica del Norte, Instituto de Astronomía, Avenida Angamos 0610, Antofagasta, Chile*
[10]*Polish Academy of Sciences, Nicolaus Copernicus Astronomical Center, Bartycka 18, 00-716 Warszawa, Poland*

(Received —; Revised —-; Accepted —-)

ABSTRACT

We present the results of a photometric reverberation mapping (PRM) survey of the Hα emission line in nearby ($0.01 \lesssim z \lesssim 0.05$) Seyfert Galaxies, which was conducted over nearly a decade using small ($\gtrsim 10$ cm-class) telescopes. Broad-band filters were used to trace the continuum emission, and narrow-band filters tracked the Hα-line emission. To determine the time delay between continuum and line emission, we introduce a new PRM formalism, which is easily implementable using combinations of (interpolated) auto- and cross-correlation functions. We obtain robust delays for 33 of the objects from which the broad-line region (BLR) size is estimated. Additionally, we measure multi-epoch delays for 6 objects whose scatter per source is much smaller than the scatter in the BLR size-luminosity relation. Our study enhances the existing Hα size-luminosity relation by adding high-quality results for 31 objects, whose nuclear luminosities were estimated using the flux-variation gradient method, resulting in a scatter of 0.26 dex within our sample. The scatter further reduces to 0.17 dex when the 6 lowest luminosity sources are discarded thereby leading to a scatter comparable to that found in the size-luminosity relation for the Hβ line. Single-epoch spectra enable us to estimate black hole masses using the Hα line and derive mass accretion rates based on the iron-blend feature adjacent to Hβ. We corroborate the trend previously reported for the Hβ line whereby highly accreting objects tend to lie below the size-luminosity relation of the general population. Our works demonstrates the highly competitive role of small telescopes in carrying high-fidelity PRM campaigns of prominent emission lines in bright active galactic nuclei.

Keywords: Active galactic nuclei, supermassive black holes, quasars, reverberation mapping, narrowband photometry, spectroscopy, surveys, scaling relations

1. INTRODUCTION

Active galactic nuclei (AGN) are among the most luminous sources in the universe (Padovani et al. 2017), and mark a phase in the lifetime of galaxies, whereby their central supermassive black holes (SMBH) are rapidly growing by the accretion of material from their immediate environs (Soltan 1982; Farrah et al. 2022). Therefore, AGN provide a means by which the cosmic SMBH census may be quantified out to high redshifts, and SMBH-galaxy co-evolution may be traced (Kormendy & Ho 2013). This has profound implications for understanding SMBH growth in the general context of structure formation in the universe, as well as for gravitational-wave signals in the NANOGrav and LISA era (Agazie et al. 2023; Amaro-Seoane et al. 2022).

SMBH mass estimations in AGN are based on two observables: the size of the broad line region, $r_{\rm BLR}$, and a measure of the velocity dispersion of the lines, $\sigma_{\rm BLR}$. Assuming that the latter is a proxy for the virial speed at the location of the line-emitting gas, then up to (often loosely constrained) geometrical factors, the SMBH mass may be estimated as, $M_{\rm SMBH} \sim \sigma^2_{\rm BLR} r_{\rm BLR}/G$, where G is Newton's constant (Peterson & Wandel 2000). While $\sigma_{\rm BLR}$ may be estimated

* Gemini Science Fellow and CNPq Fellow

from the mean or the root-mean-square (RMS) spectrum of the target, $r_{\rm BLR}$ is too small to be spatially resolved in all but for a few cases and particular emission lines (e.g., Gravity Collaboration et al. 2018), and reverberation mapping is the main means by which the BLR size is assessed (Bentz et al. 2013).

Reverberation mapping (RM), as applies to AGN, is a technique in which light echoes are used to place constraints on the geometrical attributes of the BLR (Cackett et al. 2021, and references therein). This is supported by the fact that the BLR is photoionized by the AGN continuum emission, and line emission therefore responds to continuum fluctuations. In its simplest form, RM is used to measure the size of the BLR by quantifying the time-delay (the first moment of the transfer function), $t_{\rm BLR}$, between line and continuum emission. This timescale is interpreted as the light crossing time across the BLR since radiative reprocessing time-scales are comparatively very short due to the high gas densities involved, and since en-route photon diffusion is negligible at the implied optical depths (Peterson 1993). Therefore, $r_{\rm BLR} = ct_{\rm BLR}$, where c is the speed of light.

Meaningful time-delay measurements between line and continuum emission are available for $\sim 10^2$ sources and are mostly associated with the Hβ line (Peterson et al. 2004; Wang et al. 2023), which is easily observable from the ground, and for which the host-galaxy contamination may be mitigated using the adjacent [OIII] λ5007 line (van Groningen & Wanders 1992). These revealed an intriguing relation between the size of the BLR and the source optical luminosity, $L_{\rm opt}$, which is consistent with $r_{\rm BLR} \propto L_{\rm opt}^{1/2}$ (Bentz et al. 2013). This relation forms the basis for current prescriptions for estimating SMBH masses also in sources for which RM results are unavailable, thereby leading to the current cosmic SMBH census (Vestergaard 2004; Vestergaard & Osmer 2009; Kelly & Merloni 2012). It has been further proposed that the size-luminosity relation may be used as a standard ruler for cosmology (Watson et al. 2011; Martínez-Aldama et al. 2019; Panda & Marziani 2023, and references therein).

There are, however, several limitations to the aforementioned use of quasars for cosmology and the SMBH census: 1) there is non-negligible scatter in the size-luminosity relation which is further exacerbated when attempting to cross-calibrate the relations for different sets of lines (Coatman et al. 2016), 2) different AGN sub-types may be characterized by different size-luminosity relations (Du et al. 2016b), 3) local size-luminosity relations for low-luminosity sources are extrapolated to much more luminous targets and at high redshifts, where they may not hold, at least not without further corrections (e.g., Dalla Bontà et al. 2020, who considered corrections due to the Eddington ratio). Interestingly, RM campaigns of individual sources, which undergo long-term luminosity variations, show an intrinsic size-luminosity relation for their BLR, whose slope may be different than the extrinsic (multi-source) relation, and shedding light on the physical origin of the BLR (Lu et al. 2016). Therefore, increasing the sample size and diversity of AGN with good RM data, with repeated campaigns for individual sources, is crucial for properly assessing the SMBH census, and uncovering AGN physics.

To perform RM and obtain line-to-continuum time-delays, high-cadence spectroscopic observations are often employed whereby spectroscopic decomposition is used to separate line and continuum signals at each epoch, and multiple epochs are used to form their respective light curves (Kaspi et al. 2000). The need for high-cadence spectroscopic data means that RM is a challenging technique to implement, especially for faint targets, as telescope time is scarce. This shortcoming of RM motivated several groups to propose photometric RM (PRM) as a means to achieve high-quality RM using smaller telescopes for which telescope time is more abundant (Haas et al. 2011; Chelouche & Daniel 2012). Specifically, both narrowband (NB) and broadband photometric RM versions have been proposed and implemented for a handful of sources, as well as statistically for numerous sources using general-purpose survey data (Panda et al. 2024a)(REFs).

The typical implementation of PRM requires monitoring in two bands[1], one of which is used as a proxy for the time-varying ionizing continuum, and the other includes in addition to the ionizing continuum also the contribution of an emission line (Czerny et al. 2023). To constrain the line-to-continuum time-delay one may use the slew of statistical tools available for spectroscopic RM if the pure line light-curve may be extracted based on prior knowledge of the relative contribution of the emission line to the band (Haas et al. 2011). Often, however, all photometric bands contain a finite contribution of emission lines to their signal, and the contribution of the varying component of the emission line to the line-rich band is poorly constrained. In such cases, other statistical measures may be used to simultaneously constrain both the line-to-continuum time-delay and the relative contribution of the line to the band (Chelouche & Zucker 2013; Zu et al. 2016, but see Chelouche & Daniel 2012 for the case of broadband data).

Here we present the results of PRM campaigns on 80 AGN targeting the Hα line, which is significantly brighter than Hβ and lies in a spectral range free of iron line-blends contamination. The campaigns were performed between 2010 and 2018. Each campaign typically lasts 5-6 months, and 12 AGN have been monitored in 2-3 campaigns. Section 2 describes the sample selection, the available observations, and the light-curves extraction and their characteristics. In Section 3 we outline the methods used: the correlation formalism used for PRM time lag determination, the host-galaxy subtraction, and black hole mass estimation. Results for the AGN luminosities, Hα BLR sizes, BH masses as well as size-luminosity relation for the sample are given in Section 4. We discuss the implications of our results for AGN physics and provide a summary in Section 5.

[1] Single-band versions of PRM have been proposed, which rely on the statistical properties of quasar continuum variability (Zu et al. 2016)

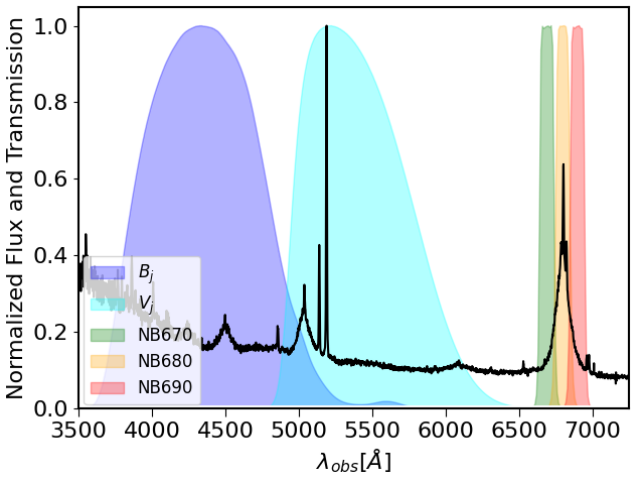

Figure 1. Normalized spectrum of Mrk 841 at $z = 0.03642$. The normalized transmission for the different photometric filters are overplotted. The continuum signal is traced in this work by the broad bands, while the Hα line is covered by the NB680 filter. The significantly different relative contributions of emission lines to the broad and narrow bands allows for PRM analysis. Note that partial coverage of the emission line may occur for specific targets (see also § E).

2. DATA

2.1. *The Sample*

Our sample is selected from the 13th edition of the AGN catalog of Véron-Cetty & Véron (2010) using the following criteria: 1) object visibility at our observatory near Cerro Armazones (OCA); 2) V < 16 mag (including the host galaxy); 3) the redshift range is such that Hα shifts into available narrow-band filters centered at 6700Å, 6800Å, 6900Å, or 6720Å(SII). This yields a sample of 80 Seyfert galaxies with $0.015 < z < 0.045$ and declination $\lesssim +25°$, which were monitored with a varying degree of success.

We acquired data for a total of 80 AGN. In the following analysis, we rejected objects for which the observational conditions were not favorable and the observation cadence was sub-optimal. Approximately 60 objects remained viable for reverberation analysis. After filtering out objects with noisy light curves and low variability, the final sample consists of 48 objects, with 12 of them observed across multiple epochs, resulting in a total of 65 RM light curves to be analyzed. Details about filtering the original dataset, as well as information on variability and cadence, are provided in Appendix A. Table 1 lists the sample with the redshift and luminosity distance values taken from NED[2]. Galaxy type and V magnitudes were taken from Véron-Cetty & Véron (2010). We note that independent reverberation-based SMBH masses have been reported in the literature for ~ 10 sources in our sample (see below).

2.2. *Photometric Observations & Light-curve Extraction*

Photometric observations were robotically carried out at OCA (Ramolla et al. 2016) using the RoBoT, VYSOS 6 (Haas et al. 2012, a twin refractor telescope with an aperture of 15 cm), BESTII (Kabath et al. 2009, a 25 cm aperture telescope), and the BMT (a 41 cm aperture telescope) or VYSOS 16 (Ramolla et al. 2013, a 41 cm aperture telescope). In our study the AGN continuum is tracked with the broad-band Johnson filters B ($\langle\lambda\rangle \simeq$4330Å) and V ($\langle\lambda\rangle \simeq$5500Å). When available, we opt to use B-band data as it is free of Hβ line emission. For $0.015 < z < 0.045$, Hα emission may be traced with the available narrowband (NB) filters; see Fig. 1 for the case of Mrk841.

The observations cover the years 2010-2018 with campaigns on individual sources being 5-6 months long on average, which suffices to search for BLR delays < 100 days, and hence consistent with the delays expected for our targets having an optical luminosity $L_{5100} = \lambda L_\lambda(5100\,\text{Å}) < 10^{44.5}\,\text{erg s}^{-1}$ (Kaspi et al. 2000; Bentz et al. 2013, but see Shen et al. 2023). With an average cadence of 3 days, the time series should lead to reliable delays for all sources with $L_{5100} > 10^{42}\,\text{erg s}^{-1}$ (Bentz et al. 2013). For 11 sources in our sample, multi-campaigns are available thus allowing to test the stability of our results and search for possible long-term variations in the BLR properties (Cackett & Horne 2006).

Light curves were obtained using calibration stars close to the object. We first create a normalized light curve by comparing the flux of the object with 20-40 field stars that are stable and show no variation during the observing period. The uncertainty estimation is done by the median of the error of the calibration stars together with the error of the object. Then, for the absolute flux calibration, we used standard stars from Landolt (2009) observed on the same night, as well as non-variable stars from the Pan-STARRS catalog[3] in the same image as the AGN. Cross-calibration of data from different telescopes was accomplished by determining an optimal relative rescaling factor between the datasets such that von Neumann's mean square successive difference (von Neumann 1941) for the combined interlaced time-series is minimized; see also Appendix A. All fluxes were corrected for the foreground Galactic extinction values of Schlafly & Finkbeiner (2011).

The effective seeing for our observations was 2″- 3″, which is significantly worse than the typical atmospheric seeing at the site ($\lesssim 0.7''$)[4], and is dominated by telescope jitter due to winds. All light curves were obtained for an aperture diameter of 7.5″, which maximizes the signal-to-noise ratio while minimizing the influence of the host galaxy. An exem-

[2] A $H_0 = 67.8\,\text{km s}^{-1}\text{Mpc}^{-1}$, $\Omega_M = 0.308$, $\Omega_\Lambda = 0.692$ cosmology was assumed (Planck Collaboration et al. 2016).

[3] https://catalogs.mast.stsci.edu/

[4] https://elt.eso.org/about/location/

Table 1. Summary of the observation sample (alphabetically ordered). Redshifts were taken from NED, and source type and V-mag values from Véron-Cetty & Véron (2006), * B-mag from Jones et al. (2009). Spectroscopic data for Hα is denoted in the last column. MK06 = Moustakas & Kennicutt (2006)

Object	z[1]	D_L[1]	RA			DEC			Type[2]	Vmag[2]	Available spectra
		[Mpc]	h	min	sec	°	′	″			
1H2107-097	0.02698	117	21	09	9.9	-09	40	15	S1.2	14.39	6dF NED
3C120	0.03301	149	04	33	11.1	+05	21	15	S1.5	15.05	FAST/HET
AKN120	0.03271	148	05	16	11.4	-00	08	59	S1	14.59	6dF/HET
CTSG03_04	0.04002	181	19	38	04.3	-51	09	49.6	S1.2	15.2	6dF NED
ESO141-G55	0.03711	168	19	21	14.3	-58	40	13	S1.2	13.64	SALT/6dF
ESO323-G77	0.01501	71.3	13	06	26.2	-40	24	52	S1.2	13.42	BAT DR1
ESO374-G25	0.02367	111	10	03	23.6	-37	33	39	S1	15.29	SALT
ESO399-IG20	0.0250	110	20	06	58.1	-34	32	55	NLS1	14.51	SALT
ESO438-G09	0.02401	113	11	10	48	-28	30	4	S1	14.17	SALT
ESO490-IG26	0.02485	114	06	40	11.8	-25	53	38	S1	15	6dF NED
ESO511-G030	0.02239	104	14	19	22.3	-26	38	41	S1	14.9	6dF NED
ESO549-G49	0.02627	117	04	02	25.8	-18	02	52	S1	14.2	6dF NED
ESO578-G09	0.03502	163	13	56	36.7	-19	31	44	S1	15.2	FAST
F1041	0.03347	148	23	17	30.2	-42	47	05.3	S1	15.2	6dF NED
HE0003-5023	0.0345	149	0	05	43.1	-50	06	55	S1	14	Tremou et al. (2015)
HE1136-2304	0.0270	127	11	38	51.2	-23	21	35	CL	17.4	SALT
HE1143-1810	0.03295	155	11	45	40.4	-18	27	15.51	S1.5	14.7*	6dF NED
HE2128-0221	0.05248	236	21	30	49.9	-02	08	14.7	S1	17.4*	6dF NED
IC4329A	0.01605	75.9	13	49	19.3	-30	18	34	S1.2	13.66	6dF NED
IRAS01089-4743	0.02392	105	01	11	09.7	-47	27	37.23	S1	14.53	6dF NED
IRAS09595-0755	0.055	246.9	10	02	0.1	-08	09	41	S1	14.64	FAST
IRAS23226-3843	0.03590	159	23	25	24.2	-38	26	49.2	S1	14.24	BAT
MCG+03-47-002	0.04000	180	18	27	14.7	+19	56	19.0	S1	15.3	6dF NED
MCG-02.12.050	0.03600	164	04	38	14.1	-10	47	45	S1	15	FAST
MRK1239	0.01993	94.7	09	52	19.1	+01	36	44	NLS1	14.39	6dF Chen et al. (2018)
MRK1347	0.04995	234	13	22	55.5	+08	09	42	S1	14.59	FAST
MRK335	0.02578	111	0	06	19.5	+20	12	11	NLS1	13.85	FAST
MRK509	0.0344	152	20	44	9.7	-10	43	24.5	S1.5	13.2	FAST/SALT
MRK705	0.02879	135	09	26	3.3	+12	44	3	S1.2	14.6	KPNO/ Molina et al. (2022)
MRK841	0.03642	168	15	04	1.2	+10	26	16	S1.5	14.27	FAST
NGC1019	0.02434	106	02	38	27.4	+01	54	28	S1.5	14.95	FAST/SALT
NGC4726	0.02543	120	12	51	32.3	-14	13	17	S1	14.2	6dF NED/Zaw et al. (2019)
NGC5940	0.03408	157	15	31	18.1	+07	27	27	S1	14.9	FAST
NGC6860	0.01488	65.3	20	08	47.1	-61	06	0	S1.5	13.53	6dF NED
NGC7214	0.02385	103	22	09	07.6	-27	48	34.1	S1.2	14.10	6dF NED
NGC7469	0.01627	67.2	23	03	15.6	+08	52	26.39	S1.5	13.04	BAT/MK06
NGC7603	0.02876	124	23	18	56.6	+00	14	38	S1.5	14.01	FAST/SALT
NGC985	0.04314	193	02	34	37.7	-08	47	15.44	S1.5	14.28	FAST
PG1149-110	0.0490	230	11	52	3.5	-11	22	23	S1.2	15.46	BAT DR2
PGC50427	0.02346	109	14	08	6.7	-30	23	53	S1.5	15.3	SALT
PGC64989	0.01937	83.5	20	34	31.4	-30	37	29	S1	13.3	FAST
RXSJ06225-2317	0.03778	174	06	22	33.4	-23	17	42	S1	14.85	FAST/SALT
RX J1103.2-0654	0.02606	123	11	03	15.8	-06	54	10	S1	13.34	FAST/SALT
RXSJ17414+0348	0.0230	103	17	41	28.1	+03	48	51	S1	15.3	SALT
UGC12138	0.02509	107	22	40	17.0	+08	03	14.09	S1.8	14.45	BAT DR2
UM163	0.03343	146	23	39	32.3	-02	27	45	S1.5	14.86	6dF NED
WPVS48	0.0370	173	09	59	42.6	-31	12	59	NLS1	14.78	FAST/SALT
WPVS_7	0.02861	127	0	39	15.9	-51	17	1.5	NLS1	15.28	6dF Chen et al. (2018)

plary light curve for Mrk 841 is shown in Fig. 2 while the full set of light curves is given in Appendix A.

2.3. *Spectroscopic Data*

We have spectra covering the Hα line for all sources in our sample. Of these, we acquired 24 spectra ourselves, while the remaining were obtained from the literature. Single-epoch spectra were contemporaneously obtained using the Southern African Large Telescope (SALT; Buckley et al. 2006) between 2012 and 2013 and using the Tillinghast telescope at the Whipple Observatory between 2014 and 2015. SALT observations utilized the Robert Stobie Spectrograph (RSS; Kobulnicky et al. 2003) with the EG 21, EG 274. Feige 110, G 24-9, G 93-48, Hiltner 600, LTT 1020, and LTT 4364 stars used for flux calibration. Tillinghast-telescope observations utilized the FAST Spectrograph (FAST; Fabricant et al. 1998) with BD+174708, BD+284211, Feige 34, Feige 110, and HD 84937 used as standard stars for flux calibration. Additionally, single-epoch spectra were taken for

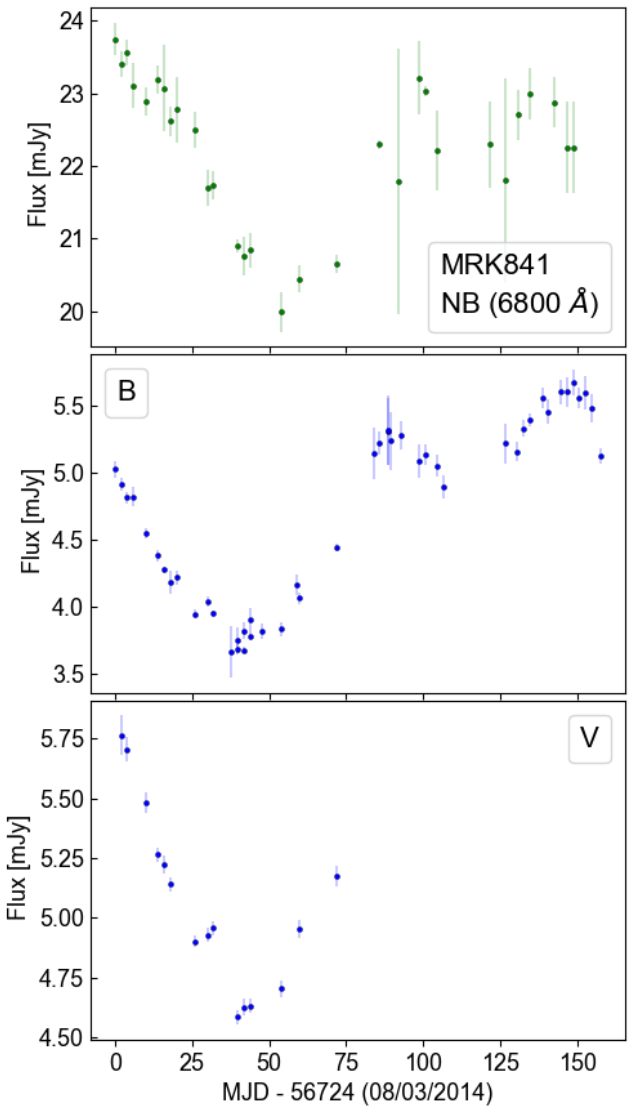

Figure 2. Photometric light curves for Mrk 841. Data for the NB680 band appear to be delayed with respect to the adjacent broadband data due to the significant contribution of the broad Hα line to the flux in the narrow band. Nevertheless, as the contribution of the Hα line to the band is only partial, direct cross-correlation techniques are inadequate to recover the time-delay associated with the line, and bivariate correlation analyses methods (Eq. 1) are more suitable.

AKN 120 and MRK 335 in 2019 with the orange channel of the second-generation Low Resolution Spectrograph (LRS2; Chonis et al. 2016) on the upgraded Hobby-Eberly Telescope (HET; Ramsey et al. 1998; Hill et al. 2018). The spectra were reduced with the automatic HET pipeline, Panacea.

Additionally, a couple of calibrated spectra were taken from the Swift BAT AGN Spectroscopic Survey (BASS DR1,DR2; see Koss et al. 2017, 2022), and a few objects in our sample are included in the 6dF catalog (Jones et al. 2009). Generally, these data are not flux calibrated, except for two NLS1s (Chen et al. 2018). Single objects with calibrated spectra were retrieved from individual publications. Table 1 lists the Hα spectra available for each of the objects in our sample and the complete log of observations is given in Table E.1.

3. METHODS

3.1. *Time-delay Determination*

In the common implementation of BLR RM, continuum and line signals are spectroscopically separable by their different spectral correlation scales. The time delay between the emission-line light curve and the continuum light curve may then be deduced via the interpolated cross-correlation function (ICCF; see Gaskell & Sparke 1986; Peterson et al. 1998). This seeks to maximize the Pearson correlation coefficient by shifting the continuum and emission-line time-series with respect to each other. Nevertheless, PRM cannot directly distinguish emission-line from continuum processes as only their combined signal is measured. By design, the NB filter in our study carries both continuum and emission-line contributions to the signal with the latter having a substantial contribution in comparison to broadband data (Fig. 1). To extract the emission-line contribution to the signal, the underlying continuum flux must be subtracted. This can be done if simultaneous observations in adjacent (either broad or narrow) bands are taken, which serve as a proxy to the pure continuum flux. Significant uncertainties may surface when the data in the line-rich and line-poor bands are not simultaneous, or if non-adjacent bands are used over which significant continuum-flux differences may occur, or if line emission to both bands is comparable. A further complication arises from the fact that the contribution of emission lines to the flux in the band may not reflect on their contribution to the RMS signal, which is the relevant signal for RM.

Here we generalize the RM formalism so that it allows for the decomposition of line and continuum signals at the light curve level using either broadband, NB, or spectroscopic data (Chelouche & Zucker 2013). When applied to our data, the light curve traced by the NB is modeled as

$$F_{\rm NB}(t) = (1-\alpha)F_{\rm BB}(t) + \alpha F_{\rm BB}(t-\tau), \qquad (1)$$

where α, τ are model parameters, and $F_{\rm BB}$ is the broadband light curve for which the BLR contribution is presumably weak. Solutions for the echo are obtained via a best-fit criterion between the model and the NB data. Specifically, $t_{\rm BLR}$ derives from the time-delay, τ, which maximizes the Pearson correlation coefficient, $\tau_{\rm peak}$. The solution method adopted here is analogous to the two-dimensional correlation algorithm for the detection and characterization of spectroscopic binaries (TODCOR; Zucker & Mazeh 1994) and is applied to PRM by transforming its wavelength dependence to time dependence. Importantly, the formalism uses combinations of CCFs and ACFs, and may thus be implemented using customary tools of trade, in which case the Pearson correlation coefficient is given by (see appendix B.1 for derivation and further details):

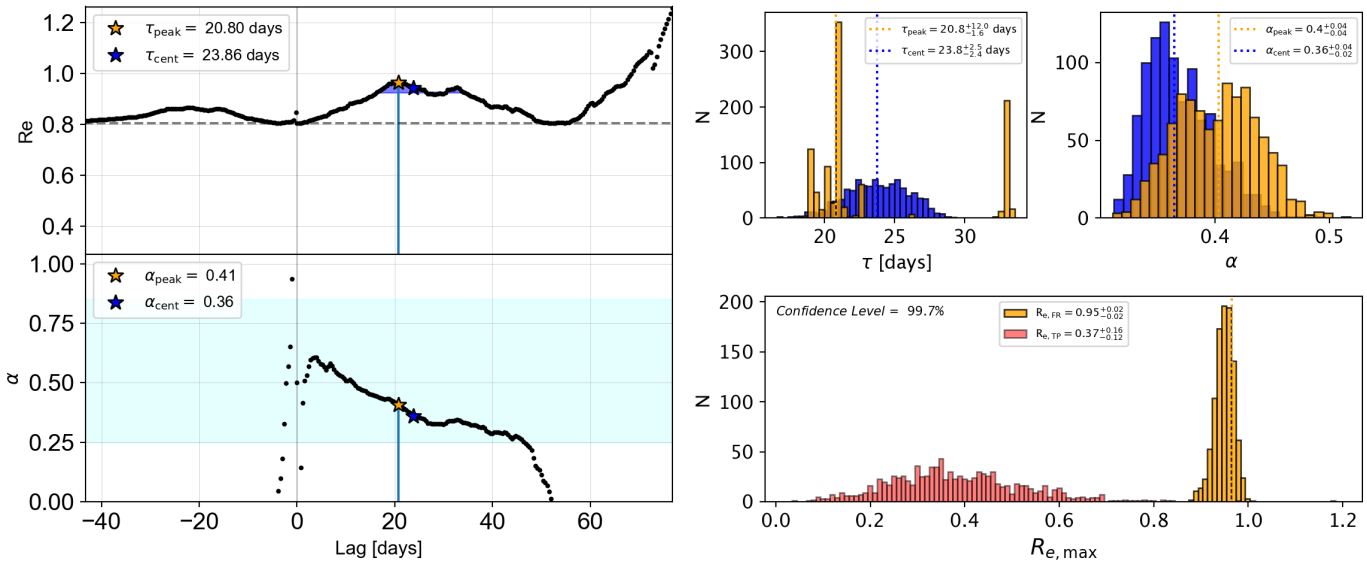

Figure 3. Left: Correlation between the B-band and NB680 light curves for MRK841. The correlation coefficient ($R_{\rm e}$) is shown at the top and the corresponding value for α is at the bottom. The value for the peak delay with its respective α value is marked with an orange star. The range for calculating the centroid is colored with a blue area and the corresponding lag is marked with a blue star. The centroid calculation is performed within a range defined as ≥ 0.8 times the peak R_e value, akin to the conventional method of RM. Right: the upper two panels illustrate the implementation of the FR algorithm for error estimation. The peak value is highlighted in orange, while the centroid is depicted in blue, with the final values labeled. The lower panel presents the histogram for the maximal correlation values $R_{\rm e,max}$ obtained via the FR method ($R_{\rm e,FR}$) is shown in orange with a value that approximates 0.95. In contrast, the histogram for the time-permuted version ($R_{\rm e,TP}$) is displayed in red, yielding an average value of approximately 0.4. This indicates a high level of confidence in the results (see text).

$$r_e(\tau) = \sqrt{\frac{\mathrm{CCF}^2(0) - 2\mathrm{CCF}(0)\mathrm{CCF}(\tau)\mathrm{ACF}_{\rm BB}(\tau) + \mathrm{CCF}^2(\tau)}{1 - \mathrm{ACF}^2_{\rm BB}(\tau)}}, \quad (2)$$

where $\mathrm{ACF}_{\rm BB}$ is the autocorrelation function of the broadband-filter light curve, and the CCF term has the usual meaning.

Throughout this work, we implement our formalism using the interpolated CCF (ICCF) approach (Gaskell & Sparke 1986; Peterson et al. 1998) with fixed (0.2 days) time steps, which are below our observing cadence for all sources. Following Welsh (1999), re-normalization and de-trending are implemented at every time step. The search window for a peak in the correlation function satisfies $\tau_{\rm peak} \in [-2/3, 2/3] \times t_{\rm duration}$, where $t_{\rm duration}$ is the total span of the time-series. This is justified in cases where the sampling is quasi-regular throughout the time-series, and the light curves in the different bands overlap over much of the observing period. As customary in RM studies (see also Appendix B and B.1), $t_{\rm BLR}$ is identified with either the peak of the correlation function or with its center of mass around the peak; in the latter case, the centroid calculation is carried out within a time range around the peak that is bracketed by R_e values greater than 80% of the peak value (see Fig 3). This results in the centroid time delay, $\tau_{\rm cent}$.

We note that the implementation of our PRM algorithm may yield values for the correlation coefficient, which are larger than unity (note the rising peak at $>$ 65 days lag in Fig. 3). This results from our choice to a) use common adaptations for the ICCF, which would make the formalism easily implementable, and b) reduce the number of interpolated points to a minimum, thereby mitigating artificial structure in the correlation function. As verified by simulations (Appendix B.1), the effect is exacerbated when the search window for time delays extends to a significant fraction of the time-series (for the case of Mrk841 values exceeding unity are obtained for lags that are $\gtrsim 50\%$ of the total duration of the campaign), and the number of overlapping points between the bands is significantly reduced due to the relative time-shifts employed. Significantly non-uniform sampling of the time-series is a further factor contributing to this effect. For more information refer to Appendix B.1. To prevent correlation values from exceeding unity, a commonly applied time-stamp interpolation should be applied to all the terms used to calculate the correlation coefficient, namely $\mathrm{CCF}(0)$, $\mathrm{CCF}(\tau)$, and $\mathrm{ACF}(\tau)$ (see Eq. B10), which could result in the signal being dominated by interpolated data, thus potentially leading to spurious peaks, which we wish to avoid.

3.1.1. *Incorporating bounds on line emission in photometric data*

Useful constraints on the model concern the bounds on the value of α in the model (Eq. 2). Physically, $\alpha \in [0, 1]$ hence peaks in the correlation function, which are associated, for example, with $\alpha < 0$ solutions may be discarded (e.g. the rising peak at long delays for Mrk 841; see Fig. 3).

Refined estimates for the time-delays may be obtained by considering further information about the value of α. For

example, noting that $0.2 < \alpha < 0.9$ for NB data (Haas et al. 2011; Chelouche & Daniel 2012, for comparison, $\alpha < 0.1$ for broadband data) can be used to discard spurious peaks in R_e and obtain a more meaningful solution. Specifically, if R-band observations, which overlap with our NB bands, are available then we estimate the value of α by photometric means such that

$$\alpha_{\rm phot} = 1 - \frac{\langle F_R \rangle}{\langle F_{\rm NB} \rangle}, \quad (3)$$

where, F_R is the flux in the R band, and $\langle . \rangle$ denotes averaging over the time series. Broadbands other than R may also be used to estimate $\alpha_{\rm phot}$ although the degree to which these data may serve as a proxy for the continuum emission under the Hα line is unclear, and should be verified on a case-by-case basis, especially when large apertures are employed. The photometric estimate for α is likely a lower limit and $\alpha \gtrsim \alpha_{\rm phot}$ due to the contribution of the host galaxy within the aperture. For NB data, $\alpha < 0.3$ only in cases where the emission line is partially covered by the band or if during the observation campaign, the varying part of the emission line is particularly weak.

3.1.2. *Uncertainty and confidence-level estimations*

We estimate the uncertainty on $t_{\rm BLR}$ using the flux-randomization method (Peterson et al. 1998) with 1000 repetitions, and calculating the correlation peak (or centroid) distribution, from which 15% and 85% percentile bounds are calculated, and the measurement uncertainties evaluated. We do not use the random subset selection approach, which results in significantly over-estimated uncertainties for $\alpha < 1$ but instead introduce a confidence-level estimation procedure (Chelouche & Zucker 2013).

As the delayed signal in PRM of the BLR contributes only partly to the NB signal, we wish to ascertain whether the detection of the delayed component at the light curve level is robust. To this end, we repeatedly calculate R_e assuming $F_{\rm NB}(t) = (1-\alpha)F_{\rm BB}(t) + \alpha \mathcal{F}_{\rm BB}(t-\tau)$, where $\mathcal{F}_{\rm BB}$ is a randomly time-permuted version of $F_{\rm BB}$ (c.f. Eq. 1). The confidence level is then given by the percentage of iterations where the maximum correlation value $R_{\rm e,max}$ for the flux-randomized light curves ($R_{\rm e,FR}$) exceeds the one obtained with the time-permuted versions ($R_{\rm e,TP}$).

A typical implementation of the above formalism for the case of Mrk 841 is shown in figure 3 for which the B band was used as a proxy for the continuum light curve, and the NB6800 band was used to trace the Hα line. Figure 3 on the right shows the application of the FR algorithm for the error estimation. The upper two panels show the results for the delay (τ) and the line contribution (α), which results in $\tau_{\rm peak} = 20.8^{+12.0}_{-1.6}$ days, and $\tau_{\rm cent} = 23.7^{+2.4}_{-3.5}$ days, where the former (latter) is based on the peak (centroid) statistics. Identifying $t_{\rm BLR}$ with either of the measures leads to consistent conclusions. The lower panel of the Figure shows the results for the maximal correlation coefficient value $R_{\rm e,max}$ obtained via the FR method $R_{\rm e,FR}(\sim 0.95)$ and the time-permuted version $R_{\rm e,TP}$ ($\sim$0.4), which leads in this example to a high confidence level.

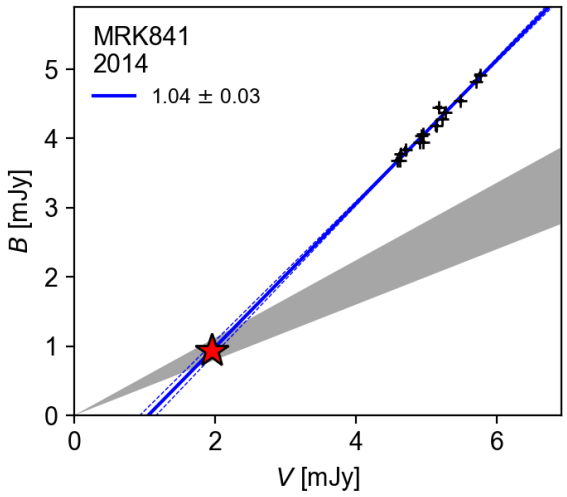

Figure 4. An example of a flux-flux diagram for Mrk 841 exhibiting variability behavior that is consistent with a linear trend between the B and the V bands. A linear fit intersects the galaxy-colors wedge (Sakata et al. 2010; gray area) at the host-galaxy flux levels within the aperture (red star) , and should be subtracted to reveal the net AGN flux (see text).

3.2. *Host-galaxy–light Subtraction*

We apply the Flux Variation Gradient (FVG) method, proposed by Choloniewski (1981, see also Winkler et al. 1992; Winkler 1997; Sakata et al. 2010; Haas et al. 2011; Giannniotis et al. 2022) to subtract the host galaxy component from the total flux. This method uses the fact that the time-varying optical emission of Seyfert galaxies shows little to no color changes over BLR light-crossing timescales, and that host colors are also fixed over the relevant timescales. In that case, we can disentangle both components by using flux-flux diagrams (Ramolla et al. 2015). Specifically, the intersection between AGN and host slopes, which are set by their colors, provides the contribution of the host component to the observed flux in each of the bands. In our sample, we mostly have observations in $BVR(r)$, and we construct flux-flux diagrams for their combinations. If available, we opt for the BV diagrams to avoid R-band contamination by the Hα line. We use the Ordinary Least Squares Bisector (OLSB) method to fit the flux-flux slopes (Isobe et al. 1990; Winkler 1997; Ramolla et al. 2015).

The contribution of the host-galaxy light within the aperture delineates wedges in the flux-flux diagram whose margins are set by the galaxy colors. These are taken from the sample of AGN host galaxies in Sakata et al. (2010), which results in the following slope (i.e. colors) ranges per filter combination: $BV = 0.48 \pm 0.08$, $Br_s = 0.35 \pm 0.07$, $BR = 0.29 \pm 0.07$ and $VR = 0.71 \pm 0.03$. The intersection of the best-fit linear trend of the flux-flux data with that expected given the host colors allows us to estimate the contribution of the latter to the bands. The host galaxy color

range used in our analysis is an average across different types of galaxies (refer to Table 1 in Sakata et al. (2010)). Since the objects have redshift from 0.01 until 0.05, there is minimal impact on the host color. The range of host slopes across different redshifts falls within the host's error margin. Therefore, we assume that the previously mentioned host colors apply to all objects. While this is a suitable approach for our purposes, it's important to note that the specific choice of host galaxy color and its subtraction can impact the final host-subtracted flux values and finally the luminosity value.

A typical FVG diagram is shown for Mrk841 (Fig. 4), where the contribution of the host to the total flux within the aperture is modest, and of order 25-40%, and is increasing to longer wavelengths, as expected.

With the FVG for 39 sources robustly constrained (see Appendix D), we can estimate the net AGN luminosity, L_{5100}. Sources for which the FVG is ill-defined and the intersection between host and AGN transects is doubtful, we report an upper limit for the luminosity, this is the case for 8 of our sources. For objects with multi-epoch data, we take the average host flux from the combined FVG (after verifying that the values are not markedly different between epochs and between different filter combinations). On average the BV AGN slopes (colors) are 1.0 ± 0.2, in agreement with the color studies carried out in Winkler et al. (1992) and Winkler (1997), where the BV slopes are close to unity. BR slopes are on average shallower, 0.9 ± 0.3, showing the influence of the Hα emission line within the R-band.

To estimate the optical luminosity at 5100Å λL_{5100}, we interpolated the host-subtracted flux using a power-law form ($F_\nu \propto \lambda^\beta$) with the adopted cosmology (see Table 2). Figure 5 demonstrates the scheme for Mrk841 resulting in a power-law slope, $\beta \simeq -1.2$, which is bluer than predicted by standard thin-disk models for which $\beta = -1/3$ (Shakura & Sunyaev 1973), and likely results from the significant contribution of the small blue bump to the B-band in this source (see Fig. 1).

The mean luminosity of our sample, $\log(\langle L_{5100} \rangle) \simeq 43.6$ with 68% of the sources in the range $43 < \log(L_{5100}) < 44$. Thus, sources in our sample bridge the luminosity gap between sources with Hα RM measurements in the Bentz et al. (2010) and those in the Shen et al. (2023) samples.

3.3. *Broad-line Characterization*

We apply the PYSPEC package to determine the full width at half maximum (FWHM) of the broad Hα line using available spectroscopic data (Table 1). Specifically, we subtract the continuum contribution by fitting a linear trend between flanking continuum windows. We then fit the residual emission by the sum of Gaussian curves. The combined fit often includes two narrow Gaussians for the SII $\lambda\lambda 6718, 6732$, two narrow Gaussians for the NII $\lambda\lambda 6548, 6584$, and narrow and broad Gaussian components for the Hα line. Further, we set the narrow components to match those of the SII line (or the NII line when data quality is insufficient). Upon subtraction of the narrow components, the broad Hα emission component may be fit by single or double broad Gaussian compo-

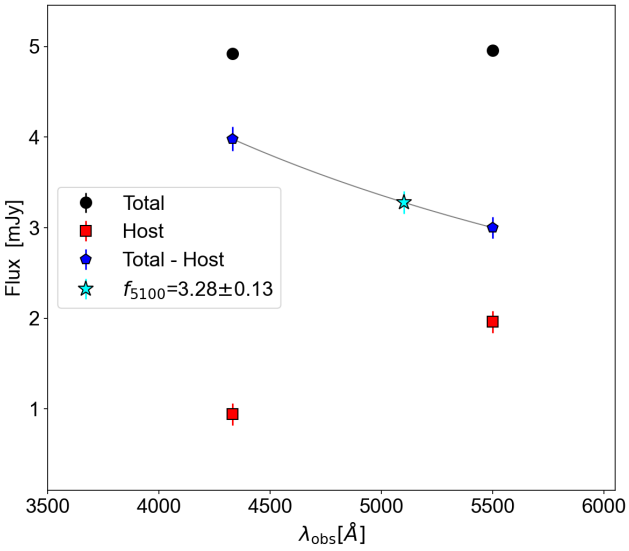

Figure 5. An example of host galaxy subtraction and flux interpolation at 5100Å for Mrk841. Black circles represent the median total flux, with errors reflecting the median of all errors. Host galaxy values derived from the FVG method are shown as red squares, where error bars indicate the range of intersection between AGN and host slopes. Host subtracted fluxes trace the nuclear emission, and are depicted in blue. A powerlaw fit of the form $f_\nu \propto \lambda^\beta$ is illustrated by a solid line. The final subtracted host value from this fit is denoted by a cyan star, accompanied by its corresponding flux label.

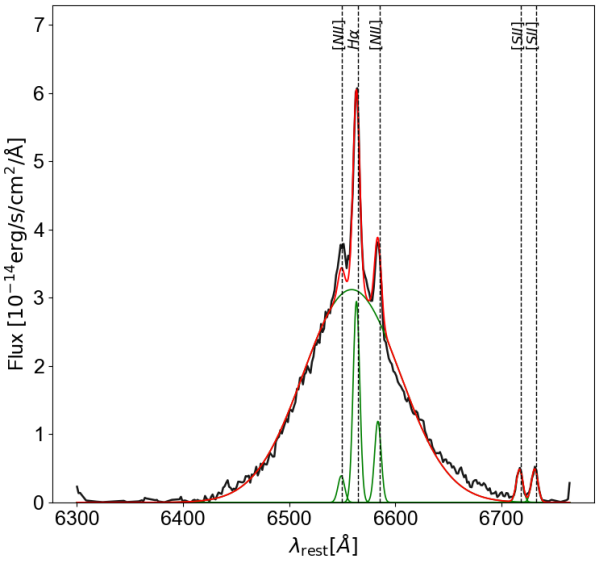

Figure 6. An example of a continuum subtracted FAST spectrum of Mrk 841 showing the broad Hα emission line and the narrow [SII] and N[II] lines. A best-fit model to the data is shown in red, which consists of broad- and narrow-line components (green curves). The FWHM of the broad component is used for BH mass estimatations.

nents. The FWHM of the line is estimated in two complementary ways: 1) from the fit of the broad components, or 2) from the observed broad line residuals. The quoted FWHM value is an average of both measurements and the error is the deviation between both estimations. A typical example of the fit quality is shown in figure 6 with the full set of spectroscopic data shown in Appendix E.

We do not report FWHM values for two of the objects, IRAS23226-3843, and MCG+03-47-002, due to a very weak emission line and noisy spectrum. For NGC4726, in the 6dF available spectra we could not fit any line, therefore we quoted the FWHM provided in Zaw et al. (2019). For the object HE0003-5023 we adopt the FWHM value reported in Tremou et al. (2015). In addition to the objects already classified as NLS1 in the catalog (Véron-Cetty & Véron 2006), we have identified NLS1 candidates exhibiting FWHM values below 2000 km/s. These candidates include: IRAS01089-4743, RXSJ06225-2317, MRK705, MRK1347, HE2128-0221, and NGC7469.

In those high-quality spectra that include the Hβ region, we fit an iron template to extract the optical Fe signal. Taking inspiration from PyQSOFit (Guo et al. 2018), we employ the optical Fe II emission template, covering 3686-7484Å, from Boroson & Green (1992), and fit it to the spectra employing normalization, broadening, and wavelength shift. We refer the readers to Panda & Śniegowska (2024); Panda et al. (2024b) for more details.

Two examples illustrating the fit for extracting the ratio of the iron-blend flux to the broad-Hβ flux, $R_{\rm Fe}$, are shown in Figure 7. The top panel shows Mrk841 having a low $R_{\rm Fe}$ value with iron-blend emission being hardly discernible, while the bottom panel depicts the spectrum of RXSJ17414+2304 with a significant iron-blend contribution, thereby implying high $R_{\rm Fe}$ values.

4. RESULTS

4.1. *BLR time Lag*

Applying our lag-estimation algorithm to all targets and epochs (refer to Table G.1), we find that $\tau_{\rm cent} \simeq \tau_{\rm peak} \equiv (1+z)t_{\rm BLR}$, where z is the source redshift. Correlation functions, from which the time delays associated with light reverberation in the BLR, are shown for all sources and all epochs in Appendix C. Approximately 80% of the lag measurements in our sample exhibit a confidence level exceeding 90%.

Figure 8 illustrates the quality of the time delays. Out of the 65 initial light curves, 61 were utilized for determining the time delay. We restrict our analysis to those sources satisfying $R_{\rm e,FR} > 0.7$, $R_{\rm e,FR}/R_{\rm e,TP}$ is greater than approximately 1.6, and the confidence level is above 85%. Both criteria are marked in the figure 8 with corresponding horizontal and vertical lines. The top right region of the plot indicates where good delay estimations are located. Additionally, the points corresponding to good delays are marked with a black edge. The source IRAS23226-3843 meets these criteria, but its delay is not considered optimal. The light curves exhibit noise with $\eta \sim 0.9$ for both continuum and NB band, moreover the broad component of the Hα line is very weak. Therefore, we exclude this object from further analysis. On the other hand, we include four objects that do not fully meet all criteria; they exhibit a high confidence level (¿95%) but have a low $R_{\rm e,FR}$ value. This applies to MRK335 (observed in epoch 2014), MRK509, NGC7214, and WPVS007. Despite their lower $R_{\rm e,FR}$ values, the variability of their light curves is well-covered, and their quality is considered acceptable (with $\eta_{\rm cont}$ and η_{NB} being smaller than unity). Therefore, we include them in the analysis. Finally, we derived 40 reliable delays from the initial 61 light curves, accounting for 67% of the analyzed data.

Of the initial 12 sources observed across multiple epochs, average delay values for 6 are presented in Table 3 together with the results showing high confidence values. Lag determination for 3C120 and ESO374-G25 was conducted for only one observing epoch due to low variability and noisy light curves in some epochs. The first two epochs of MRK335 exhibit low confidence levels and a low ratio between $R_{\rm e,FR}/R_{\rm e,TP}$, likely due to sparse sampling and short duration of the light curves. Therefore, we report only one epoch delay for MRK335 from the observation year 2014. Similarly, HE1136-2304 shows a low $R_{\rm e,FR}/R_{\rm e,TP}$ ratio for its second and third observing epochs; hence, we report the optimal delay found for the 2015 season. For PGC64989, the first observing epoch also exhibits a low confidence level, leading us to discard this delay measurement. For the object RX J1103.2-0654, none of the epochs provided adequate data quality to report any delay. Refer to the light curves and correlation functions in Appendix for details.

4.2. *AGN-emission properties*

We construct flux-flux diagrams per source for all available filter combinations (see Appendix D). Summing over all objects and epochs, we have 25 BV AGN slopes and 52 $BR(r)$ AGN slopes with mean values of 1.02 ± 0.22 (for BV) and 0.90 ± 0.30 (for BR), which are in agreement with previous findings (Winkler et al. 1992). The BR slopes distribution shows a larger scatter and lower values compared to the deduced BV slopes, which could be explained by the contribution of (time lagging) Hα emission to the R band, and/or by nuclear reddening.

Multiple observing campaigns were carried out for 12 targets in our sample, and allow to look for changes in AGN colors over years timescales. Among those sources, 8 have observations with the same filters, thus we can construct a multi-epoch FVG. Figure 9 shows multi-epoch FVGs for 3C120, HE1136-2304, and WPVS48. These demonstrate three types of time dependent behaviours observed across the sample. The first (termed constant FVG) is consistent with AGN colors remaining fixed over time and across different luminosity states of the source (see also Ramolla et al. 2015). The second behavior (termed varying FVG) shows a change of slope (i.e. color) of the varying nuclear component, which may be associated with variations in the properties of the accretion flow (Dexter & Begelman 2019) or with diffuse BLR emission, which may contribute to the optical band (Chelouche et al. 2019), or with time-varying nuclear reddening,

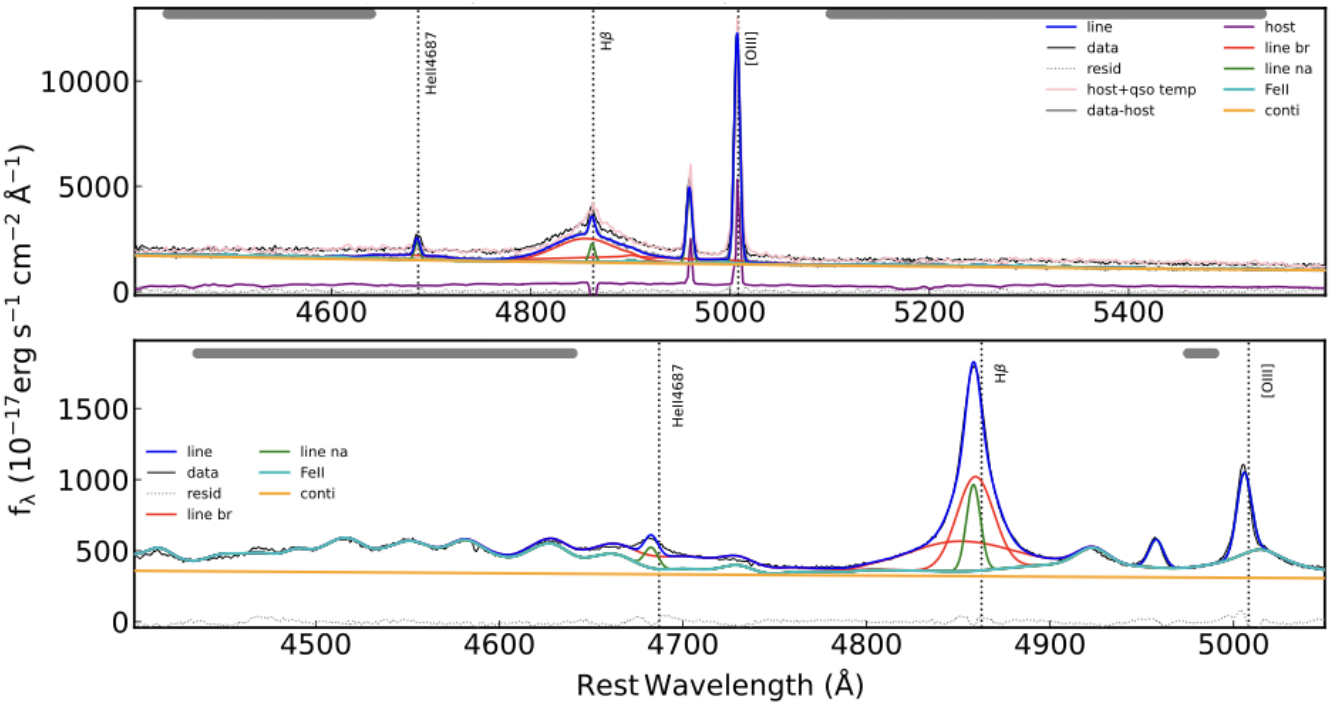

Figure 7. Iron-template and multi-component Hβ model fit to the optical spectrum of Mrk841 (top) and RXSJ17414+2304 (bottom). The fit includes a model for the host, where applicable. The derived fluxes for the iron blend and Hβ are then used to calculate their ratio, $R_{\rm Fe}$, which may be used to estimate the mass-accretion rate (§4.4.2).

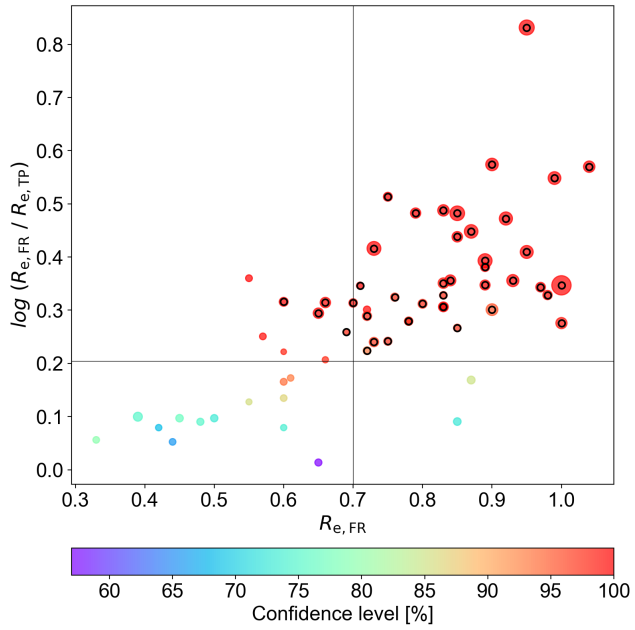

Figure 8. Ratio $R_{\rm e,FR}/R_{\rm e,TP}$ against $R_{\rm e,FR}$ (see Section 3.1.2 for details), with color-coded according to the confidence level and size indicating the quality of the Continuum and NB light curve (being larger for better quality of the light curve, based on the η value). Criteria of $R_{\rm e,FR} \geq 0.7$ and ratio $R_{\rm e,FR}/R_{\rm e,TP} \geq 1.6$ are marked with vertical and horizontal lines respectively. Good delay candidates are highlighted with a black edge.

or a combination thereof. Interestingly, such behavior is only seen in HE1136-2304, which is classified as a changing look AGN (Kollatschny et al. 2018; Zetzl et al. 2018). The third type of time-dependent behavior is associated with FVG offsets, which do not affect the slopes that remain consistent between individual campaigns. The most likely explanation is a change to our observing setup in-between campaigns, which is known to have occurred but was not adequately documented. This demonstrates the limitations of the FVG method in accurately subtracting the host signal.

We note that within the confines of our sample and wavelength coverage, we do not find evidence for the "bluer when brighter" effect (Sun et al. 2014).

4.3. *BH mass*

We estimate the mass of the central SMBH via

$$M_{\rm BH} = \langle f \rangle \frac{c t_{\rm BLR} \sigma^2_{\rm BLR}}{G}, \quad (4)$$

where $t_{\rm BLR}$ is light crossing time across the Hα emission region as deduced from the correlation analysis (§3.1), and identify $\sigma_{\rm BLR}$ with the FWHM of the broad component of the Hα emission line as measured from single-epoch spectra. $\langle f \rangle$ is the population-mean geometrical scale factor, which is of order unity. Depending on the BLR geometry and dynamics (Peterson et al. 2004; Peterson & Wandel 2000), $\langle f \rangle$ is often bracketed in the range $2 - 7$ (Onken et al. 2004; Park et al. 2012; Batiste et al. 2017; Grier et al. 2013; Graham et al. 2011), but may substantially differ on an object by object basis (Williams et al. 2018). For tractability we set $\langle f \rangle =$

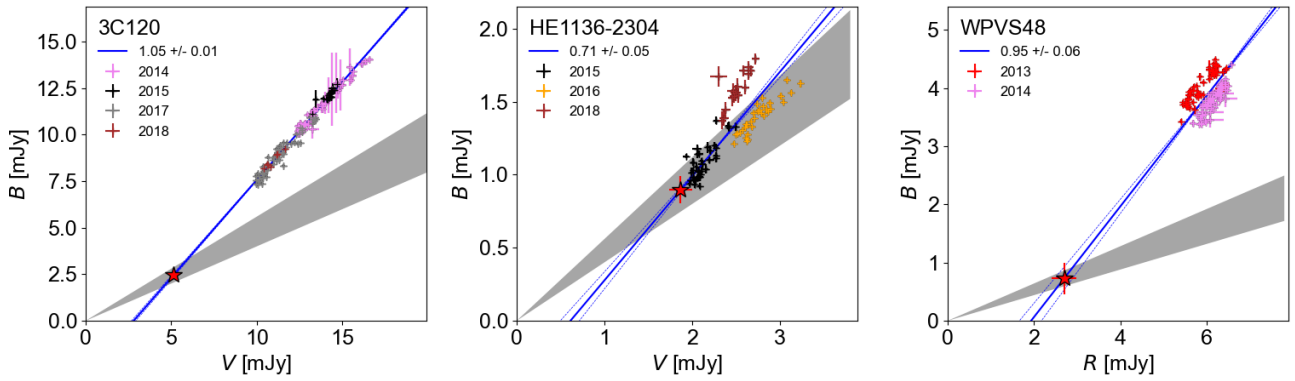

Figure 9. Multi-epoch BV flux-flux diagrams for the objects 3C120 (left), HE1136-2304 (middle) and WPVS48 (right). The FVGs are contructed by the combination of different observation campaings. Fluxes are plotted as crosses and the different colors mean different observing years. The bisector-fit for the AGN slope is plotted as blue lines and the BV and BR host slope from Sakata et al. (2010) as a colored gray area. The red star marks the intersection between AGN and host slope and represents the assumed host value for the object.

1, which is consistent with the approach taken by Martínez-Aldama et al. (2019) for the Hβ line.

All estimated BH masses are listed in Table G.1. We collect previous BH mass estimates from the literature for comparison with our results, focusing on BH masses estimated via RM. The catalog by Bentz & Katz (2015) provides an updated database of BH masses derived from spectroscopic RM, including six sources that are included in our sample. The BH masses in this database are primarily calculated using an average of all available RM lines and their σ, with an adopted scale factor $f = 4.3$. To align with our results, we gather data from various studies and recalculate the BH masses using their reported centroid time lag of the $H\beta$ line and its FWHM. We choose the Hβ line since is available for all the sources, whereas Hα is only available for two of them. In our recalculation, we adopt $f = 1$, following this work approach. In cases where multiple RM estimations are available, we average the BH masses obtained from the different studies. Furthermore, BH mass estimates for the objects HE1136-2304 and IC4329A were provided by two individual studies: Kollatschny et al. (2018) and Bentz et al. (2023) and NCG985 and Mrk841 are within Lick AGN Monitoring Project in U et al. (2022). For those we conducted identical recalculations using the Hβ line and its FWHM. All recalculated BH masses are summarized in Table 2. This approach ensures a standardized comparison between the BH masses derived from RM in previous studies and those obtained in our work.

Figure 10 shows the comparison between this work and the re-calculated BH masses. The y-axis represents $M_{\rm BH}$ from the current work and x-axis from the literature. The black line represents a one-to-one correlation between the two estimations and the grey shaded area an uncertainty of 0.3dex. It shows that BH masses obtained in this work from the Hα line RM and from single epoch spectra are mostly in agreement with previous studies, and within the scatter typical of the field (McLure & Dunlop 2004).

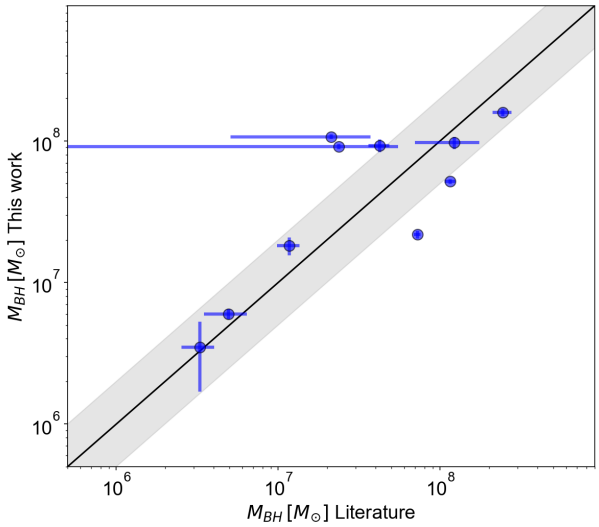

Figure 10. Comparison between BH masses estimated in this work and previously reported BH masses (after adjusting for the same $\langle f \rangle$ factor (see text)). The resulting scatter is at the 0.3 dex level, which is typical of the field.

4.4. *The size-luminosity relation for the Hα emitting BLR*

Figure 11 shows the resulting size-luminosity relation for the sources in our sample for which time delays were obtained ($r_{\rm BLR} = ct_{\rm BLR}$). Sources with host-subtracted AGN luminosity estimations are denoted by cyan circles. Those include single-epoch delays as well as the average values for multi-epoch observations. Additional 2 sources, for which $r_{\rm BLR}$ values were deduced but reliable host-subtracted source luminosities are not available (IC4329A and ESO374-G25), are depicted as yellow stars in Fig.11.

Figure 11 also incorporates previously reported size measurements based on the RM of the Hα line: 7 low-luminosity sources from Bentz et al. (2010, 2013); 14 high-luminosity sources (PG quasars for which the host contribution to the flux is negligible) as documented in Kaspi et al. 2000; re-

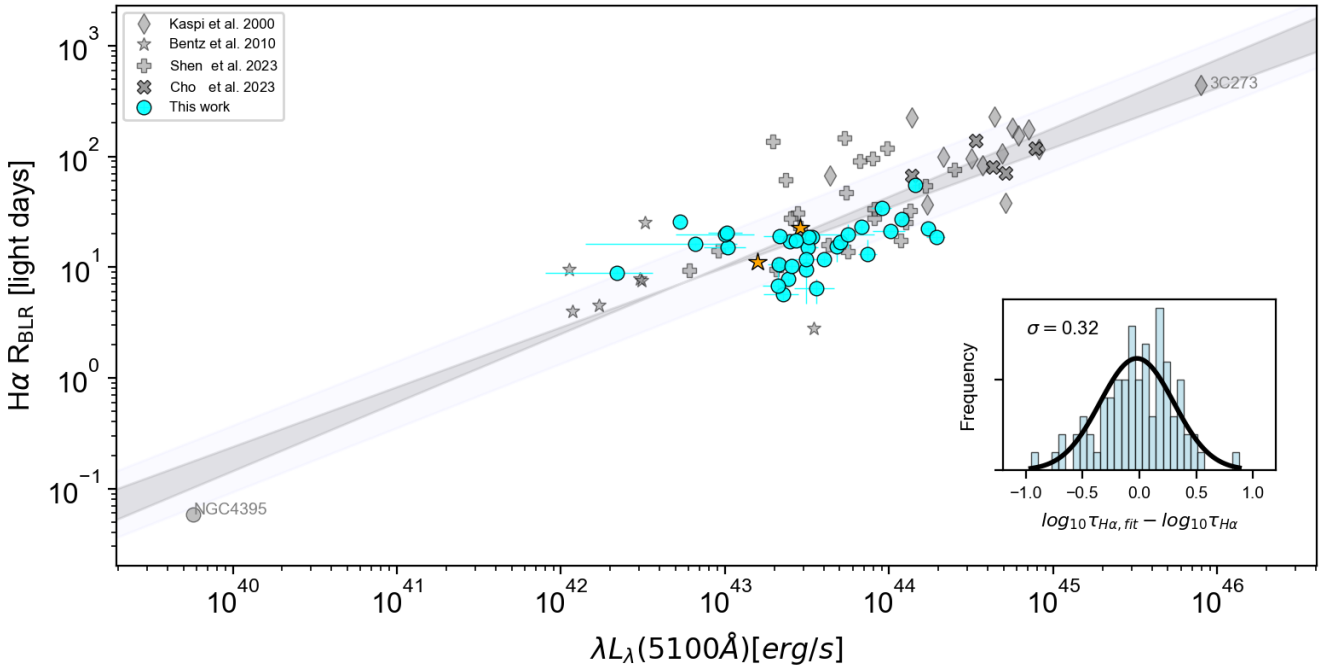

Figure 11. Hα $r_{\rm BLR}$-L diagram. Cyan circles show the results obtained in this work and orange stars the objects from this work where the host subtraction was not succesful. Grey diamonds, stars, pluses and crosses represent previous results from Kaspi et al. (2000), Bentz et al. (2010), Shen et al. (2023) and Cho et al. (2023) respectively. The result for NGC4395 from Cho et al. (2021) is marked with a circle and labeled as well as 3C273 at the high luminous end. Grey shaded area represents the best linear-fit with the value $K = 1.51 \pm 0.05$ and $\gamma = 0.57 \pm 0.05$ (see text). The enclosed pannel shows the distribution of the difference between the RM delays and the expected value from the best-fit. The total scatter for the relation is $\sigma = 0.32$dex, which is also shown as light blue area around the best fit.

Table 2. This work and previous reported BH masses.

	This work	Literature	
Object	$M_{\rm BH}$ $[10^7 M_\odot]$	$M_{\rm BH,Lit}$ $[10^7 M_\odot]$	Ref.
3C120	$9.27^{+0.96}_{-0.96}$	4.23 ± 0.63	(1) (2) (3)
AKN120	$15.9^{+0.82}_{-0.94}$	24.31 ± 3.24	(1)
HE1136-2304	$2.18^{+0.14}_{-0.06}$	2.11 ± 1.60	(4)
IC4329A	$10.69^{+0.38}_{-0.38}$	7.22 ± 0.36	(5)
MRK335	$0.60^{+0.04}_{-0.05}$	0.49 ± 0.15	(1), (3), (6)
MRK509	$5.17^{+0.2}_{-0.2}$	11.50 ± 0.88	(1)
NGC5940	$1.82^{+0.26}_{-0.22}$	1.17 ± 0.18	(7)
NGC7469	$0.35^{+0.13}_{-0.18}$	0.32 ± 0.07	(1) (8)
Mrk841	$9.72^{+0.92}_{-0.89}$	12.19 ± 5.22	(9)
NGC985	$9.12^{+0.32}_{-0.37}$	2.37 ± 3.10	(9)

NOTE—Ref: (1) Peterson et al. (2004), (2) Kollatschny et al. (2014), (3) Grier et al. (2012a), (4) Kollatschny et al. (2018), (5) Bentz et al. (2023), (6) Du et al. (2014), (7) Barth et al. (2013), (8) Collier et al. (1998), (9) U et al. (2022)

cent findings for 23 intermediate-luminosity sources from the SDSS-RM project (Shen et al. 2023, see also Grier et al. 2017); 5 high-luminosity AGN recently studied by Cho et al. (2023) and the intermediate-mass AGN NGC4395 presented in Cho et al. (2021, see also Edri et al. 2012). All the values from the literature are listed in Table F.1 in the Appendix. Combined, this totals in 82 sources with varying measurement quality comprising the size-luminosity relation for Hα, which covers 4 dex in source luminosity.

A best-fit relation for the combined sample is shown in Figure 11 with a grey area , which is of the form:

$$\log(r_{\rm BLR,ld}) = K + \gamma \log(L_{5100,44}) \quad (5)$$

where $r_{\rm BLR,ld} = r_{\rm BLR}/1$ light-days, $L_{5100,44} = L_{5100}/10^{44}$erg s^{-1}. We employed orthogonal distance regression (ODR) fitting (Isobe et al. 1990) to determine the optimal parameters K and γ, considering uncertainties in both luminosity and time lag and found $K = 1.51 \pm 0.05$ for the normalization constant and $\gamma = 0.57 \pm 0.05$ for the slope. The latest findings from Cho et al. (2023) report values of $K = 1.59 \pm 0.05$ and $\gamma = 0.58 \pm 0.04$, nearly identical to this work. The luminosities in our sample span the mid-range and generally exhibit smaller sizes compared to SDSS values, but the overall slope is not affected.

These values are in very agreement with the best-fit values deduced by Bentz et al. (2013, see their Table 14) for the Hβ line with $K = 1.527 \pm 0.031$ and $\gamma = 0.533 \pm 0.035$. Restricting the fit to sources in our sample yields a flatter relation with $\gamma = 0.17 \pm 0.04$, which is dominated by the lowest luminosity targets having larger luminosity uncertainties. Further restricting to the fit to the 29 most luminous sources in our sample with $\lambda L_\lambda(5100\,\text{Å}) > 1.5 \times 10^{43}$ erg s^{-1} yields a slope $\gamma = 0.48 \pm 0.08$.

Table 3. Time delays, luminosities, $M_{\rm BH}$ and accretion rate estimations. Time lags are expressed in observers frame. L_{5100} notes the restframe luminosity at 5100Å and the accretion rate estimators $\log\dot{\mathscr{M}}$ and $\log\dot{\mathscr{M}}_{R_{\rm Fe}}$ are obtained from Equation 6 and 7 respectively.

Object	z	$\tau_{\rm cent,H\alpha}$ [days]	$\tau_{\rm peak,H\alpha}$ [days]	L_{5100} [10^{43}erg/s]	$M_{\rm BH}$ [$10^7 M_\odot$]	$\log\dot{\mathscr{M}}$	$\log\dot{\mathscr{M}}_{R_{\rm Fe}}$
1H2107-097	0.02698	$15.7^{+4.2}_{-4.2}$	$11.2^{+1.4}_{-1.4}$	4.77 ± 0.12	$1.63^{+0.45}_{-0.45}$	$1.34^{+0.24}_{-0.24}$	-0.55 ± 0.01
3C120	0.03301	$57.1^{+5.9}_{-5.9}$	$55.2^{+30.0}_{-4.4}$	14.34 ± 0.37	$9.27^{+0.99}_{-0.99}$	$-0.48^{+0.09}_{-0.09}$	-1.88 ± 0.22
AKN120	0.0327	$28.1^{+1.4}_{-1.6}$	$18.6^{+23.0}_{-1.4}$	11.91 ± 0.43	$15.98^{+0.82}_{-0.94}$	$-1.85^{+0.05}_{-0.05}$	0.56 ± 0.0
CTSG03_04	0.04002	$17.8^{+0.9}_{-0.9}$	$14.8^{+0.4}_{-1.4}$	2.47 ± 0.41	$3.11^{+0.16}_{-0.16}$	$-0.93^{+0.09}_{-0.09}$	-2.19 ± 0.43
ESO374-G25	0.02367	$11.2^{+1.0}_{-2.0}$	$7.6^{+14.2}_{-2.5}$	$< 1.58^{*}$	$4.31^{+0.39}_{-0.79}$	–	1.47 ± 0.001
ESO399-IG20	0.025	$19.6^{+0.4}_{-0.8}$	$24.4^{+0.8}_{-5.2}$	2.16 ± 0.45	$1.27^{+0.03}_{-0.05}$	$0.65^{+0.1}_{-0.11}$	-0.3 ± 0.01
ESO578-G09	0.03502	$19.5^{+0.6}_{-0.6}$	$19.6^{+2.0}_{-12.8}$	3.39 ± 0.17	$9.7^{+0.31}_{-0.31}$	$-2.74^{+0.04}_{-0.04}$	-0.31 ± 0.01
F1041	0.03347	$15.7^{+0.7}_{-1.0}$	$16.4^{+0.4}_{-0.0}$	1.04 ± 0.3	$4.03^{+0.19}_{-0.27}$	$-2.75^{+0.15}_{-0.15}$	–
HE1136-2304	0.027	$9.1^{+0.5}_{-0.2}$	$10.6^{+1.0}_{-1.0}$	0.22 ± 0.14	$2.18^{+0.12}_{-0.05}$	$-3.85^{+0.31}_{-0.31}$	-1.42 ± 0.07
HE1143-1810	0.03295	$17.5^{+2.5}_{-2.4}$	$21.2^{+0.2}_{-1.2}$	5.01 ± 0.44	$1.53^{+0.23}_{-0.22}$	$1.55^{+0.14}_{-0.13}$	-1.83 ± 0.23
HE2128-0221	0.05248	$8.3^{+0.7}_{-0.9}$	$9.2^{+5.6}_{-5.8}$	2.43 ± 0.21	$0.44^{+0.04}_{-0.05}$	$2.96^{+0.09}_{-0.11}$	0.12 ± 0.01
IC4329A	0.01605	$22.7^{+0.8}_{-0.8}$	$13.4^{+14.0}_{-0.6}$	2.87*	$10.69^{+0.38}_{-0.38}$	–	-1.55 ± 0.153
MCG+03-47-002	0.04	$16.8^{+0.4}_{-0.5}$	$18.8^{+0.0}_{-0.2}$	0.66 ± 0.52	–	–	–
MRK1347	0.04995	$13.8^{+4.6}_{-1.7}$	$21.2^{+1.0}_{-16.8}$	7.41 ± 0.97	$0.64^{+0.22}_{-0.08}$	$3.87^{+0.31}_{-0.13}$	0.76 ± 0.0
MRK335	0.02578	$12.0^{+0.9}_{-1.1}$	$11.2^{+0.2}_{-5.2}$	3.99 ± 0.22	$0.6^{+0.05}_{-0.06}$	$3.09^{+0.07}_{-0.09}$	-1.06 ± 0.04
MRK509	0.0344	$22.9^{+0.8}_{-0.8}$	$24.4^{+0.4}_{-1.6}$	17.31 ± 1.53	$5.17^{+0.19}_{-0.19}$	$0.97^{+0.05}_{-0.05}$	-1.59 ± 0.11
MRK705	0.02879	$15.5^{+1.0}_{-0.7}$	$11.6^{+0.0}_{-0.8}$	3.21 ± 0.48	$1.09^{+0.07}_{-0.05}$	$1.56^{+0.09}_{-0.08}$	-0.44 ± 0.01
MRK841	0.03642	$23.8^{+2.5}_{-2.4}$	$20.8^{+12.0}_{-1.6}$	6.75 ± 0.27	$9.72^{+1.06}_{-1.02}$	$-1.71^{+0.1}_{-0.09}$	-1.8 ± 0.18
NGC5940	0.03408	$5.9^{+0.8}_{-0.7}$	$5.2^{+0.8}_{-0.4}$	2.26 ± 0.54	$1.82^{+0.26}_{-0.22}$	$0.002^{+0.17}_{-0.16}$	0.32 ± 0.0
NGC7214	0.02385	$6.9^{+5.2}_{-0.9}$	$5.2^{+0.4}_{-0.4}$	2.1 ± 0.41	$1.77^{+1.37}_{-0.24}$	$-0.05^{+0.68}_{-0.15}$	3.16 ± 0.0
NGC7469	0.01627	$9.6^{+3.5}_{-4.8}$	$16.0^{+0.0}_{-0.4}$	3.12 ± 0.31	$0.35^{+0.13}_{-0.18}$	$3.8^{+0.33}_{-0.44}$	-1.11 ± 0.06
NGC7603	0.02876	$35.1^{+1.5}_{-1.3}$	$36.8^{+4.0}_{-1.2}$	9.04 ± 1.22	$22.34^{+0.98}_{-0.85}$	$-2.93^{+0.08}_{-0.07}$	0.31 ± 0.0
NGC985	0.04314	$22.2^{+0.7}_{-0.8}$	$24.0^{+0.4}_{-0.4}$	10.2 ± 2.3	$9.12^{+0.3}_{-0.34}$	$-0.96^{+0.11}_{-0.11}$	-2.1 ± 0.35
PGC64989	0.01937	$26.0^{+0.3}_{-0.3}$	$26.8^{+0.2}_{-2.4}$	0.53 ± 0.02	$5.37^{+0.06}_{-0.06}$	$-4.33^{+0.02}_{-0.02}$	-1.59 ± 0.13
RXSJ06225-2317	0.03778	$19.5^{+0.2}_{-1.4}$	$20.0^{+0.0}_{-0.4}$	3.23 ± 0.46	$0.84^{+0.01}_{-0.06}$	$2.1^{+0.07}_{-0.1}$	-1.98 ± 0.27
UM163	0.03343	$10.9^{+0.4}_{-0.5}$	$10.0^{+0.8}_{-0.4}$	2.12 ± 0.31	$4.97^{+0.19}_{-0.24}$	$-2.1^{+0.08}_{-0.08}$	-0.81 ± 0.05
WPVS007	0.02861	$10.6^{+0.9}_{-1.0}$	$10.4^{+0.0}_{-0.4}$	2.56 ± 0.21	$0.49^{+0.04}_{-0.05}$	$2.82^{+0.09}_{-0.09}$	4.24 ± 0.0
ESO141-G55	0.03711	$19.6^{+2.4}_{-2.4}$	$19.2^{+4.4}_{-4.4}$	19.35 ± 2.58	$9.15^{+1.17}_{-1.17}$	$-0.002^{+0.13}_{-0.13}$	-0.62 ± 0.01
ESO438-G09	0.02401	$12.1^{+0.6}_{-0.6}$	$10.2^{+6.2}_{-6.2}$	3.13 ± 0.66	$1.23^{+0.06}_{-0.06}$	$1.28^{+0.11}_{-0.11}$	5.19 ± 0.0
ESO511-G030	0.02239	$20.1^{+1.2}_{-1.2}$	$17.9^{+0.4}_{-0.4}$	1.0 ± 0.5	$5.15^{+0.3}_{-0.3}$	$-3.3^{+0.25}_{-0.25}$	-1.11 ± 0.06
PGC50247	0.02346	$21.0^{+1.4}_{-1.4}$	$19.9^{+1.6}_{-1.6}$	1.02 ± 0.24	$2.27^{+0.16}_{-0.16}$	$-1.63^{+0.13}_{-0.13}$	-1.57 ± 0.13
RXSJ17414+0348	0.023	$17.8^{+1.9}_{-1.9}$	$17.8^{+5.6}_{-5.6}$	2.69 ± 0.69	$1.69^{+0.18}_{-0.18}$	$0.41^{+0.16}_{-0.16}$	0.98 ± 0.0
WPVS48	0.037	$20.3^{+4.6}_{-4.6}$	$20.7^{+5.0}_{-5.0}$	5.59 ± 2.49	$1.41^{+0.34}_{-0.34}$	$1.87^{+0.3}_{-0.3}$	-0.75 ± 0.02

NOTE—* not possible to obtain host-subtractd fluxes, L_{5100} reported for the 5100Å interpolated observed fluxes

The residual scatter of the full Hα sample around the best-fit Hα relation is $\simeq$ 0.32 dex (see distribution in Fig. 11), which is larger than the value deduced for the Hβ line ($\simeq$ 0.19 dex Bentz et al. 2013). In comparison, the residual scatter in our sample of 31 sources is 0.26 dex, which is lower than that which characterizes the SDSS-RM sample (0.34 dex). Further restricting the analysis to the 29 brightest sources, yields a scatter of $\simeq$ 0.17 dex, which is comparable to that reported for the Hβ line.

We note that the lags in our sample tend to lie below the current size-luminosity relation, by $\sim 9\%$, on average, which could be at least partly due to over-estimated nuclear luminosities for some of the sources (see above and Appendix H for comments on individual objects). Nevertheless, comparing the Hα to existing Hβ size measurement shows consistency with previous studies (see §4.4.3).

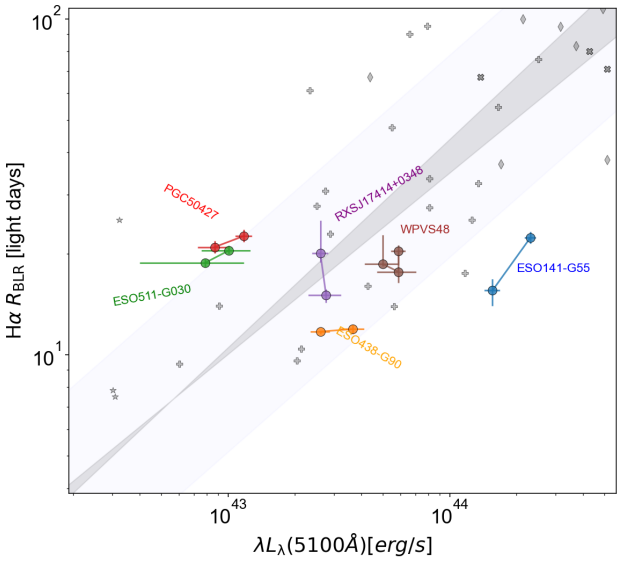

Figure 12. The BLR size-luminosity relation for multi-epoch sources. The results for our objects are shown with different colors, connected with lines and labeled. Values for single-epoch results for Hα from the literature are also shown (same as Figure 11).. The tight clustering of the measureents per object indicates the stability of our PRM approach. The modest luminosity variations of the sources preclude a detailed analysis of the intrinsic size-luminosity relation.

4.4.1. *Testing for an intrinsic size-luminosity relation and lag stability*

Our campaign spans a long enough timeline so that intrinsic changes to the BLR size in response to substantial luminosity variations of the sources could be detected (Cackett & Horne 2006). Multi-epoch campaigns spanning two or more years were conducted for 12 sources in our sample, yielding Hα delays for 6 of them (refer to the Table 3 for averaged values and Table G.1 for single-epoch results). These multi-epoch observation campaigns provide independent size-luminosity measurements, as illustrated in Figure 12.

The lag-measurement uncertainties and the modest luminosity variations of the sources do not allow to confidently quantify an intrinsic size-luminosity relation and a consistent intrinsic $r - L$ relation cannot be deduced. Time-delay differences between epochs of individual sources are consistent with a scatter of $\sim$ 0.10 on average, which is significantly smaller than the scatter deduced for the entire sample.

4.4.2. *The size-luminosity relation and the accretion rate*

Previous works based on the RM results for the Hβ line found that high accreting sources tend to lie below the population-average $r_{\rm BLR} - L$ relation (Du et al. 2016b, 2018; Martínez-Aldama et al. 2019; Panda & Marziani 2023). Using the single epoch spectra, we estimate the value for the BH mass (see Section 4.3) and calculate the dimensionless accretion rate of our sample as described in Du et al. (2016b):

$$\dot{\mathscr{M}} = 20.1 \left[\frac{L_{5100,44}}{\cos(\theta)}\right]^{3/2} M_{\rm BH,7}^{-2} \qquad (6)$$

where θ is the AGN inclination, and $M_{\rm BH,7} = M_{\rm BH}/10^7\, M_\odot$. We set $\cos(\theta) = 0.75$ as in Du et al. (2016b) taking into account the mean AGN disk inclination. This is justified for our sources over the optical range for which the optical emission, after host-subtraction, is thought to be dominated by the self-similar part of the disk. $\dot{\mathscr{M}}$-values are given in Table 3, implying that, on (geometrical) average, the sources in our full sample (Table G.1) emit with $\dot{\mathscr{M}} \sim 0.6$, but with $\sim 20\%$ of the sources exceeding unity and reaching up to $\dot{\mathscr{M}} \sim 40$, and hence deep within the super-Eddington accretion limit.

While it is tempting to locate our highly accreting sources on the $r_{\rm BLR} - L$ relation, we note a natural tendency for sources in our sample with shorter time-delays (hence smaller black hole masses) to exhibit a higher accretion rate for a given source luminosity. We, therefore, opt to use a second estimator, which is independent of our BLR size measurements and is based on the ratio of the iron-blend flux to the broad Hβ-line flux, $R_{\rm Fe}$ (Marziani et al. 2001; Panda et al. 2019). Specifically, we consider the scaling of Du et al. (2016a) wherein

$$\dot{\mathscr{M}} \simeq \exp\left[7.7(R_{\rm Fe} - 0.66)\right]. \qquad (7)$$

The above linear relation likely breaks at the highest $R_{\rm Fe}$ values, and results in severely over-estimated mass-accretion rates, and yet it preserves monotonicity, and is not biased by our time-lag measurements. The resulting $r_{\rm BLR} - L$ shows the tendency for objects with high $\dot{\mathscr{M}}$ values to lie below the general population (Fig. 13), a result which is consistent with previous studies using the Hβ line (Du et al. 2018), but is corroborated here for the first time using a different emission line, and applying a different RM technique for an independent sample of sources. Using a permutation scheme which randomly reassigns $\dot{\mathscr{M}}$ values to sources we find that the formal confidence level of the result is $> 98\%$. We further note that the result holds also when considering $\dot{\mathscr{M}}$ estimates derived by Eq. 6 further implying that our lag measurements are meaningful.

4.4.3. *Hα to Hβ lag ratio*

Some of the sources in our sample have published Hβ time-delays from previous campaigns. A comparison between non-contemporaneous Hα and Hβ time-delays measurements is not meaningful on an object-by-object basis, but can be instructive across the sample as a whole. The objects from our study, with corresponding values and references is listed in Table 4. For our sample, we determine the Hα to Hβ ratios for MRK335, 3C120, AKN120, NGC5940, MRK509, NGC7469, HE1136-2304, IC4329A, NGC985, and MRK841 as 1.34, 1.98, 0.73, 1.00, 0.27, 0.87, 1.18, 1.37, 2.87, and 2.05, respectively. MRK509 exhibits an unusually

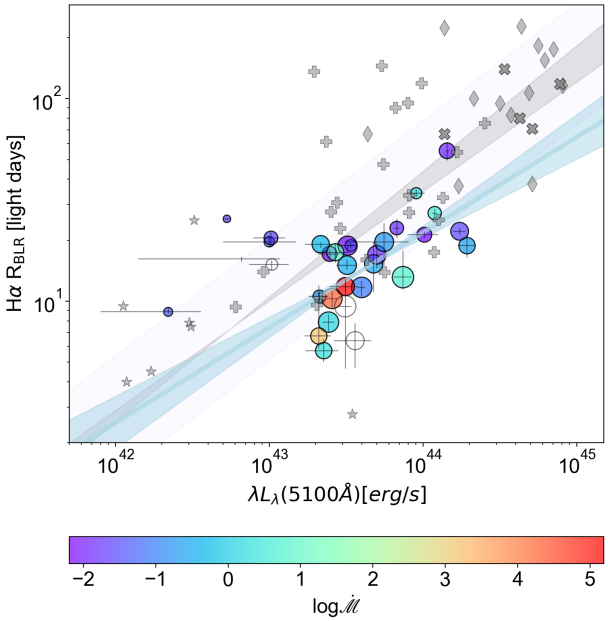

Figure 13. The BLR size-luminosity relation for the Hα line color coded by the dimensionless accretion rate, $\dot{\mathscr{M}}$ (see text), as estimated by $R_{\rm Fe}$ (see Equation 7 and note that the method, while maintaining monotonicty, likely overestimates the highest accretion rates by a large factor). There is a tendency for highly accreting sources to lie below the population mean, which is in agreement with studies based on the Hβ line. The size of the symbols corresponds to the value of $\dot{\mathscr{M}}$ (in log units) as deduced by Eq. 6 (see text for an inherent bias with this method). The blue shaded area represents the best fit for our sample with luminosities $> 1.5 \times 10^{43}$erg/s.

Table 4. Hα (this work) and Hβ (literature) restframe delays.

Object	z	$\tau_{H\alpha}$ [days]	$\tau_{H\beta}$ [days]	Ref.
3C120	0.03301	$55.3^{+5.9}_{-5.9}$	$27.9^{+7.1}_{-5.9}$	(1)
AKN120	0.0327	$27.2^{+1.4}_{-1.4}$	$37.1^{+4.8}_{-5.4}$	(2)
HE1136-2304	0.027	$8.9^{+0.5}_{-0.5}$	$7.5^{+4.6}_{-5.7}$	(3)
IC4329A	0.01601	$22.3^{+0.8}_{-0.8}$	$16.3^{+2.6}_{-2.3}$	(4)
Mrk335	0.02578	$11.7^{+1.0}_{-1.0}$	$8.7^{+1.6}_{-1.9}$	(5)
Mrk509	0.0344	$22.1^{+0.8}_{-0.8}$	$79.6^{+6.1}_{-5.4}$	(2)
Mrk841	0.03642	$23.0^{+2.5}_{-2.5}$	$11.2^{+4.8}_{-1.9}$	(6)
NGC5940	0.03408	$5.7^{+0.8}_{-0.8}$	$5.70^{+0.90}_{-0.82}$	(7)
NGC7469	0.01627	$9.4^{+3.5}_{-4.5}$	$10.8^{+3.4}_{-1.3}$	(8)
NGC985	0.04314	$21.3^{+0.7}_{-0.7}$	$7.4^{+9.7}_{-9.4}$	(6)

NOTE—Ref: (1) Kollatschny et al. (2014), (2) Peterson et al. (2004), (3) Kollatschny et al. (2018), (4) Bentz et al. (2023), (5) Du et al. (2016b), (6) U et al. (2022), (7) Barth et al. (2013), (8) Peterson et al. (2014).

low Hα to Hβ ratio, possibly due to insufficient cadence in Hβ observations affecting the reliability of the delay recovery. When considering only the objects included in our study, the median is 1.26 ± 0.71, and the average is 1.36 ± 0.71. Despite variations in observational epochs among objects, Hα ratios are generally found to be slightly larger than those of Hβ. For comparison, the median ratio of Hα to Hβ across all sources in the samples from Kaspi et al. (2000), Bentz et al. (2010) and Shen et al. (2023) is 1.39±0.845, with an average of 1.57±0.85.

5. SUMMARY AND CONCLUSIONS

We present the results of a first-of-its-kind multi-epoch PRM survey of a sample of 80 AGN, which was carried out over the course of about a decade (2010-2018) using small aperture ($\gtrsim 0.1$ m-class) telescopes at the Cerro Armazones Observatory (OCA) in the Atacama Desert. The photometric data were augmented with single-epoch spectroscopy, and allow us to characterize the properties of the Hα emitting BLR in those sources. Below is a summary of the main points of the paper:

- Using small aperture telescopes, PRM can provide highly competitive results compared to spectroscopic RM (SRM), which typically uses larger ($\gtrsim$ 1 m) aperture instruments with two fold greater light collecting area. This is demonstrated in this work for the prominent Hα line in nearby ($0.01 < z < 0.05$) sources whose line emission coincides with a set of off-the-shelf narrowband filters.

- We introduce a new PRM correlation scheme, which is drawn from spectroscopic binary identification, and implement it using a combination of (interpolated) auto- and cross-correlation functions, which are commonly used in the field. The method quantifies the properties of the delayed signal being the time-delay and the relative contribution of the delayed component to the narrowband data, but is generally applicable to PRM and SRM data. Applying it to our sample, we are able to successfully measure time-delays between line and continuum emission (traced by broadband photometry) in $\simeq 60\%$ of our sources.

- Augmenting our photometric data with single-epoch high-quality optical spectra, and using detailed multi-component fit to the Hα emission line, we estimate the BH masses for our sample, which are consistent with previously reported estimates for 10 of our targets to within 0.3 dex. Fitting for the Hβ line and the iron-blend emission in its vicinity, we are able estimate the mass accretion rate for most objects in our sample in a way which is independent of our lag measurements.

- To estimate the nuclear luminosity of our sources, we apply the FVG method for host-galaxy subtraction based on our set of photometric bands. Successful host subtraction was achieved for 84% of our sample. For sources with multi-epoch data, we generally find consistent result, but note a few exceptions in our data, which can be traced to

observational effects (filter changes) or to physical effects (changing-look sources).

- We add a total of 31 objects to the $r_{\rm BLR} - L$ relation for Hα. The scatter for the total sample is $\simeq$ 0.32 dex and for our sample is $\simeq$ 0.26 dex. For the luminous ($L_{5100} > 10^{43}$ erg s^{-1}) sources in our sample, the scatter around the best-fit relation is $\simeq$ 0.17 dex, and hence comparable to that found for the Hβ.

- Taking our measured Hα time-delays and comparing to Hβ lags from the literature, we find an average $\tau_{\rm H\alpha}/\tau_{\rm H\beta}$ of 1.36 ± 0.71, which agrees for the total compilation with previous studies with 1.57 ± 0.85. This consistency shows that the time-delays measured here are not significantly under- or overestimated.

- We report multi-epoch time-delays for 6 sources in our sample, which are found to be stable with an overall scatter of $\simeq$ 0.04 dex, which is much smaller than that which characterizes the size-luminosity relation ($\gtrsim$ 0.2 dex depending on the sample used) thereby suggesting another origin for the latter perhaps associated with physical differences between the sources (see below) or to residual uncertainties in luminosity determination). Given the modest luminosity variations of individual sources during our campaign, we cannot robustly constrain an intrinsic size-luminosity relation.

- We corroborate, for the first time using an emission line other than Hβ, the trend whereby highly accreting sources tend to lie below the general-population BLR size-luminosity relation. Specifically, the trend is observed for two independent methods for assessing $\dot{\mathscr{M}}$, and their consistency further supports our lag measurements.

ACKNOWLEDGEMENTS

Michael Ramolla, Christian Westhues, Hector Labra, Gerardo Pino, Roberto Munoz, Francisco Arraya, Zohreh Ghaffari, Victor Oknyanskyi, Saar Katalan, Carina Fian, Sina Chen, SNS. NED. This research has made use of the VizieR catalogue access tool, CDS, Strasbourg, France (DOI : 10.26093/cds/vizier). The original description of the VizieR service was published in 2000, A&AS 143, 23. This work was partly supported by grants from the German Research Foundation (HA3555-14/1, CH71-34-3) and by a grant from the Israeli Science Foundation (2398/19). Computations made use of high-performance computing facilities at the University of Haifa, which are partly supported by a grant from the Israeli Science Foundation (grant 2155/15). SP acknowledges the financial support of the Conselho Nacional de Desenvolvimento Científico e Tecnológico (CNPq) Fellowships 300936/2023-0 and 301628/2024-6. SP is supported by the international Gemini Observatory, a program of NSF NOIRLab, which is managed by the Association of Universities for Research in Astronomy (AURA) under a cooperative agreement with the U.S. National Science Foundation, on behalf of the Gemini partnership of Argentina, Brazil, Canada, Chile, the Republic of Korea, and the United States of America.

DATA AVAILABILITY

We provide all light curves and the results presented in Table G.1 in ...

REFERENCES

Agazie, G., Anumarlapudi, A., Archibald, A. M., et al. 2023, ApJL, 952, L37, doi: 10.3847/2041-8213/ace18b

Amaro-Seoane, P., Andrews, J., Arca Sedda, M., et al. 2022, arXiv e-prints, arXiv:2203.06016. https://arxiv.org/abs/2203.06016

Barth, A. J., Pancoast, A., Bennert, V. N., et al. 2013, ApJ, 769, 128, doi: 10.1088/0004-637X/769/2/128

Barth, A. J., Bennert, V. N., Canalizo, G., et al. 2015, ApJS, 217, 26, doi: 10.1088/0067-0049/217/2/26

Batiste, M., Bentz, M. C., Raimundo, S. I., Vestergaard, M., & Onken, C. A. 2017, ApJL, 838, L10, doi: 10.3847/2041-8213/aa6571

Bentz, M. C., & Katz, S. 2015, PASP, 127, 67, doi: 10.1086/679601

Bentz, M. C., Onken, C. A., Street, R., & Valluri, M. 2023, ApJ, 944, 29, doi: 10.3847/1538-4357/acab62

Bentz, M. C., Walsh, J. L., Barth, A. J., et al. 2010, ApJ, 716, 993, doi: 10.1088/0004-637X/716/2/993

Bentz, M. C., Denney, K. D., Grier, C. J., et al. 2013, ApJ, 767, 149, doi: 10.1088/0004-637X/767/2/149

Boris, N. V., Donzelli, C. J., Pastoriza, M. G., Rodriguez-Ardila, A., & Ferreiro, D. L. 2002, A&A, 384, 780, doi: 10.1051/0004-6361:20020066

Boroson, T. A., & Green, R. F. 1992, ApJS, 80, 109, doi: 10.1086/191661

Buckley, D. A. H., Swart, G. P., & Meiring, J. G. 2006, in Society of Photo-Optical Instrumentation Engineers (SPIE) Conference Series, Vol. 6267, Society of Photo-Optical Instrumentation Engineers (SPIE) Conference Series, ed. L. M. Stepp, 62670Z, doi: 10.1117/12.673750

Cackett, E. M., Bentz, M. C., & Kara, E. 2021, iScience, 24, 102557, doi: 10.1016/j.isci.2021.102557

Cackett, E. M., & Horne, K. 2006, MNRAS, 365, 1180, doi: 10.1111/j.1365-2966.2005.09795.x

Chelouche, D. 2013, ApJ, 772, 9, doi: 10.1088/0004-637X/772/1/9

Chelouche, D., & Daniel, E. 2012, ApJ, 747, 62, doi: 10.1088/0004-637X/747/1/62
Chelouche, D., Pozo Nuñez, F., & Kaspi, S. 2019, Nature Astronomy, 3, 251, doi: 10.1038/s41550-018-0659-x
Chelouche, D., & Zucker, S. 2013, ApJ, 769, 124, doi: 10.1088/0004-637X/769/2/124
Chen, S., Berton, M., La Mura, G., et al. 2018, A&A, 615, A167, doi: 10.1051/0004-6361/201832678
Cho, H., Woo, J.-H., Treu, T., et al. 2021, ApJ, 921, 98, doi: 10.3847/1538-4357/ac1e92
Cho, H., Woo, J.-H., Wang, S., et al. 2023, ApJ, 953, 142, doi: 10.3847/1538-4357/ace1e5
Choloniewski, J. 1981, AcA, 31, 293
Chonis, T. S., Hill, G. J., Lee, H., et al. 2016, Society of Photo-Optical Instrumentation Engineers (SPIE) Conference Series, Vol. 9908, LRS2: design, assembly, testing, and commissioning of the second-generation low-resolution spectrograph for the Hobby-Eberly Telescope, 99084C, doi: 10.1117/12.2232209
Coatman, L., Hewett, P. C., Banerji, M., & Richards, G. T. 2016, MNRAS, 461, 647, doi: 10.1093/mnras/stw1360
Collier, S. J., Horne, K., Kaspi, S., et al. 1998, ApJ, 500, 162, doi: 10.1086/305720
Cracco, V., Ciroi, S., Berton, M., et al. 2016, MNRAS, 462, 1256, doi: 10.1093/mnras/stw1689
Czerny, B., Nikołajuk, M., Różańska, A., et al. 2003, A&A, 412, 317, doi: 10.1051/0004-6361:20031441
Czerny, B., Panda, S., Prince, R., et al. 2023, A&A, 675, A163, doi: 10.1051/0004-6361/202345844
Dalla Bontà, E., Peterson, B. M., Bentz, M. C., et al. 2020, ApJ, 903, 112, doi: 10.3847/1538-4357/abbc1c
Dexter, J., & Begelman, M. C. 2019, MNRAS, 483, L17, doi: 10.1093/mnrasl/sly213
Du, P., Wang, J.-M., Hu, C., et al. 2016a, ApJL, 818, L14, doi: 10.3847/2041-8205/818/1/L14
Du, P., Hu, C., Lu, K.-X., et al. 2014, ApJ, 782, 45, doi: 10.1088/0004-637X/782/1/45
Du, P., Lu, K.-X., Zhang, Z.-X., et al. 2016b, ApJ, 825, 126, doi: 10.3847/0004-637X/825/2/126
Du, P., Zhang, Z.-X., Wang, K., et al. 2018, ApJ, 856, 6, doi: 10.3847/1538-4357/aaae6b
Edri, H., Rafter, S. E., Chelouche, D., Kaspi, S., & Behar, E. 2012, ApJ, 756, 73, doi: 10.1088/0004-637X/756/1/73
Fabricant, D., Cheimets, P., Caldwell, N., & Geary, J. 1998, PASP, 110, 79, doi: 10.1086/316111
Farrah, D., Efstathiou, A., Afonso, J., et al. 2022, MNRAS, 513, 4770, doi: 10.1093/mnras/stac980
Gaskell, C. M., & Peterson, B. M. 1987, ApJS, 65, 1, doi: 10.1086/191216
Gaskell, C. M., & Sparke, L. S. 1986, ApJ, 305, 175, doi: 10.1086/164238
Ghosh, R., & Laha, S. 2021, ApJ, 908, 198, doi: 10.3847/1538-4357/abd40c
Gianniotis, N., Pozo Nuñez, F., & Polsterer, K. L. 2022, A&A, 657, A126, doi: 10.1051/0004-6361/202141710
Graham, A. W., Onken, C. A., Athanassoula, E., & Combes, F. 2011, MNRAS, 412, 2211, doi: 10.1111/j.1365-2966.2010.18045.x
Gravity Collaboration, Sturm, E., Dexter, J., et al. 2018, Nature, 563, 657, doi: 10.1038/s41586-018-0731-9
Grier, C. J., Peterson, B. M., Pogge, R. W., et al. 2012a, ApJL, 744, L4, doi: 10.1088/2041-8205/744/1/L4
—. 2012b, ApJ, 755, 60, doi: 10.1088/0004-637X/755/1/60
Grier, C. J., Martini, P., Watson, L. C., et al. 2013, ApJ, 773, 90, doi: 10.1088/0004-637X/773/2/90
Grier, C. J., Trump, J. R., Shen, Y., et al. 2017, ApJ, 851, 21, doi: 10.3847/1538-4357/aa98dc
Guo, H., Shen, Y., & Wang, S. 2018, PyQSOFit: Python code to fit the spectrum of quasars, Astrophysics Source Code Library, record ascl:1809.008
Haas, M., Chini, R., Ramolla, M., et al. 2011, A&A, 535, A73, doi: 10.1051/0004-6361/201117325
Haas, M., Hackstein, M., Ramolla, M., et al. 2012, Astronomische Nachrichten, 333, 706, doi: 10.1002/asna.201211717
Hill, G. J., Drory, N., Good, J. M., et al. 2018, in Society of Photo-Optical Instrumentation Engineers (SPIE) Conference Series, Vol. 10700, Proc. SPIE, 107000P, doi: 10.1117/12.2312350
Isobe, T., Feigelson, E. D., Akritas, M. G., & Babu, G. J. 1990, ApJ, 364, 104, doi: 10.1086/169390
Jones, D. H., Read, M. A., Saunders, W., et al. 2009, MNRAS, 399, 683, doi: 10.1111/j.1365-2966.2009.15338.x
Kabath, P., Erikson, A., Rauer, H., et al. 2009, A&A, 506, 569, doi: 10.1051/0004-6361/200911909
Kaspi, S., Smith, P. S., Netzer, H., et al. 2000, ApJ, 533, 631, doi: 10.1086/308704
Kelly, B. C., Bechtold, J., & Siemiginowska, A. 2009, ApJ, 698, 895, doi: 10.1088/0004-637X/698/1/895
Kelly, B. C., & Merloni, A. 2012, Advances in Astronomy, 2012, 970858, doi: 10.1155/2012/970858
Kobulnicky, H. A., Nordsieck, K. H., Burgh, E. B., et al. 2003, in Society of Photo-Optical Instrumentation Engineers (SPIE) Conference Series, Vol. 4841, Instrument Design and Performance for Optical/Infrared Ground-based Telescopes, ed. M. Iye & A. F. M. Moorwood, 1634–1644, doi: 10.1117/12.460315
Kollatschny, W., Bischoff, K., & Dietrich, M. 2000, A&A, 361, 901

Kollatschny, W., Ochmann, M. W., Zetzl, M., et al. 2018, A&A, 619, A168, doi: 10.1051/0004-6361/201833727
Kollatschny, W., Ulbrich, K., Zetzl, M., Kaspi, S., & Haas, M. 2014, A&A, 566, A106, doi: 10.1051/0004-6361/201423901
Kollatschny, W., Grupe, D., Parker, M. L., et al. 2020, A&A, 638, A91, doi: 10.1051/0004-6361/202037897
—. 2023, A&A, 670, A103, doi: 10.1051/0004-6361/202244786
Kormendy, J., & Ho, L. C. 2013, ARA&A, 51, 511, doi: 10.1146/annurev-astro-082708-101811
Koss, M., Trakhtenbrot, B., Ricci, C., et al. 2017, ApJ, 850, 74, doi: 10.3847/1538-4357/aa8ec9
Koss, M. J., Ricci, C., Trakhtenbrot, B., et al. 2022, ApJS, 261, 2, doi: 10.3847/1538-4365/ac6c05
Landolt, A. U. 2009, AJ, 137, 4186, doi: 10.1088/0004-6256/137/5/4186
Lu, K.-X., Du, P., Hu, C., et al. 2016, ApJ, 827, 118, doi: 10.3847/0004-637X/827/2/118
Martínez-Aldama, M. L., Czerny, B., Kawka, D., et al. 2019, ApJ, 883, 170, doi: 10.3847/1538-4357/ab3728
Marziani, P., Sulentic, J. W., Zwitter, T., Dultzin-Hacyan, D., & Calvani, M. 2001, ApJ, 558, 553, doi: 10.1086/322286
McLure, R. J., & Dunlop, J. S. 2004, MNRAS, 352, 1390, doi: 10.1111/j.1365-2966.2004.08034.x
Molina, J., Ho, L. C., Wang, R., et al. 2022, ApJ, 935, 72, doi: 10.3847/1538-4357/ac7d4d
Moustakas, J., & Kennicutt, Robert C., J. 2006, ApJS, 164, 81, doi: 10.1086/500971
Onken, C. A., Ferrarese, L., Merritt, D., et al. 2004, ApJ, 615, 645, doi: 10.1086/424655
Padovani, P., Alexander, D. M., Assef, R. J., et al. 2017, A&A Rv, 25, 2, doi: 10.1007/s00159-017-0102-9
Panda, S., & Marziani, P. 2023, Frontiers in Astronomy and Space Sciences, 10, 1130103, doi: 10.3389/fspas.2023.1130103
Panda, S., Marziani, P., & Czerny, B. 2019, ApJ, 882, 79, doi: 10.3847/1538-4357/ab3292
Panda, S., Pozo Nuñez, F., Bañados, E., & Heidt, J. 2024a, ApJL, 968, L16, doi: 10.3847/2041-8213/ad5014
Panda, S., & Śniegowska, M. 2024, ApJS, 272, 13, doi: 10.3847/1538-4365/ad344f
Panda, S., Kozłowski, S., Gromadzki, M., et al. 2024b, ApJS, 272, 11, doi: 10.3847/1538-4365/ad3549
Park, D., Kelly, B. C., Woo, J.-H., & Treu, T. 2012, ApJS, 203, 6, doi: 10.1088/0067-0049/203/1/6
Peterson, B. M. 1993, PASP, 105, 247, doi: 10.1086/133140
Peterson, B. M., & Wandel, A. 2000, ApJL, 540, L13, doi: 10.1086/312862
Peterson, B. M., Wanders, I., Horne, K., et al. 1998, PASP, 110, 660, doi: 10.1086/316177
Peterson, B. M., Ferrarese, L., Gilbert, K. M., et al. 2004, ApJ, 613, 682, doi: 10.1086/423269
Peterson, B. M., Grier, C. J., Horne, K., et al. 2014, ApJ, 795, 149, doi: 10.1088/0004-637X/795/2/149
Planck Collaboration, Ade, P. A. R., Aghanim, N., et al. 2016, A&A, 594, A13, doi: 10.1051/0004-6361/201525830
Pozo Nuñez, F., Haas, M., Chini, R., et al. 2014, A&A, 561, L8, doi: 10.1051/0004-6361/201323178
Pozo Nuñez, F., Ramolla, M., Westhues, C., et al. 2015, A&A, 576, A73, doi: 10.1051/0004-6361/201525910
Ramolla, M. 2012, PhD thesis, Ruhr University, Bochum, Germany
Ramolla, M., Pozo Nuñez, F., Westhues, C., Haas, M., & Chini, R. 2015, A&A, 581, A93, doi: 10.1051/0004-6361/201526846
Ramolla, M., Pozo Nunez, F., Westhues, C., et al. 2014, Revista Mexicana de Astronomia y Astrofisica: Serie de Conferencias, 45
Ramolla, M., Drass, H., Lemke, R., et al. 2013, Astronomische Nachrichten, 334, 1115, doi: 10.1002/asna.201311912
Ramolla, M., Westhues, C., Hackstein, M., et al. 2016, in Society of Photo-Optical Instrumentation Engineers (SPIE) Conference Series, Vol. 9911, Modeling, Systems Engineering, and Project Management for Astronomy VI, ed. G. Z. Angeli & P. Dierickx, 99112M, doi: 10.1117/12.2234018
Ramolla, M., Haas, M., Westhues, C., et al. 2018, A&A, 620, A137, doi: 10.1051/0004-6361/201732081
Ramsey, L. W., Adams, M. T., Barnes, T. G., et al. 1998, in Society of Photo-Optical Instrumentation Engineers (SPIE) Conference Series, Vol. 3352, Advanced Technology Optical/IR Telescopes VI, ed. L. M. Stepp, 34–42, doi: 10.1117/12.319287
Sakata, Y., Minezaki, T., Yoshii, Y., et al. 2010, ApJ, 711, 461, doi: 10.1088/0004-637X/711/1/461
Schlafly, E. F., & Finkbeiner, D. P. 2011, ApJ, 737, 103, doi: 10.1088/0004-637X/737/2/103
Shakura, N. I., & Sunyaev, R. A. 1973, A&A, 24, 337
Shen, Y., Grier, C. J., Horne, K., et al. 2023, arXiv e-prints, arXiv:2305.01014, doi: 10.48550/arXiv.2305.01014
Smith, K. L., Mushotzky, R. F., Boyd, P. T., et al. 2018, ApJ, 857, 141, doi: 10.3847/1538-4357/aab88d
Sobrino Figaredo, C., Nuñez, F. P., Ramolla, M., et al. 2018, in Revisiting Narrow-Line Seyfert 1 Galaxies and their Place in the Universe, 57, doi: 10.22323/1.328.0057
Soltan, A. 1982, MNRAS, 200, 115, doi: 10.1093/mnras/200.1.115
Sun, Y.-H., Wang, J.-X., Chen, X.-Y., & Zheng, Z.-Y. 2014, ApJ, 792, 54, doi: 10.1088/0004-637X/792/1/54
Timmer, J., & Koenig, M. 1995, A&A, 300, 707
Tremou, E., Garcia-Marin, M., Zuther, J., et al. 2015, A&A, 580, A113, doi: 10.1051/0004-6361/201525707
U, V., Barth, A. J., Vogler, H. A., et al. 2022, ApJ, 925, 52, doi: 10.3847/1538-4357/ac3d26
Ursini, F., Petrucci, P. O., Bianchi, S., et al. 2020, A&A, 634, A92, doi: 10.1051/0004-6361/201936486

van Groningen, E., & Wanders, I. 1992, PASP, 104, 700, doi: 10.1086/133039

Vaughan, S., Edelson, R., Warwick, R. S., & Uttley, P. 2003, MNRAS, 345, 1271, doi: 10.1046/j.1365-2966.2003.07042.x

Véron-Cetty, M. P., & Véron, P. 2006, A&A, 455, 773, doi: 10.1051/0004-6361:20065177

—. 2010, A&A, 518, A10, doi: 10.1051/0004-6361/201014188

Vestergaard, M. 2004, ApJ, 601, 676, doi: 10.1086/379758

Vestergaard, M., & Osmer, P. S. 2009, ApJ, 699, 800, doi: 10.1088/0004-637X/699/1/800

von Neumann, J. 1941, The Annals of Mathematical Statistics, 12, 367 , doi: 10.1214/aoms/1177731677

Wang, S., Guo, H., & Woo, J.-H. 2023, ApJL, 948, L23, doi: 10.3847/2041-8213/accf96

Watson, D., Denney, K. D., Vestergaard, M., & Davis, T. M. 2011, ApJL, 740, L49, doi: 10.1088/2041-8205/740/2/L49

Welsh, W. F. 1999, PASP, 111, 1347, doi: 10.1086/316457

Williams, P. R., Pancoast, A., Treu, T., et al. 2018, ApJ, 866, 75, doi: 10.3847/1538-4357/aae086

Winge, C., Peterson, B. M., Pastoriza, M. G., & Storchi-Bergmann, T. 1996, ApJ, 469, 648, doi: 10.1086/177812

Winkler, H. 1997, MNRAS, 292, 273, doi: 10.1093/mnras/292.2.273

Winkler, H., Glass, I. S., van Wyk, F., et al. 1992, MNRAS, 257, 659, doi: 10.1093/mnras/257.4.659

Zaw, I., Chen, Y.-P., & Farrar, G. R. 2019, ApJ, 872, 134, doi: 10.3847/1538-4357/aaffaf

Zetzl, M., Kollatschny, W., Ochmann, M. W., et al. 2018, A&A, 618, A83, doi: 10.1051/0004-6361/201732506

Zu, Y., Kochanek, C. S., Kozłowski, S., & Peterson, B. M. 2016, ApJ, 819, 122, doi: 10.3847/0004-637X/819/2/122

Zu, Y., Kochanek, C. S., Kozłowski, S., & Udalski, A. 2013, ApJ, 765, 106, doi: 10.1088/0004-637X/765/2/106

Zucker, S., & Mazeh, T. 1994, ApJ, 420, 806, doi: 10.1086/173605

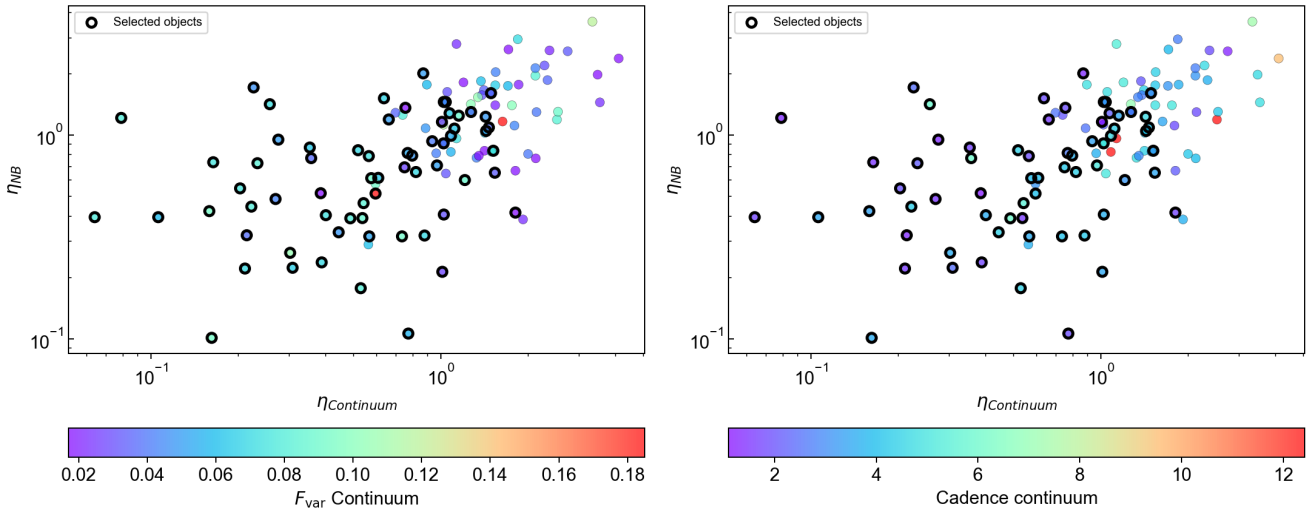

Figure A.1. Observation and selection sample: η values for NB light curves versus the continuum band light curves. Values are color-coded based on $F_{\rm var}$ (left) and cadence (right). Objects marked with a black edge mark the final selected light curves for the RM analysis. Same process was done for the NB band (not shown).

APPENDIX

A. LIGHT CURVES

This Appendix presents the absolute flux calibrated optical light curves for the 48 Seyfert galaxies used in this study. Optical filters are $BVR(r)$ and the corresponding narrow band (NB) centered at 670nm, 680nm, 690nm or SII(λ672 nm) depending on the redshift. Time is expressed in modified Julian day (MJD) and fluxes in mJy. For a discretely measured light curve at time stamps t_i ($i \in [1:n]$) with fluxes f_i and measurement uncertainties, δf_i, we define the excess variance $F_{\rm var}$ (Vaughan et al. 2003), and the regularity measure, η:

$$F_{var} = \frac{\left(\sigma^2 - \Delta^2\right)^{1/2}}{\bar{f}}\,, \qquad \sigma^2 = \frac{1}{n-1}\sum_{i=1}^{n}\left(f_i - \bar{f}\right)^2\,, \qquad \Delta^2 = \frac{1}{n}\sum_{i=1}^{n}\delta f_i^2 \tag{A1}$$

$$\eta = \frac{\delta^2}{\sigma^2}, \qquad \delta^2 = \frac{1}{n-1}\sum_{i=1}^{n-1}\left(f_{i+1} - f_i\right)^2, \tag{A2}$$

where $\bar{f}$ is the mean of the light curve. The regularity measure η (Equation A2) represents the ratio between the mean square successive difference (or the von Neumann estimator δ^2) and the variance. The η value serve as indicator for the regularity of the light curve, which is sensitive to the measurement-noise level and to the sampling of the process by the time-series. Smaller η value imply better quality data, indicating less random fluctuations due to noise or sparse sampling of a rapidly varying signal. In both equations A1 and A2, f represents the normalized flux of the detrended light curve. In addition, we define the cadence of the light curve as the total duration of the observation campaign divided by the number of observations, noting that when large observation gaps exist, the cadence might be overestimated compared to the median of the time step of the light curves. We list the above light-curve properties for the continuum (B or V) as well as for the NB of each object in Table A.1.

The preliminary selection criteria for identifying objects and light curves suitable for Reverberation Mapping (RM) are as follows: 1) Record the values of $F_{\rm var}$, η, and cadence for both continuum and Narrow Band (NB) light curves. 2) Prioritize light curves where $F_{\rm var}$ exceeds 0.01 for both continuum and NB. 3) Select light curves with η values below unity, with a few exceptions made upon eyeinspection of the light curves, and ensure that the cadence is within 10 days. This choice is motivated by the luminosity and redshift of the Seyfert galaxies, where time delays are predicted to be of a similar order. The outlined selection procedure is depicted in Figure A.1, which illustrates η values for NB versus those for the continuum band. The figures are color-coded based on $F_{\rm var}$ (on the left) and cadence (on the right). In total, observations were conducted for 80 objects, comprising a total of 120 light curves, accounting for observations across multiple epochs. The ultimately chosen light curves are

delineated with a black border, constituting the final sample presented in Table 1. This final sample comprises 48 objects, with 12 of them observed across multiple epochs, resulting in a total of 65 light curves.

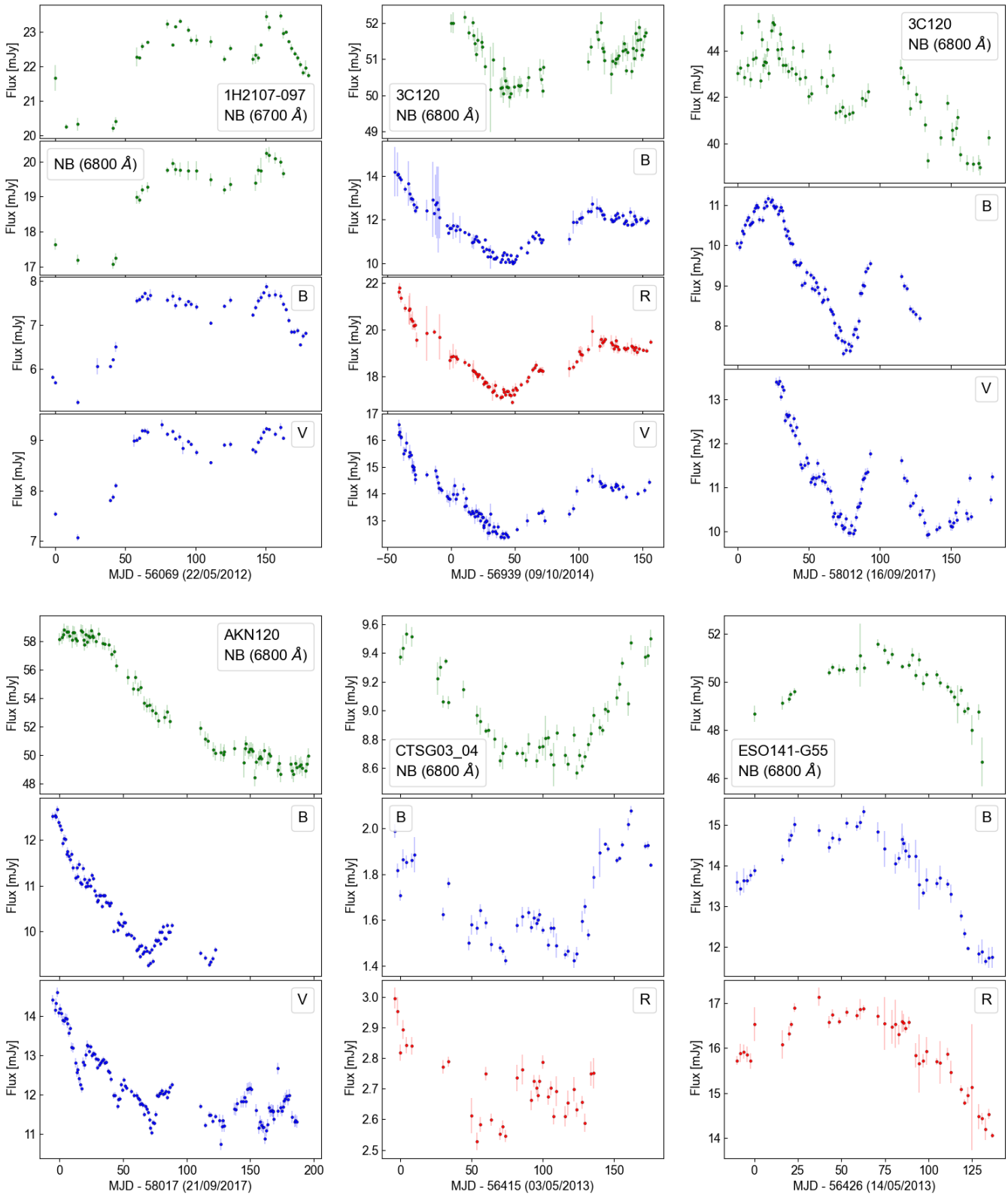

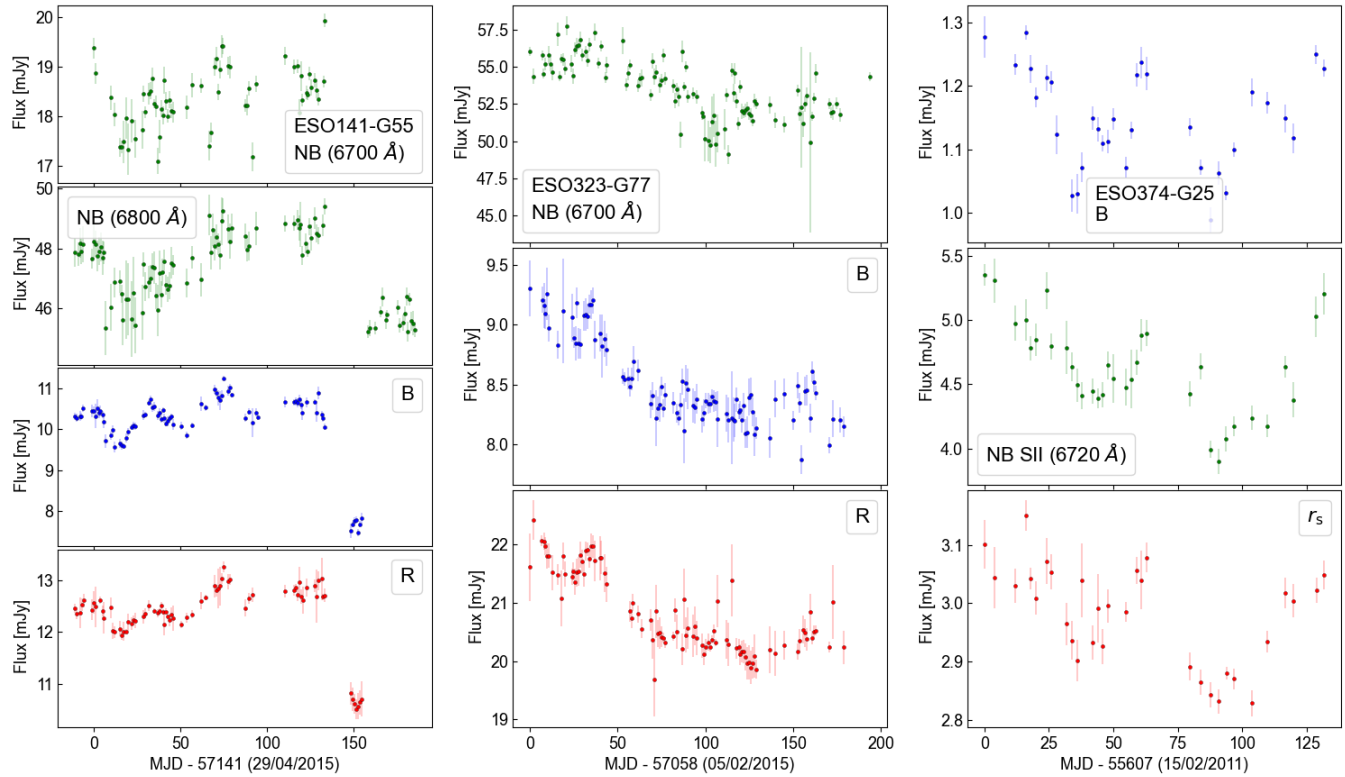
ESO141-G55
NB (6700 Å)
NB (6800 Å)
B
R
Flux [mJy]
MJD - 57141 (29/04/2015)
ESO323-G77
NB (6700 Å)
B
R
Flux [mJy]
MJD - 57058 (05/02/2015)
ESO374-G25
B
NB SII (6720 Å)
r_s
Flux [mJy]
MJD - 55607 (15/02/2011)

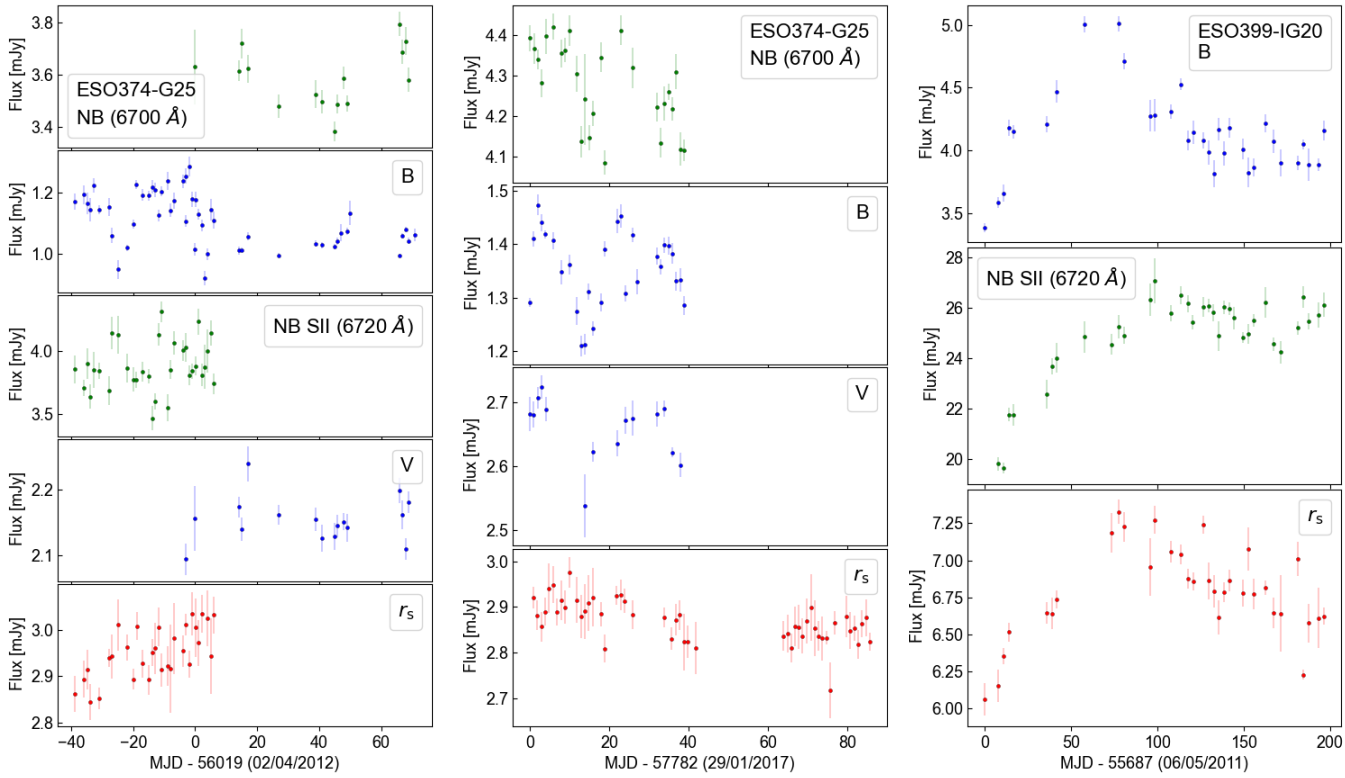
ESO374-G25
NB (6700 Å)
B
NB SII (6720 Å)
V
r_s
Flux [mJy]
MJD - 56019 (02/04/2012)
ESO374-G25
NB (6700 Å)
B
V
r_s
Flux [mJy]
MJD - 57782 (29/01/2017)
ESO399-IG20
B
NB SII (6720 Å)
r_s
Flux [mJy]
MJD - 55687 (06/05/2011)

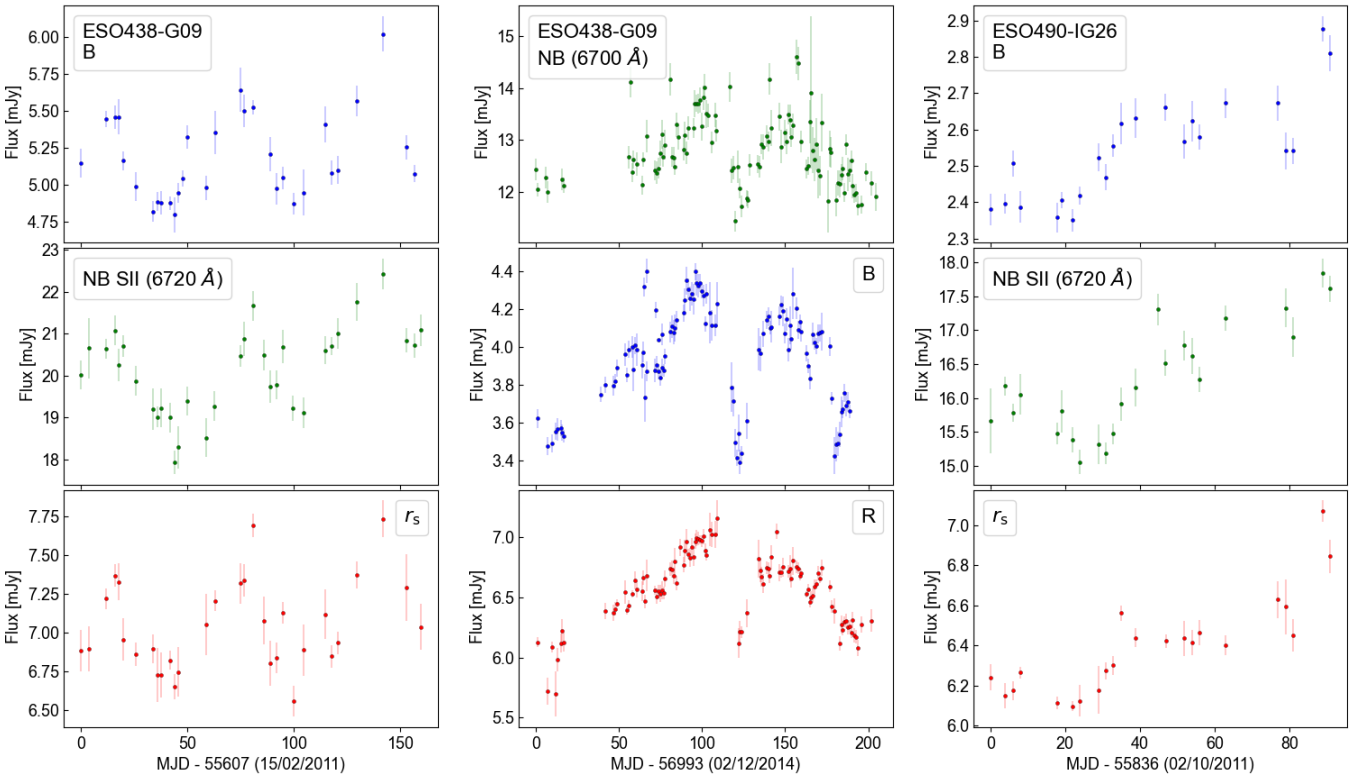
ESO438-G09
B
NB SII (6720 Å)
r_s
Flux [mJy]
MJD - 55607 (15/02/2011)
ESO438-G09
NB (6700 Å)
B
R
MJD - 56993 (02/12/2014)
ESO490-IG26
B
NB SII (6720 Å)
r_s
MJD - 55836 (02/10/2011)

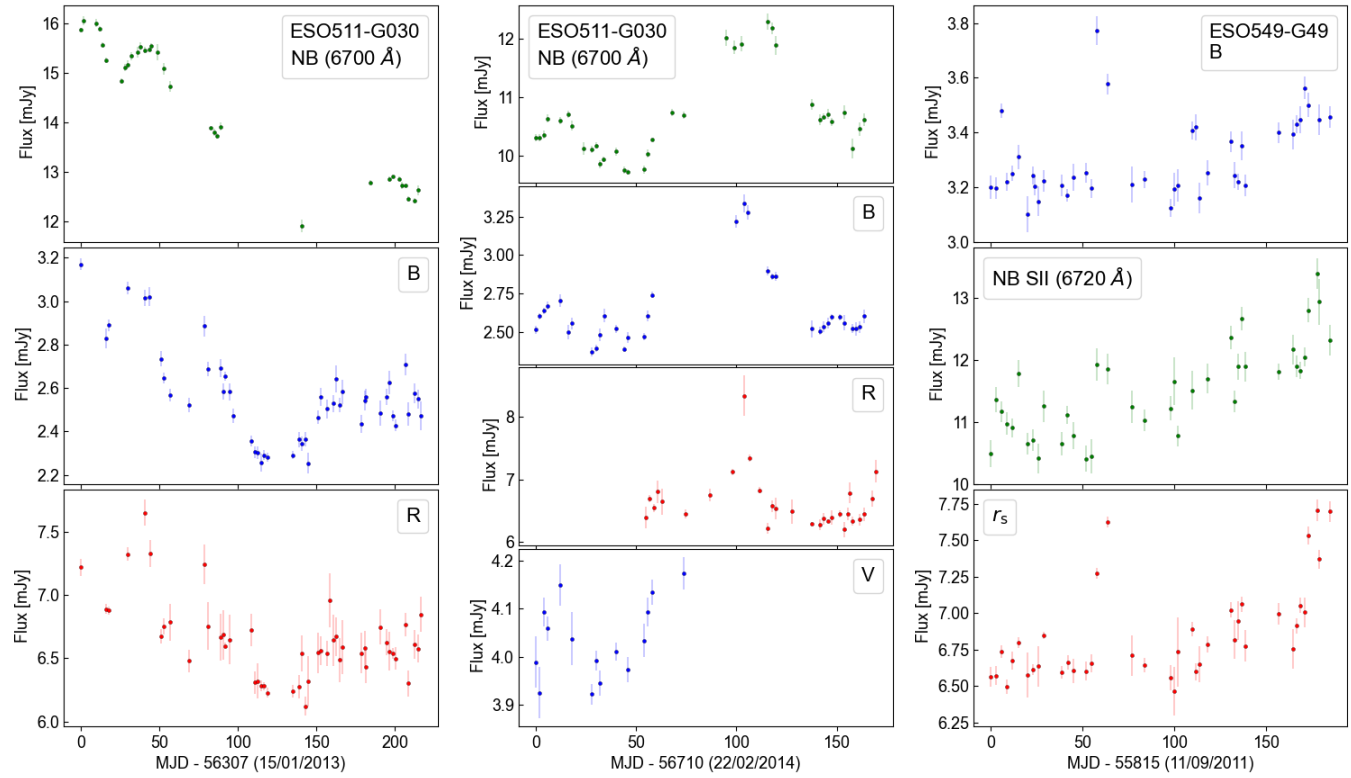
ESO511-G030
NB (6700 Å)
B
R
MJD - 56307 (15/01/2013)
ESO511-G030
NB (6700 Å)
B
R
V
MJD - 56710 (22/02/2014)
ESO549-G49
B
NB SII (6720 Å)
r_s
MJD - 55815 (11/09/2011)

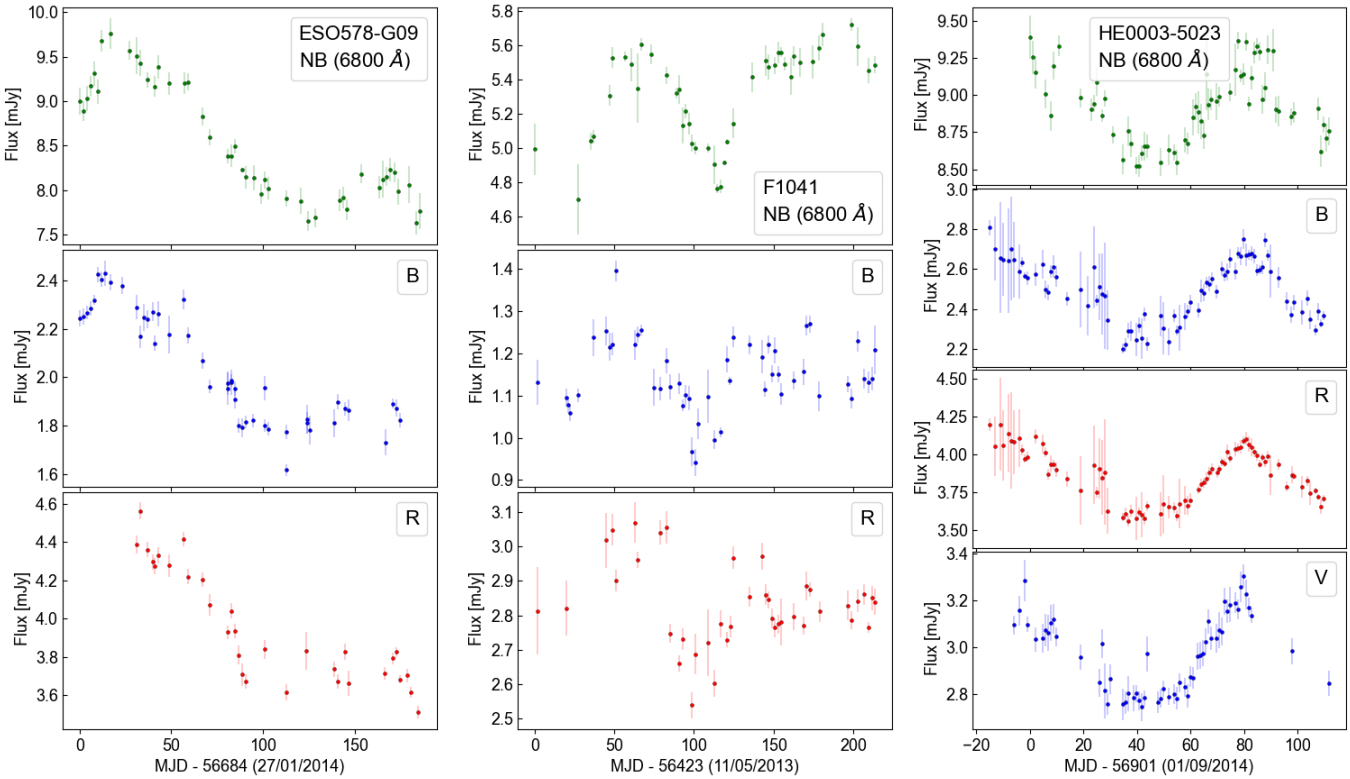
ESO578-G09
NB (6800 Å)
B
R
Flux [mJy]
MJD - 56684 (27/01/2014)
F1041
NB (6800 Å)
B
R
Flux [mJy]
MJD - 56423 (11/05/2013)
HE0003-5023
NB (6800 Å)
B
R
V
Flux [mJy]
MJD - 56901 (01/09/2014)

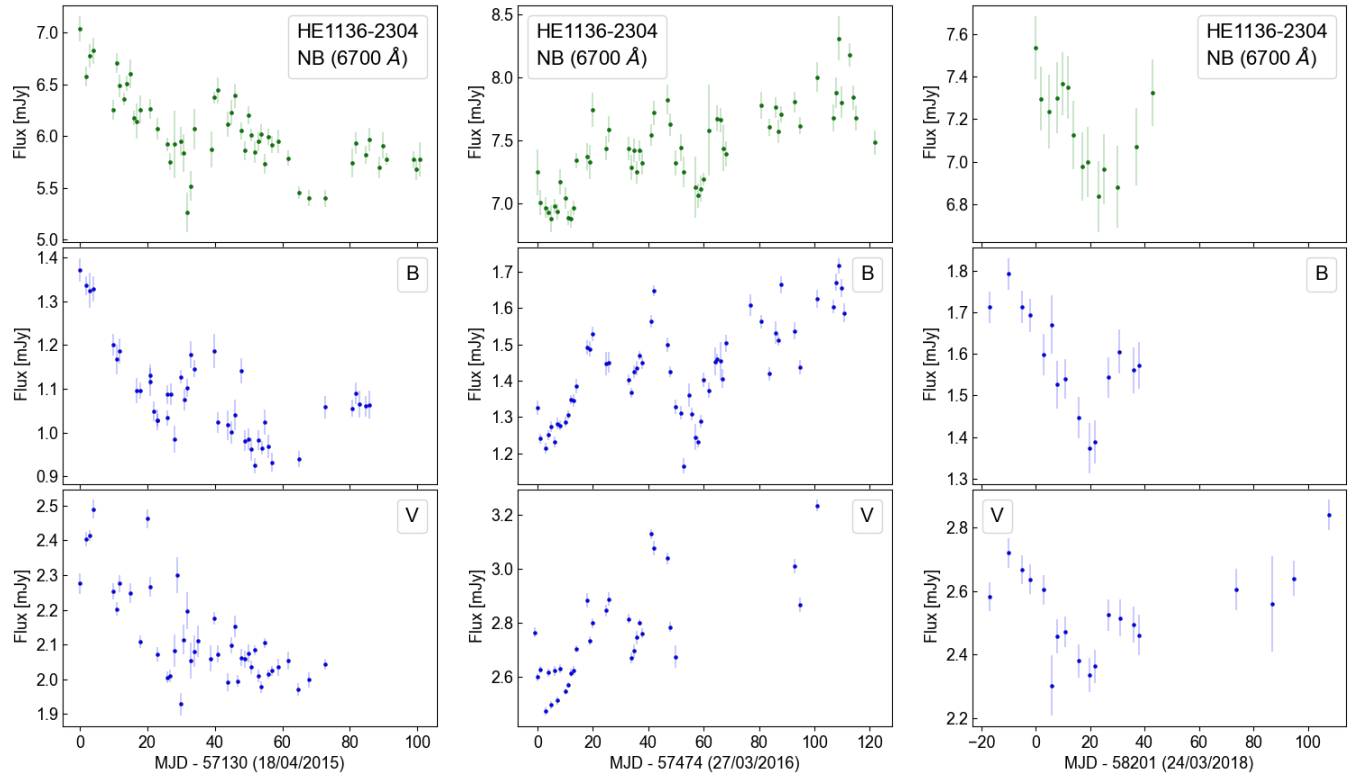
HE1136-2304
NB (6700 Å)
B
V
Flux [mJy]
MJD - 57130 (18/04/2015)
HE1136-2304
NB (6700 Å)
B
V
Flux [mJy]
MJD - 57474 (27/03/2016)
HE1136-2304
NB (6700 Å)
B
V
Flux [mJy]
MJD - 58201 (24/03/2018)

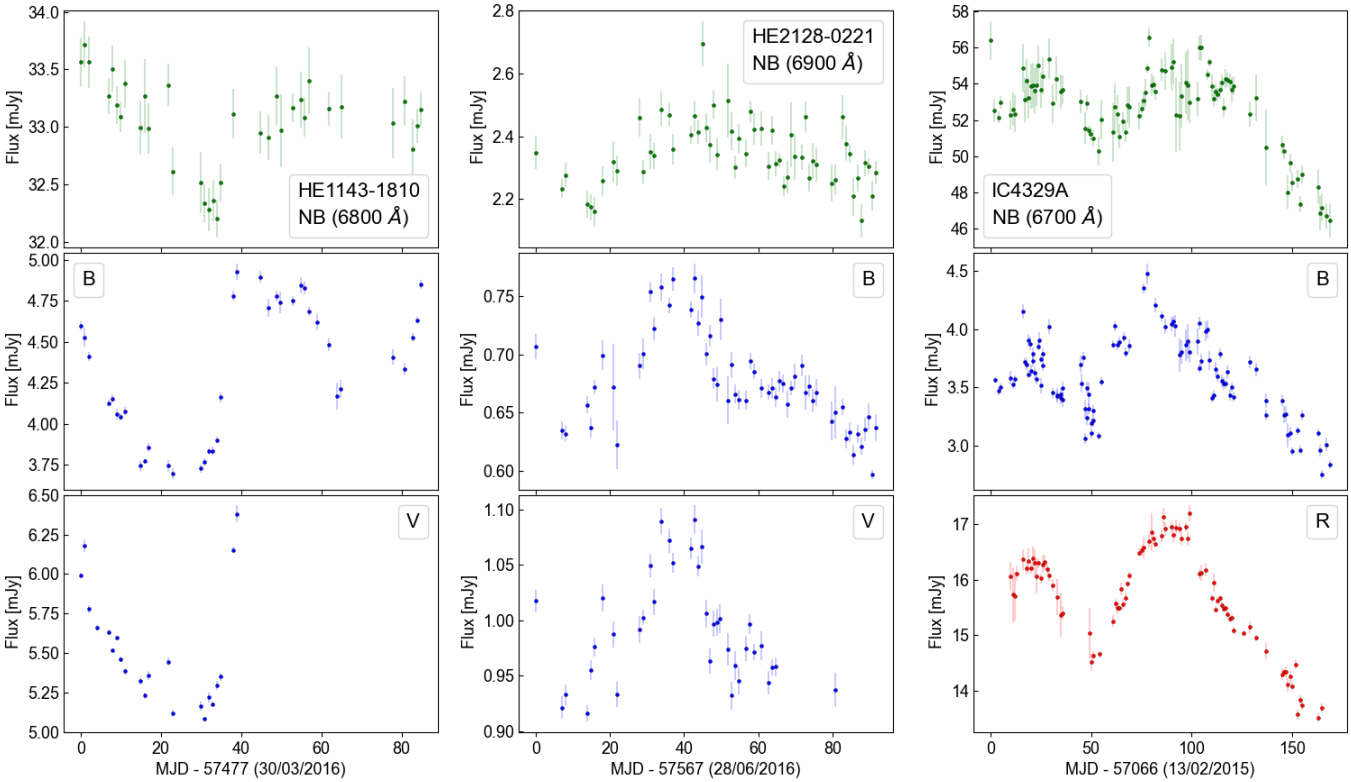
HE1143-1810
NB (6800 Å)
B
V
Flux [mJy]
MJD - 57477 (30/03/2016)
HE2128-0221
NB (6900 Å)
B
V
Flux [mJy]
MJD - 57567 (28/06/2016)
IC4329A
NB (6700 Å)
B
R
Flux [mJy]
MJD - 57066 (13/02/2015)

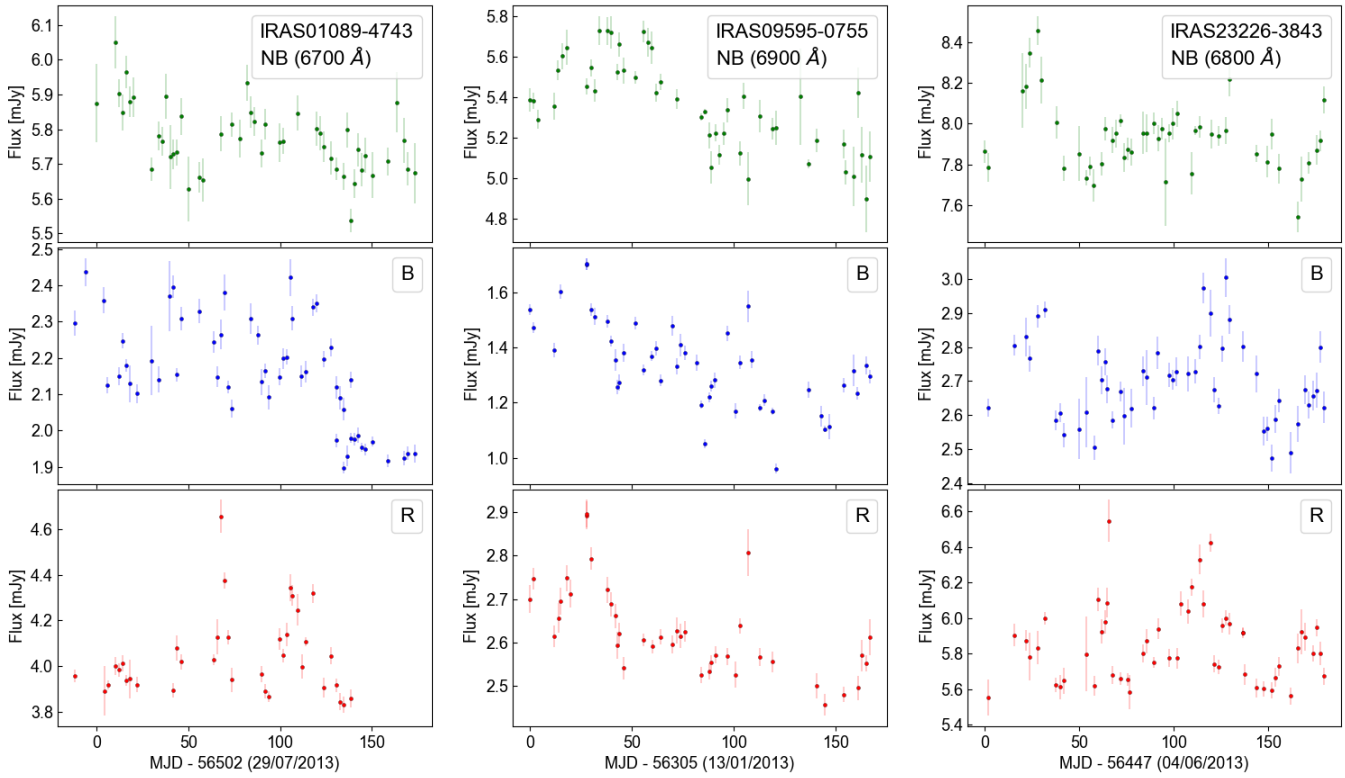
IRAS01089-4743
NB (6700 Å)
B
R
Flux [mJy]
MJD - 56502 (29/07/2013)
IRAS09595-0755
NB (6900 Å)
B
R
Flux [mJy]
MJD - 56305 (13/01/2013)
IRAS23226-3843
NB (6800 Å)
B
R
Flux [mJy]
MJD - 56447 (04/06/2013)

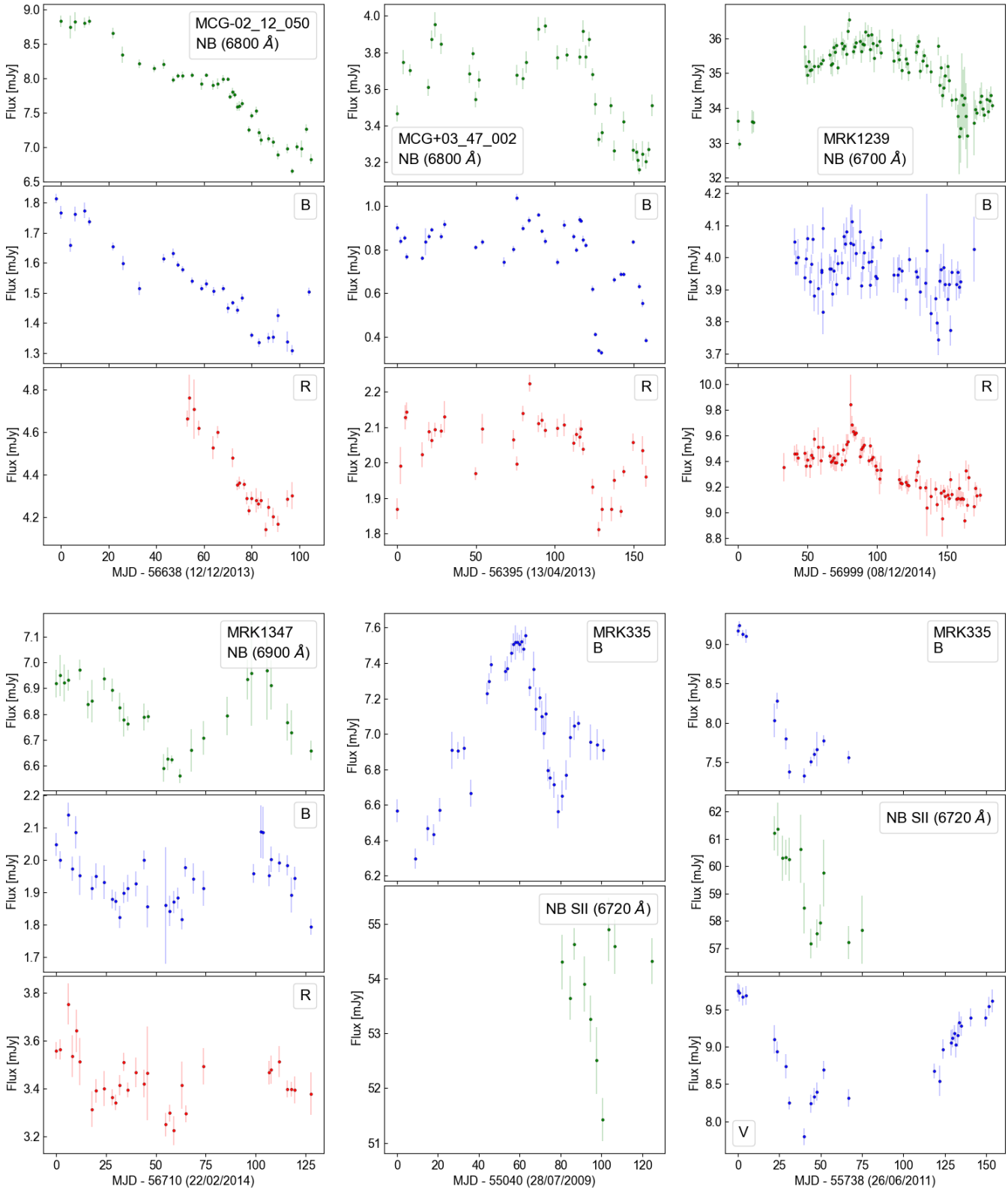
MCG-02_12_050
NB (6800 Å)
B
R
Flux [mJy]
MJD - 56638 (12/12/2013)
MCG+03_47_002
NB (6800 Å)
B
R
Flux [mJy]
MJD - 56395 (13/04/2013)
MRK1239
NB (6700 Å)
B
R
Flux [mJy]
MJD - 56999 (08/12/2014)
MRK1347
NB (6900 Å)
B
R
Flux [mJy]
MJD - 56710 (22/02/2014)
MRK335
B
NB SII (6720 Å)
Flux [mJy]
MJD - 55040 (28/07/2009)
MRK335
B
NB SII (6720 Å)
V
Flux [mJy]
MJD - 55738 (26/06/2011)

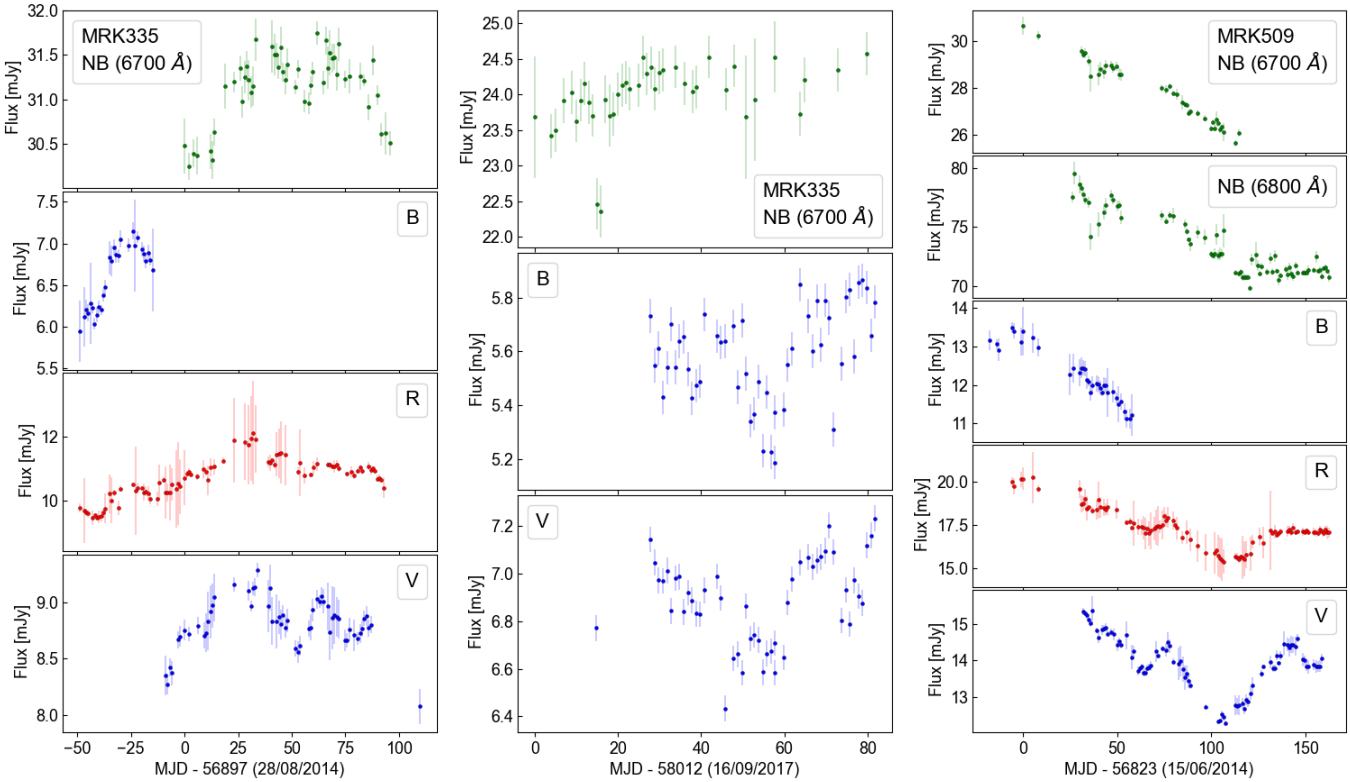
MRK335
NB (6700 Å)
B
R
V
Flux [mJy]
MJD - 56897 (28/08/2014)
MRK335
NB (6700 Å)
B
V
Flux [mJy]
MJD - 58012 (16/09/2017)
MRK509
NB (6700 Å)
NB (6800 Å)
B
R
V
Flux [mJy]
MJD - 56823 (15/06/2014)

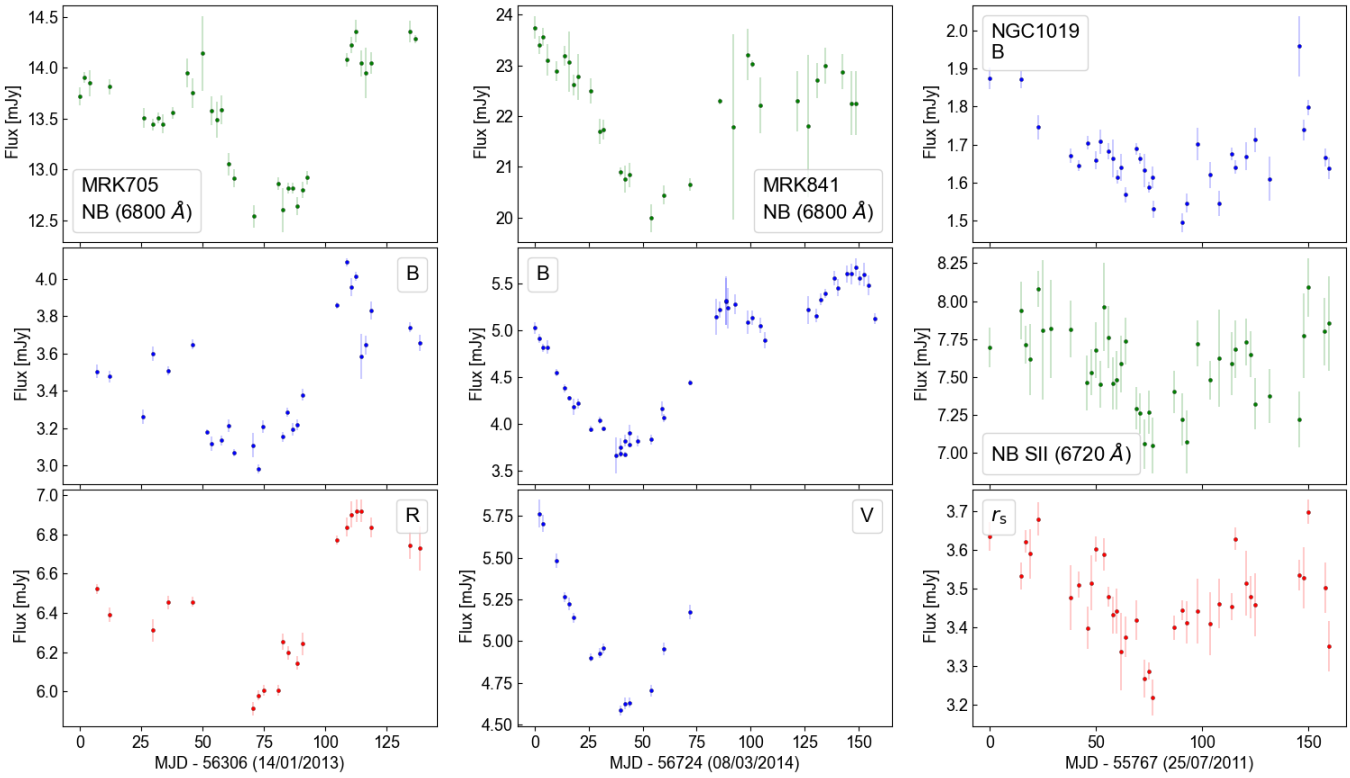
MRK705
NB (6800 Å)
B
R
Flux [mJy]
MJD - 56306 (14/01/2013)
MRK841
NB (6800 Å)
B
V
Flux [mJy]
MJD - 56724 (08/03/2014)
NGC1019
B
NB SII (6720 Å)
r_s
Flux [mJy]
MJD - 55767 (25/07/2011)

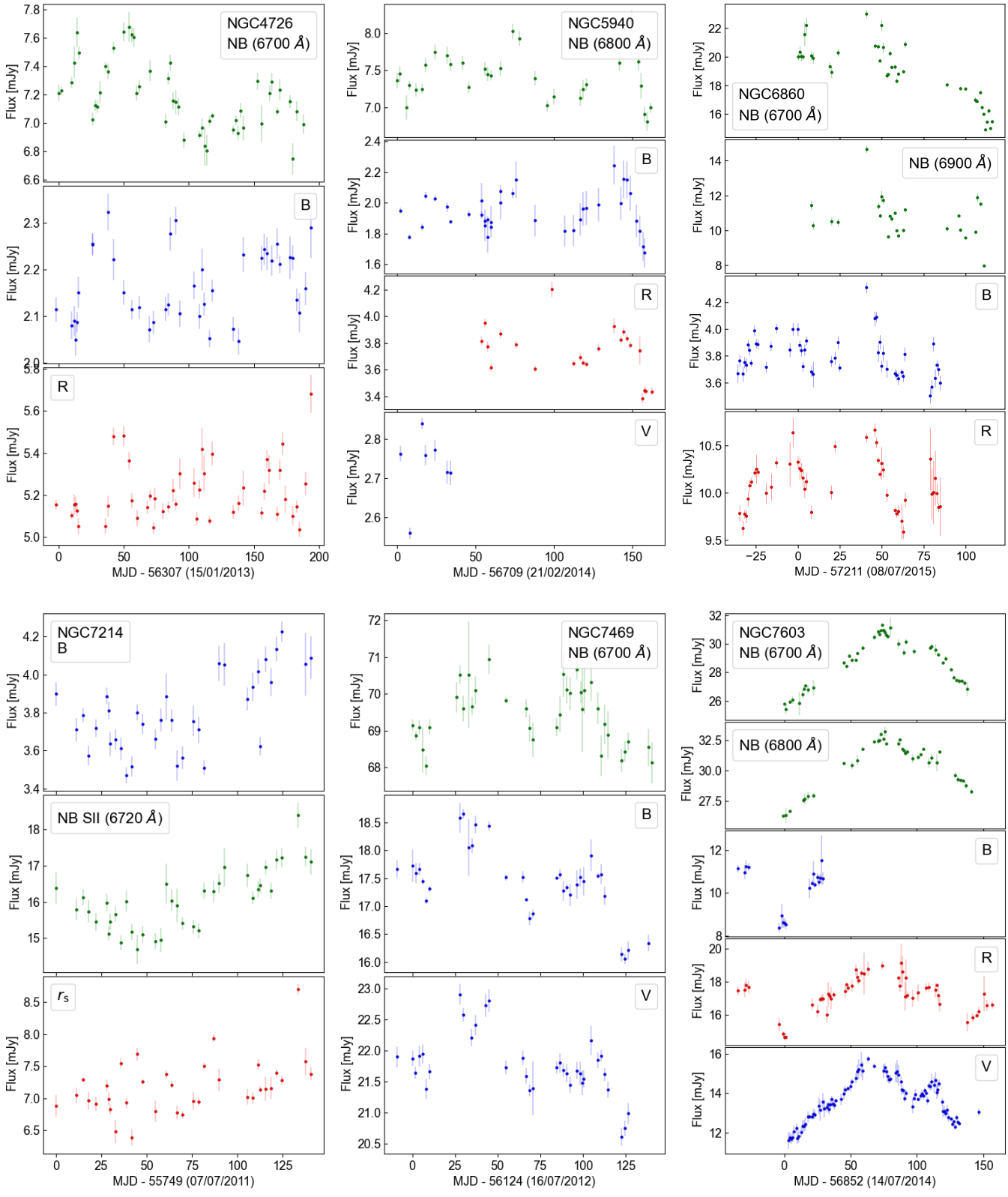
NGC4726
NB (6700 Å)
B
R
Flux [mJy]
MJD - 56307 (15/01/2013)
NGC5940
NB (6800 Å)
B
R
V
Flux [mJy]
MJD - 56709 (21/02/2014)
NGC6860
NB (6700 Å)
NB (6900 Å)
B
R
Flux [mJy]
MJD - 57211 (08/07/2015)
NGC7214
B
NB SII (6720 Å)
r_s
Flux [mJy]
MJD - 55749 (07/07/2011)
NGC7469
NB (6700 Å)
B
V
Flux [mJy]
MJD - 56124 (16/07/2012)
NGC7603
NB (6700 Å)
NB (6800 Å)
B
R
V
Flux [mJy]
MJD - 56852 (14/07/2014)

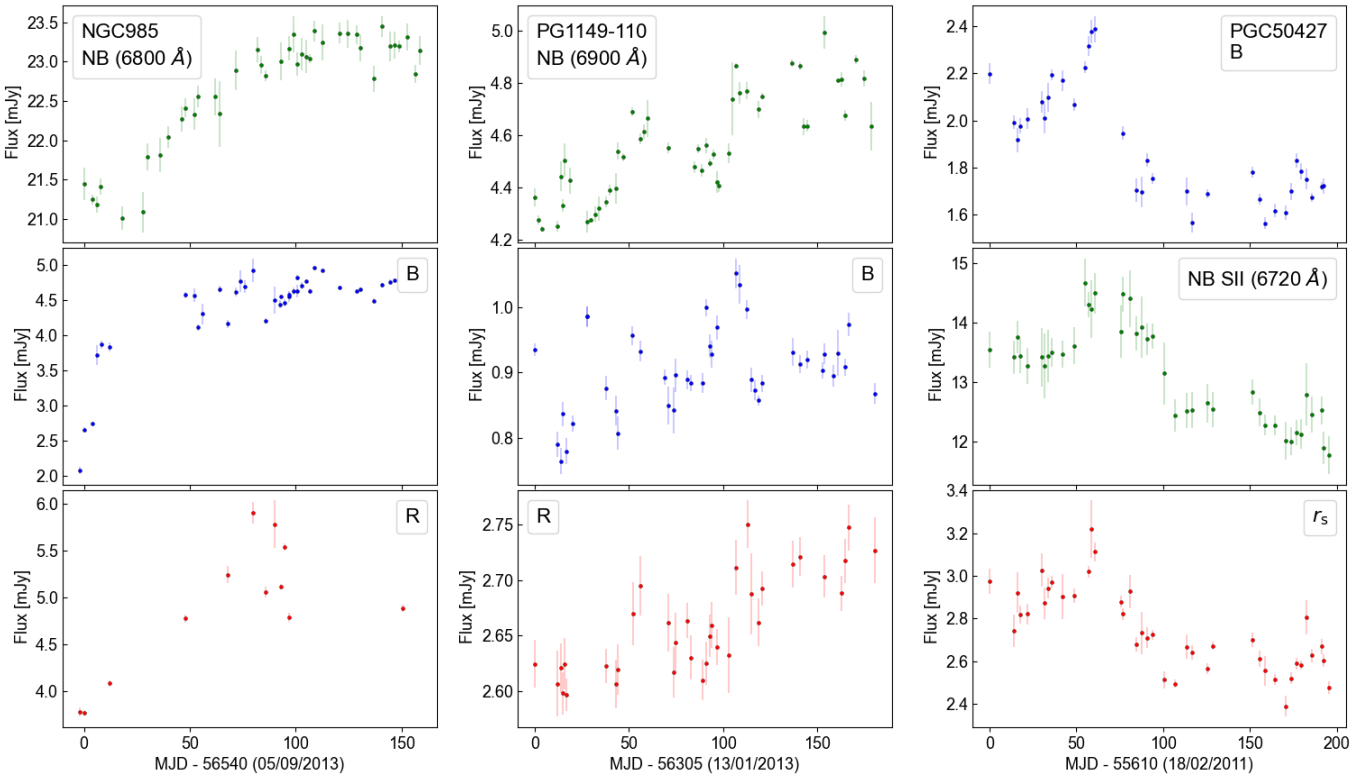
NGC985
NB (6800 Å)
B
R
Flux [mJy]
MJD - 56540 (05/09/2013)
PG1149-110
NB (6900 Å)
B
R
Flux [mJy]
MJD - 56305 (13/01/2013)
PGC50427
B
NB SII (6720 Å)
r_s
Flux [mJy]
MJD - 55610 (18/02/2011)

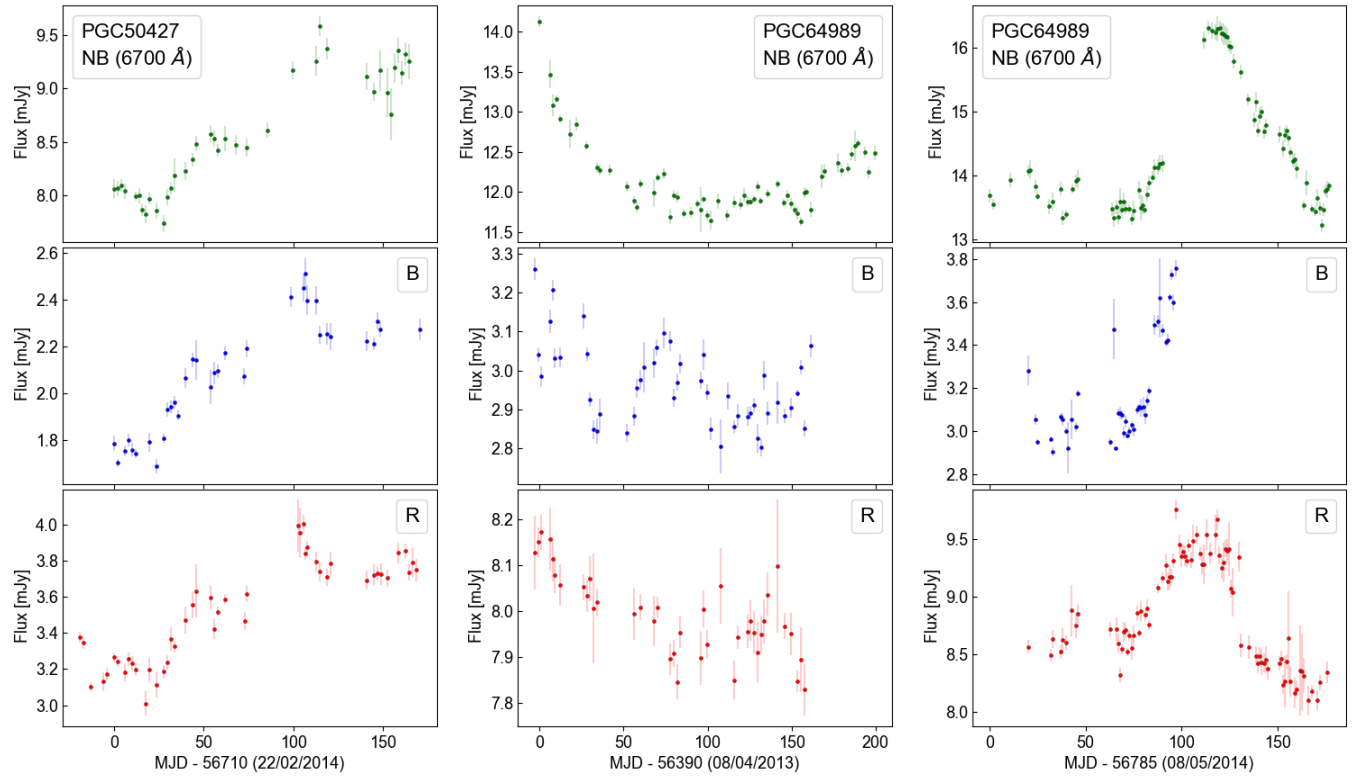
PGC50427
NB (6700 Å)
B
R
Flux [mJy]
MJD - 56710 (22/02/2014)
PGC64989
NB (6700 Å)
B
R
Flux [mJy]
MJD - 56390 (08/04/2013)
PGC64989
NB (6700 Å)
B
R
Flux [mJy]
MJD - 56785 (08/05/2014)

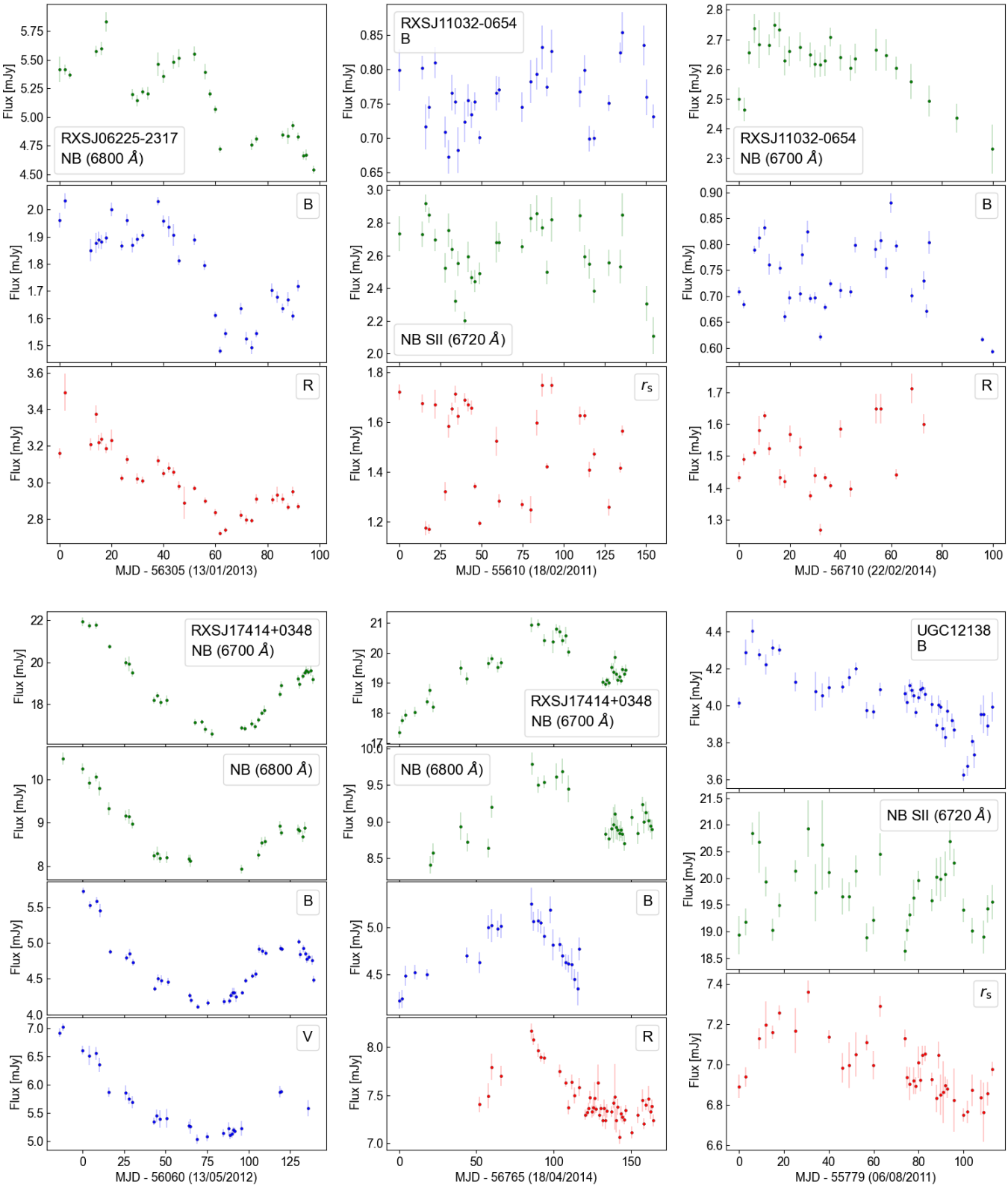
RXSJ06225-2317
NB (6800 Å)
B
R
Flux [mJy]
MJD - 56305 (13/01/2013)
RXSJ11032-0654
B
NB SII (6720 Å)
r_s
MJD - 55610 (18/02/2011)
RXSJ11032-0654
NB (6700 Å)
B
R
MJD - 56710 (22/02/2014)
RXSJ17414+0348
NB (6700 Å)
NB (6800 Å)
B
V
MJD - 56060 (13/05/2012)
RXSJ17414+0348
NB (6700 Å)
NB (6800 Å)
B
R
MJD - 56765 (18/04/2014)
UGC12138
B
NB SII (6720 Å)
r_s
MJD - 55779 (06/08/2011)

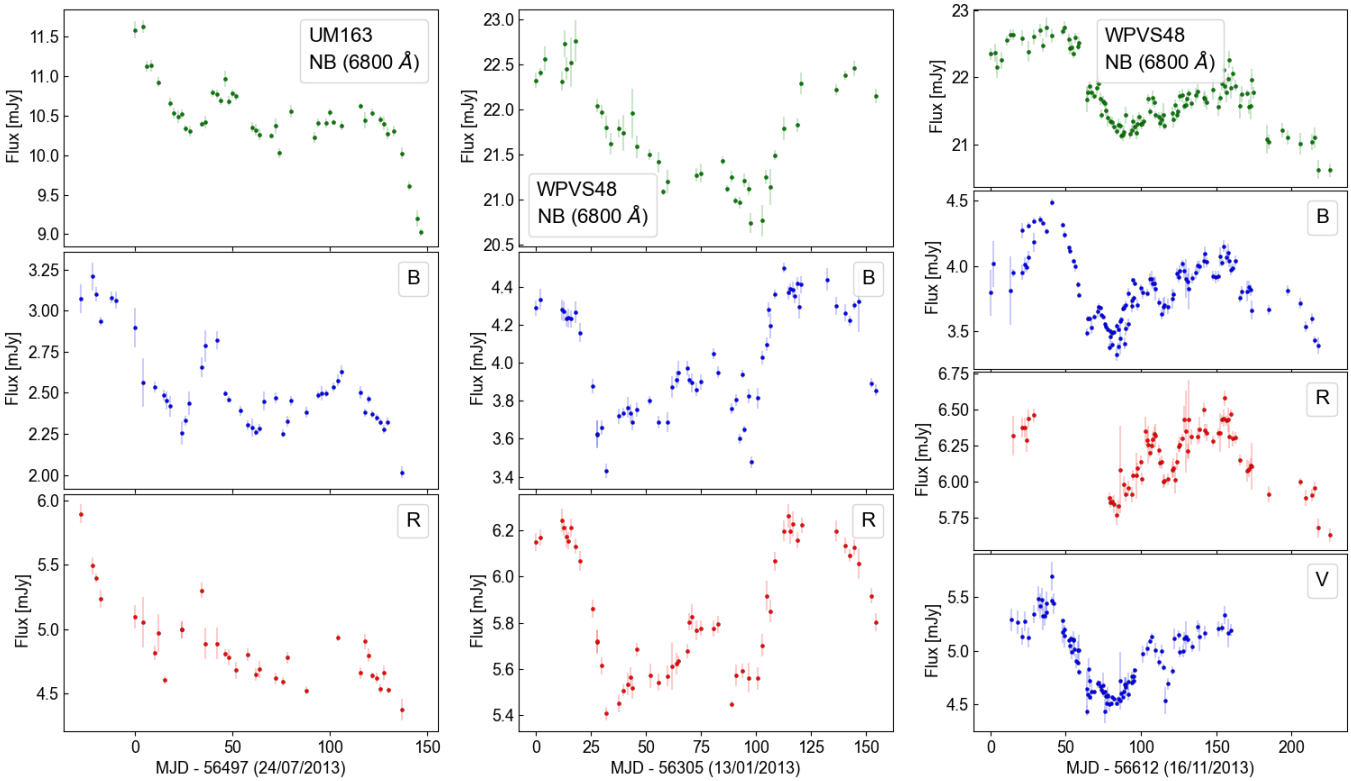
UM163
NB (6800 Å)
B
R
Flux [mJy]
MJD - 56497 (24/07/2013)
WPVS48
NB (6800 Å)
B
R
Flux [mJy]
MJD - 56305 (13/01/2013)
WPVS48
NB (6800 Å)
B
R
V
Flux [mJy]
MJD - 56612 (16/11/2013)

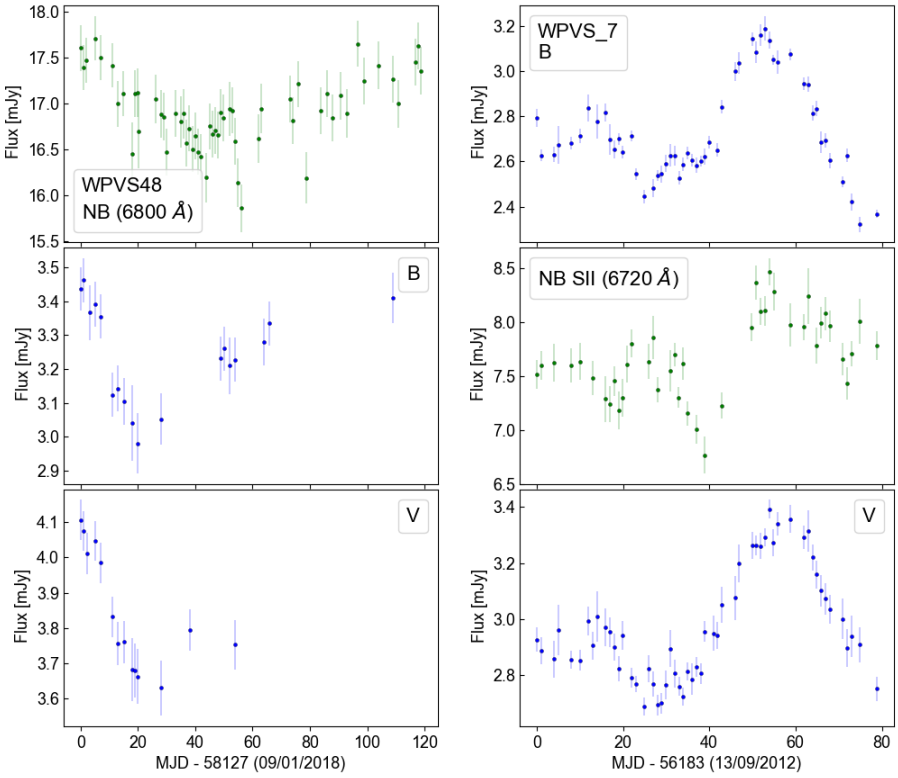
WPVS48
NB (6800 Å)
B
V
Flux [mJy]
MJD - 58127 (09/01/2018)
WPVS_7
B
NB SII (6720 Å)
V
Flux [mJy]
MJD - 56183 (13/09/2012)

Table A.1. Light curves properties for each source (F_{var} in per-cent, η, and cadence in days) for the continuum (B or V) as well as for the NB filter.

Object	Year	B or V Continuum $F_{\rm var}/\eta$/cadence	NB Filter $F_{\rm var}/\eta$/cadence	Object	Year	B or V Continuum $F_{\rm var}/\eta$/cadence	NB Filter $F_{\rm var}/\eta$/cadence
1H2107-097	2012	8.0 / 0.222 / 4.3	3.3 / 0.445 / 4.9	MRK335	2010	4.7 / 0.226 / 2.5	1.7 / 1.712 / 4.4
3C120	2014	7.8 / 0.064 / 1.8	1.0 / 0.395 / 2.4	MRK335	2011	7.2 / 0.257 / 5.9	0.7 / 1.416 / 4.1
AKN120	2018	4.5 / 0.188 / 1.4	1.5 / 0.322 / 2.3	MRK335	2014	1.3 / 0.385 / 1.2	1.0 / 0.518 / 1.9
CTSG03_04	2013	10.5 / 0.302 / 3.6	3.0 / 0.264 / 3.4	MRK509	2014	5.0 / 0.275 / 1.4	1.3 / 0.949 / 2.2
ESO141-G55	2013	5.9 / 0.106 / 3.5	1.9 / 0.395 / 3.7	MRK705	2013	8.1 / 0.529 / 4.5	3.8 / 0.177 / 6.1
ESO141-G55	2015	7.6 / 0.203 / 2.0	2.2 / 0.547 / 2.1	MRK841	2014	9.2 / 0.159 / 3.4	3.8 / 0.423 / 4.9
ESO323-G77	2015	1.7 / 0.754 / 1.9	1.9 / 1.36 / 1.9	NGC1019	2011	5.4 / 1.083 / 4.7	2.2 / 0.991 / 4.0
ESO374-G25	2011	6.3 / 0.608 / 4.0	6.5 / 0.616 / 3.9	NGC4726	2013	3.1 / 1.021 / 4.8	2.6 / 0.91 / 3.9
ESO399	2011	8.0 / 0.487 / 6.0	4.8 / 0.39 / 5.5	NGC5940	2014	7.7 / 1.516 / 4.2	3.9 / 0.837 / 5.2
ESO438	2011	5.1 / 0.969 / 5.1	4.2 / 0.709 / 4.8	NGC6860	2015	3.6 / 1.27 / 2.5	6.2 / 1.02 / 2.8
ESO438	2015	6.4 / 0.353 / 1.7	4.6 / 0.868 / 2.0	NGC7214	2011	3.8 / 1.463 / 4.0	3.3 / 1.089 / 3.8
ESO490	2011	2.7 / 1.431 / 4.0	2.5 / 1.047 / 4.0	NGC7469	2012	2.8 / 0.749 / 4.2	0.9 / 0.694 / 3.9
ESO511	2013	6.9 / 0.518 / 4.5	3.0 / 0.842 / 6.7	NGC7603	2014	7.0 / 0.211 / 1.6	5.4 / 0.221 / 3.7
ESO511	2014	9.1 / 0.734 / 4.1	6.0 / 0.318 / 4.7	NGC985	2014	8.9 / 0.575 / 3.9	1.3 / 0.614 / 4.0
ESO549	2012	3.7 / 1.488 / 4.6	3.7 / 1.605 / 4.9	PG1149-110	2013	6.4 / 1.113 / 4.4	2.4 / 1.075 / 3.7
ESO578	2014	5.3 / 0.566 / 3.6	3.6 / 0.318 / 4.1	PGC50427	2011	8.3 / 0.541 / 5.5	3.1 / 0.463 / 4.8
F1041	2013	6.9 / 0.878 / 4.2	4.2 / 0.321 / 5.0	PGC502	2014	6.9 / 0.82 / 4.4	2.3 / 0.658 / 4.3
HE0003	2014	4.3 / 0.269 / 1.5	2.5 / 0.485 / 1.8	PGC649	2013	2.8 / 1.011 / 3.5	3.5 / 0.213 / 3.3
HE1136-2304	2015	7.4 / 0.564 / 1.9	4.2 / 0.788 / 1.9	PGC649	2014	4.8 / 0.496 / 1.8	6.3 / 0.106 / 2.2
HE1136	2016	6.8 / 0.636 / 1.9	2.9 / 1.514 / 2.1	RXSJ06	2013	5.4 / 0.768 / 2.7	3.6 / 0.816 / 3.5
HE1136	2018	4.9 / 0.796 / 3.7	0.9 / 0.792 / 3.1	RXSJ11	2011	4.9 / 1.426 / 4.7	6.6 / 1.229 / 4.8
HE1143	2016	8.2 / 0.233 / 2.2	0.8 / 0.727 / 2.4	RXSJ11	2014	8.8 / 1.209 / 3.2	2.4 / 0.601 / 3.8
HE2128	2016	5.0 / 0.661 / 1.6	3.7 / 1.192 / 1.6	RXSJ17	2012	9.2 / 0.162 / 3.6	7.3 / 0.101 / 4.3
IC4329	2015	8.7 / 0.536 / 1.6	3.2 / 0.391 / 1.9	RXSJ17414+0348	2014	4.8 / 0.444 / 4.5	3.9 / 0.333 / 4.1
IRAS01	2013	6.7 / 0.64 / 3.4	1.4 / 1.09 / 3.7	UGC121	2012	2.2 / 1.039 / 2.6	2.5 / 1.452 / 3.3
IRAS09	2013	11.5 / 0.67 / 3.5	3.8 / 0.63 / 3.5	UM163	2013	7.4 / 0.401 / 3.6	3.1 / 0.404 / 3.3
IRAS23	2013	4.1 / 0.933 / 3.4	1.8 / 0.932 / 3.8	WPVS00	2012	7.6 / 0.164 / 1.5	3.7 / 0.735 / 1.9
MCG+03	2013	19.0 / 0.595 / 4.0	5.3 / 0.516 / 4.4	WPVS48	2013	6.6 / 0.308 / 2.5	2.4 / 0.223 / 3.8
MCG021	2014	3.4 / 1.534 / 3.5	2.4 / 0.653 / 2.6	WPVS48	2014	7.0 / 0.388 / 1.8	1.7 / 0.237 / 2.0
MRK123	2015	1.0 / 1.806 / 1.8	1.9 / 0.416 / 2.0	WPVS48	2018	3.7 / 0.357 / 6.0	1.8 / 0.77 / 2.1
MRK134	2014	3.1 / 1.023 / 3.7	1.3 / 0.407 / 4.6				

B. TIME-DELAY MEASUREMENTS FORMALISM

In this work we implement the multivariate correlation-function formalism Zucker & Mazeh (1994) for PRM but do so in a way which is easily implementable with commonly available tools of the trade, namely, cross-correlation functions. As discussed in Chelouche & Zucker (2013), PRM operates on two light curves which differ by the relative contribution of (delayed) BLR emission to them. Following the nomenclature of Chelouche & Daniel (2012), the band for which the BLR contribution is small is denoted by f_c while the relatively BLR-rich light curve is denoted by f_{lc}. As in Chelouche & Zucker (2013), we approximate f_{lc} to first order (see Chelouche & Zucker 2013, for the inclusion of finite transfer function effects) by the following model:

$$f^m_{lc}(t) = (1-\alpha) f_c(t) + \alpha f_c(t-\tau). \tag{B3}$$

Here, α is a parameter representing the contribution of the lagging component to the signal ($0 \leq \alpha \leq 1$), and $\tau > 0$ is the time-delay (continuum time-delays between the different wavelength bands are ignored here, which seems to provide a good approximation for quasar data over the optical band; Chelouche 2013).

The model parameters, α and τ, may be deduced by searching for the best agreement between the model, f^m_{lc}, and the data, f_{lc}. In RM studies, this is often accomplished by searching for the parameter values that maximize the Pearson correlation coefficient, r, which for our model yields:

$$r(\tau,\alpha) = \frac{1}{N\sigma_{lc}\sigma^m_{lc}} \sum_{n=1}^{N} f_{lc}(t_n) f^m_{lc}(t_n-\tau) = \frac{1-\alpha}{N\sigma_{lc}\sigma_c} \sum_{n=1}^{N} f_{lc}(t_n) f_c(t_n) + \frac{\alpha}{N(\tau)\sigma_{lc}(\tau)\sigma_c(\tau)} \sum_{n=1}^{N(\tau)} f_{lc}(t_n) f_c(t_n-\tau), \tag{B4}$$

where we work with light curve averages set to zero. For *stationary* lightcurves, the standard deviations[5] $\sigma_c(\tau)=\sigma_c$, $\sigma_{lc}(\tau)=\sigma_{lc}$, and the light curve averages do not depend on the part of the light curve sampled (i.e., is independent of the time-shift), where it is understood that light curve extrapolations are ignored. In the limit $N\to\infty$, $N(\tau)\to N$ and the expressions simplify considerably. For realistic quasar light curves, which are often characterized by large-amplitude variations at the lowest frequencies probed, this requires de-trending (Welsh 1999). For finite N, finite deviations from the true definition of the correlation function will arise whose effect on the time-lag determination depends much on the particular light curve and its sampling. In the limit of stationary infinite time-series,

$$\sigma_{lc}^m=\sqrt{(1-2\alpha+2\alpha^2)\sigma_c^2+\frac{2\alpha(1-\alpha)}{N}\sum_{i=1}^{N}f_c(t_n)f_c(t_n-\tau)}=\sigma_c\sqrt{1-2\alpha+2\alpha^2+2\alpha(1-\alpha)\mathrm{ACF}_c(\tau)}. \tag{B5}$$

Here, the autocorrelation function, ACF_c is evaluated for f_c, and we obtain

$$r(\tau,\alpha)=\frac{(1-\alpha)\sum_{n=1}^{N}f_{lc}(t_n)f_c(t_n)+\alpha\sum_{n=1}^{N}f_{lc}(t_n)f_c(t_n-\tau)}{N\sigma_{lc}\sigma_c\sqrt{1-2\alpha+2\alpha^2+2\alpha(1-\alpha)\mathrm{ACF}_c(\tau)}}=\frac{(1-\alpha)\mathrm{CCF}(0)+\alpha\mathrm{CCF}(\tau)}{\sqrt{1-2\alpha+2\alpha^2+2\alpha(1-\alpha)\mathrm{ACF}_c(\tau)}}, \tag{B6}$$

where $\mathrm{CCF}(\tau)$ is the cross correlation function between the lightcurves in the bands evaluated at time-delay τ, and specifically, $\mathrm{CCF}(0)$=$\mathrm{CCF}(\tau=0)$.

The above expression for the Pearson correlation coefficient has two noteworthy limits: in case f_{lc} is just the lagging emission signal (e.g., continuum emission has been subtracted from band containing the BLR signal) then $\alpha=1$ and we obtain the standard cross-correlation function term commonly used in spectroscopic RM,

$$r(\tau,\alpha=1)=\mathrm{CCF}(\tau). \tag{B7}$$

In the opposite limit, $\alpha\ll1$, and Taylor-expanding Equation B6 to first order in α yields

$$r(\tau,\alpha)\simeq\mathrm{CCF}(0)+\alpha\left[\mathrm{CCF}(\tau)-\mathrm{CCF}(0)\mathrm{ACF}_c(\tau)\right]. \tag{B8}$$

Neglecting the normalization factors $\mathrm{CCF}(0)$ and α, the time-delay may be obtained by searching for the maximum of $\mathrm{CCF}(\tau)-\mathrm{CCF}(0)\mathrm{ACF}_c(\tau)$. Interestingly, for $\alpha\ll1$ the light curves in both bands across the optical range are highly correlated by virtue of continuum emission processes dominating them[6] hence $\mathrm{CCF}(0)\simeq1$. In this limit, we therefore seek to maximize the expression $\mathrm{CCF}(\tau)-\mathrm{ACF}_c(\tau)$, which is the estimator considered by Chelouche & Daniel (2012) for performing RM using broadband data.

Recalling the general expression (Eq. B6), one may significantly reduce the computational cost of searching for an extremum in 2D space, to searching for a maximum in r along a path by requiring that $\partial r(\tau,\alpha)/\partial\alpha=0$. The latter requirement defines a path in 2D space defined by

$$\alpha(\tau)=\frac{\mathrm{CCF}(0)\mathrm{ACF}_c(\tau)-\mathrm{CCF}(\tau)}{[\mathrm{CCF}(\tau)+\mathrm{CCF}(0)][\mathrm{ACF}_c(\tau)-1]}. \tag{B9}$$

Estimating the Pearson correlation coefficient over this path results in a one-dimensional calculation for which $r_e(\tau)\equiv r(\tau,\alpha(\tau))$ is extremal (maximal), and is given by

$$r_e(\tau)=\sqrt{\frac{\mathrm{CCF}^2(0)-2\mathrm{CCF}(0)\mathrm{CCF}(\tau)\mathrm{ACF}_c(\tau)+\mathrm{CCF}^2(\tau)}{1-\mathrm{ACF}_c^2(\tau)}}. \tag{B10}$$

The above expressions are simple to code and efficient to evaluate by standard means, as they include combinations of auto- and cross-correlation functions, which are commonly used in the field.

Implementing the above for non-uniformly sampled time-series with gaps, we use the linearly interpolated scheme (Gaskell & Sparke 1986; Peterson et al. 1998, and references therein) often used in RM. Specifically, we verify that the sampled light curve (when calculating auto-/cross-correlations) are characterized by zero mean with their appropriate standard deviations evaluated at each time step (the local correlation function formalism defined by Welsh 1999). Further, as noted in Welsh (1999) in the context of spectroscopic RM and in Chelouche & Daniel (2012, see also Chelouche & Zucker 2013) in the context of PRM, detrending of the light curves by a first degree polynomial is recommended as it leads to more stationary behavior for sources with soft power-density spectra, and to improved time-delays. We therefore de-trend the light curves by subtracting a first order polynomial.

[5] Here, $\sigma_c=\sqrt{N_c^{-1}\sum_{i=1}^{N_c}f_c(t_n)^2}$ and $\sigma_{lc}=\sqrt{N_{lc}^{-1}\sum_{i=1}^{N_{lc}}f_{lc}(t_n)^2}$

[6] This is true over the optical wavelength range, but may not be true for bands that are significantly removed in wavelength for which continuum time-delays may be relevant.

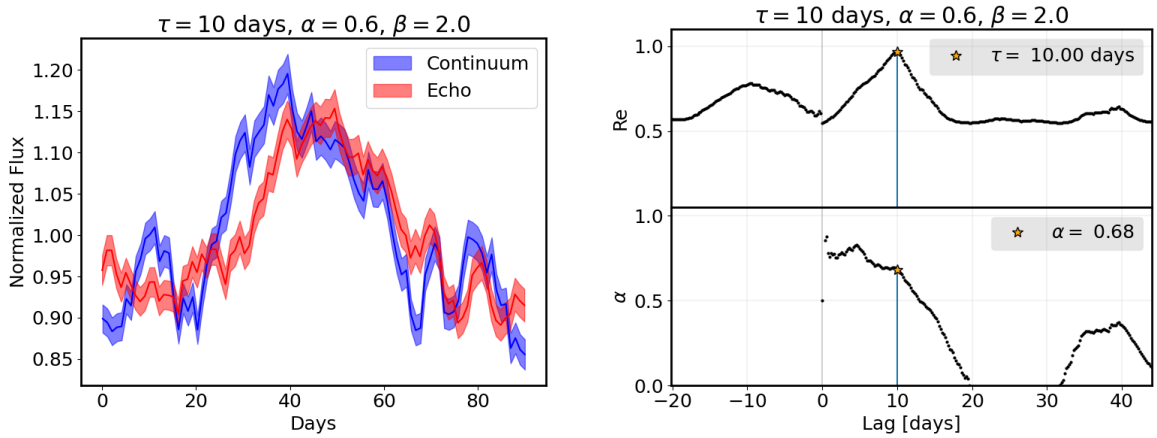

Figure B.1. Left: 100 days long simulated continuum light curve with an exponent $\beta = -2$ in blue and simulated echo light curve with $\alpha = 0.6$ and $\tau = 10$ days in red. Right: Correlation coefficient Re in the upper pannel with its corresponding α value in the bottom pannel. The peak delay $\tau_{\rm peak}$ and $\alpha_{\rm peak}$ are marked with an orange star and labeled.

B.1. *Light curves simulations*

We test the time lag determination formalism presented in Equations B9 and B10 via simulations. Specifically, we simulate continuum light curves as a sum of modes drawn from a power spectrum of the form $f(\omega) \propto \omega^{\beta}$ (ω is the frequency) with $\beta \sim -2$, as is typical for describing AGN variability (Timmer & Koenig 1995; Czerny et al. 2003; Kelly et al. 2009; Smith et al. 2018), and is consistent with damped random-walk models (Zu et al. 2013). However, more recent studies (e.g., Smith et al. 2018, using *Kepler* data) indicate somewhat steeper slopes ($\beta \sim -3$) over lightcrossing timescales of the BLR. For our simulations we therefore assume $-3 \leq \beta \leq -1$. To simulate the line-rich band, as assume equation B3, which implies a transfer function of the Dirac's δ-function form. The resulting light curve is determined by specifying the delay, $\tau_{\rm echo}$, and the relative contribution of the delayed component to the line-rich band, $\alpha_{\rm echo}$.

We define the total duration, $N_{\rm tot}$, of the continuum light curves as 100 days and consider two different time-delays, $\tau_{\rm echo} = 10$ days and $\tau_{\rm echo} = 30$ days. To mimic the observed signal, we add Gaussian noise at different levels corresponding to 1%, 5%, and 10% of the signal, and distinguish between uniform and non-uniform sampling. We analyze the mock light curves with our PRM formalism, by computing $R_e(\tau)$ as well as $\alpha(\tau)$ following expressions B9 and B10, thereby attempting to recover the input parameters. The correlation functions are implemented using a linear interpolation scheme, as commonly employed in reverberation studies (Gaskell & Peterson 1987; Peterson 1993; Welsh 1999). The time-delay recovered from the mock data is identified with the lag, which maximizes the coefficient $Re(\tau)$, $\tau_{\rm peak}$, and for which $0 < \alpha(\tau_{\rm peak}) \leq 1$.

The left panel of Figure B.1 shows an example for simulated continnuum and line-rich light curves with uniform sampling and a total duration $N_{\rm tot}$ of 100 days ($\beta = -2$, $F_{\rm var} = 0.1$, and $\tau_{\rm echo} = 10$ days, $\alpha_{\rm echo} = 0.6$ were assumed). Figure B.1 shows the resulting $R_e(\tau)$, which peaks at $\tau_{\rm echo} \simeq 10$ days, and implies $\alpha_{\rm peak} \simeq 0.68$. This example shows that the time delay is well reproduced with this formalism, while $\alpha_{\rm peak}$ is less accurately constrained.

To identify potential deviations of the measured time-delay from the input lag, we repeat the above calculation for 10^3 different light curves. Figure B.2 shows $\tau_{\rm peak}$ for uniformly sampled light curves with $N_{\rm tot} = 100$ days and an assumed noise level of 1%. The Figure shows the recovered time delay, $\tau_{\rm peak}$, versus the input value for the relative contribution of the delayed component to the band, $\alpha_{\rm echo}$. The results obtained with the PRM formalism introduced here are compared to those obtained via the standard cross-correlation (ICCF) technique: while the results from both methods converge for high $\alpha_{\rm echo}$ values (above 0.6), for lower values the new method is able to recover the input lag down to much lower values, which often characterize broadband data ($\alpha_{\rm echo} = 0.1$; Chelouche & Daniel 2012), whereas the time delay obtained with the ICCF method is biased towards lower values for $\alpha_{\rm echo} < 0.6$, and hence inapplicable for narrowband data (at $\alpha_{\rm echo} \lesssim 0.4$, as appropriate for some narrow-band and broadband data, the ICCF method leads to zero delays for our model). Figure B.2 also shows the case for non-uniformly sampled data, for which $\sim 30\%$ of the points have been eliminated using a random subset selection process (Peterson et al. 1998). Evidently, the scatter in the recovered lags by our PRM method is substantial for small values of $\alpha_{\rm echo}$ which are typical of broadband data, although the mean is still comparable to the input lag. For $\alpha_{\rm echo}$ values typical of narrowband data, our PRM formalism correctly recovers the input lag. This contrasts the ICCF results, which results in erroneous measurements also for broad and narrowband data.

Formally, $Re(\tau) \leq 1$ and yet in certain cases, our implementation of the formalism can lead to $Re(\tau) > 1$. This may occur when the cadence is non-uniform, and/or the time delay represents a considerable fraction of the total duration of the time series. Figure B.3 shows the statistics of the maximum $Re(\tau)$ value for simulated data. Clearly, a higher fraction of

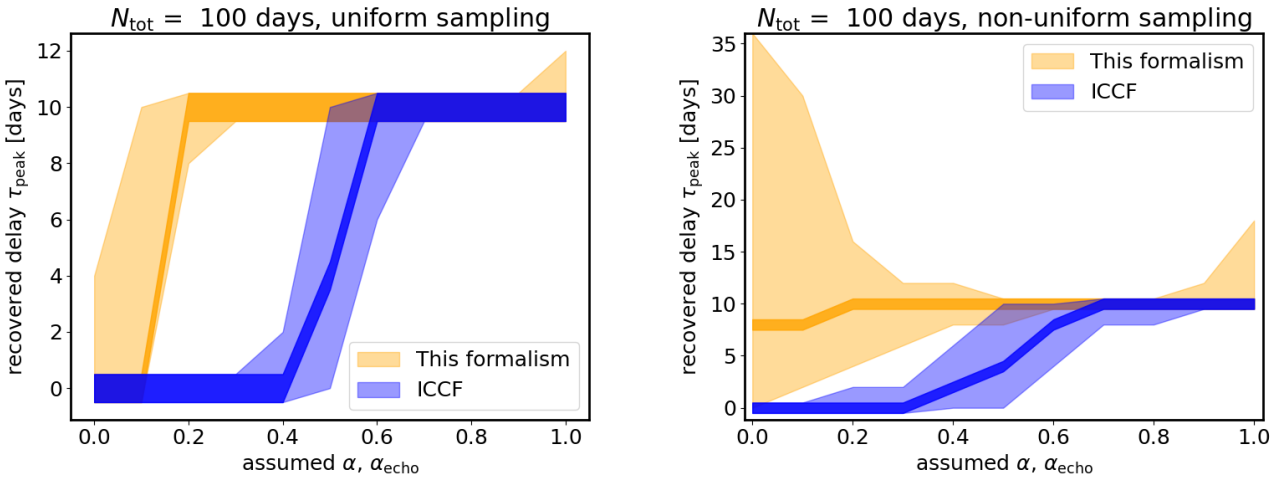

Figure B.2. Recovered time delay $\tau_{\rm peak}$ versus the assumed value for $\alpha_{\rm echo}$. The results obtained with this new formalism are shown in orange, while the results obtained directly with the ICCF method are shown in blue. Left pannel: results for uniform light curves with $N_{rmtot} = 100$ days and noise of 1%. Right pannel: Same for non-uniform light curves.

$Re(\tau) > 1$ occurrences is obtained when the time-delay is a significant fraction of the total duration of the time-series, and when considerable gaps exist, as in the case of non-uniform sampling. Therefore, great care must be taken when interpreting the results of the correlation functions at long time-delays, wherein the period overlap between the shifted time-series reduces by $\sim 50\%$. The reason for such effects is due to the implementation of the formalism with using ICCF 'building blocks' to evaluate equation 2. Partial remedy would be to define a common grid to all auto- and cross-correlation functions, and yet this may lead to a greater reliance on interpolated data than on real data, leading in some cases to erroneous results, which we opt to avoid. A further advantage of our current scheme is the use of readily available ICCF codes when calculating R_e. A more in-depth investigation of the limitations of this approach is beyond the scope of the present work.

Lastly, we note that the recovered contribution of the delayed component, $\alpha_{\rm peak}$, agrees with the simulated values for $\alpha_{\rm echo} \gtrsim 0.6$; see Figure B.4. This conclusion depends little on the noise level, and is relatively insensitive to the sampling. It shows that $\alpha_{\rm echo}$ is well recovered down to $\alpha_{\rm echo} \sim 0.2$, where it plateaus for the simulations conducted here. Thus, while time delays can be relatively well reproduced, the corresponding values for α may be biased to higher values for broadband data.

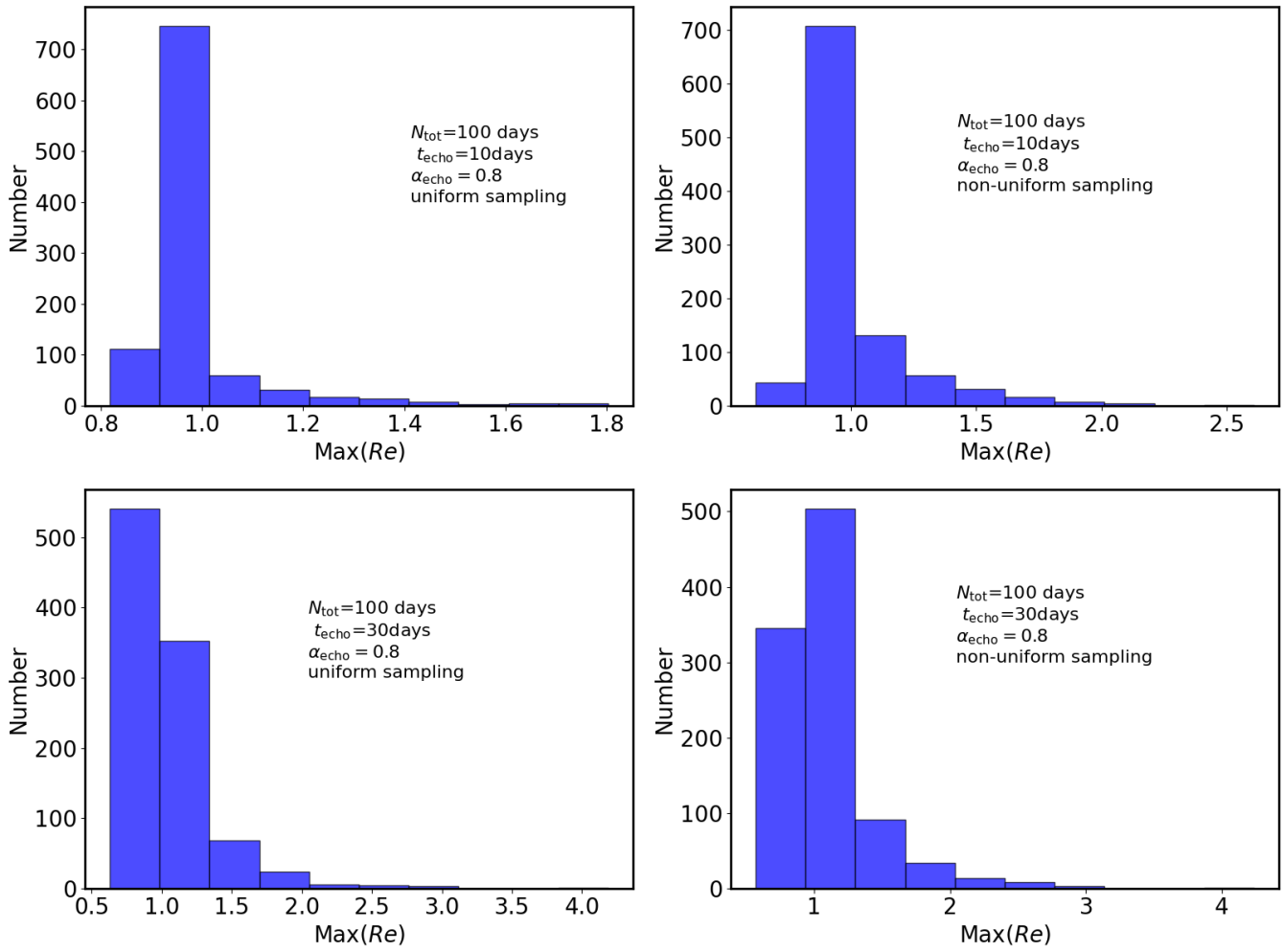

Figure B.3. Maximal value reached by the correlation coefficient Re for different kind of simulation settings. Simulated light curves with a total duration $N_{\rm tot} = 100$ days, $\tau_{\rm echo} = 10$ days and uniform sampling (top left); for $N_{\rm tot} = 100$ days, $\tau_{\rm echo} = 10$ days and non-uniform sampling (top right); for $N_{\rm tot} = 100$ days, $\tau_{\rm echo} = 30$ days and uniform sampling (bottom left) and for $N_{\rm tot} = 100$ days, $\tau_{\rm echo} = 30$ days and non-uniform sampling (bottom right).

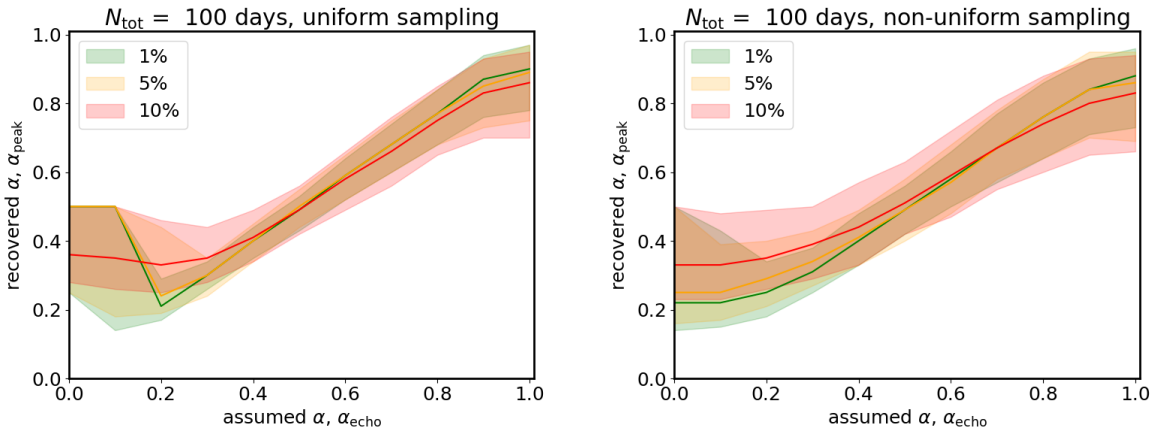

Figure B.4. Recovered $\alpha_{\rm peak}$ versus assumed $\alpha_{\rm echo}$ values for different noise values and uniform sampling (left) and non-uniform sampling(right).

Table C.1. Values for the peak and center of gravity ($\alpha_{\rm peak}$ and $\alpha_{\rm cent}$) obtain with the formalism and $\alpha_{\rm phot}$ expected from the photometry estimation.

Object	Year	$\alpha_{\rm peak}$	$\alpha_{\rm cent}$	$\alpha_{\rm phot}$	Object	Year	$\alpha_{\rm peak}$	$\alpha_{\rm cent}$	$\alpha_{\rm phot}$
1H2107	2012	$0.83^{+0.02}_{-0.02}$	$0.54^{+0.04}_{-0.12}$		MRK335	2010	$0.73^{+0.1}_{-0.08}$	$0.74^{+0.11}_{-0.09}$	
3C120	2014	$0.55^{+0.05}_{-0.05}$	$0.48^{+0.05}_{-0.05}$	0.63 ± 0.05	MRK335	2011	$0.61^{+0.07}_{-0.05}$	$0.61^{+0.06}_{-0.07}$	
AKN120	2018	$0.57^{+0.05}_{-0.05}$	$0.62^{+0.04}_{-0.06}$		MRK335	2014	$0.66^{+0.13}_{-0.06}$	$0.61^{+0.06}_{-0.05}$	0.65 ± 0.05
CTSG03_04	2013	$0.5^{+0.02}_{-0.02}$	$0.44^{+0.03}_{-0.03}$	0.7	MRK509	2014	$0.62^{+0.05}_{-0.04}$	$0.65^{+0.03}_{-0.03}$	0.76 ± 0.05
ESO141-G55	2015	$0.46^{+0.01}_{-0.01}$	$0.46^{+0.01}_{-0.01}$	0.73 ± 0.04	MRK705	2013	$0.59^{+0.05}_{-0.02}$	$0.45^{+0.03}_{-0.03}$	0.52 ± 0.07
ESO141-G55	2013	$0.77^{+0.06}_{-0.34}$	$0.49^{+0.03}_{-0.03}$	0.68 ± 0.05	MRK841	2014	$0.4^{+0.04}_{-0.04}$	$0.36^{+0.04}_{-0.02}$	
ESO323-G77	2015	$0.74^{+0.07}_{-0.06}$	$0.73^{+0.06}_{-0.07}$	0.61 ± 0.06	NGC101	2011	$0.75^{+0.08}_{-0.08}$	$0.74^{+0.07}_{-0.11}$	
ESO374-G25	2011	$0.4^{+0.09}_{-0.08}$	$0.3^{+0.03}_{-0.03}$		NGC472	2013	$0.78^{+0.04}_{-0.04}$	$0.79^{+0.03}_{-0.02}$	0.27 ± 0.09
ESO399	2011	$0.56^{+0.04}_{-0.04}$	$0.58^{+0.04}_{-0.04}$		NGC594	2014	$0.58^{+0.07}_{-0.06}$	$0.55^{+0.05}_{-0.06}$	0.49 ± 0.1
ESO438-G09	2011	$0.32^{+0.15}_{-0.03}$	$0.31^{+0.03}_{-0.03}$		NGC686	2015	$0.43^{+0.02}_{-0.03}$	$0.38^{+0.04}_{-0.03}$	0.46 ± 0.15
ESO438	2015	$0.35^{+0.02}_{-0.02}$	$0.3^{+0.04}_{-0.03}$	0.48 ± 0.11	NGC721	2011	$0.61^{+0.05}_{-0.05}$	$0.5^{+0.09}_{-0.1}$	
ESO490	2011	$0.55^{+0.05}_{-0.04}$	$0.53^{+0.05}_{-0.04}$		NGC746	2012	$0.3^{+0.05}_{-0.03}$	$0.26^{+0.06}_{-0.01}$	0.0 ± 0.0
ESO511	2013	$0.62^{+0.02}_{-0.02}$	$0.54^{+0.02}_{-0.01}$	0.53 ± 0.13	NGC760	2014	$0.2^{+0.0}_{-0.01}$	$0.18^{+0.01}_{-0.02}$	0.43 ± 0.14
ESO511	2014	$0.52^{+0.01}_{-0.01}$	$0.51^{+0.01}_{-0.01}$	0.37 ± 0.17	NGC985	2014	$0.78^{+0.05}_{-0.05}$	$0.72^{+0.05}_{-0.04}$	0.77 ± 0.0
ESO549	2012	$0.49^{+0.05}_{-0.05}$	$0.41^{+0.12}_{-0.14}$		PG1149	2013	$0.8^{+0.04}_{-0.09}$	$0.73^{+0.08}_{-0.05}$	0.41 ± 0.06
ESO578	2014	$0.51^{+0.11}_{-0.07}$	$0.48^{+0.03}_{-0.03}$	0.53 ± 0.12	PGC504	2014	$0.81^{+0.03}_{-0.06}$	$0.74^{+0.04}_{-0.03}$	0.58 ± 0.1
F1041	2013	$0.59^{+0.02}_{-0.02}$	$0.6^{+0.02}_{-0.02}$	0.46 ± 0.1	PGC504	2011	$0.65^{+0.04}_{-0.04}$	$0.65^{+0.03}_{-0.03}$	
HE0003	2014	$0.58^{+0.07}_{-0.25}$	$0.36^{+0.05}_{-0.05}$	0.56 ± 0.05	PGC649	2013	$0.63^{+0.03}_{-0.05}$	$0.6^{+0.04}_{-0.07}$	0.34 ± 0.07
HE1136-2304	2016	$0.47^{+0.04}_{-0.04}$	$0.38^{+0.09}_{-0.07}$		PGC649	2014	$0.42^{+0.01}_{-0.01}$	$0.42^{+0.01}_{-0.01}$	0.38 ± 0.12
HE1136	2018	$0.62^{+0.11}_{-0.09}$	$0.59^{+0.09}_{-0.07}$		RXSJ06	2013	$0.41^{+0.01}_{-0.01}$	$0.41^{+0.01}_{-0.02}$	0.41 ± 0.15
HE1136	2015	$0.65^{+0.05}_{-0.03}$	$0.69^{+0.04}_{-0.04}$		RXSJ11	2011	$0.53^{+0.06}_{-0.06}$	$0.50^{+0.09}_{-0.19}$	
HE1143	2016	$0.43^{+0.02}_{-0.02}$	$0.43^{+0.02}_{-0.03}$		RXSJ11	2014	$0.52^{+0.20}_{-0.21}$	$0.33^{+0.17}_{-0.06}$	
HE2128	2016	$0.44^{+0.23}_{-0.06}$	$0.43^{+0.05}_{-0.05}$		RXSJ17	2012	$0.52^{+0.01}_{-0.01}$	$0.44^{+0.02}_{-0.02}$	
IC4329	2015	$0.52^{+0.03}_{-0.12}$	$0.38^{+0.02}_{-0.02}$	0.7 ± 0.07	RXSJ17	2014	$0.53^{+0.06}_{-0.02}$	$0.57^{+0.03}_{-0.04}$	0.60
IRAS01089-4743	2013	$0.45^{+0.04}_{-0.03}$	$0.36^{+0.13}_{-0.12}$	0.30	UGC121	2012	$0.61^{+0.03}_{-0.03}$	$0.64^{+0.05}_{-0.04}$	
IRAS09	2013	$0.84^{+0.01}_{-0.02}$	$0.81^{+0.03}_{-0.05}$	0.5 ± 0.08	UM163	2013	$0.84^{+0.01}_{-0.01}$	$0.79^{+0.02}_{-0.02}$	0.53 ± 0.13
IRAS23	2013	$0.47^{+0.1}_{-0.04}$	$0.27^{+0.11}_{-0.02}$	0.25	WPVS00	2012	$0.5^{+0.03}_{-0.03}$	$0.48^{+0.03}_{-0.03}$	
MCG+03	2013	$0.46^{+0.01}_{-0.01}$	$0.45^{+0.01}_{-0.01}$	0.44	WPVS48	2014	$0.48^{+0.02}_{-0.02}$	$0.46^{+0.02}_{-0.02}$	0.71 ± 0.04
MCG021	2014	$0.54^{+0.03}_{-0.04}$	$0.53^{+0.04}_{-0.04}$	0.43 ± 0.12	WPVS48	2013	$0.45^{+0.01}_{-0.01}$	$0.42^{+0.01}_{-0.01}$	0.73 ± 0.03
MRK123	2015	$0.79^{+0.05}_{-0.11}$	$0.79^{+0.04}_{-0.13}$	0.73 ± 0.03	WPVS48	2018	$0.52^{+0.02}_{-0.02}$	$0.52^{+0.02}_{-0.02}$	
MRK134	2014	$0.47^{+0.18}_{-0.05}$	$0.39^{+0.07}_{-0.07}$	0.49 ± 0.06					

C. Hα CORRELATIONS AND CONTINUUM CONTRIBUTION TO THE EMISSION LINE

This appendix presents time-lag estimations for all the sources in our sample. Each of the plots contains four panels: the top panel shows the normalized and detrended light curves for the continuum signal (blue) and the NB band (red). $F_{\rm var}$ and η values associated with the original light curves is also noted (see Appendix A). The left panel on the second row of each figuredisplays the distribution of the time-lag estimations following 10^3 flux-randomization iterations; the blue histogram represents the peak delays and the red histogram represents the centroid delays. The resulting values for the 50% percentile and the errors (15% and 85% percentiles) are labeled. The right panel on the second row of each depicts the distribution for the deduced α values (see Appendix B), with a similar meaning as for the time delays. The bottom panel in each figure presents the distribution for the maximal correlation coefficient, $R_{\rm e,max}$, hence is a measure of the goodness of fit from which time-delay determination follows. The blue histogram shows the distribution obtained after many flux-randomization iterations are performed, and the orange histogram represents the $R_{\rm e,max}$ value for the time-permutation (TP) scheme (see Section 3.1). The confidence level of our results is denoted in per-cent next to the *Conf* label.

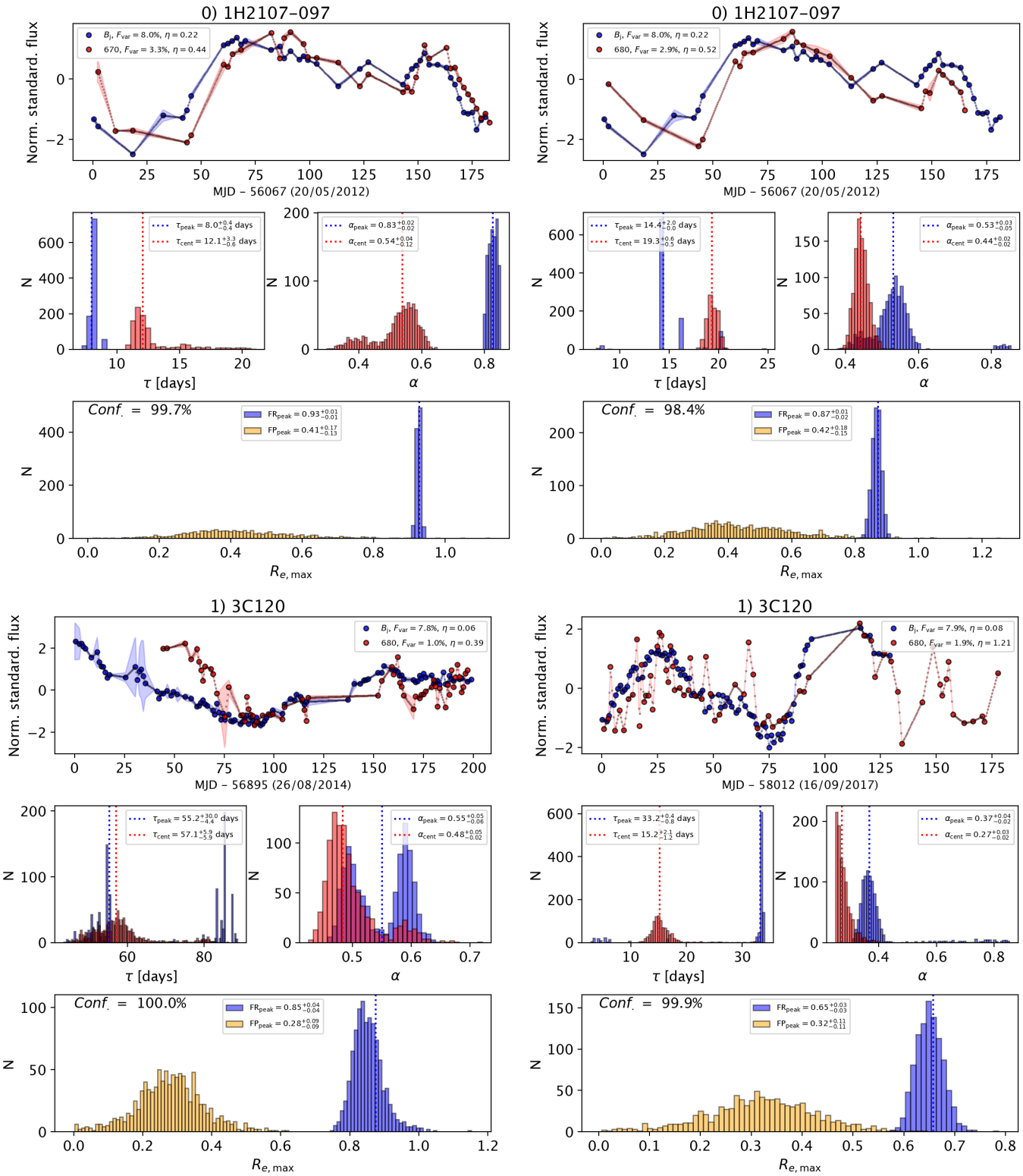
0) 1H2107−097
Norm. standard. flux
MJD − 56067 (20/05/2012)
τ [days]
α
N
Conf. = 99.7%
Conf. = 98.4%
$R_{e,\max}$
1) 3C120
MJD − 58012 (16/09/2017)
MJD − 56895 (26/08/2014)
Conf. = 100.0%
Conf. = 99.9%

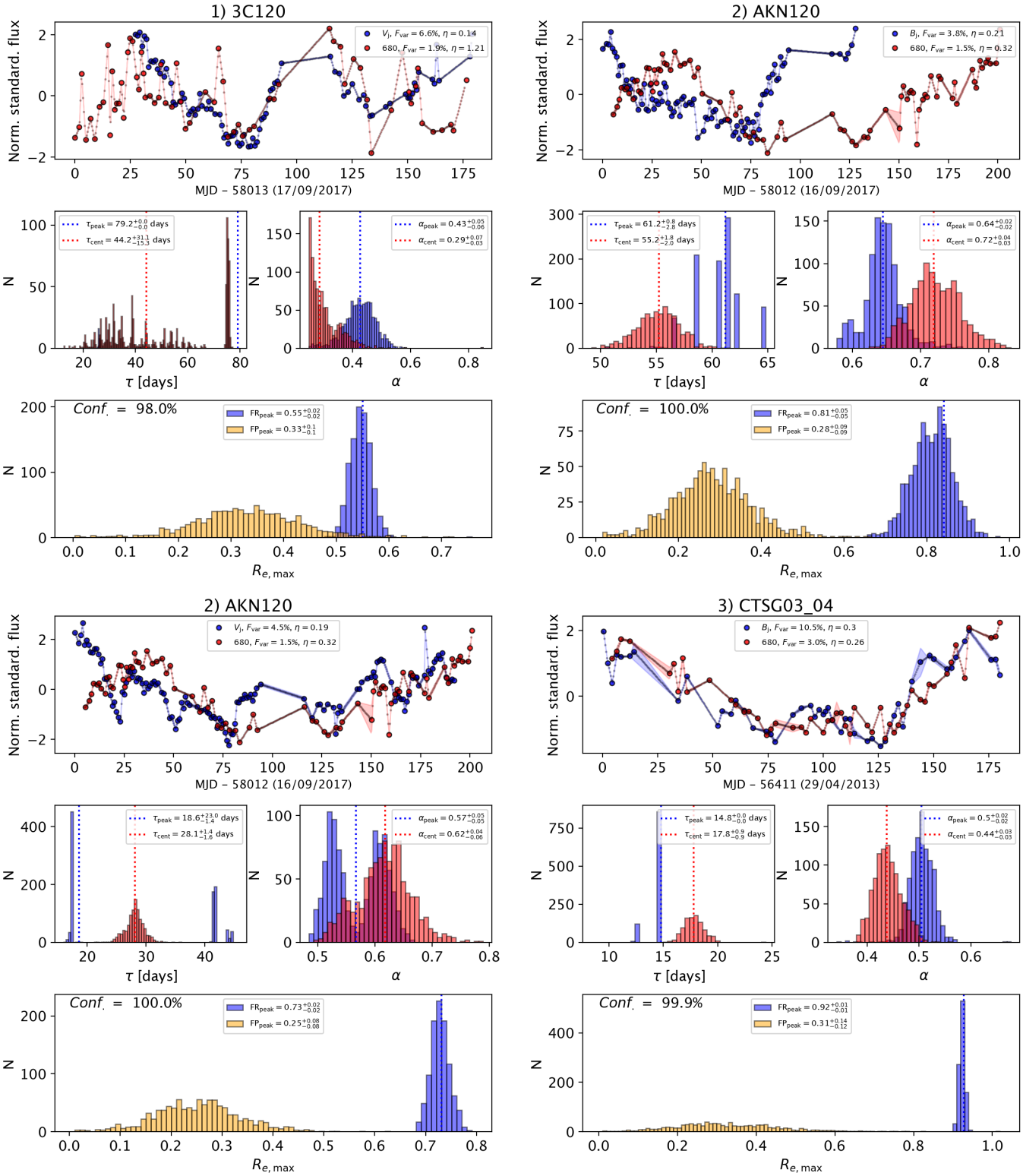
1) 3C120
Norm. standard. flux
MJD − 58013 (17/09/2017)
$\tau_{peak} = 79.2^{+0.0}_{-0.0}$ days
$\tau_{cent} = 44.2^{+31.1}_{-15.3}$ days
τ [days]
$\alpha_{peak} = 0.43^{+0.05}_{-0.06}$
$\alpha_{cent} = 0.29^{+0.07}_{-0.03}$
α
Conf. = 98.0%
$FR_{peak} = 0.55^{+0.02}_{-0.02}$
$FP_{peak} = 0.33^{+0.1}_{-0.1}$
$R_{e,max}$
2) AKN120
Norm. standard. flux
MJD − 58012 (16/09/2017)
$\tau_{peak} = 61.2^{+0.8}_{-2.8}$ days
$\tau_{cent} = 55.2^{+1.8}_{-2.0}$ days
τ [days]
$\alpha_{peak} = 0.64^{+0.02}_{-0.02}$
$\alpha_{cent} = 0.72^{+0.04}_{-0.03}$
α
Conf. = 100.0%
$FR_{peak} = 0.81^{+0.05}_{-0.05}$
$FP_{peak} = 0.28^{+0.09}_{-0.09}$
$R_{e,max}$
2) AKN120
Norm. standard. flux
MJD − 58012 (16/09/2017)
$\tau_{peak} = 18.6^{+23.0}_{-1.4}$ days
$\tau_{cent} = 28.1^{+1.4}_{-1.6}$ days
τ [days]
$\alpha_{peak} = 0.57^{+0.05}_{-0.05}$
$\alpha_{cent} = 0.62^{+0.04}_{-0.06}$
α
Conf. = 100.0%
$FR_{peak} = 0.73^{+0.02}_{-0.02}$
$FP_{peak} = 0.25^{+0.08}_{-0.08}$
$R_{e,max}$
3) CTSG03_04
Norm. standard. flux
MJD − 56411 (29/04/2013)
$\tau_{peak} = 14.8^{+0.0}_{-0.0}$ days
$\tau_{cent} = 17.8^{+0.9}_{-0.9}$ days
τ [days]
$\alpha_{peak} = 0.5^{+0.02}_{-0.02}$
$\alpha_{cent} = 0.44^{+0.03}_{-0.03}$
α
Conf. = 99.9%
$FR_{peak} = 0.92^{+0.01}_{-0.01}$
$FP_{peak} = 0.31^{+0.14}_{-0.12}$
$R_{e,max}$

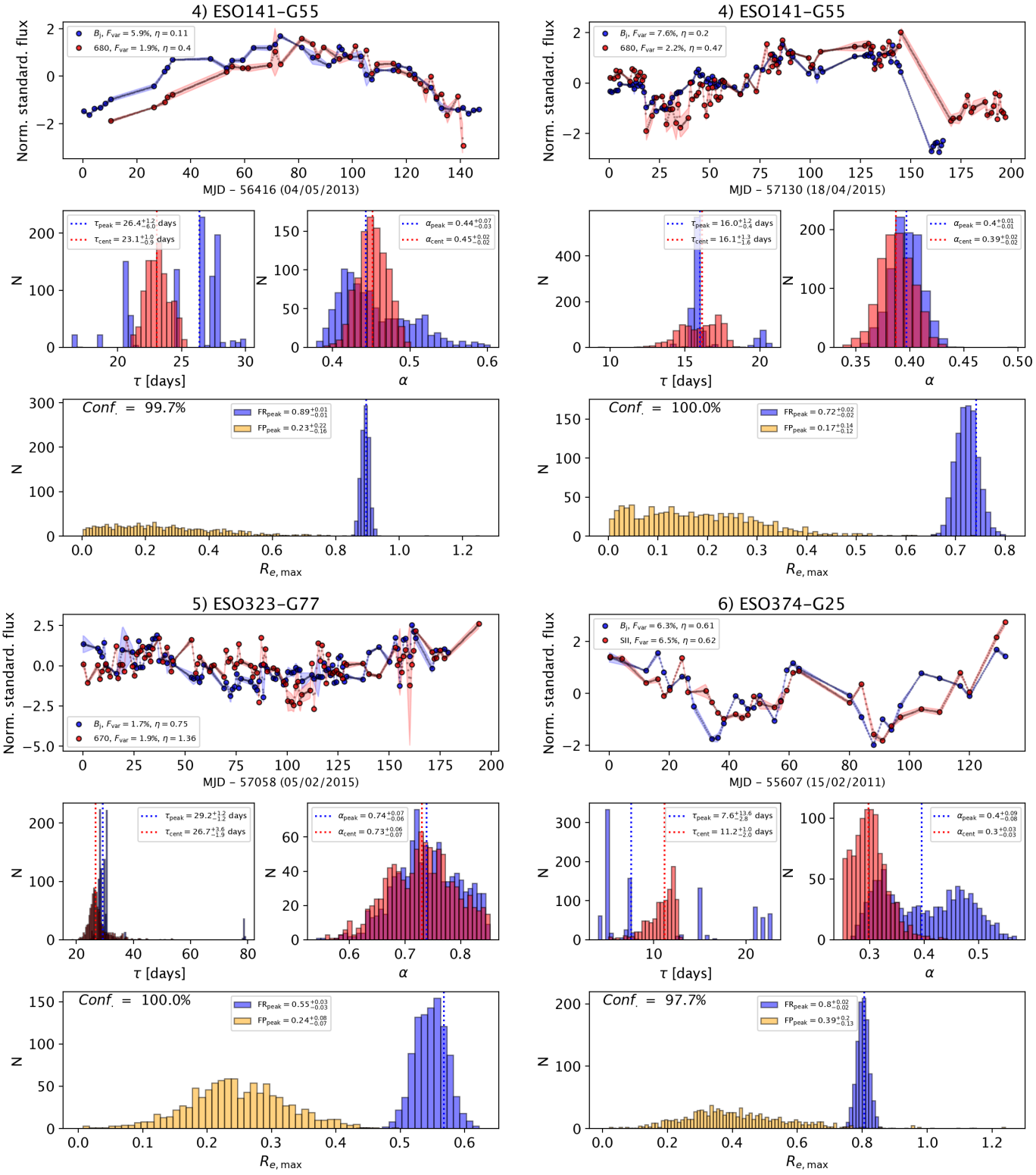
4) ESO141−G55
Norm. standard. flux
B_J, $F_{var} = 5.9\%$, $\eta = 0.11$
680, $F_{var} = 1.9\%$, $\eta = 0.4$
MJD − 56416 (04/05/2013)
$\tau_{peak} = 26.4^{+1.2}_{-6.0}$ days
$\tau_{cent} = 23.1^{+1.0}_{-0.9}$ days
$\alpha_{peak} = 0.44^{+0.07}_{-0.03}$
$\alpha_{cent} = 0.45^{+0.02}_{-0.02}$
N
τ [days]
α
Conf. = 99.7%
$FR_{peak} = 0.89^{+0.01}_{-0.01}$
$FP_{peak} = 0.23^{+0.22}_{-0.16}$
$R_{e,max}$
4) ESO141−G55
Norm. standard. flux
B_J, $F_{var} = 7.6\%$, $\eta = 0.2$
680, $F_{var} = 2.2\%$, $\eta = 0.47$
MJD − 57130 (18/04/2015)
$\tau_{peak} = 16.0^{+1.2}_{-1.4}$ days
$\tau_{cent} = 16.1^{+1.3}_{-1.6}$ days
$\alpha_{peak} = 0.4^{+0.01}_{-0.01}$
$\alpha_{cent} = 0.39^{+0.02}_{-0.02}$
N
τ [days]
α
Conf. = 100.0%
$FR_{peak} = 0.72^{+0.02}_{-0.02}$
$FP_{peak} = 0.17^{+0.14}_{-0.12}$
$R_{e,max}$
5) ESO323−G77
Norm. standard. flux
B_J, $F_{var} = 1.7\%$, $\eta = 0.75$
670, $F_{var} = 1.9\%$, $\eta = 1.36$
MJD − 57058 (05/02/2015)
$\tau_{peak} = 29.2^{+1.2}_{-1.2}$ days
$\tau_{cent} = 26.7^{+3.6}_{-1.9}$ days
$\alpha_{peak} = 0.74^{+0.07}_{-0.06}$
$\alpha_{cent} = 0.73^{+0.06}_{-0.07}$
N
τ [days]
α
Conf. = 100.0%
$FR_{peak} = 0.55^{+0.03}_{-0.03}$
$FP_{peak} = 0.24^{+0.08}_{-0.07}$
$R_{e,max}$
6) ESO374−G25
Norm. standard. flux
B_J, $F_{var} = 6.3\%$, $\eta = 0.61$
SII, $F_{var} = 6.5\%$, $\eta = 0.62$
MJD − 55607 (15/02/2011)
$\tau_{peak} = 7.6^{+13.6}_{-2.8}$ days
$\tau_{cent} = 11.2^{+1.0}_{-2.0}$ days
$\alpha_{peak} = 0.4^{+0.09}_{-0.08}$
$\alpha_{cent} = 0.3^{+0.03}_{-0.03}$
N
τ [days]
α
Conf. = 97.7%
$FR_{peak} = 0.8^{+0.02}_{-0.02}$
$FP_{peak} = 0.39^{+0.2}_{-0.13}$
$R_{e,max}$

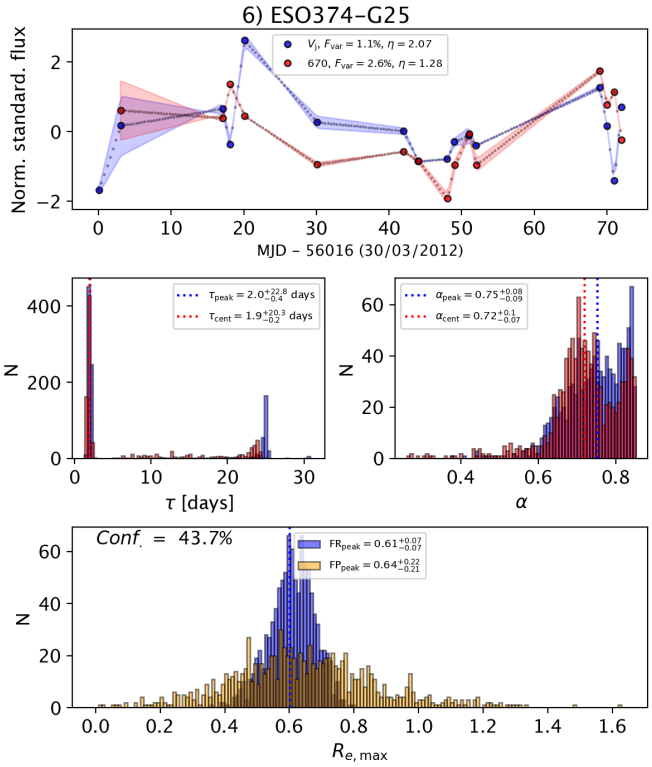
6) ESO374-G25
Norm. standard. flux
MJD − 56016 (30/03/2012)
τ [days]
α
N
Conf. = 43.7%
$R_{e,\max}$

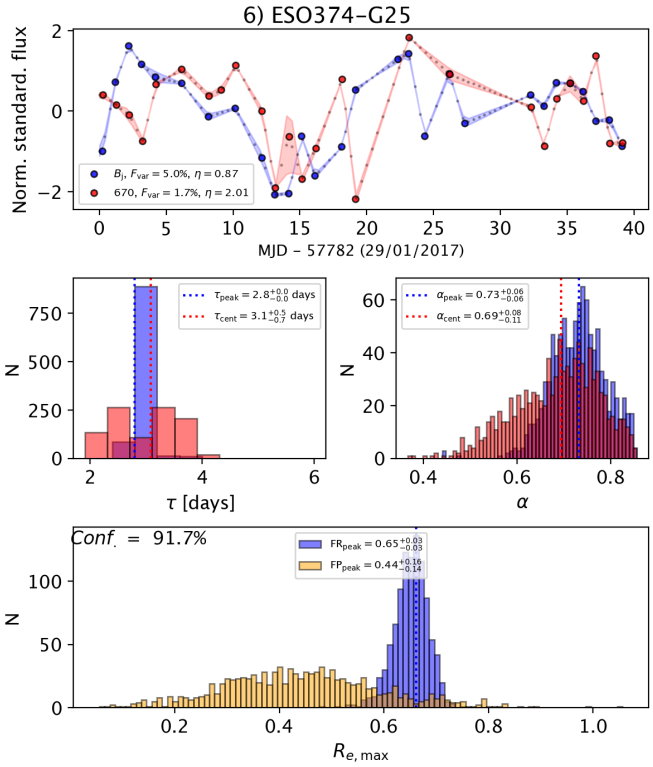
6) ESO374-G25
Norm. standard. flux
MJD − 57782 (29/01/2017)
τ [days]
α
N
Conf. = 91.7%
$R_{e,\max}$

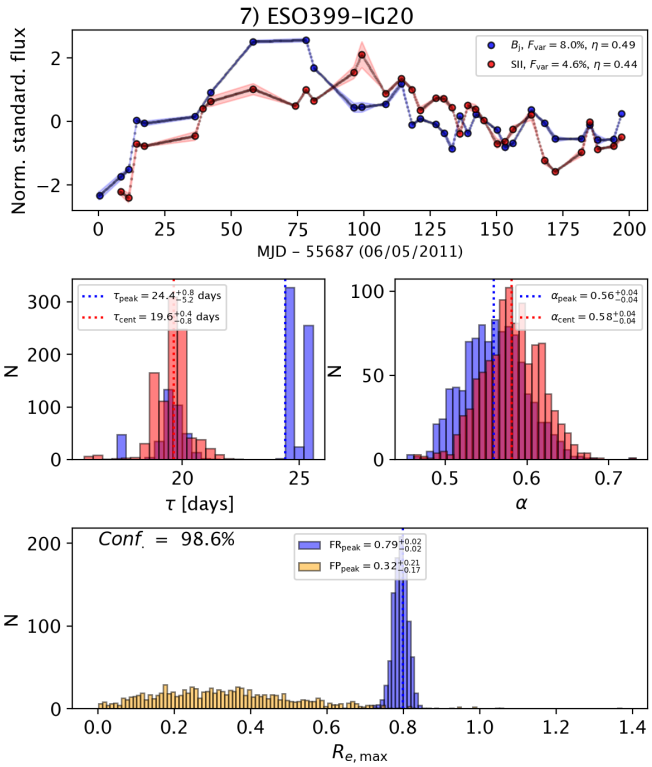
7) ESO399-IG20
Norm. standard. flux
MJD − 55687 (06/05/2011)
τ [days]
α
N
Conf. = 98.6%
$R_{e,\max}$

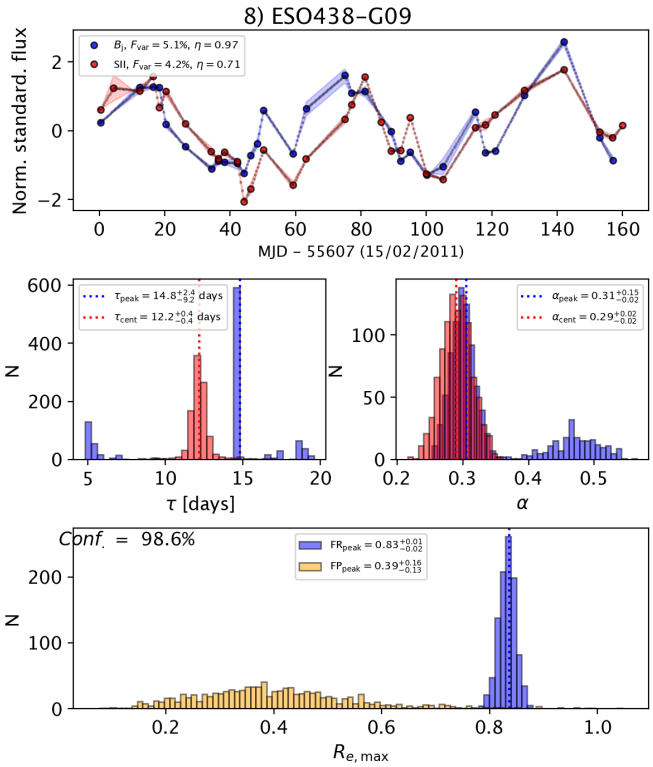
8) ESO438-G09
Norm. standard. flux
MJD − 55607 (15/02/2011)
τ [days]
α
N
Conf. = 98.6%
$R_{e,\max}$

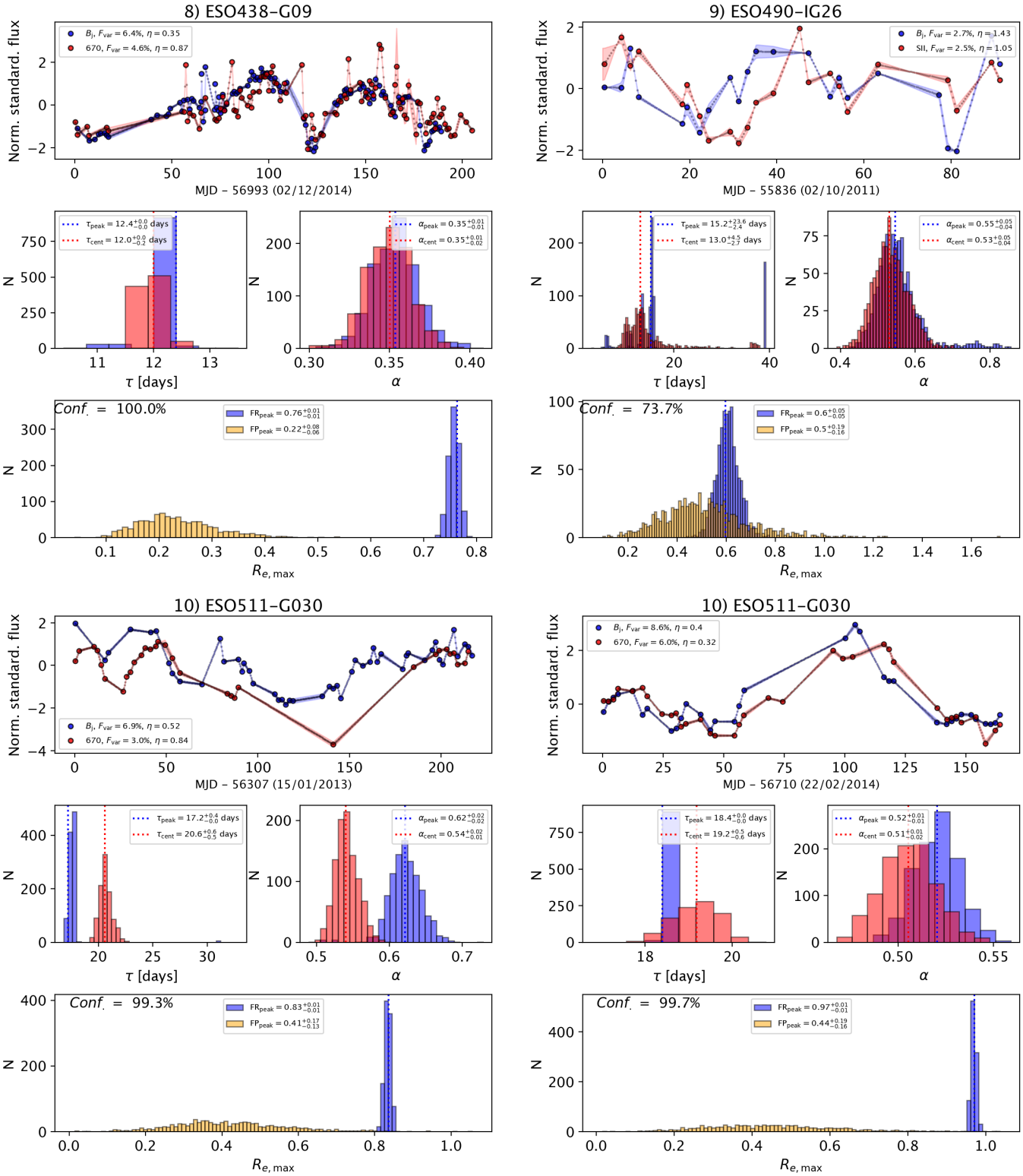
8) ESO438-G09
Norm. standard. flux
B_J, $F_{var} = 6.4\%$, $\eta = 0.35$
670, $F_{var} = 4.6\%$, $\eta = 0.87$
MJD − 56993 (02/12/2014)
$\tau_{peak} = 12.4^{+0.0}_{-0.0}$ days
$\tau_{cent} = 12.0^{+0.0}_{-0.2}$ days
τ [days]
$\alpha_{peak} = 0.35^{+0.01}_{-0.01}$
$\alpha_{cent} = 0.35^{+0.01}_{-0.02}$
α
Conf. = 100.0%
$FR_{peak} = 0.76^{+0.01}_{-0.01}$
$FP_{peak} = 0.22^{+0.08}_{-0.06}$
$R_{e,max}$
9) ESO490-IG26
Norm. standard. flux
B_J, $F_{var} = 2.7\%$, $\eta = 1.43$
SII, $F_{var} = 2.5\%$, $\eta = 1.05$
MJD − 55836 (02/10/2011)
$\tau_{peak} = 15.2^{+23.6}_{-2.4}$ days
$\tau_{cent} = 13.0^{+4.5}_{-2.7}$ days
τ [days]
$\alpha_{peak} = 0.55^{+0.05}_{-0.04}$
$\alpha_{cent} = 0.53^{+0.05}_{-0.04}$
α
Conf. = 73.7%
$FR_{peak} = 0.6^{+0.05}_{-0.05}$
$FP_{peak} = 0.5^{+0.19}_{-0.16}$
$R_{e,max}$
10) ESO511-G030
Norm. standard. flux
B_J, $F_{var} = 6.9\%$, $\eta = 0.52$
670, $F_{var} = 3.0\%$, $\eta = 0.84$
MJD − 56307 (15/01/2013)
$\tau_{peak} = 17.2^{+0.4}_{-0.0}$ days
$\tau_{cent} = 20.6^{+0.6}_{-0.5}$ days
τ [days]
$\alpha_{peak} = 0.62^{+0.02}_{-0.02}$
$\alpha_{cent} = 0.54^{+0.02}_{-0.01}$
α
Conf. = 99.3%
$FR_{peak} = 0.83^{+0.01}_{-0.01}$
$FP_{peak} = 0.41^{+0.17}_{-0.13}$
$R_{e,max}$
10) ESO511-G030
Norm. standard. flux
B_J, $F_{var} = 8.6\%$, $\eta = 0.4$
670, $F_{var} = 6.0\%$, $\eta = 0.32$
MJD − 56710 (22/02/2014)
$\tau_{peak} = 18.4^{+0.0}_{-0.0}$ days
$\tau_{cent} = 19.2^{+0.5}_{-0.6}$ days
τ [days]
$\alpha_{peak} = 0.52^{+0.01}_{-0.01}$
$\alpha_{cent} = 0.51^{+0.01}_{-0.02}$
α
Conf. = 99.7%
$FR_{peak} = 0.97^{+0.01}_{-0.01}$
$FP_{peak} = 0.44^{+0.19}_{-0.16}$
$R_{e,max}$

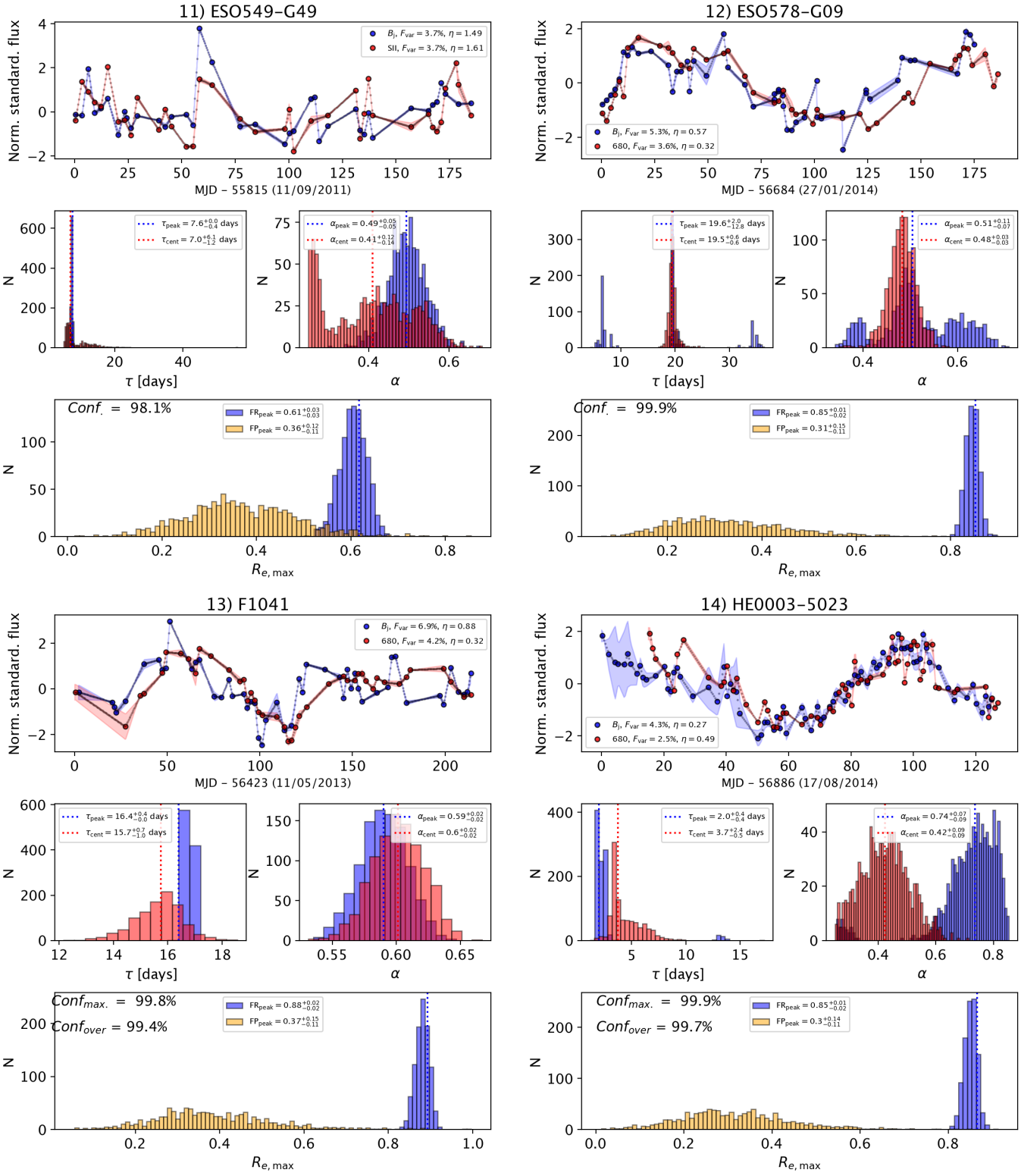
11) ESO549-G49
Norm. standard. flux
MJD − 55815 (11/09/2011)
τ [days]
α
$R_{e,\max}$
12) ESO578-G09
MJD − 56684 (27/01/2014)
13) F1041
MJD − 56423 (11/05/2013)
14) HE0003-5023
MJD − 56886 (17/08/2014)
N

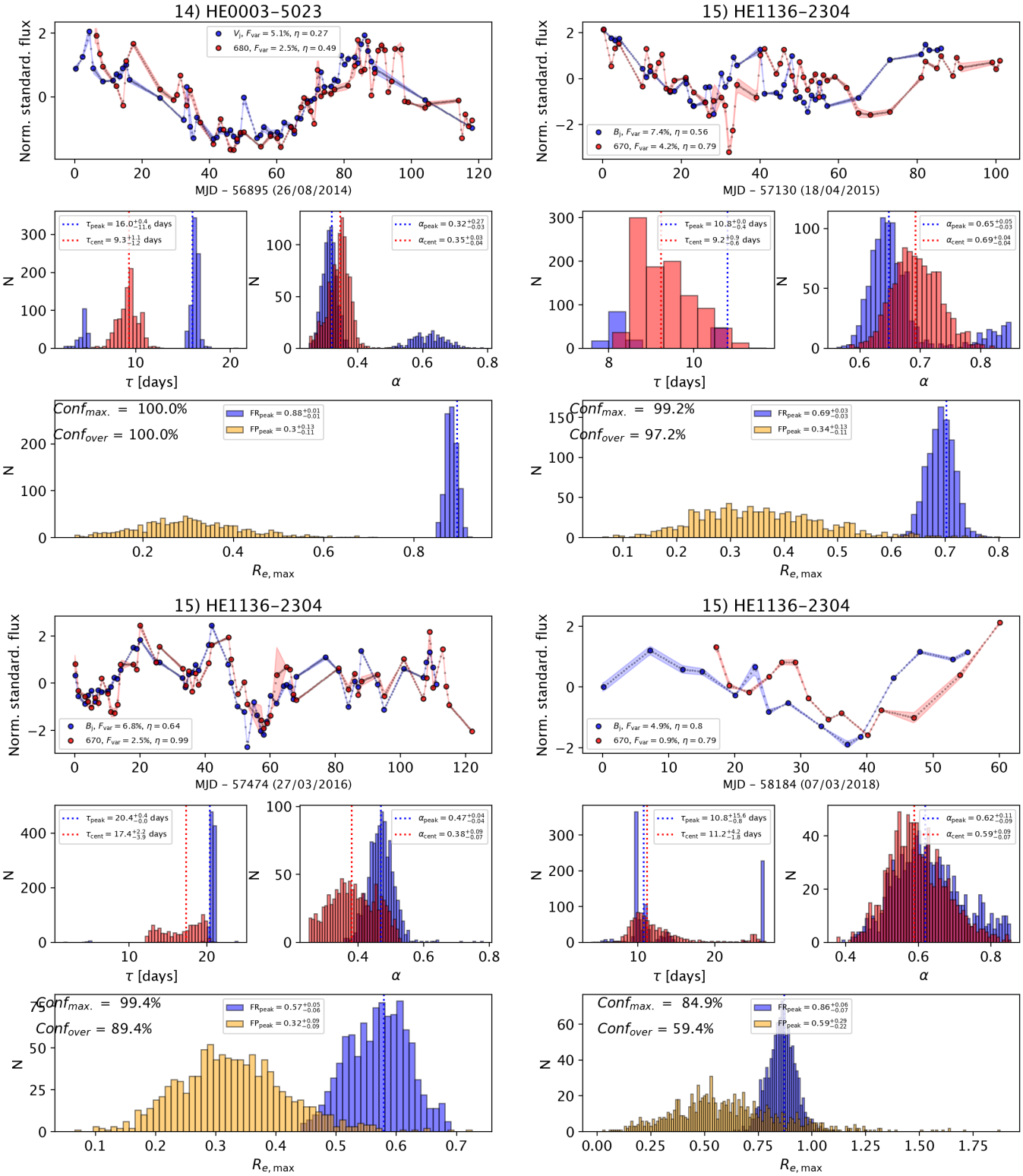
14) HE0003-5023
15) HE1136-2304
15) HE1136-2304
15) HE1136-2304
Norm. standard. flux
MJD - 56895 (26/08/2014)
MJD - 57130 (18/04/2015)
MJD - 57474 (27/03/2016)
MJD - 58184 (07/03/2018)
τ [days]
α
N
$R_{e,\max}$
$Conf_{max.}$ = 100.0%
$Conf_{over}$ = 100.0%
$Conf_{max.}$ = 99.2%
$Conf_{over}$ = 97.2%
$Conf_{max.}$ = 99.4%
$Conf_{over}$ = 89.4%
$Conf_{max.}$ = 84.9%
$Conf_{over}$ = 59.4%

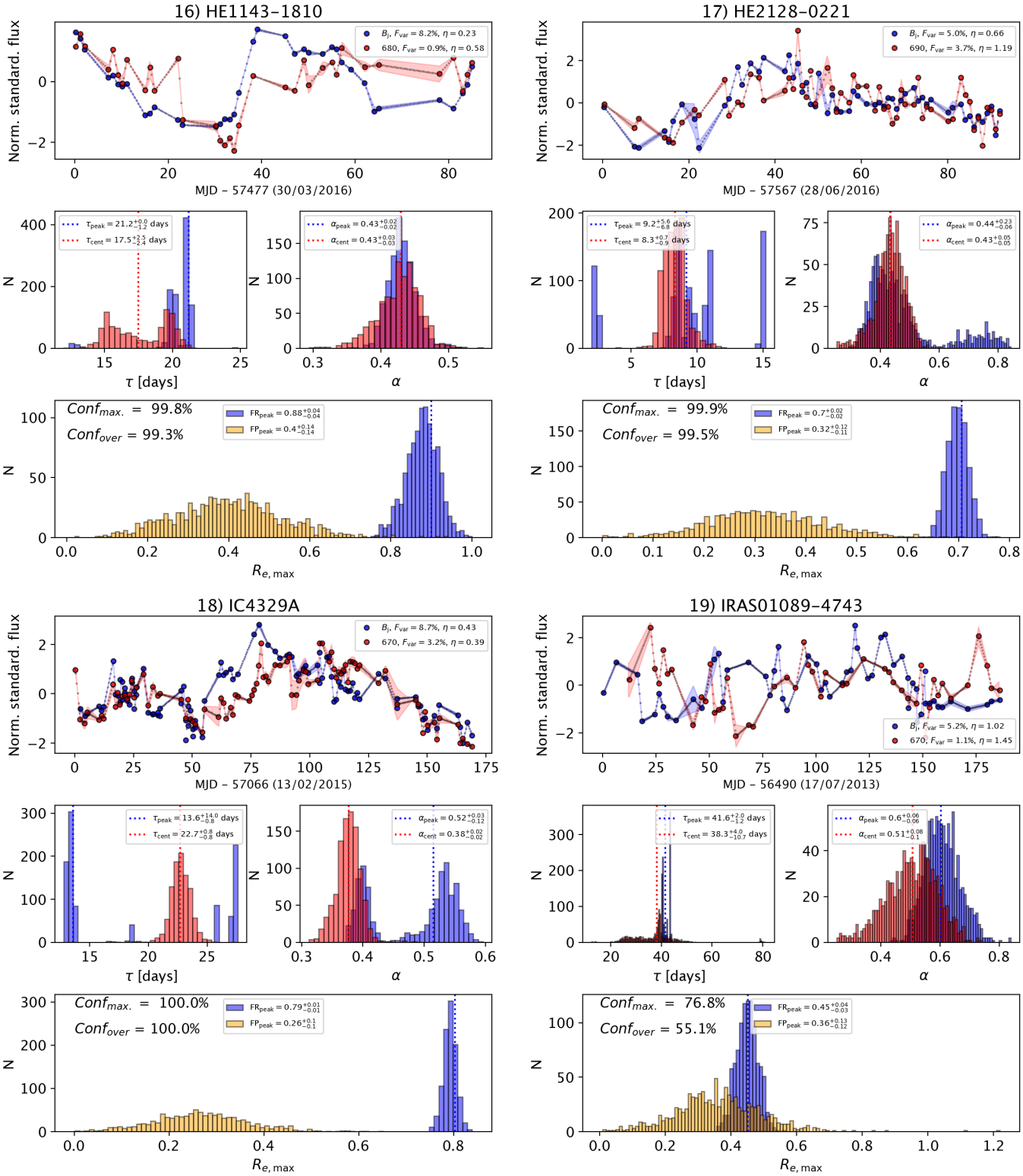
16) HE1143−1810
Norm. standard. flux
MJD − 57477 (30/03/2016)
17) HE2128−0221
MJD − 57567 (28/06/2016)
τ [days]
α
N
Conf_max. = 99.8%
Conf_over = 99.3%
Conf_max. = 99.9%
Conf_over = 99.5%
R_e, max
18) IC4329A
MJD − 57066 (13/02/2015)
19) IRAS01089−4743
MJD − 56490 (17/07/2013)
Conf_max. = 100.0%
Conf_over = 100.0%
Conf_max. = 76.8%
Conf_over = 55.1%

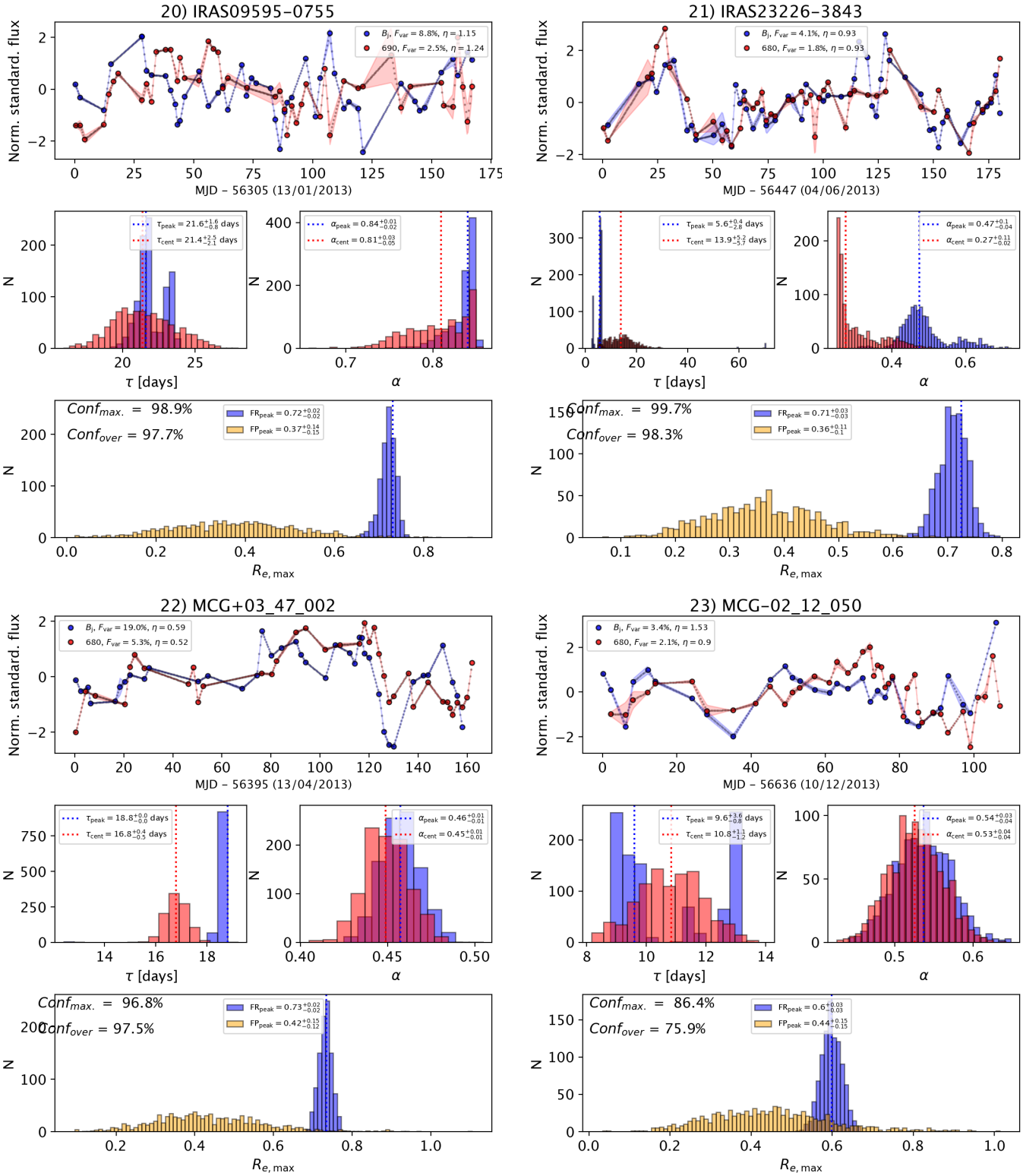
20) IRAS09595−0755
Norm. standard. flux
MJD − 56305 (13/01/2013)
τ [days]
α
$R_{e,\max}$
$Conf_{max.}$ = 98.9%
$Conf_{over}$ = 97.7%
21) IRAS23226−3843
MJD − 56447 (04/06/2013)
$Conf_{max.}$ = 99.7%
$Conf_{over}$ = 98.3%
22) MCG+03_47_002
MJD − 56395 (13/04/2013)
$Conf_{max.}$ = 96.8%
$Conf_{over}$ = 97.5%
23) MCG−02_12_050
MJD − 56636 (10/12/2013)
$Conf_{max.}$ = 86.4%
$Conf_{over}$ = 75.9%

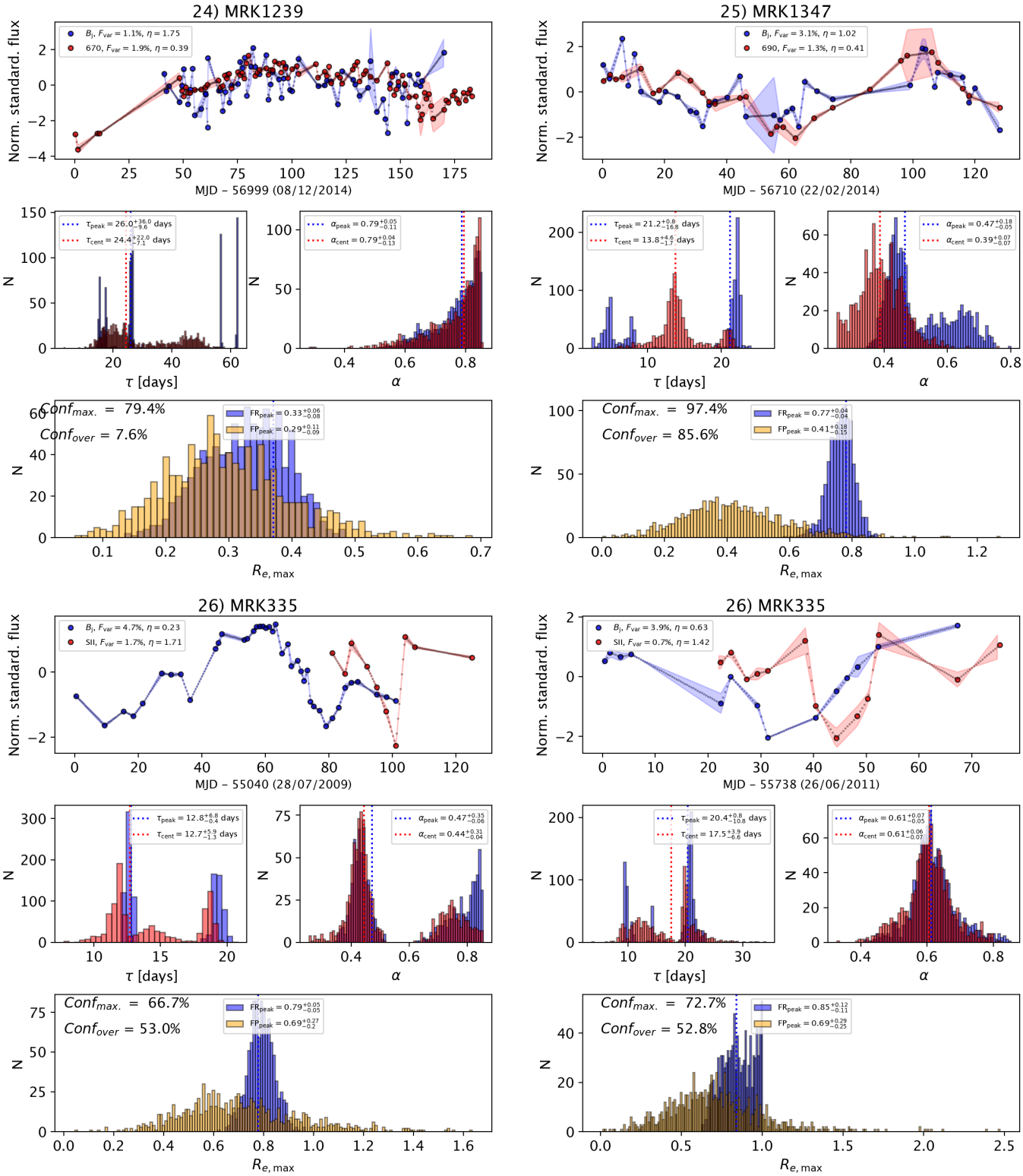
24) MRK1239
Norm. standard. flux
MJD − 56999 (08/12/2014)
τ [days]
α
$R_{e,\max}$
$Conf_{max.}$ = 79.4%
$Conf_{over}$ = 7.6%
25) MRK1347
MJD − 56710 (22/02/2014)
$Conf_{max.}$ = 97.4%
$Conf_{over}$ = 85.6%
26) MRK335
MJD − 55040 (28/07/2009)
$Conf_{max.}$ = 66.7%
$Conf_{over}$ = 53.0%
26) MRK335
MJD − 55738 (26/06/2011)
$Conf_{max.}$ = 72.7%
$Conf_{over}$ = 52.8%

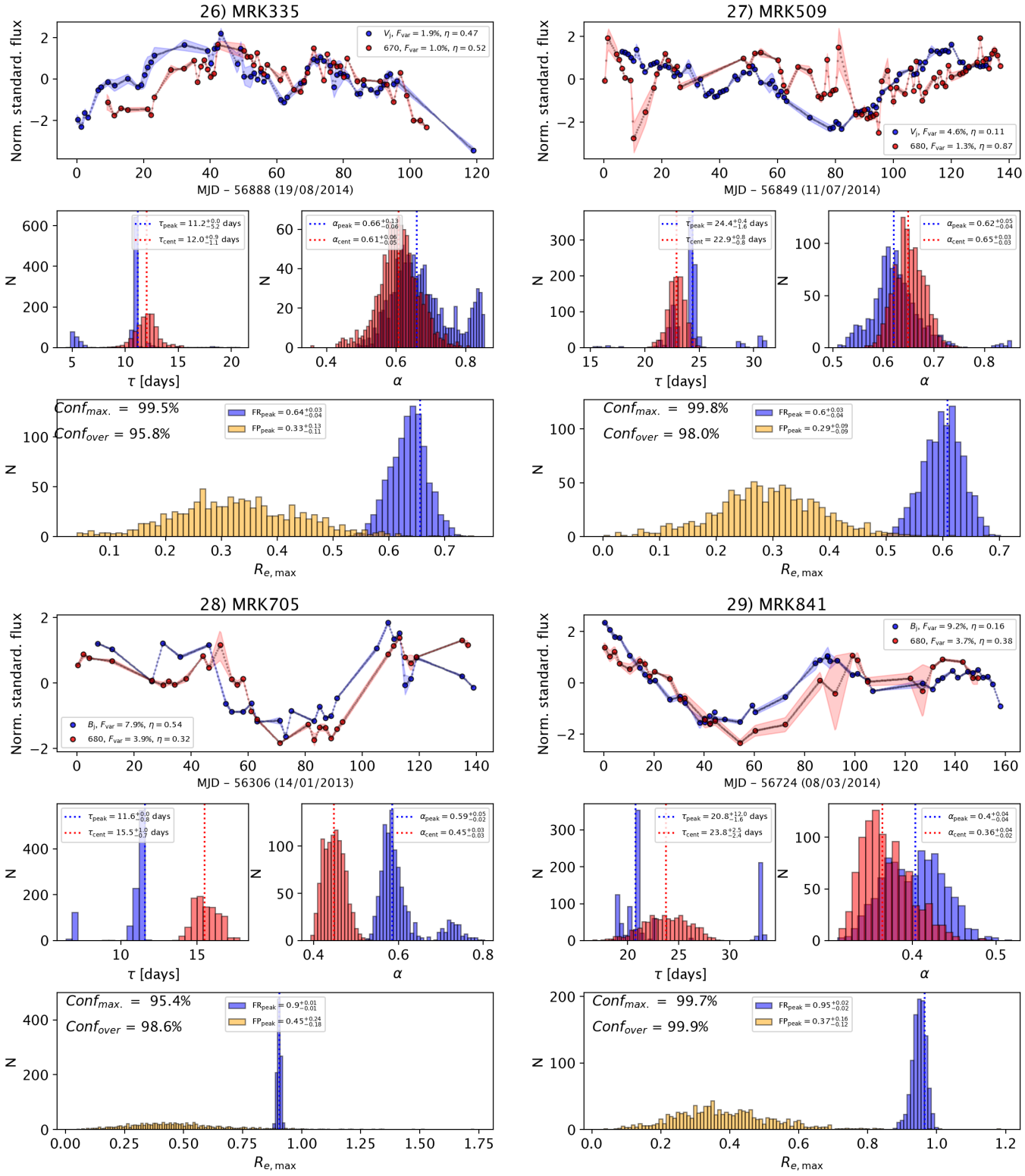
26) MRK335
Norm. standard. flux
MJD − 56888 (19/08/2014)
V_J, $F_{var} = 1.9\%$, $\eta = 0.47$
670, $F_{var} = 1.0\%$, $\eta = 0.52$
$\tau_{peak} = 11.2^{+0.0}_{-0.2}$ days
$\tau_{cent} = 12.0^{+0.9}_{-1.1}$ days
τ [days]
$\alpha_{peak} = 0.66^{+0.13}_{-0.06}$
$\alpha_{cent} = 0.61^{+0.06}_{-0.05}$
α
$Conf_{max.}$ = 99.5%
$Conf_{over}$ = 95.8%
$FR_{peak} = 0.64^{+0.03}_{-0.04}$
$FP_{peak} = 0.33^{+0.13}_{-0.11}$
$R_{e,max}$
27) MRK509
MJD − 56849 (11/07/2014)
B_J, $F_{var} = 4.6\%$, $\eta = 0.11$
680, $F_{var} = 1.3\%$, $\eta = 0.87$
$\tau_{peak} = 24.4^{+0.4}_{-1.6}$ days
$\tau_{cent} = 22.9^{+0.8}_{-0.8}$ days
$\alpha_{peak} = 0.62^{+0.05}_{-0.04}$
$\alpha_{cent} = 0.65^{+0.03}_{-0.03}$
$Conf_{max.}$ = 99.8%
$Conf_{over}$ = 98.0%
$FR_{peak} = 0.6^{+0.03}_{-0.04}$
$FP_{peak} = 0.29^{+0.09}_{-0.09}$
28) MRK705
MJD − 56306 (14/01/2013)
B_J, $F_{var} = 7.9\%$, $\eta = 0.54$
680, $F_{var} = 3.9\%$, $\eta = 0.32$
$\tau_{peak} = 11.6^{+0.0}_{-0.6}$ days
$\tau_{cent} = 15.5^{+1.0}_{-0.7}$ days
$\alpha_{peak} = 0.59^{+0.05}_{-0.02}$
$\alpha_{cent} = 0.45^{+0.03}_{-0.03}$
$Conf_{max.}$ = 95.4%
$Conf_{over}$ = 98.6%
$FR_{peak} = 0.9^{+0.01}_{-0.01}$
$FP_{peak} = 0.45^{+0.24}_{-0.18}$
29) MRK841
MJD − 56724 (08/03/2014)
B_J, $F_{var} = 9.2\%$, $\eta = 0.16$
680, $F_{var} = 3.7\%$, $\eta = 0.38$
$\tau_{peak} = 20.8^{+12.0}_{-1.6}$ days
$\tau_{cent} = 23.8^{+2.5}_{-2.4}$ days
$\alpha_{peak} = 0.4^{+0.04}_{-0.04}$
$\alpha_{cent} = 0.36^{+0.04}_{-0.02}$
$Conf_{max.}$ = 99.7%
$Conf_{over}$ = 99.9%
$FR_{peak} = 0.95^{+0.02}_{-0.02}$
$FP_{peak} = 0.37^{+0.16}_{-0.12}$

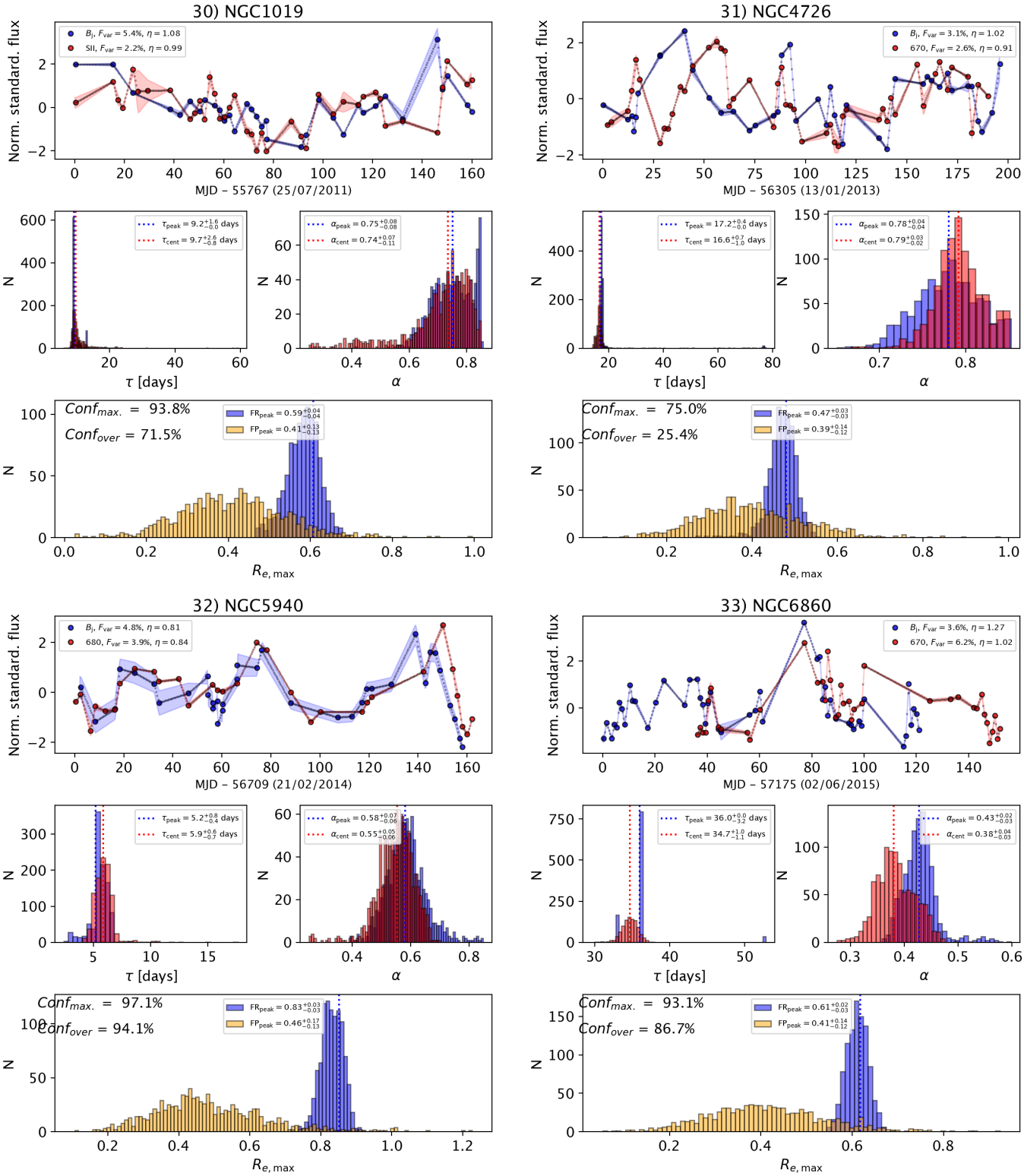
30) NGC1019
Bj, Fvar = 5.4%, η = 1.08
SII, Fvar = 2.2%, η = 0.99
Norm. standard. flux
MJD − 55767 (25/07/2011)
τpeak = 9.2 days
τcent = 9.7 days
N
τ [days]
αpeak = 0.75
αcent = 0.74
α
Confmax. = 93.8%
Confover = 71.5%
FRpeak = 0.59
FPpeak = 0.41
Re, max
31) NGC4726
Bj, Fvar = 3.1%, η = 1.02
670, Fvar = 2.6%, η = 0.91
MJD − 56305 (13/01/2013)
τpeak = 17.2 days
τcent = 16.6 days
αpeak = 0.78
αcent = 0.79
Confmax. = 75.0%
Confover = 25.4%
FRpeak = 0.47
FPpeak = 0.39
32) NGC5940
Bj, Fvar = 4.8%, η = 0.81
680, Fvar = 3.9%, η = 0.84
MJD − 56709 (21/02/2014)
τpeak = 5.2 days
τcent = 5.9 days
αpeak = 0.58
αcent = 0.55
Confmax. = 97.1%
Confover = 94.1%
FRpeak = 0.83
FPpeak = 0.46
33) NGC6860
Bj, Fvar = 3.6%, η = 1.27
670, Fvar = 6.2%, η = 1.02
MJD − 57175 (02/06/2015)
τpeak = 36.0
τcent = 34.7
αpeak = 0.43
αcent = 0.38
Confmax. = 93.1%
Confover = 86.7%
FRpeak = 0.61
FPpeak = 0.41

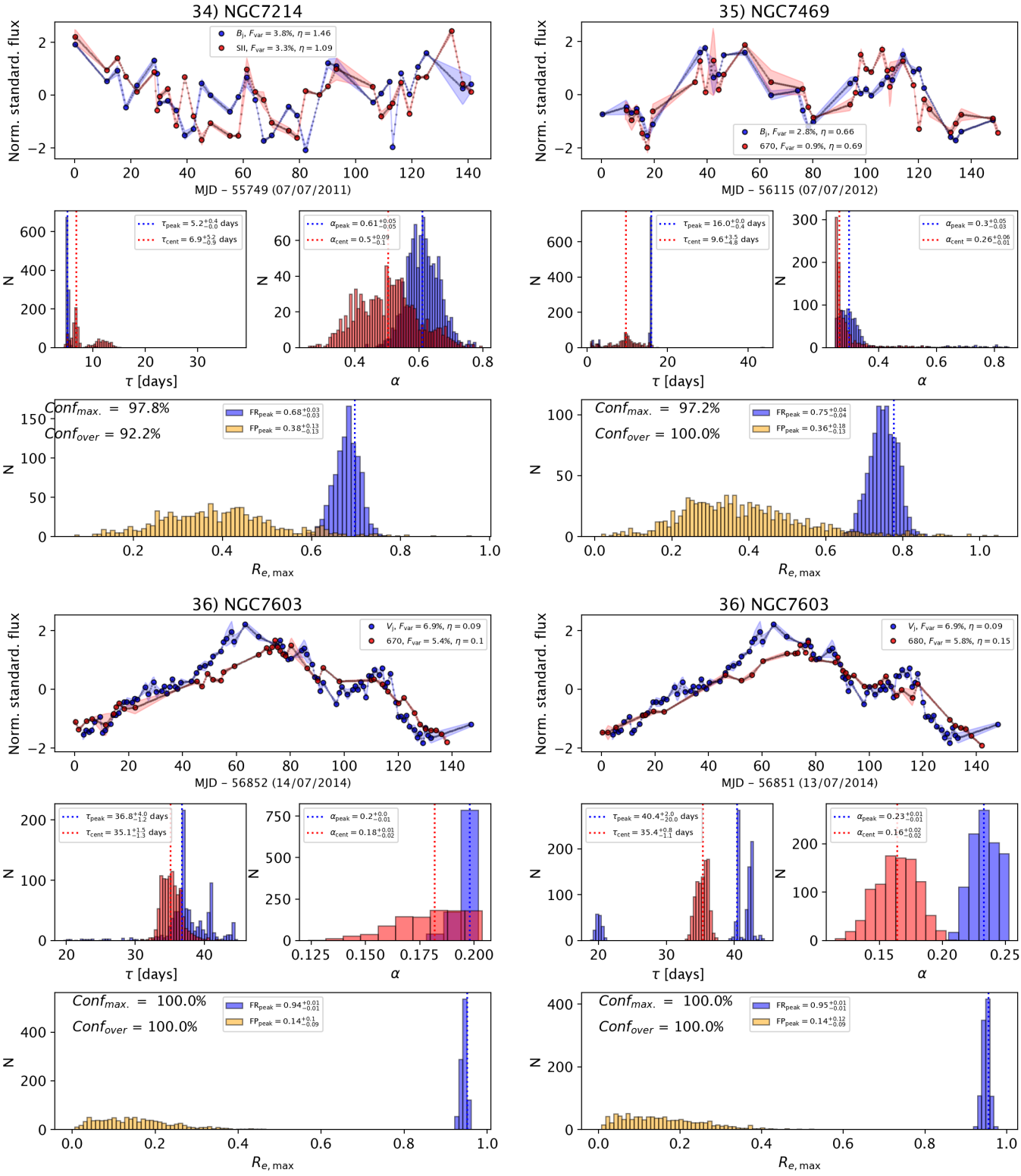
34) NGC7214
Norm. standard. flux
MJD − 55749 (07/07/2011)
35) NGC7469
MJD − 56115 (07/07/2012)
τ [days]
α
N
Conf_max. = 97.8%
Conf_over = 92.2%
Conf_max. = 97.2%
Conf_over = 100.0%
R_e, max
36) NGC7603
MJD − 56852 (14/07/2014)
MJD − 56851 (13/07/2014)
Conf_max. = 100.0%
Conf_over = 100.0%

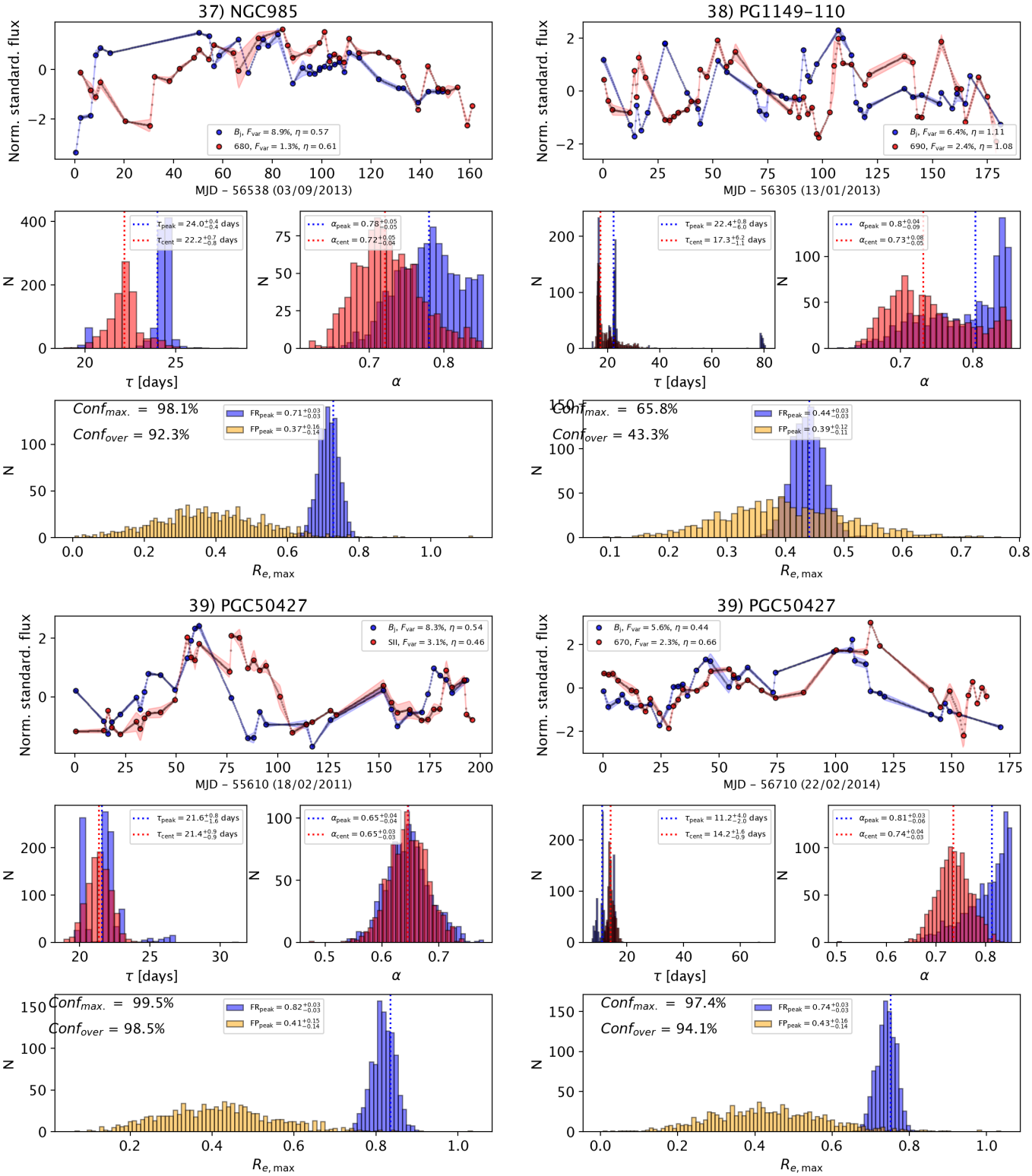
37) NGC985
Norm. standard. flux
MJD − 56538 (03/09/2013)
τ [days]
α
N
$R_{e,\max}$
$Conf_{max.}$ = 98.1%
$Conf_{over}$ = 92.3%
38) PG1149−110
MJD − 56305 (13/01/2013)
$Conf_{max.}$ = 65.8%
$Conf_{over}$ = 43.3%
39) PGC50427
MJD − 55610 (18/02/2011)
$Conf_{max.}$ = 99.5%
$Conf_{over}$ = 98.5%
39) PGC50427
MJD − 56710 (22/02/2014)
$Conf_{max.}$ = 97.4%
$Conf_{over}$ = 94.1%

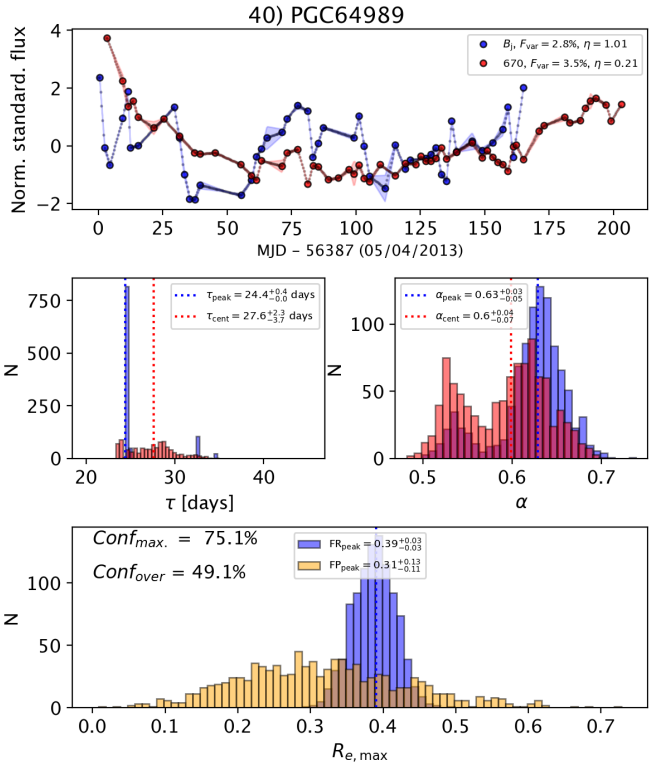
40) PGC64989
Norm. standard. flux
MJD − 56387 (05/04/2013)
τ [days]
α
N
$Conf_{max.}$ = 75.1%
$Conf_{over}$ = 49.1%
$R_{e,\,max}$

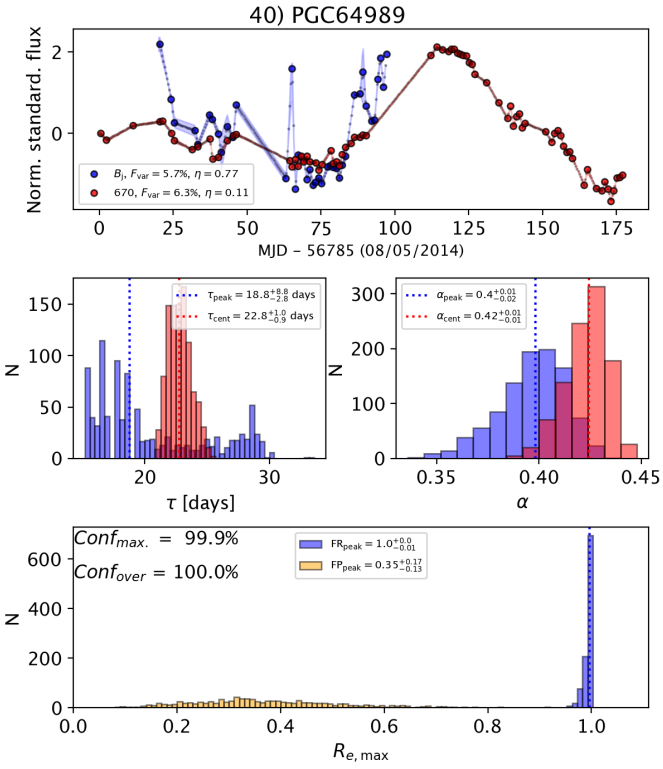
40) PGC64989
Norm. standard. flux
MJD − 56785 (08/05/2014)
τ [days]
α
N
$Conf_{max.}$ = 99.9%
$Conf_{over}$ = 100.0%
$R_{e,\,max}$

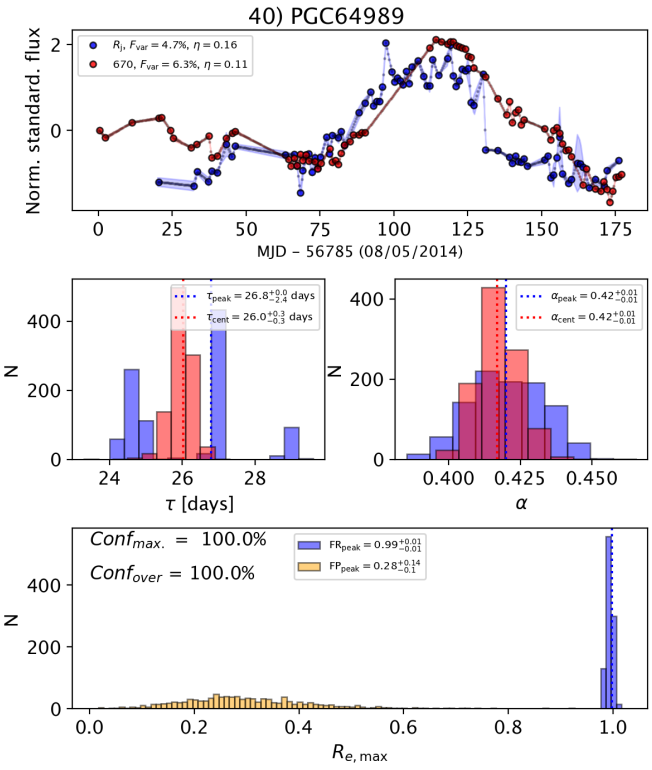
40) PGC64989
Norm. standard. flux
MJD − 56785 (08/05/2014)
τ [days]
α
N
$Conf_{max.}$ = 100.0%
$Conf_{over}$ = 100.0%
$R_{e,\,max}$

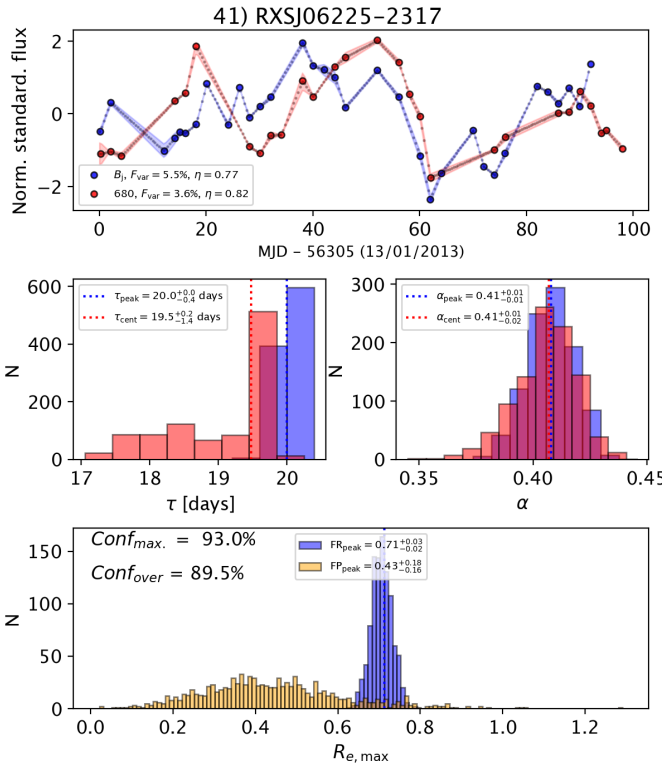
41) RXSJ06225−2317
Norm. standard. flux
MJD − 56305 (13/01/2013)
τ [days]
α
N
$Conf_{max.}$ = 93.0%
$Conf_{over}$ = 89.5%
$R_{e,\,max}$

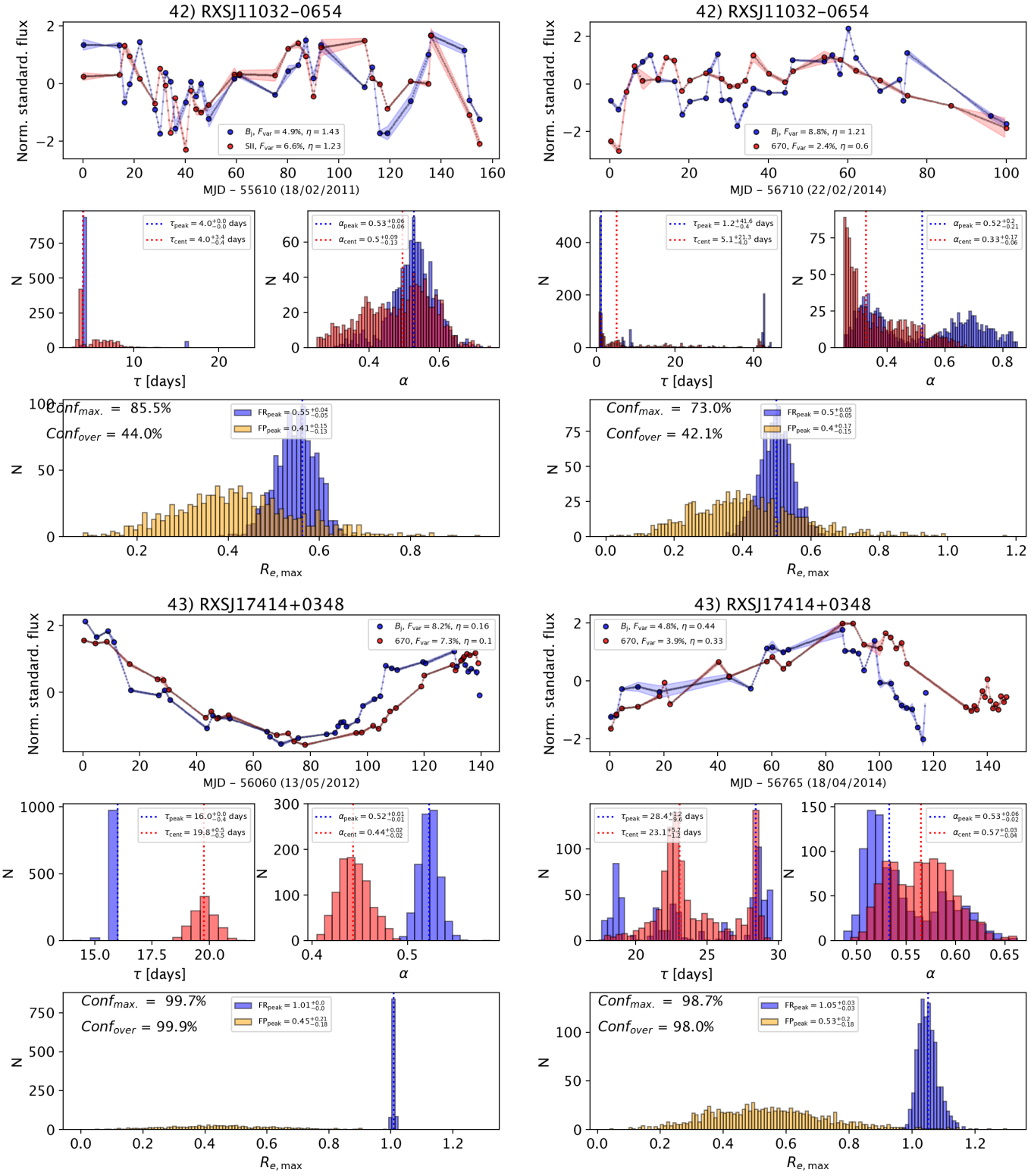
42) RXSJ11032-0654
Norm. standard. flux
MJD − 55610 (18/02/2011)
B_J, $F_{var} = 4.9\%$, $\eta = 1.43$
SII, $F_{var} = 6.6\%$, $\eta = 1.23$
$\tau_{peak} = 4.0^{+0.0}_{-0.0}$ days
$\tau_{cent} = 4.0^{+3.4}_{-0.4}$ days
τ [days]
$\alpha_{peak} = 0.53^{+0.06}_{-0.06}$
$\alpha_{cent} = 0.5^{+0.09}_{-0.13}$
α
$Conf_{max.} = 85.5\%$
$Conf_{over} = 44.0\%$
$FR_{peak} = 0.55^{+0.04}_{-0.05}$
$FP_{peak} = 0.41^{+0.15}_{-0.13}$
$R_{e,max}$
42) RXSJ11032-0654
Norm. standard. flux
MJD − 56710 (22/02/2014)
B_J, $F_{var} = 8.8\%$, $\eta = 1.21$
670, $F_{var} = 2.4\%$, $\eta = 0.6$
$\tau_{peak} = 1.2^{+41.6}_{-0.4}$ days
$\tau_{cent} = 5.1^{+21.3}_{-4.0}$ days
τ [days]
$\alpha_{peak} = 0.52^{+0.2}_{-0.21}$
$\alpha_{cent} = 0.33^{+0.17}_{-0.06}$
α
$Conf_{max.} = 73.0\%$
$Conf_{over} = 42.1\%$
$FR_{peak} = 0.5^{+0.05}_{-0.05}$
$FP_{peak} = 0.4^{+0.17}_{-0.15}$
$R_{e,max}$
43) RXSJ17414+0348
Norm. standard. flux
MJD − 56060 (13/05/2012)
B_J, $F_{var} = 8.2\%$, $\eta = 0.16$
670, $F_{var} = 7.3\%$, $\eta = 0.1$
$\tau_{peak} = 16.0^{+0.0}_{-0.4}$ days
$\tau_{cent} = 19.8^{+0.5}_{-0.5}$ days
τ [days]
$\alpha_{peak} = 0.52^{+0.01}_{-0.01}$
$\alpha_{cent} = 0.44^{+0.02}_{-0.02}$
α
$Conf_{max.} = 99.7\%$
$Conf_{over} = 99.9\%$
$FR_{peak} = 1.01^{+0.0}_{-0.0}$
$FP_{peak} = 0.45^{+0.21}_{-0.18}$
$R_{e,max}$
43) RXSJ17414+0348
Norm. standard. flux
MJD − 56765 (18/04/2014)
B_J, $F_{var} = 4.8\%$, $\eta = 0.44$
670, $F_{var} = 3.9\%$, $\eta = 0.33$
$\tau_{peak} = 28.4^{+1.2}_{-9.6}$ days
$\tau_{cent} = 23.1^{+5.2}_{-1.2}$ days
τ [days]
$\alpha_{peak} = 0.53^{+0.06}_{-0.02}$
$\alpha_{cent} = 0.57^{+0.03}_{-0.04}$
α
$Conf_{max.} = 98.7\%$
$Conf_{over} = 98.0\%$
$FR_{peak} = 1.05^{+0.03}_{-0.03}$
$FP_{peak} = 0.53^{+0.2}_{-0.18}$
$R_{e,max}$

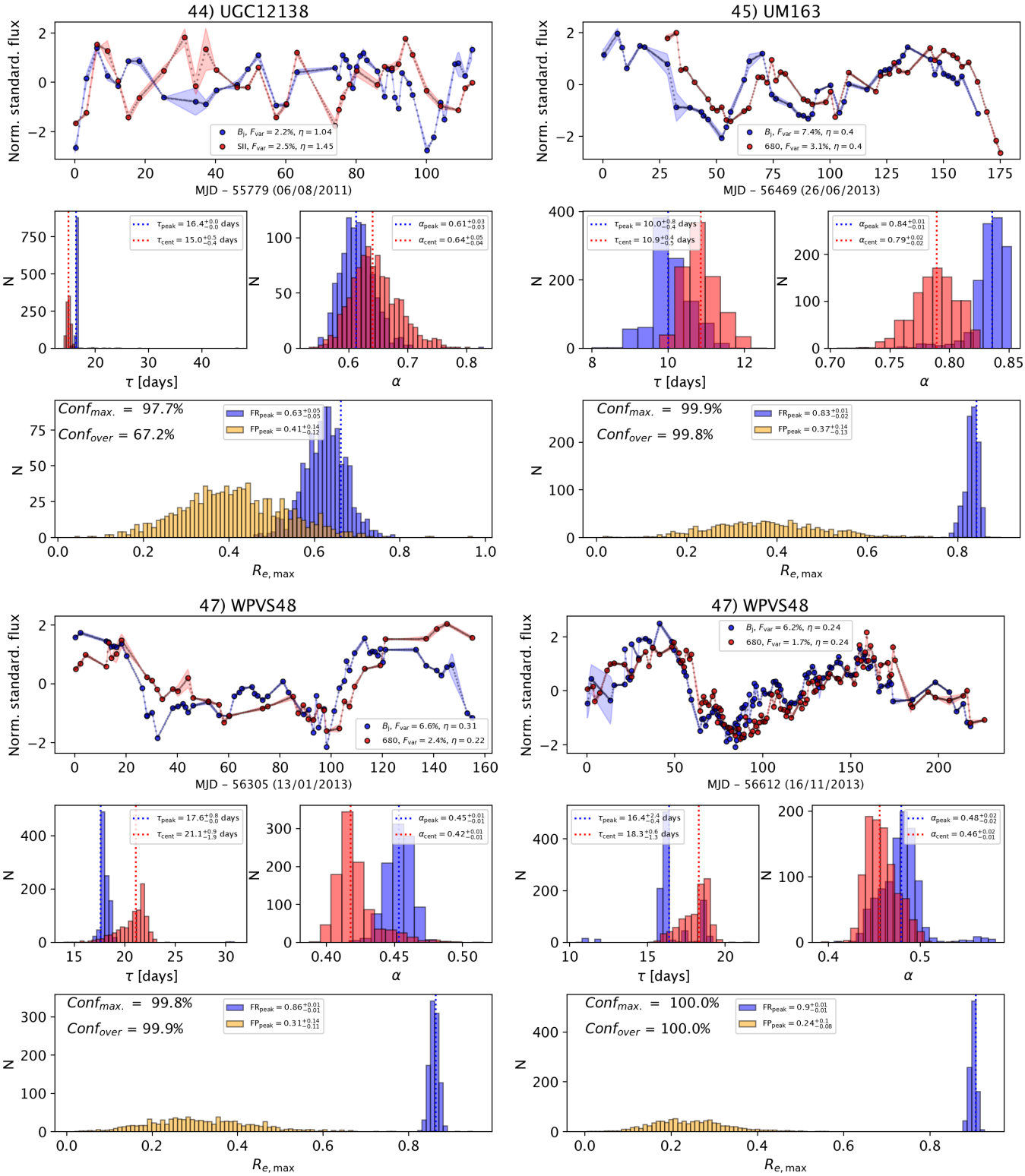
44) UGC12138
Norm. standard. flux
MJD − 55779 (06/08/2011)
45) UM163
MJD − 56469 (26/06/2013)
τ [days]
α
N
47) WPVS48
MJD − 56305 (13/01/2013)
MJD − 56612 (16/11/2013)
Conf_max. = 97.7%
Conf_over = 67.2%
Conf_max. = 99.9%
Conf_over = 99.8%
Conf_max. = 99.8%
Conf_over = 99.9%
Conf_max. = 100.0%
Conf_over = 100.0%
R_e, max

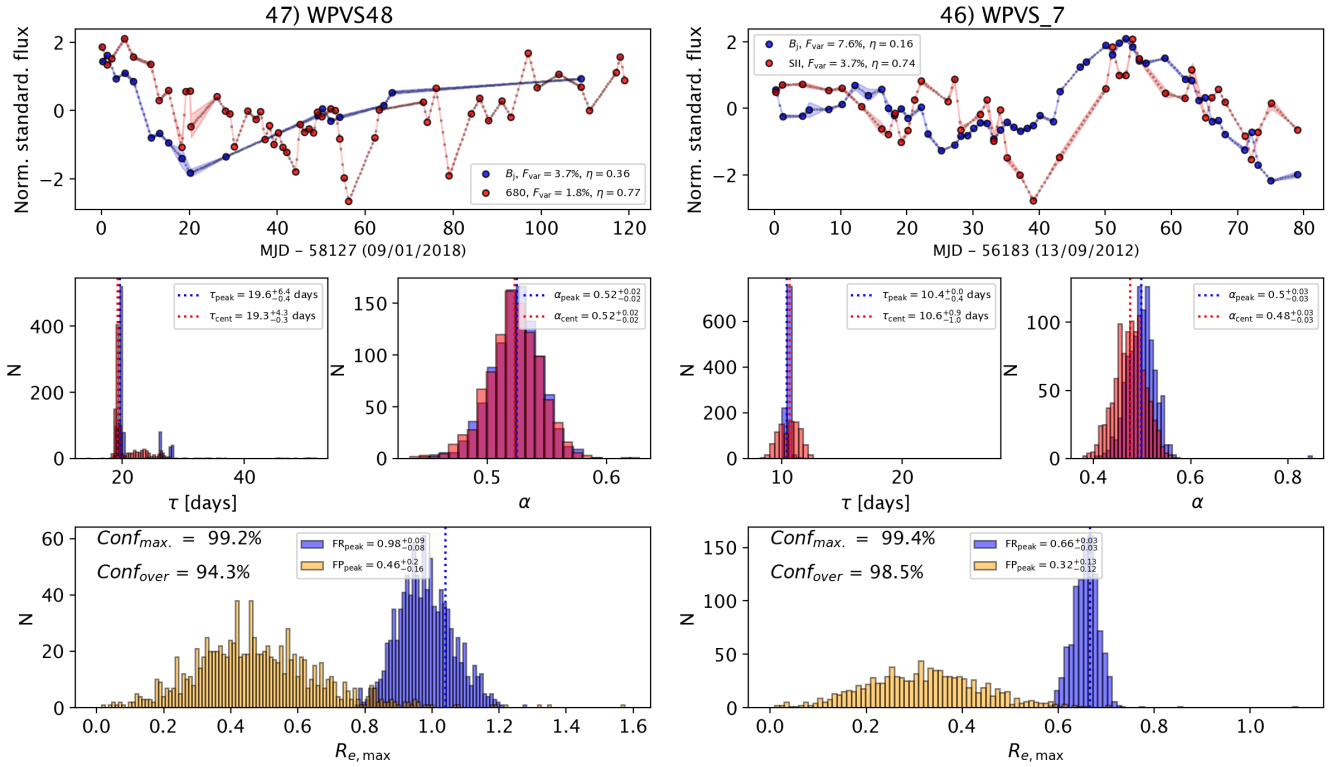
47) WPVS48
Norm. standard. flux
MJD – 58127 (09/01/2018)
B_J, $F_{var} = 3.7\%$, $\eta = 0.36$
680, $F_{var} = 1.8\%$, $\eta = 0.77$
$\tau_{peak} = 19.6^{+6.4}_{-0.4}$ days
$\tau_{cent} = 19.3^{+4.3}_{-0.3}$ days
$\alpha_{peak} = 0.52^{+0.02}_{-0.02}$
$\alpha_{cent} = 0.52^{+0.02}_{-0.02}$
N
τ [days]
α
$Conf_{max.}$ = 99.2%
$Conf_{over}$ = 94.3%
$FR_{peak} = 0.98^{+0.09}_{-0.08}$
$FP_{peak} = 0.46^{+0.2}_{-0.16}$
$R_{e,max}$
46) WPVS_7
Norm. standard. flux
MJD – 56183 (13/09/2012)
B_J, $F_{var} = 7.6\%$, $\eta = 0.16$
SII, $F_{var} = 3.7\%$, $\eta = 0.74$
$\tau_{peak} = 10.4^{+0.0}_{-0.4}$ days
$\tau_{cent} = 10.6^{+0.9}_{-1.0}$ days
$\alpha_{peak} = 0.5^{+0.03}_{-0.03}$
$\alpha_{cent} = 0.48^{+0.03}_{-0.03}$
N
τ [days]
α
$Conf_{max.}$ = 99.4%
$Conf_{over}$ = 98.5%
$FR_{peak} = 0.66^{+0.03}_{-0.03}$
$FP_{peak} = 0.32^{+0.13}_{-0.12}$
$R_{e,max}$

D. FLUX VARIATION GRADIENT DIAGRAMS

BV, BR and Br_s flux-flux diagrams for each object and filter combination. For objects with multi-epoch observations, the different colors mean different observation seasons. The bisector fit for the AGN slope is shown as a blue line and its value is denoted in the figure legend. Host-slope ranges were derived from Sakata et al. (2010), and are delineated by grey wedges. The intersection between the host and AGN slopes, provides an estimate for the host contribution to the bands, and is marked by a red star. A summary for all the FVG slopes is provided in Table D.1, and the complete list of flux values (total and host) for each source is summarized in Table D.2.

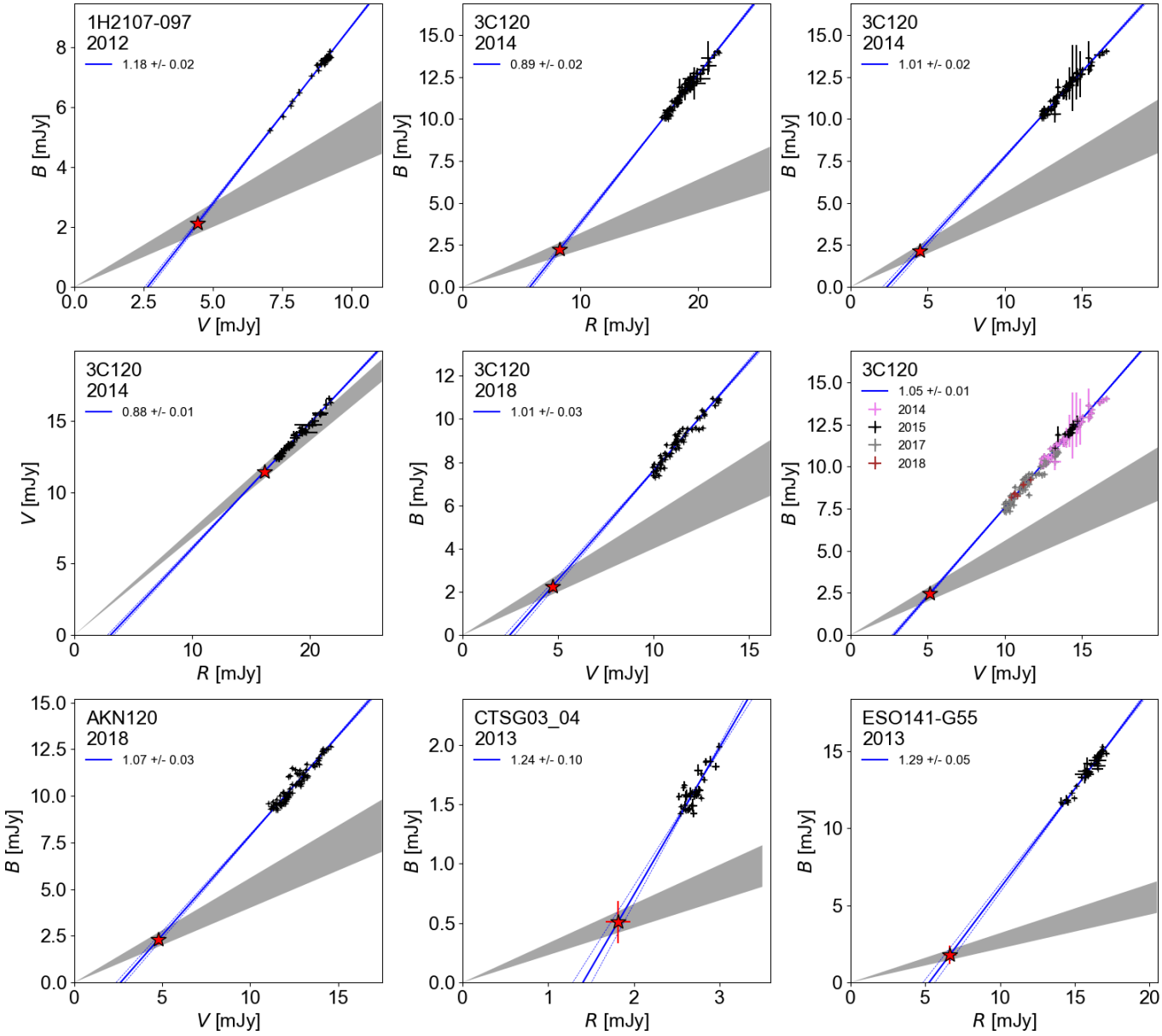

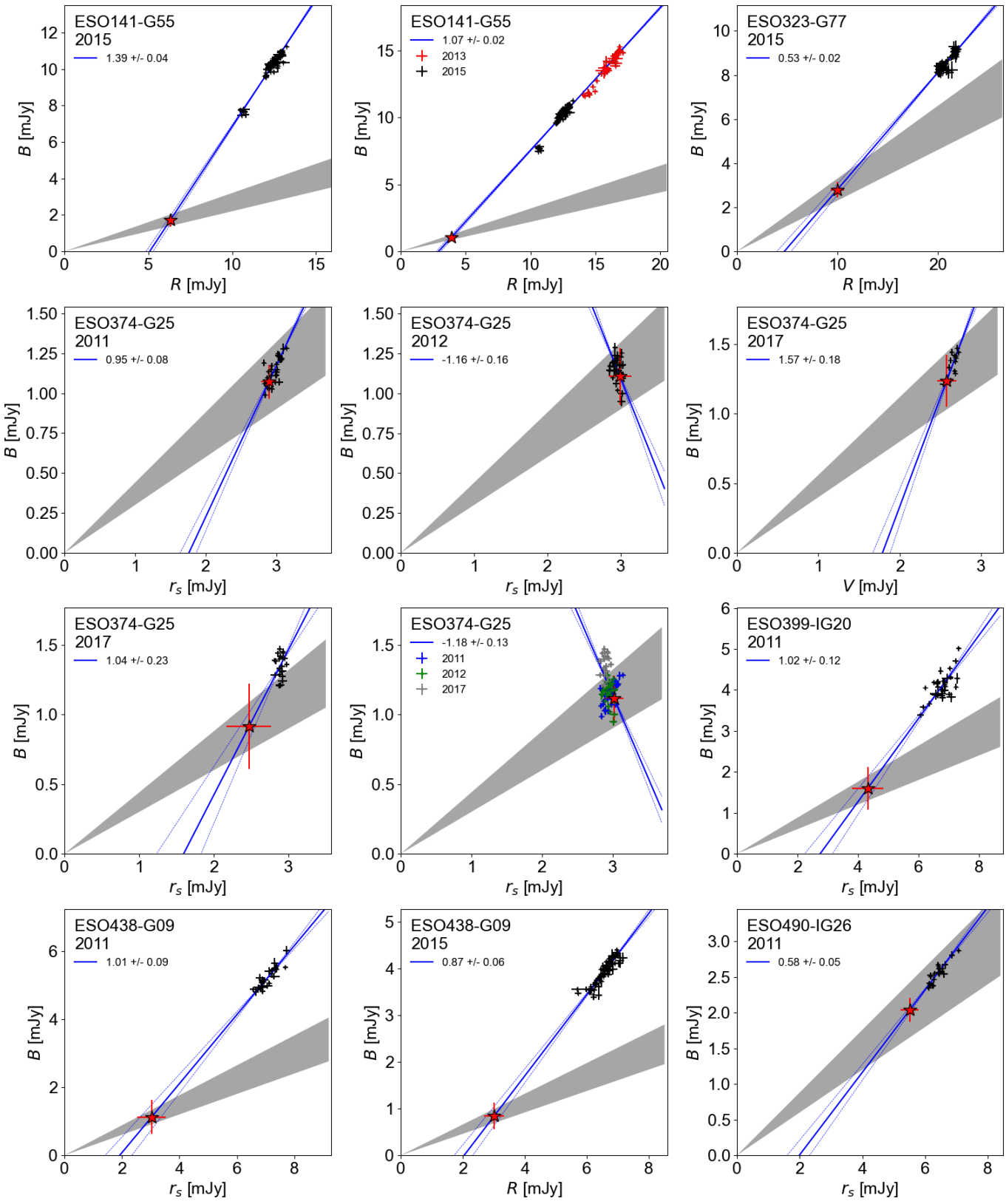
ESO141-G55
2015
1.39 +/- 0.04
B [mJy]
R [mJy]
ESO141-G55
1.07 +/- 0.02
2013
2015
B [mJy]
R [mJy]
ESO323-G77
2015
0.53 +/- 0.02
B [mJy]
R [mJy]
ESO374-G25
2011
0.95 +/- 0.08
B [mJy]
r_s [mJy]
ESO374-G25
2012
-1.16 +/- 0.16
B [mJy]
r_s [mJy]
ESO374-G25
2017
1.57 +/- 0.18
B [mJy]
V [mJy]
ESO374-G25
2017
1.04 +/- 0.23
B [mJy]
r_s [mJy]
ESO374-G25
-1.18 +/- 0.13
2011
2012
2017
B [mJy]
r_s [mJy]
ESO399-IG20
2011
1.02 +/- 0.12
B [mJy]
r_s [mJy]
ESO438-G09
2011
1.01 +/- 0.09
B [mJy]
r_s [mJy]
ESO438-G09
2015
0.87 +/- 0.06
B [mJy]
R [mJy]
ESO490-IG26
2011
0.58 +/- 0.05
B [mJy]
r_s [mJy]

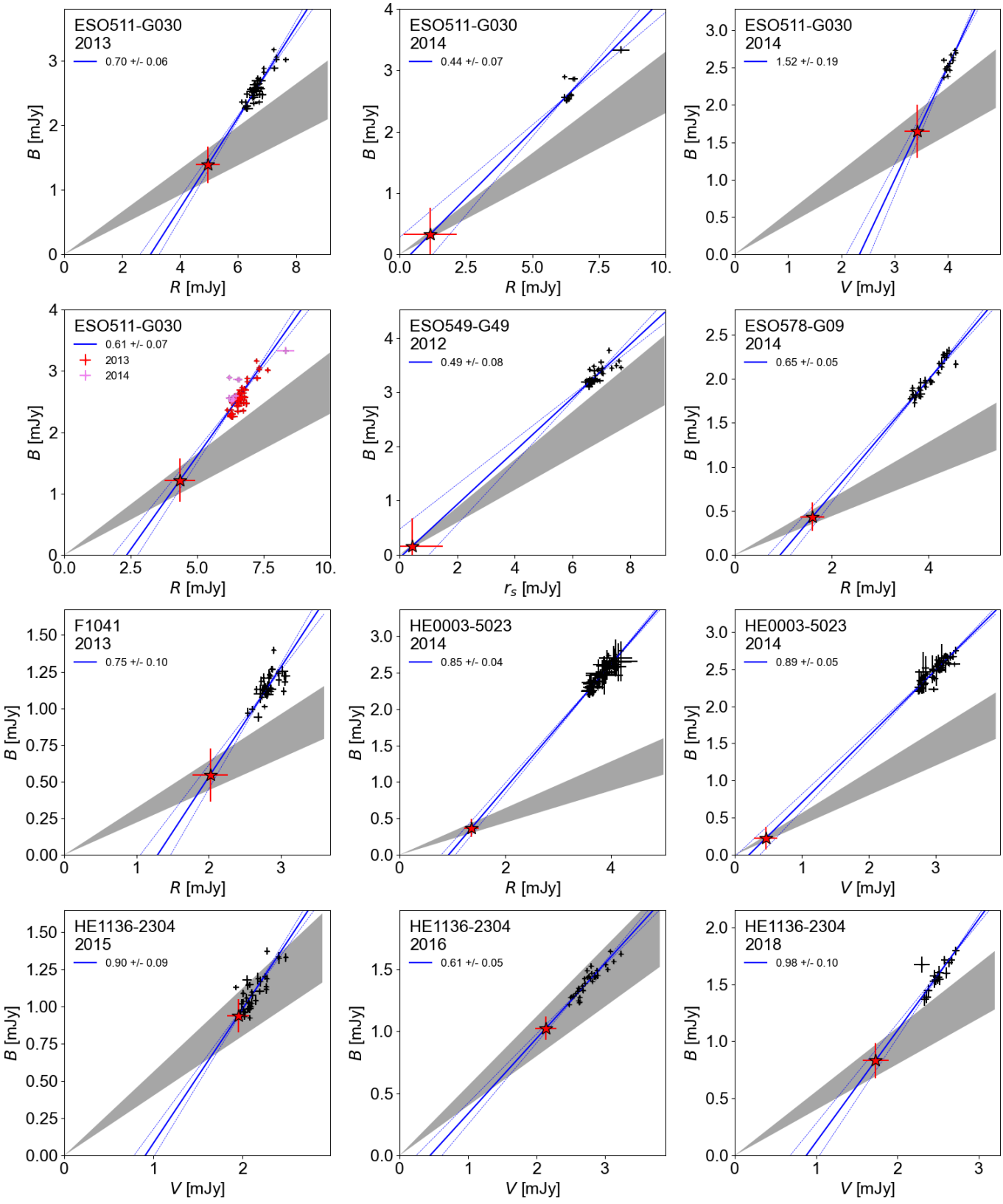
ESO511-G030
2013
0.70 +/- 0.06
B [mJy]
R [mJy]
ESO511-G030
2014
0.44 +/- 0.07
B [mJy]
R [mJy]
ESO511-G030
2014
1.52 +/- 0.19
B [mJy]
V [mJy]
ESO511-G030
0.61 +/- 0.07
2013
2014
B [mJy]
R [mJy]
ESO549-G49
2012
0.49 +/- 0.08
B [mJy]
r_s [mJy]
ESO578-G09
2014
0.65 +/- 0.05
B [mJy]
R [mJy]
F1041
2013
0.75 +/- 0.10
B [mJy]
R [mJy]
HE0003-5023
2014
0.85 +/- 0.04
B [mJy]
R [mJy]
HE0003-5023
2014
0.89 +/- 0.05
B [mJy]
V [mJy]
HE1136-2304
2015
0.90 +/- 0.09
B [mJy]
V [mJy]
HE1136-2304
2016
0.61 +/- 0.05
B [mJy]
V [mJy]
HE1136-2304
2018
0.98 +/- 0.10
B [mJy]
V [mJy]

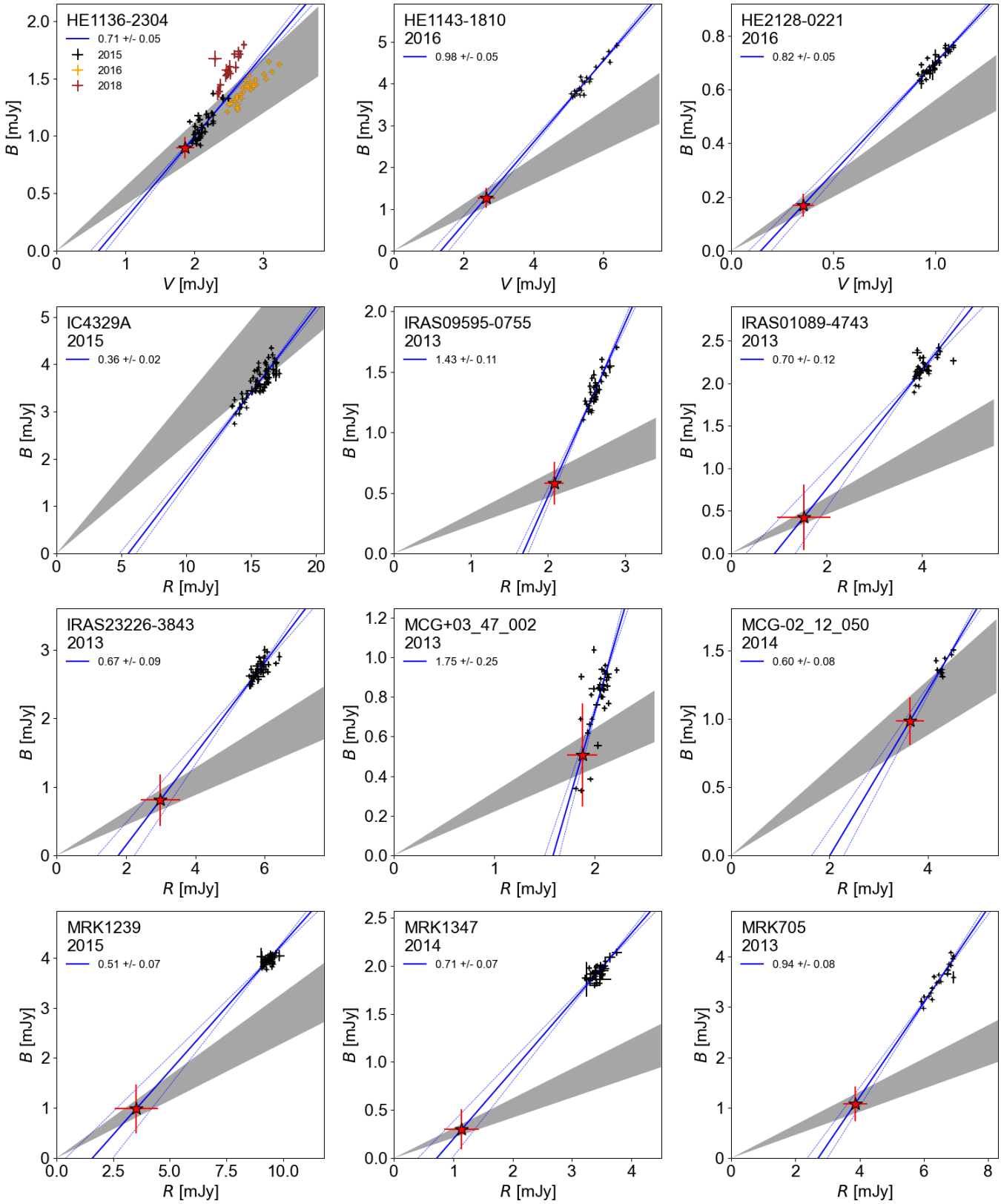
HE1136-2304
0.71 +/- 0.05
2015
2016
2018
B [mJy]
V [mJy]
HE1143-1810
2016
0.98 +/- 0.05
B [mJy]
V [mJy]
HE2128-0221
2016
0.82 +/- 0.05
B [mJy]
V [mJy]
IC4329A
2015
0.36 +/- 0.02
B [mJy]
R [mJy]
IRAS09595-0755
2013
1.43 +/- 0.11
B [mJy]
R [mJy]
IRAS01089-4743
2013
0.70 +/- 0.12
B [mJy]
R [mJy]
IRAS23226-3843
2013
0.67 +/- 0.09
B [mJy]
R [mJy]
MCG+03_47_002
2013
1.75 +/- 0.25
B [mJy]
R [mJy]
MCG-02_12_050
2014
0.60 +/- 0.08
B [mJy]
R [mJy]
MRK1239
2015
0.51 +/- 0.07
B [mJy]
R [mJy]
MRK1347
2014
0.71 +/- 0.07
B [mJy]
R [mJy]
MRK705
2013
0.94 +/- 0.08
B [mJy]
R [mJy]

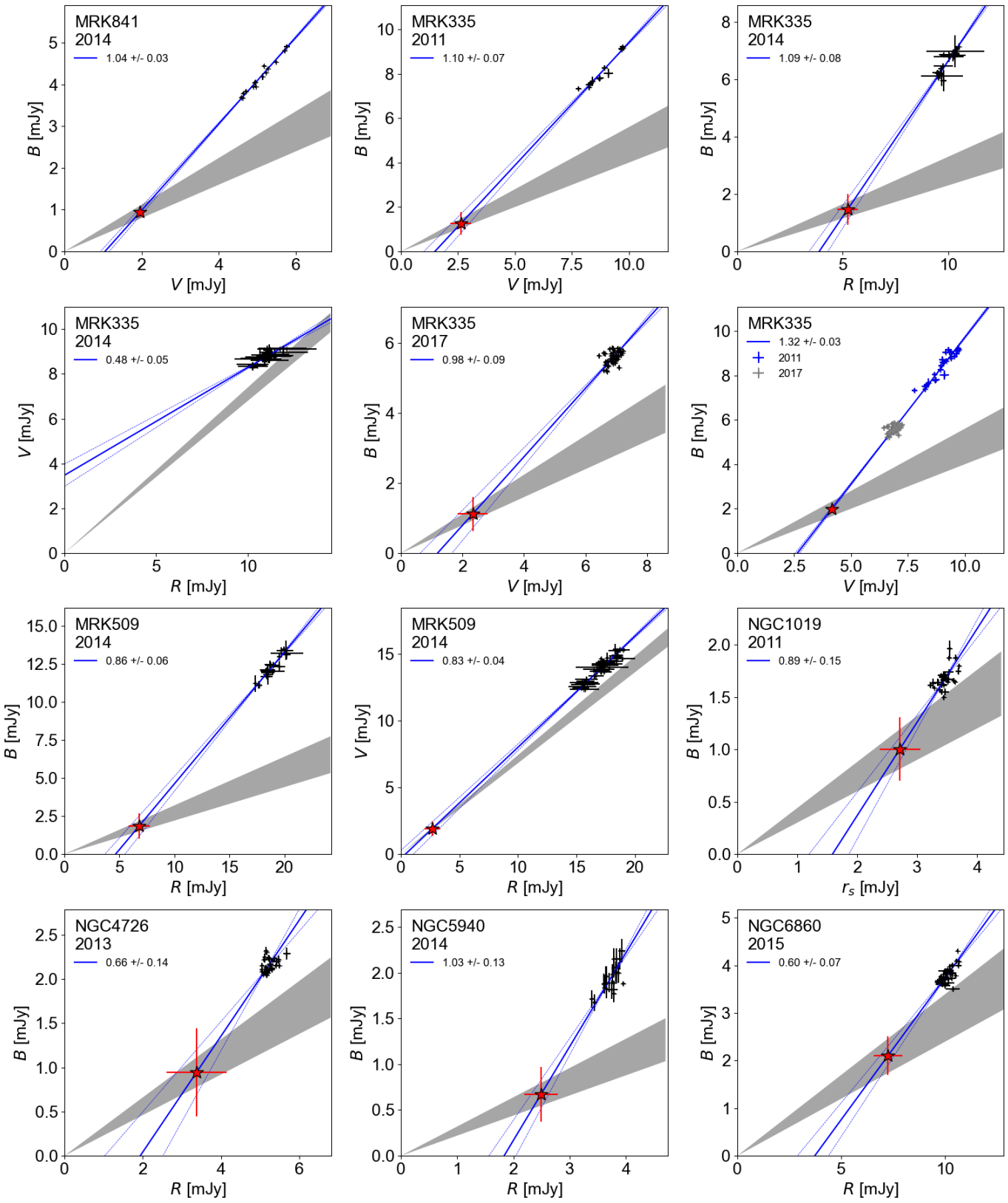
MRK841
2014
1.04 +/- 0.03
B [mJy]
V [mJy]
MRK335
2011
1.10 +/- 0.07
B [mJy]
V [mJy]
MRK335
2014
1.09 +/- 0.08
B [mJy]
R [mJy]
MRK335
2014
0.48 +/- 0.05
V [mJy]
R [mJy]
MRK335
2017
0.98 +/- 0.09
B [mJy]
V [mJy]
MRK335
1.32 +/- 0.03
2011
2017
B [mJy]
V [mJy]
MRK509
2014
0.86 +/- 0.06
B [mJy]
R [mJy]
MRK509
2014
0.83 +/- 0.04
V [mJy]
R [mJy]
NGC1019
2011
0.89 +/- 0.15
B [mJy]
r_s [mJy]
NGC4726
2013
0.66 +/- 0.14
B [mJy]
R [mJy]
NGC5940
2014
1.03 +/- 0.13
B [mJy]
R [mJy]
NGC6860
2015
0.60 +/- 0.07
B [mJy]
R [mJy]

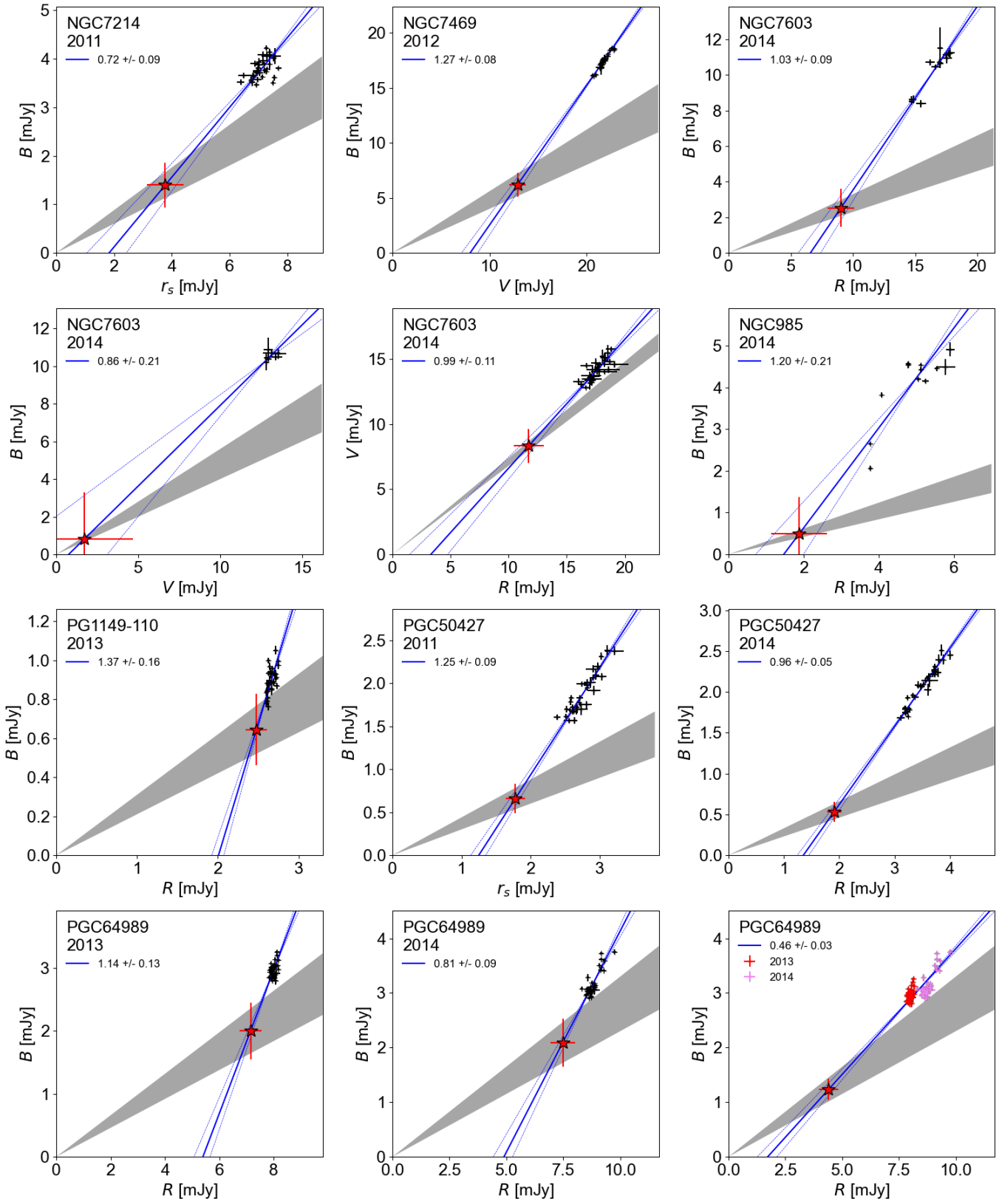
NGC7214
2011
0.72 +/- 0.09
B [mJy]
r_s [mJy]
NGC7469
2012
1.27 +/- 0.08
B [mJy]
V [mJy]
NGC7603
2014
1.03 +/- 0.09
B [mJy]
R [mJy]
NGC7603
2014
0.86 +/- 0.21
B [mJy]
V [mJy]
NGC7603
2014
0.99 +/- 0.11
V [mJy]
R [mJy]
NGC985
2014
1.20 +/- 0.21
B [mJy]
R [mJy]
PG1149-110
2013
1.37 +/- 0.16
B [mJy]
R [mJy]
PGC50427
2011
1.25 +/- 0.09
B [mJy]
r_s [mJy]
PGC50427
2014
0.96 +/- 0.05
B [mJy]
R [mJy]
PGC64989
2013
1.14 +/- 0.13
B [mJy]
R [mJy]
PGC64989
2014
0.81 +/- 0.09
B [mJy]
R [mJy]
PGC64989
0.46 +/- 0.03
2013
2014
B [mJy]
R [mJy]

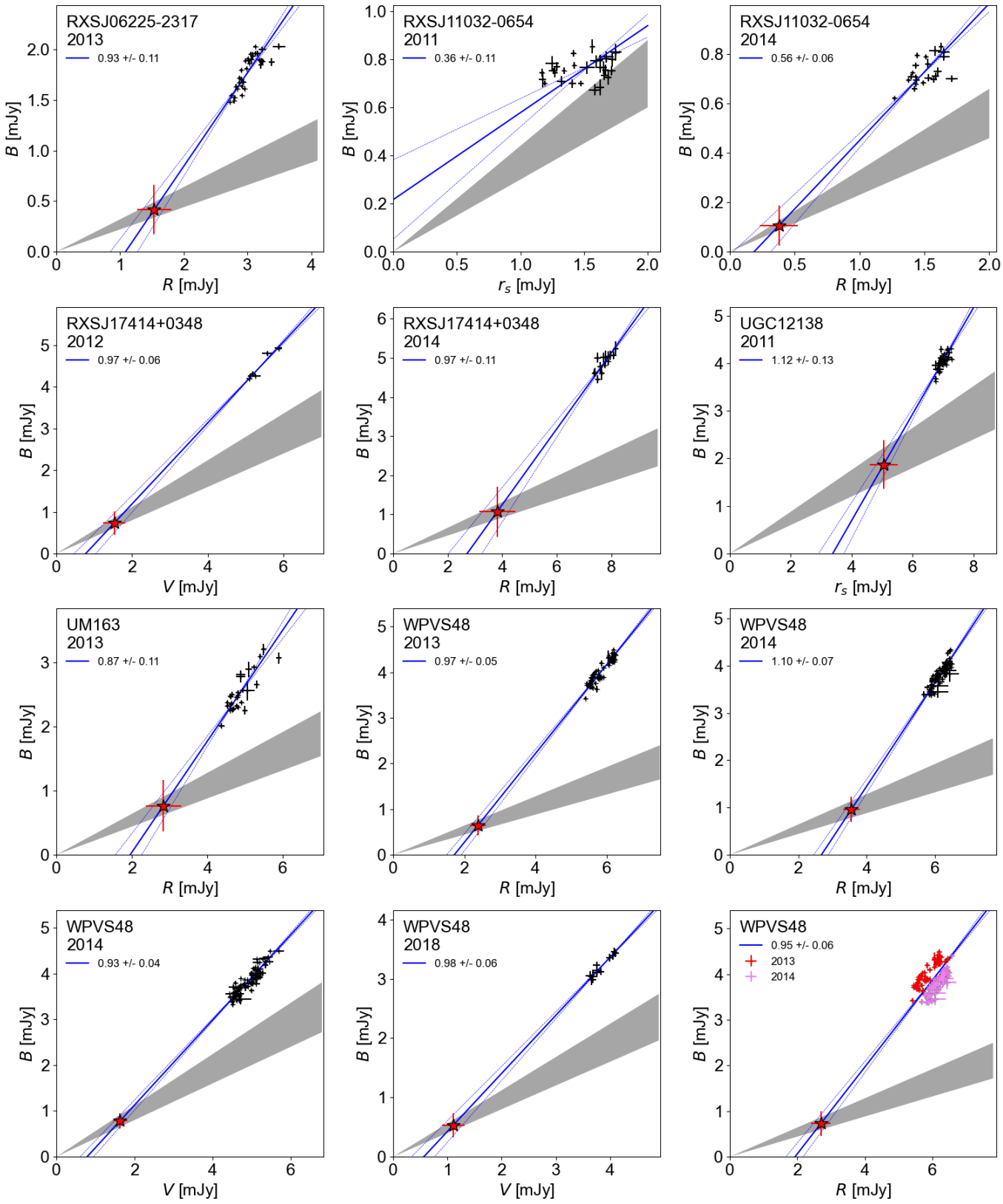
RXSJ06225-2317
2013
0.93 +/- 0.11
B [mJy]
R [mJy]
RXSJ11032-0654
2011
0.36 +/- 0.11
B [mJy]
r_s [mJy]
RXSJ11032-0654
2014
0.56 +/- 0.06
B [mJy]
R [mJy]
RXSJ17414+0348
2012
0.97 +/- 0.06
B [mJy]
V [mJy]
RXSJ17414+0348
2014
0.97 +/- 0.11
B [mJy]
R [mJy]
UGC12138
2011
1.12 +/- 0.13
B [mJy]
r_s [mJy]
UM163
2013
0.87 +/- 0.11
B [mJy]
R [mJy]
WPVS48
2013
0.97 +/- 0.05
B [mJy]
R [mJy]
WPVS48
2014
1.10 +/- 0.07
B [mJy]
R [mJy]
WPVS48
2014
0.93 +/- 0.04
B [mJy]
V [mJy]
WPVS48
2018
0.98 +/- 0.06
B [mJy]
V [mJy]
WPVS48
0.95 +/- 0.06
2013
2014
B [mJy]
R [mJy]

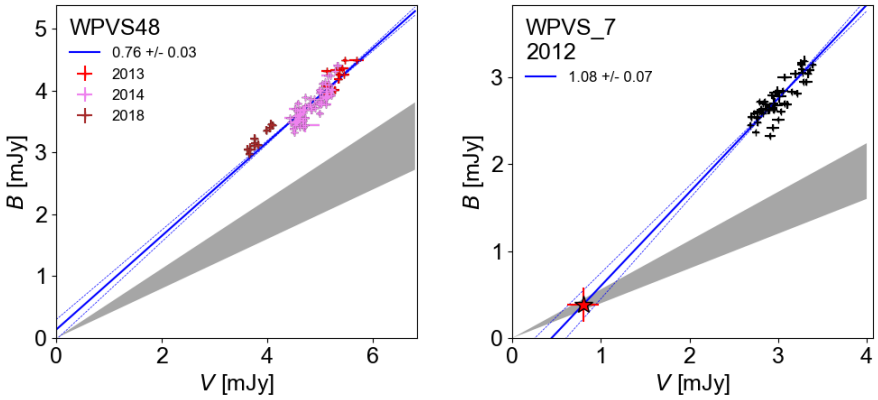

Table D.1. FVG slope results for filter combinations BR, Br, BV and VR for single observation campaigns and for combined observations

Object	Year	B/R	Object	year	B/V	Object	Year	B/r_s
HE0003-5023	2014	0.85±0.04	HE0003-5023	2014	0.89±0.05	NGC1019	2011	0.89±0.15
MRK335	2014	1.09±0.08	MRK335	2011	1.1±0.07	ESO549-G49	2012	0.49±0.08
IRAS01089-4743	2013	0.7±0.12	MRK335	2017	0.98±0.09	ESO490-IG26	2011	0.58±0.05
NGC985	2014	1.2±0.21	MRK335	All	1.32±0.03	ESO374-G25	2011	0.95±0.08
3C120	2014	0.89±0.02	WPVS_7	2012	1.08±0.07	ESO374-G25	2012	-1.16±0.16
MCG-02_12_050	2014	0.6±0.08	3C120	2014	1.01±0.02	ESO374-G25	2017	1.04±0.23
RXSJ06225-2317	2013	0.93±0.11	3C120	2018	1.01±0.03	ESO374-G25	All	-1.18±0.13
MRK705	2013	0.94±0.08	3C120	All	1.05±0.01	RXSJ11032-0654	2011	0.36±0.11
MRK1239	2015	0.51±0.07	AKN120	2018	1.07±0.03	ESO438-G09	2011	1.01±0.09
WPVS48	2013	0.97±0.05	WPVS48	2014	0.93±0.04	PGC50427	2011	1.25±0.09
WPVS48	2014	1.1±0.07	WPVS48	2018	0.98±0.06	ESO399-IG20	2011	1.02±0.12
WPVS48	All	0.95±0.06	WPVS48	All	0.76±0.03	NGC7214	2011	0.72±0.09
IRAS09595-0755	2013	1.43±0.11	ESO374-G25	2017	1.57±0.18	UGC12138	2011	1.12±0.13
RXSJ11032-0654	2014	0.56±0.06	HE1136-2304	2015	0.9±0.09	—-	—-	V/R
ESO438-G09	2015	0.87±0.06	HE1136-2304	2016	0.61±0.05	MRK335	2014	0.48±0.05
PG1149-110	2013	1.37±0.16	HE1136-2304	2018	0.98±0.1	3C120	2014	0.88±0.01
NGC4726	2013	0.66±0.14	HE1136-2304	All	0.71±0.05	MRK509	2014	0.83±0.04
ESO323-G77	2015	0.53±0.02	HE1143-1810	2016	0.98±0.05	NGC7603	2014	0.99±0.11
MRK1347	2014	0.71±0.07	ESO511-G030	2014	1.52±0.19	—-	—-	—-
IC4329A	2015	0.36±0.02	MRK841	2014	1.04±0.03			
ESO578-G09	2014	0.65±0.05	RXSJ17414+0348	2012	0.97±0.06			
PGC50427	2014	0.96±0.05	1H2107-097	2012	1.18±0.02			
ESO511-G030	2014	0.44±0.07	HE2128-0221	2016	0.82±0.05			
NGC5940	2014	1.03±0.13	NGC7469	2012	1.26±0.08			
RXSJ17414+0348	2014	0.97±0.11	NGC7603	2014	0.86±0.21			
MCG+03_47_002	2013	1.75±0.25	—	—-	—-			
ESO141-G55	2013	1.29±0.05						
ESO141-G55	2015	1.39±0.04						
ESO141-G55	All	1.07±0.02						
CTSG03_04	2013	1.24±0.1						
NGC6860	2015	0.6±0.07						
PGC64989	2013	1.14±0.13						
PGC64989	2014	0.81±0.09						
PGC64989	All	0.46±0.03						
MRK509	2014	0.86±0.06						
F1041	2013	0.75±0.1						
NGC7603	2014	1.03±0.09						
IRAS23226-3843	2013	0.67±0.09						
UM163	2013	0.87±0.11						

Table D.2. Total and host fluxes for B V r_s and R obtained via the FVG method (see text). The interpolated optical flux at 5100Å, $f_{5100,\mathrm{obs}}$, is noted as are the values for β from the fit to the nuclear optical broadband spectrum ($f_\nu \propto \lambda^\beta$).

Object	Year	B_{tot} [mJy]	B_{host} [mJy]	V_{tot} [mJy]	V_{host} [mJy]	$R_{\mathrm{tot}}/r_{\mathrm{s,tot}}$ [mJy]	$R_{\mathrm{host}}/r_{\mathrm{s,host}}$ [mJy]	$f_{5100,\mathrm{obs}}$ [mJy]	β
1H2107-097	2012	7.45 ± 0.03	2.14 ± 0.13	9.01 ± 0.02	4.45 ± 0.11	–	–	4.78 ± 0.12	-0.64
3C120	2014	11.79 ± 0.34	2.22 ± 0.27	–	–	18.76 ± 0.18	8.22 ± 0.31	9.89 ± 0.41	0.2
3C120	2014	11.79 ± 0.34	2.14 ± 0.29	13.83 ± 0.07	4.46 ± 0.29	–	–	9.46 ± 0.35	-0.12
3C120	2014	11.79 ± 0.34	2.47 ± 0.15	13.83 ± 0.07	5.15 ± 0.14	–	–	8.88 ± 0.23	-0.3
3C120	2018	9.34 ± 0.0	2.26 ± 0.27	10.97 ± 0.0	4.71 ± 0.27	–	–	6.51 ± 0.27	-0.51
3C120	comb	10.75 ± 0.27	2.47 ± 0.15	12.67 ± 0.06	5.15 ± 0.14	–	–	7.75 ± 0.21	-0.4
AKN120	2018	10.29 ± 0.01	2.29 ± 0.28	11.98 ± 0.04	4.77 ± 0.26	–	–	7.45 ± 0.27	-0.43
CTSG03_04	2013	1.62 ± 0.02	0.51 ± 0.18	–	–	2.7 ± 0.01	1.82 ± 0.14	1.03 ± 0.17	-0.48
ESO141-G55	2013	13.96 ± 0.11	1.8 ± 0.58	–	–	16.0 ± 0.22	6.65 ± 0.45	11.12 ± 0.56	-0.55
ESO141-G55	2013	13.96 ± 0.11	1.75 ± 0.66	–	–	16.0 ± 0.22	6.5 ± 0.5	11.21 ± 0.63	-0.52
ESO141-G55	2015	10.34 ± 0.05	1.7 ± 0.35	–	–	12.43 ± 0.1	6.31 ± 0.25	7.68 ± 0.33	-0.72
ESO141-G55	2015	10.34 ± 0.05	1.75 ± 0.66	–	–	12.43 ± 0.1	6.5 ± 0.5	7.57 ± 0.62	-0.77
ESO141-G55	comb	10.63 ± 0.09	1.06 ± 0.22	–	–	12.8 ± 0.16	3.91 ± 0.2	9.33 ± 0.24	-0.15
ESO323-G77	2015	8.4 ± 0.06	2.8 ± 0.35	–	–	20.53 ± 0.13	9.99 ± 0.66	6.95 ± 0.45	1.32
ESO374-G25	2011	1.15 ± 0.01	1.07 ± 0.1	–	–	3.0 ± 0.01	2.9 ± 0.11	0.09 ± 0.1	0.57
ESO374-G25	2011	1.15 ± 0.01	–	–	–	3.0 ± 0.01	–	1.72 ± 0.01	2.45
ESO374-G25	2017	1.36 ± 0.0	0.91 ± 0.31	–	–	2.87 ± 0.01	2.47 ± 0.3	0.43 ± 0.31	-0.3
ESO374-G25	2017	1.36 ± 0.0	1.24 ± 0.19	2.68 ± 0.01	2.57 ± 0.12	–	–	0.11 ± 0.14	-0.36
ESO399-IG20	2011	4.08 ± 0.03	1.6 ± 0.52	–	–	6.78 ± 0.05	4.32 ± 0.51	2.47 ± 0.52	-0.02
ESO438-G09	2011	5.1 ± 0.03	1.12 ± 0.5	–	–	6.96 ± 0.04	3.03 ± 0.5	3.96 ± 0.5	-0.03
ESO438-G09	2011	5.1 ± 0.03	1.12 ± 0.5	–	–	6.96 ± 0.04	3.03 ± 0.5	3.96 ± 0.5	-0.03
ESO438-G09	2015	4.0 ± 0.02	0.84 ± 0.28	–	–	6.61 ± 0.03	3.01 ± 0.32	3.3 ± 0.29	0.27
ESO438-G09	2015	4.0 ± 0.02	1.12 ± 0.5	–	–	6.61 ± 0.03	3.86 ± 0.31	2.84 ± 0.45	-0.1
ESO490-IG26	2011	2.54 ± 0.01	2.04 ± 0.17	–	–	6.41 ± 0.03	5.5 ± 0.29	0.64 ± 0.22	1.53
ESO490-IG26	2011	2.54 ± 0.01	–	–	–	6.41 ± 0.03	–	3.74 ± 0.02	2.37
ESO511-G030	2013	2.54 ± 0.01	1.39 ± 0.28	–	–	6.59 ± 0.05	4.96 ± 0.41	1.3 ± 0.32	0.73
ESO511-G030	2013	2.54 ± 0.01	1.46 ± 0.66	–	–	6.59 ± 0.05	5.03 ± 0.5	1.22 ± 0.61	0.77
ESO511-G030	2014	2.56 ± 0.01	0.32 ± 0.44	–	–	6.49 ± 0.06	1.15 ± 0.99	3.01 ± 0.6	1.81
ESO511-G030	2014	2.56 ± 0.01	1.65 ± 0.36	4.03 ± 0.01	3.43 ± 0.24	–	–	0.68 ± 0.28	-1.74
ESO511-G030	2014	2.56 ± 0.01	1.46 ± 0.5	4.03 ± 0.01	3.04 ± 0.5	–	–	1.02 ± 0.5	-0.44
ESO511-G030	comb	2.56 ± 0.01	1.34 ± 0.29	–	–	6.57 ± 0.05	4.78 ± 0.42	1.39 ± 0.33	0.8
ESO549-G49	2012	3.24 ± 0.01	0.17 ± 0.51	–	–	6.74 ± 0.04	0.45 ± 1.05	4.15 ± 0.71	1.84
ESO578-G09	2014	1.97 ± 0.01	0.43 ± 0.16	–	–	3.83 ± 0.01	1.6 ± 0.25	1.75 ± 0.19	0.77
F1041	2013	1.14 ± 0.01	0.55 ± 0.18	–	–	2.82 ± 0.02	2.02 ± 0.24	0.65 ± 0.2	0.63
HE0003-5023	2014	2.5 ± 0.07	0.37 ± 0.12	–	–	3.88 ± 0.08	1.36 ± 0.14	2.26 ± 0.15	0.35
HE0003-5023	2014	2.5 ± 0.07	0.22 ± 0.15	2.98 ± 0.02	0.46 ± 0.17	–	–	2.44 ± 0.17	0.42
HE1136-2304	2015	1.06 ± 0.01	0.94 ± 0.11	2.08 ± 0.01	1.96 ± 0.12	–	–	0.12 ± 0.12	0.0
HE1136-2304	2015	1.06 ± 0.01	0.9 ± 0.11	2.08 ± 0.01	1.87 ± 0.12	–	–	0.19 ± 0.12	1.14
HE1136-2304	2016	1.42 ± 0.01	1.03 ± 0.09	2.73 ± 0.01	2.14 ± 0.15	–	–	0.52 ± 0.13	1.73
HE1136-2304	2016	1.42 ± 0.01	0.9 ± 0.09	2.73 ± 0.01	1.87 ± 0.15	–	–	0.73 ± 0.13	2.1
HE1136-2304	2018	1.57 ± 0.01	0.83 ± 0.16	2.52 ± 0.02	1.73 ± 0.16	–	–	0.77 ± 0.16	0.27
HE1136-2304	2018	1.57 ± 0.01	0.9 ± 0.16	2.52 ± 0.02	1.87 ± 0.16	–	–	0.66 ± 0.16	-0.13
HE1136-2304	comb	1.35 ± 0.02	0.9 ± 0.09	2.46 ± 0.02	1.87 ± 0.13	–	–	0.54 ± 0.12	1.13
HE1136-2304	comb	1.35 ± 0.02	0.9 ± 0.09	2.46 ± 0.02	1.87 ± 0.13	–	–	0.54 ± 0.12	1.13
HE1143-1810	2016	4.37 ± 0.01	1.27 ± 0.24	5.41 ± 0.01	2.64 ± 0.25	–	–	2.87 ± 0.25	-0.47
HE2128-0221	2016	0.67 ± 0.01	0.17 ± 0.04	0.99 ± 0.0	0.35 ± 0.05	–	–	0.59 ± 0.05	1.03
IC4329A	2015	3.58 ± 0.02	–	–	–	15.73 ± 0.09	–	5.93 ± 0.04	3.08
IRAS01089-4743	2013	2.15 ± 0.02	0.43 ± 0.39	–	–	4.0 ± 0.02	1.52 ± 0.56	1.95 ± 0.44	0.76
IRAS09595-0755	2013	1.34 ± 0.01	0.58 ± 0.18	–	–	2.61 ± 0.01	2.08 ± 0.12	0.67 ± 0.16	-0.75
IRAS23226-3843	2013	2.68 ± 0.02	0.81 ± 0.38	–	–	5.8 ± 0.03	2.99 ± 0.57	2.15 ± 0.44	0.85
MCG-02_12_050	2014	1.52 ± 0.01	0.98 ± 0.17	–	–	4.3 ± 0.03	3.64 ± 0.29	0.58 ± 0.21	0.42
MCG-02_12_050	2014	1.52 ± 0.01	–	–	–	4.3 ± 0.03	–	2.17 ± 0.02	2.16
MCG+03_47_002	2013	0.84 ± 0.01	0.51 ± 0.26	–	–	2.06 ± 0.01	1.88 ± 0.15	0.27 ± 0.23	-1.26
MRK1239	2015	3.96 ± 0.02	0.99 ± 0.49	–	–	9.36 ± 0.03	3.52 ± 0.96	3.74 ± 0.63	1.41
MRK1347	2014	1.94 ± 0.03	0.3 ± 0.21	–	–	3.41 ± 0.03	1.14 ± 0.29	1.83 ± 0.24	0.68
MRK335	2011	7.79 ± 0.05	1.26 ± 0.5	9.08 ± 0.03	2.63 ± 0.45	–	–	6.48 ± 0.47	-0.05

Table D.2 *continued*

Table D.2 *(continued)*

Object	Year	$B_{\rm tot}$ [mJy]	$B_{\rm host}$ [mJy]	$V_{\rm tot}$ [mJy]	$V_{\rm host}$ [mJy]	$R_{\rm tot}/r_{\rm s,tot}$ [mJy]	$R_{\rm host}/r_{\rm s,host}$ [mJy]	$f_{5100,\rm obs}$ [mJy]	β
MRK335	2011	7.79 ± 0.05	1.99 ± 0.5	9.08 ± 0.03	4.15 ± 0.45	–	–	5.19 ± 0.47	-0.68
MRK335	2014	6.79 ± 0.14	1.47 ± 0.54	–	–	10.8 ± 0.41	5.23 ± 0.5	5.4 ± 0.58	0.1
MRK335	2014	6.79 ± 0.14	1.99 ± 0.51	–	–	10.8 ± 0.41	6.86 ± 0.47	4.49 ± 0.56	-0.41
MRK335	2017	5.61 ± 0.0	1.12 ± 0.48	6.9 ± 0.0	2.33 ± 0.49	–	–	4.54 ± 0.49	0.07
MRK335	2017	5.61 ± 0.0	1.99 ± 0.48	6.9 ± 0.0	4.15 ± 0.49	–	–	3.0 ± 0.49	-1.15
MRK335	comb	5.73 ± 0.03	1.99 ± 0.16	7.05 ± 0.04	4.15 ± 0.12	–	–	3.14 ± 0.14	-1.06
MRK335	comb	5.73 ± 0.03	1.99 ± 0.16	7.05 ± 0.04	4.15 ± 0.12	–	–	3.14 ± 0.14	-1.06
MRK509	2014	12.06 ± 0.14	1.83 ± 0.84	–	–	17.19 ± 0.4	6.78 ± 0.98	10.29 ± 0.91	0.04
MRK705	2013	3.43 ± 0.02	1.08 ± 0.35	–	–	6.45 ± 0.02	3.86 ± 0.37	2.43 ± 0.36	0.2
MRK841	2014	4.92 ± 0.06	0.94 ± 0.12	4.96 ± 0.01	1.96 ± 0.12	–	–	3.28 ± 0.13	-1.18
NGC1019	2011	1.66 ± 0.01	1.0 ± 0.3	–	–	3.47 ± 0.02	2.71 ± 0.34	0.7 ± 0.32	0.36
NGC4726	2013	2.15 ± 0.01	0.95 ± 0.5	–	–	5.16 ± 0.02	3.38 ± 0.77	1.37 ± 0.58	0.82
NGC5940	2014	1.92 ± 0.04	0.67 ± 0.3	–	–	3.76 ± 0.02	2.49 ± 0.29	1.26 ± 0.3	0.03
NGC6860	2015	3.77 ± 0.01	2.1 ± 0.41	–	–	10.08 ± 0.08	7.24 ± 0.68	2.0 ± 0.49	1.11
NGC7214	2011	3.76 ± 0.03	1.4 ± 0.46	–	–	7.15 ± 0.05	3.77 ± 0.64	2.74 ± 0.53	0.92
NGC7469	2012	17.51 ± 0.1	6.11 ± 1.1	21.69 ± 0.06	12.72 ± 0.88	–	–	9.68 ± 0.96	-1.0
NGC7603	2014	10.58 ± 0.24	0.83 ± 2.47	13.66 ± 0.12	1.73 ± 2.94	–	–	11.19 ± 2.78	0.84
NGC7603	2014	10.58 ± 0.24	2.53 ± 1.08	–	–	17.28 ± 0.28	9.03 ± 1.05	8.12 ± 1.1	0.05
NGC985	2014	4.6 ± 0.04	0.49 ± 0.88	–	–	4.97 ± 0.06	1.88 ± 0.74	3.73 ± 0.84	-0.59
PG1149-110	2013	0.9 ± 0.01	0.64 ± 0.18	–	–	2.65 ± 0.01	2.48 ± 0.13	0.22 ± 0.17	-0.88
PG1149-110	2013	0.9 ± 0.01	–	–	–	2.65 ± 0.01	–	1.3 ± 0.01	2.25
PGC50427	2011	1.83 ± 0.01	0.66 ± 0.17	–	–	2.72 ± 0.03	1.78 ± 0.14	1.07 ± 0.16	-0.56
PGC50427	2011	1.83 ± 0.01	0.66 ± 0.17	–	–	2.72 ± 0.03	1.88 ± 0.14	1.02 ± 0.16	-0.85
PGC50427	2014	2.09 ± 0.02	0.53 ± 0.12	–	–	3.57 ± 0.03	1.91 ± 0.13	1.59 ± 0.13	0.13
PGC50427	2014	2.09 ± 0.02	0.66 ± 0.12	–	–	3.57 ± 0.03	2.27 ± 0.12	1.38 ± 0.12	-0.2
PGC64989	2013	2.94 ± 0.01	2.0 ± 0.45	–	–	7.98 ± 0.02	7.15 ± 0.39	0.9 ± 0.43	-0.26
PGC64989	2014	3.08 ± 0.04	2.1 ± 0.44	–	–	8.72 ± 0.07	7.48 ± 0.54	1.06 ± 0.47	0.49
PGC64989	comb	3.02 ± 0.03	1.23 ± 0.2	–	–	8.49 ± 0.06	4.4 ± 0.42	2.37 ± 0.27	1.72
RXSJ06225-2317	2013	1.87 ± 0.01	0.41 ± 0.24	–	–	2.98 ± 0.02	1.53 ± 0.26	1.46 ± 0.25	-0.01
RXSJ11032-0654	2011	0.76 ± 0.01	–	–	–	1.58 ± 0.01	–	1.03 ± 0.01	1.87
RXSJ11032-0654	2014	0.72 ± 0.01	–	–	–	1.5 ± 0.01	–	0.92 ± 0.01	1.53
RXSJ17414+0348	2012	4.73 ± 0.01	0.73 ± 0.28	5.42 ± 0.04	1.53 ± 0.29	–	–	3.92 ± 0.29	-0.12
RXSJ17414+0348	2012	4.73 ± 0.01	1.03 ± 0.28	5.42 ± 0.04	2.14 ± 0.29	–	–	3.41 ± 0.29	-0.5
RXSJ17414+0348	2014	4.74 ± 0.03	1.07 ± 0.64	–	–	7.37 ± 0.05	3.81 ± 0.66	3.63 ± 0.65	-0.06
RXSJ17414+0348	2014	4.74 ± 0.03	1.07 ± 0.61	–	–	7.37 ± 0.05	3.81 ± 0.63	3.63 ± 0.62	-0.06
UGC12138	2011	4.03 ± 0.02	1.87 ± 0.51	–	–	6.94 ± 0.03	5.04 ± 0.46	2.05 ± 0.49	-0.33
UM163	2013	2.46 ± 0.03	0.77 ± 0.4	4.8 ± 0.04	2.84 ± 0.46	–	–	1.78 ± 0.42	0.31
WPVS_7	2012	2.68 ± 0.01	0.38 ± 0.19	2.94 ± 0.01	0.8 ± 0.18	–	–	2.19 ± 0.18	-0.3
WPVS48	2013	3.95 ± 0.02	0.64 ± 0.22	–	–	5.8 ± 0.01	2.38 ± 0.22	3.35 ± 0.22	0.07
WPVS48	2014	3.81 ± 0.04	0.78 ± 0.16	4.98 ± 0.04	1.63 ± 0.18	–	–	3.25 ± 0.18	0.42
WPVS48	2014	3.81 ± 0.04	0.96 ± 0.27	–	–	6.21 ± 0.05	3.56 ± 0.25	2.78 ± 0.27	-0.15
WPVS48	2018	3.25 ± 0.01	0.53 ± 0.2	3.78 ± 0.01	1.11 ± 0.21	–	–	2.69 ± 0.21	-0.08
WPVS48	comb	3.82 ± 0.03	0.73 ± 0.27	–	–	6.09 ± 0.04	2.7 ± 0.28	3.19 ± 0.27	0.19

NOTE—a = r_s filter; b = no host subtraction

Table E.1. Log of optical spectroscopic observations with SALT and HET.

Object	Julian Day +2 400 000	UT Date	Exp. Time [s]	Tel.
3C 120	(1)	-	-	HET
3C 120	56983.31	2014-11-22	x	FAST
AKN 120	58821.74	2019-12-04	848	HET
ESO 141-G55	56417.54	2013-05-05	900	SALT
ESO 374-G25	55972.57	2012-02-15	2×460	SALT
ESO 399-IG20	56095.41	2012-06-16	700	SALT
ESO 438-G09	55981.61	2012-02-24	2×480	SALT
ESO578-G09	57044.53	2015-01-22	x	FAST
HE 1136-2304	(2)	-	-	SALT
IRAS09595-0755	57005.54	2014-12-14	x	FAST
MCG-02.12.050	56983.33	2014-11-22	x	FAST
MRK1347	57010.53	2014-12-19	x	FAST
MRK 335	56983.24	2014-11-22	x	FAST
MRK 509	56064.55	2012-05-17	700	SALT
MRK 509	56984.11	2014-11-23		FAST
MRK841	57044.54	2015-01-22	x	FAST
NGC1019	56240.41	2012-11-08	x	SALT
NGC1019	56983.25	2014-11-22	x	FAST
NGC5940	57044.54	2015-01-22	x	FAST
NGC 7603	56984.13	2014-11-23		FAST
NGC 7603	56235.31	2012-11-03	2×480	SALT
NGC 985	56235.31	2014-11-21		FAST
PGC 50427	56071.47	2012-05-23	700	SALT
PGC64989	56985.06	2014-11-24	x	FAST
RXS J06226-2317	56983.43	2014-11-22	x	FAST
RXS J06226-2317	58122.54	2018-01-04	864	SALT
RXS J11032-0654	55976.41	2012-02-18	2×480	SALT
RXS J11032-0654	57012.54	2014-12-21	x	FAST
RXS J17414+034	56064.53	2012-05-17	700	SALT
WPVS 48	56423.34	2013-05-10	600	SALT
WPVS 48	56985.53	2014-11-24	x	FAST

NOTE—(1) We used the average spectrum from a spectroscopic campaign on 3C 120 (Kollatschny et al. 2014). (2) We used the average spectrum from a spectroscopic campaign on HE 1136-2304 (Kollatschny et al. 2018).

E. Hα SINGLE-EPOCH SPECTRA

Below we present the set of the spectra used in this work to constrain the FWHM of the broad Hα emission line in different sources (Table. E.1). The black lines show the continuum-subtracted Hα emission line in the rest frame of the source. Individual best-fit narrow components for the NII and SII lines, as well as the broad Hα, are shown in green. In cases where the Hα line is fitted with three components, the sum of the middle and broad components is represented by a blue line. The sum of all Gaussian emission components is traced by a red line. Positions of the NIIa, NIIb, SIIa, and SIIb lines are marked. The orange colored surfaces trace the throughput curves of the NB filters used (at 670nm, 680nm and 690nm), while that of the narrower SII-band (at 672nm) is shown in gray.

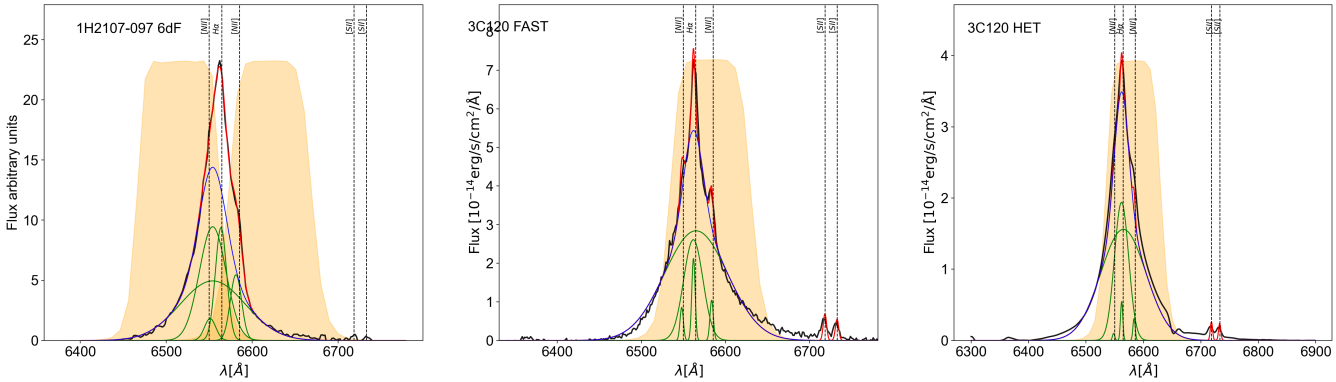

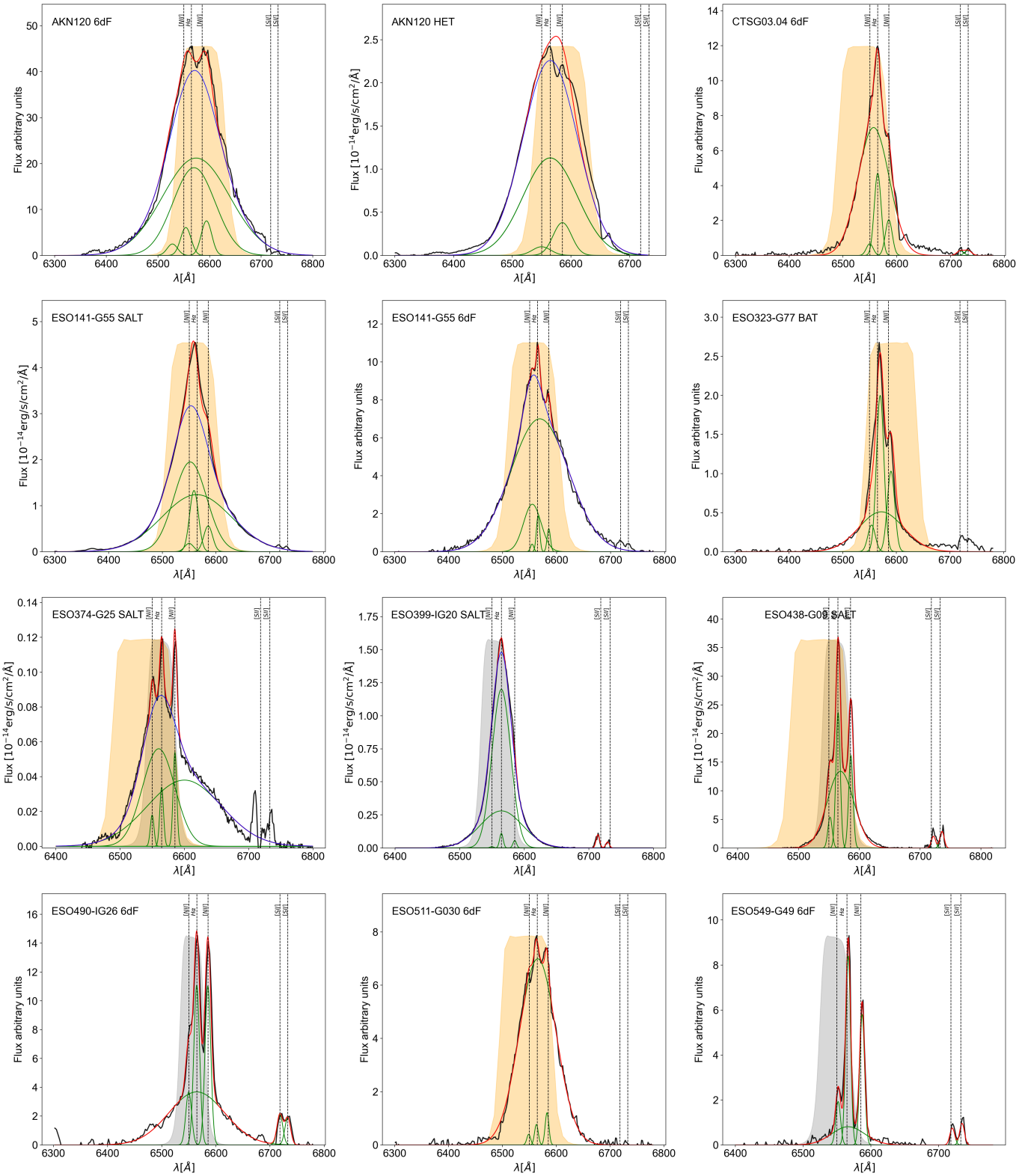
AKN120 6dF
AKN120 HET
CTSG03.04 6dF
ESO141-G55 SALT
ESO141-G55 6dF
ESO323-G77 BAT
ESO374-G25 SALT
ESO399-IG20 SALT
ESO438-G09 SALT
ESO490-IG26 6dF
ESO511-G030 6dF
ESO549-G49 6dF
[NII]
Hα
[SII]
Flux arbitrary units
Flux [10⁻¹⁴erg/s/cm²/Å]
λ[Å]

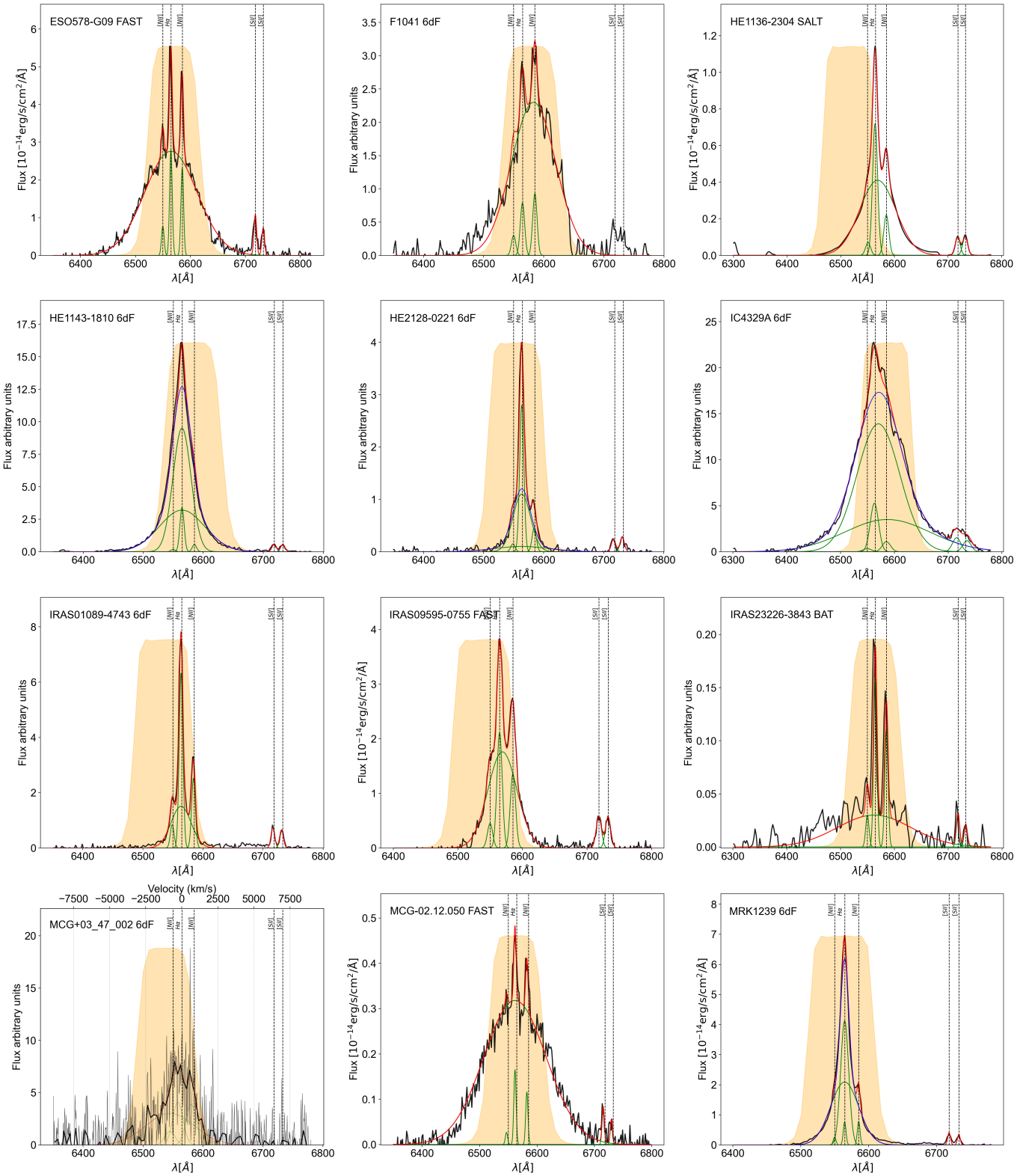
ESO578-G09 FAST
F1041 6dF
HE1136-2304 SALT
HE1143-1810 6dF
HE2128-0221 6dF
IC4329A 6dF
IRAS01089-4743 6dF
IRAS09595-0755 FAST
IRAS23226-3843 BAT
MCG+03_47_002 6dF
MCG-02.12.050 FAST
MRK1239 6dF
[NII]
Hα
[SII]
λ[Å]
Flux [10⁻¹⁴erg/s/cm²/Å]
Flux arbitrary units
Velocity (km/s)

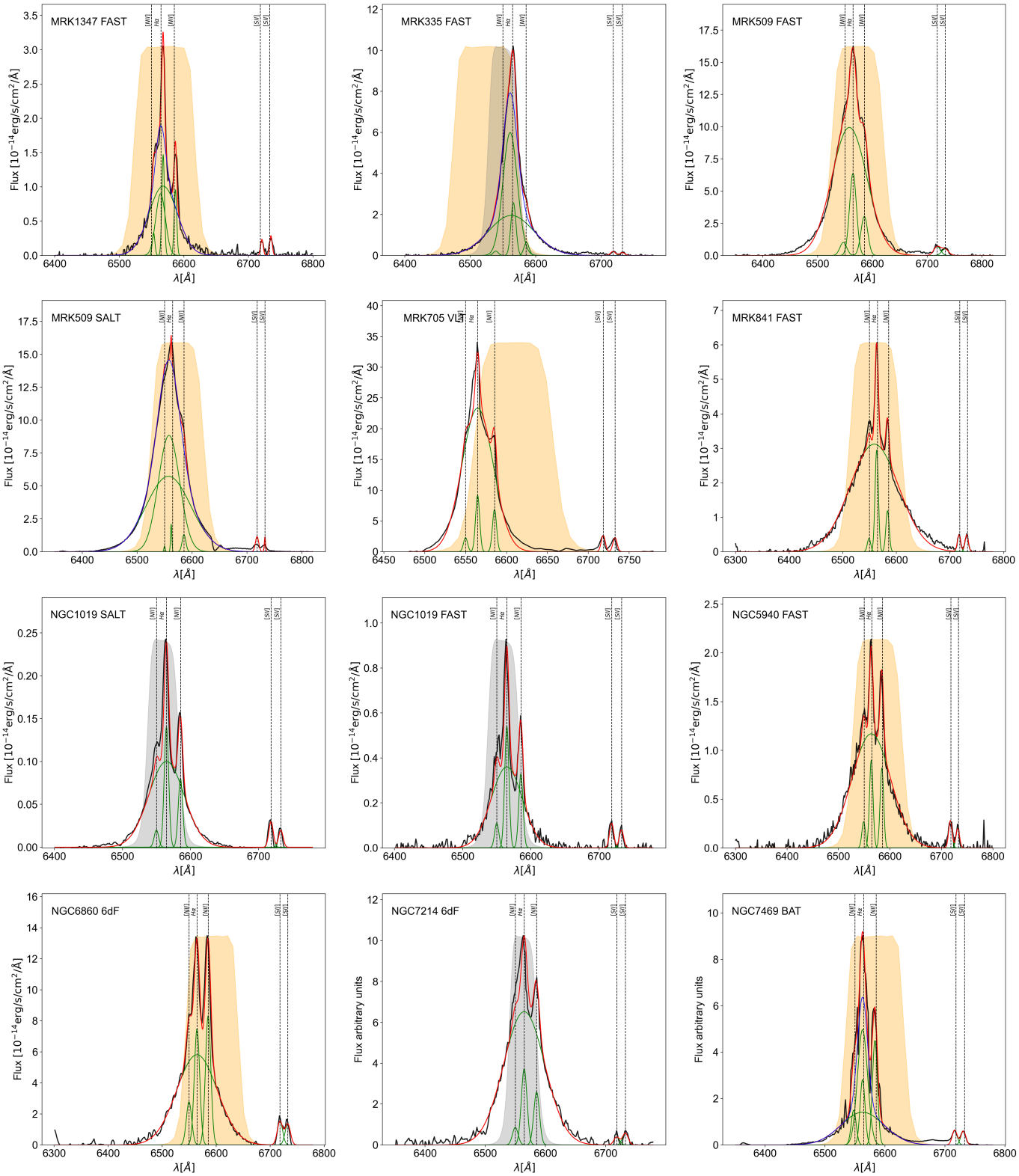
MRK1347 FAST
MRK335 FAST
MRK509 FAST
MRK509 SALT
MRK705 VLT
MRK841 FAST
NGC1019 SALT
NGC1019 FAST
NGC5940 FAST
NGC6860 6dF
NGC7214 6dF
NGC7469 BAT
[NII]
Hα
[SII]
Flux [10⁻¹⁴erg/s/cm²/Å]
Flux arbitrary units
λ[Å]

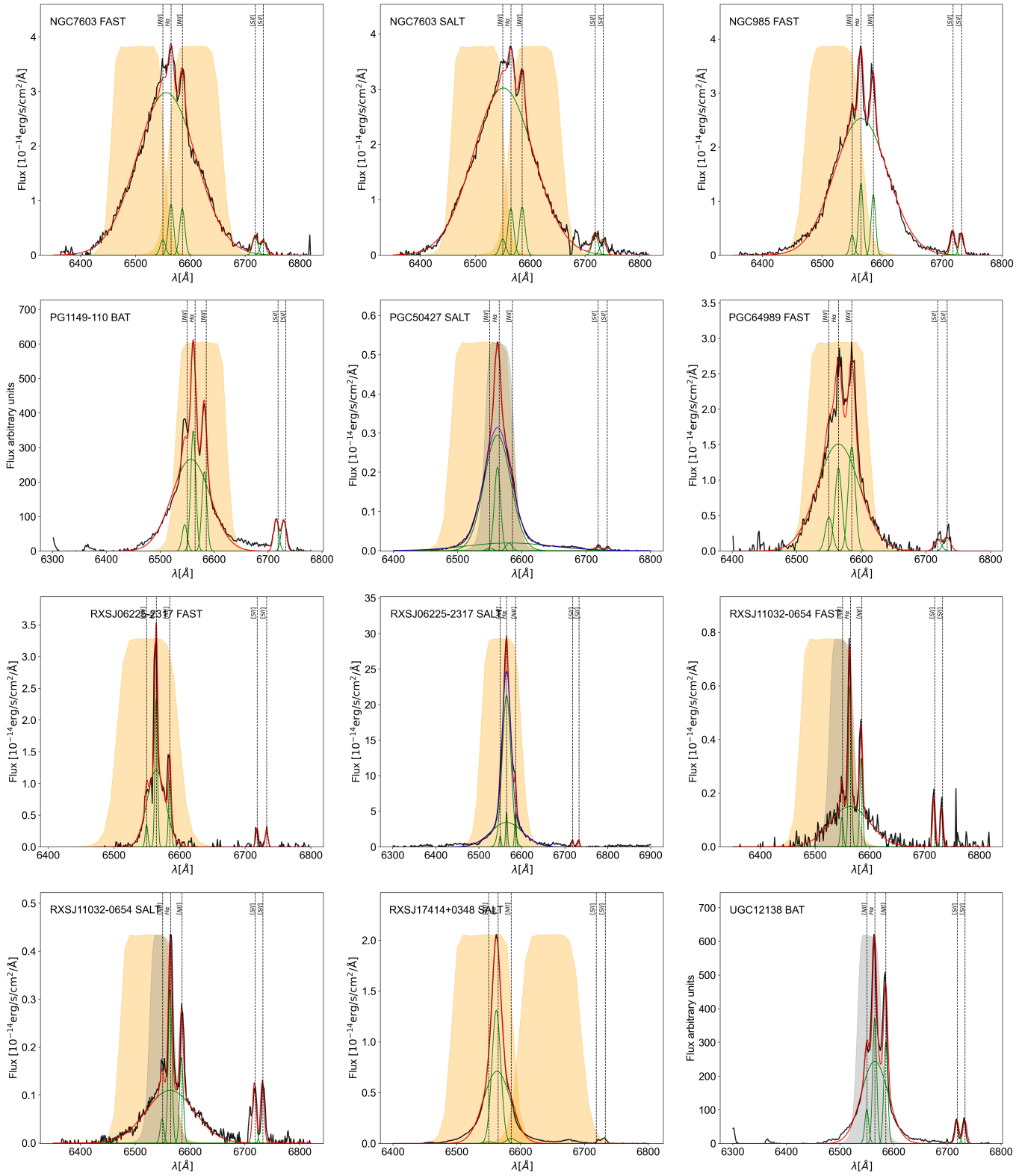
NGC7603 FAST
NGC7603 SALT
NGC985 FAST
PG1149-110 BAT
PGC50427 SALT
PGC64989 FAST
RXSJ06225-2317 FAST
RXSJ06225-2317 SALT
RXSJ11032-0654 FAST
RXSJ11032-0654 SALT
RXSJ17414+0348 SALT
UGC12138 BAT
[NII]
Hα
[SII]
λ[Å]
Flux [10⁻¹⁴erg/s/cm²/Å]
Flux arbitrary units

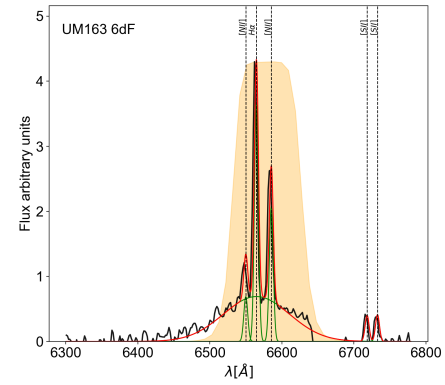
UM163 6dF
[NII]
Hα
[NII]
[SII]
[SII]
Flux arbitrary units
λ[Å]

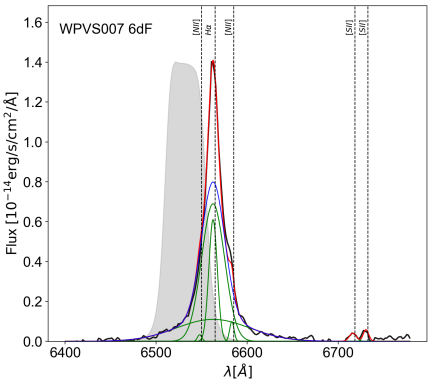
WPVS007 6dF
[NII]
Hα
[NII]
[SII]
[SII]
Flux [10⁻¹⁴erg/s/cm²/Å]
λ[Å]

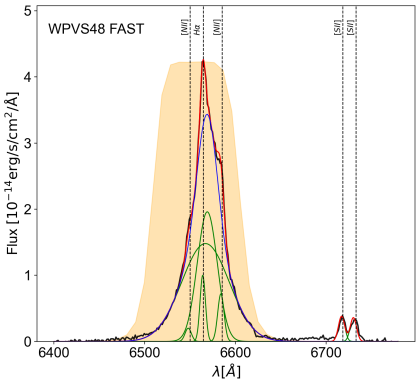
WPVS48 FAST
[NII]
Hα
[NII]
[SII]
[SII]
Flux [10⁻¹⁴erg/s/cm²/Å]
λ[Å]

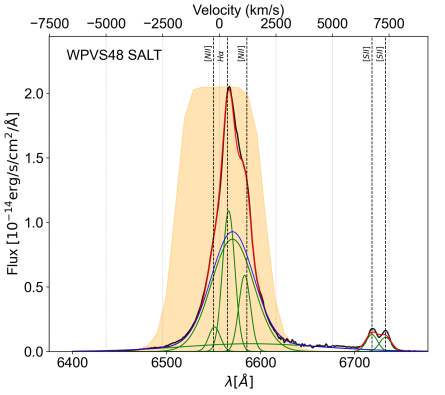
Velocity (km/s)
WPVS48 SALT
[NII]
Hα
[NII]
[SII]
[SII]
Flux [10⁻¹⁴erg/s/cm²/Å]
λ[Å]

Table F.1. Literature values for Hα Reverberation Mapping

Object	**z**	$t_{\mathrm{H}\alpha}$	$LogL_{5100}$	**Ref.**
Mrk142	0.04494	$2.78^{+1.17}_{-0.88}$	43.54 ± 0.02	B
SBS1116+583A	0.02787	$4.01^{+1.37}_{-0.95}$	42.07 ± 0.28	B
Arp151	0.02109	$7.84^{+1.03}_{-0.98}$	42.48 ± 0.11	B
Mrk1310	0.01956	$4.51^{+0.66}_{-0.61}$	42.23 ± 0.17	B
NGC4253	0.01293	$25.17^{+0.65}_{-0.85}$	42.51 ± 0.13	B
NGC4748	0.01463	$7.50^{+2.97}_{-4.57}$	42.49 ± 0.13	B
NGC6814	0.00521	$9.46^{+1.90}_{-1.56}$	42.05 ± 0.29	B
Mrk1501	0.0893	67^{+24}_{-38}	44.14 ± 0.02	C
J0101+422	0.1900	118^{+17}_{-17}	44.89 ± 0.01	C
PG0947+396	0.2059	71^{+16}_{-35}	44.71 ± 0.01	C
VIIIZw218	0.1274	140^{+26}_{-26}	44.53 ± 0.01	C
PG1440+356	0.0791	80^{+63}_{-30}	44.63 ± 0.01	C
NGC4395	0.00106	$0.058^{+0.010}_{-0.010}$	39.76 ± 0.01	NGC4395
17	0.457	$119.2^{+5.2}_{-7.9}$	43.99 ± 0	S
85	0.238	$61.3^{+13.6}_{-10.3}$	43.37 ± 0	S
101	0.458	$75.7^{+7.1}_{-8.3}$	44.4 ± 0	S
126	0.192	$136.1^{+6.9}_{-6.4}$	43.29 ± 0	S
160	0.36	$90.2^{+4.1}_{-3.9}$	43.82 ± 0	S
184	0.193	$145.4^{+58.5}_{-42.2}$	43.73 ± 0	S
291	0.532	$95.3^{+20.1}_{-19.6}$	43.9 ± 0	S
305	0.527	$54.6^{+21.3}_{-16.5}$	44.22 ± 0	S
320	0.265	$30.7^{+7.1}_{-11.7}$	43.44 ± 0	S
371	0.473	$32.4^{+2.7}_{-2.9}$	44.13 ± 0	S
645	0.474	$25.2^{+2.3}_{-2.5}$	44.1 ± 0	S
733	0.455	$27.4^{+13.5}_{-28.7}$	43.91 ± 0	S
766	0.165	$13.9^{+3.9}_{-3.9}$	43.75 ± 0	S
767	0.527	$33.4^{+14.5}_{-13.0}$	43.91 ± 0	S
768	0.259	$27.7^{+2.8}_{-2.9}$	43.4 ± 0	S
769	0.187	$14.0^{+3.4}_{-3.3}$	42.96 ± 0	S
772	0.249	$22.9^{+2.1}_{-2.3}$	43.46 ± 0	S
781	0.264	$16.0^{+4.6}_{-5.5}$	43.63 ± 0	S
789	0.425	$47.4^{+4.9}_{-5.3}$	43.74 ± 0	S
790	0.238	$10.4^{+3.6}_{-3.6}$	43.33 ± 0	S
798	0.423	$17.5^{+6.5}_{-9.7}$	44.07 ± 0	S
840	0.244	$9.6^{+1.3}_{-1.4}$	43.31 ± 0	S
845	0.273	$9.4^{+4.6}_{-4.4}$	42.78 ± 0	S
PG0026	0.142	116^{+25}_{-27}	44.91 ± 0.02	K
PG0052	0.155	183^{+57}_{-38}	44.75 ± 0.03	K
PG0804	0.1	175^{+18}_{-15}	44.85 ± 0.02	K
PG0844	0.064	37^{+15}_{-15}	44.23 ± 0.06	K
PG1211	0.085	107^{+35}_{-42}	44.69 ± 0.06	K
PG1226	0.158	444^{+56}_{-55}	45.90 ± 0.02	K
PG1229	0.064	67^{+37}_{-43}	43.64 ± 0.06	K
PG1307	0.155	155^{+81}_{-13}	44.79 ± 0.02	K
PG1351	0.087	227^{+149}_{-72}	44.64 ± 0.06	K
PG1411	0.089	95^{+37}_{-34}	44.50 ± 0.02	K
PG1426	0.086	83^{+42}_{-48}	44.57 ± 0.02	K
PG1613	0.129	38^{+35}_{-19}	44.71 ± 0.03	K
PG1617	0.114	100^{+28}_{-33}	44.33 ± 0.02	K
PG2130	0.061	223^{+50}_{-26}	44.14 ± 0.03	K

NOTE—Delays are in restframe. B: Hα time delay from Bentz et al. (2010) and luminosity from Bentz et al. (2013) . S: Values from Shen et al. (2023), object corresponds to the RMID from SDSS and luminosity is the median luminosity from whole campaing and subtracted the fraction of host. K: Hα lag values and luminosity from Kaspi et al. (2000) and if available luminosity from Bentz et al. (2013). C: Cho et al. (2023).

F. LITERATURE VALUES

G. TIME LAG, LUMINOSITIES FOR ALL OBJECTS

Table G.1. All time lags in observer frame. $\mathscr{R}_{Re}$ denotes the ratio $R_{\rm eFR}/R_{\rm e,TP}$ and $\mathscr{C}$ the confidence level for the time lag determination. Delays showing $\mathscr{R}_{Re} >$ and $\mathscr{C} > 85\%$ are considered as good results (see section 4.4.2 for details).

Object	year	$\tau_{\rm peak}$ [days]	$\tau_{\rm cent}$ [days]	$\mathscr{R}_{Re}/\mathscr{C}$ – / %	$f_{5100,\rm obs}$ [mJy]	L_{5100} [10^{43}erg/s]	FWHM [km/s]	$M_{\rm BH}$ [$10^6 M_\odot$]	$log.\dot{\mathscr{M}}$	$log.\dot{\mathscr{M}}_{R_{\rm Fe}}$
1H2107-097	2012	$8.0^{+0.4}_{-0.4}$	$12.1^{+3.3}_{-0.8}$	2.3/99.7	4.82 ± 0.12	4.77 ± 0.12	2333 ± 447	$1.26^{+0.35}_{-0.09}$	$0.809^{+0.244}_{-0.06}$	-0.553 ± 0.012
1H2107-097	2012	$14.4^{+2.0}_{-0.0}$	$19.3^{+0.6}_{-0.5}$	2.1/98.4	4.82 ± 0.12	4.77 ± 0.12	2333 ± 447	$2.01^{+0.06}_{-0.05}$	$0.404^{+0.03}_{-0.026}$	-0.553 ± 0.012
1H2107-097	avg	$11.0^{+2.0}_{-0.4}$	$15.7^{+3.4}_{-0.9}$	–	4.82 ± 0.12	4.77 ± 0.12	2333 ± 447	$1.63^{+0.36}_{-0.1}$	$0.583^{+0.194}_{-0.053}$	-0.553 ± 0.012
3C120	2014	$55.2^{+30.0}_{-4.4}$	$57.1^{+5.9}_{-5.9}$	3.0/100	8.88 ± 0.23	14.34 ± 0.37	2924 ± 66	$9.27^{+0.99}_{-0.99}$	$-0.209^{+0.094}_{-0.094}$	-1.883 ± 0.219
AKN120	2018	$18.6^{+23.0}_{-1.4}$	$28.1^{+1.4}_{-1.6}$	2.6/100	7.48 ± 0.27	11.91 ± 0.43	5759 ± 12	$17.7^{+0.91}_{-1.04}$	$-0.891^{+0.048}_{-0.054}$	0.563 ± 0.001
CTSG03_04	2013	$14.8^{+0.4}_{-1.4}$	$17.8^{+0.9}_{-0.9}$	3.0/99.9	1.03 ± 0.17	2.47 ± 0.41	3042 ± 242	$3.11^{+0.16}_{-0.16}$	$-0.405^{+0.093}_{-0.093}$	-2.193 ± 0.431
ESO141-G55	2013	$26.4^{+1.2}_{-6.0}$	$23.1^{+1.0}_{-0.9}$	3.9/100	11.21 ± 0.63	23.1 ± 1.3	4981 ± 578	$10.84^{+0.49}_{-0.44}$	$-0.034^{+0.048}_{-0.045}$	-0.62 ± 0.012
ESO141-G55	2015	$16.0^{+1.2}_{-0.4}$	$16.1^{+1.3}_{-1.6}$	4.2/100	7.57 ± 0.62	15.6 ± 1.28	4981 ± 578	$7.55^{+0.63}_{-0.78}$	$0.024^{+0.083}_{-0.098}$	-0.62 ± 0.012
ESO141-G55	avg	$21.2^{+1.7}_{-6.0}$	$19.6^{+1.6}_{-1.8}$	–	8.76 ± 0.88	18.05 ± 1.81	4981 ± 578	$9.2^{+0.78}_{-0.88}$	$-0.052^{+0.088}_{-0.096}$	-0.62 ± 0.012
ESO323-G77	2015	$29.2^{+1.2}_{-1.2}$	$26.7^{+3.6}_{-1.9}$	2.3/100	6.95 ± 0.45	2.52 ± 0.16	4246 ± 460	$9.3^{+1.27}_{-0.67}$	$-1.343^{+0.123}_{-0.07}$	3.15 ± 0
ESO374-G25	2011	$7.6^{+14.2}_{-2.5}$	$11.2^{+1.0}_{-2.0}$	2.1/97.7	1.72 ± 0.01	< 1.58	4481 ± 969	$4.31^{+0.39}_{-0.79}$	$-1.002^{+0.079}_{-0.159}$	1.47 ± 0.001
ESO399-IG20	2011	$24.4^{+0.8}_{-5.2}$	$19.6^{+0.4}_{-0.8}$	2.2/98.6	2.47 ± 0.52	2.16 ± 0.45	1843 ± 81	$1.27^{+0.03}_{-0.05}$	$0.281^{+0.104}_{-0.109}$	-0.3 ± 0.007
ESO438-G09	2011	$14.8^{+2.4}_{-9.2}$	$12.2^{+0.4}_{-0.4}$	2.1/98.6	3.96 ± 0.5	3.65 ± 0.46	2300 ± 167	$1.24^{+0.04}_{-0.04}$	$0.649^{+0.068}_{-0.068}$	5.19 ± 0
ESO438-G09	2015	$12.4^{+0.4}_{-0.4}$	$12.0^{+0.2}_{-0.2}$	3.5/100	2.84 ± 0.28	2.61 ± 0.26	2300 ± 167	$1.22^{+0.02}_{-0.02}$	$0.447^{+0.05}_{-0.05}$	5.19 ± 0
ESO438-G09	avg	$13.6^{+2.4}_{-9.2}$	$12.1^{+0.4}_{-0.4}$	–	3.44 ± 0.57	3.17 ± 0.52	2300 ± 167	$1.23^{+0.04}_{-0.04}$	$0.565^{+0.086}_{-0.086}$	5.19 ± 0
ESO490-IG26	2011	$15.2^{+2.2}_{-3.0}$	$13.0^{+4.5}_{-2.7}$	1.2/73.7	3.74 ± 0.04	< 3.64	5588 ± 412	$7.77^{+2.76}_{-1.65}$	$-0.973^{+0.308}_{-0.185}$	–
ESO549-G49	2012	–	–	1.7/98.1	4.73 ± 0.05	< 4.55	2766 ± 270	–	–	–
ESO511-G030	2013	$17.2^{+0.2}_{-0.2}$	$20.9^{+0.7}_{-0.5}$	2.0/99.3	1.3 ± 0.32	1.01 ± 0.25	3656 ± 12	$5.36^{+0.18}_{-0.13}$	$-1.46^{+0.124}_{-0.122}$	-1.113 ± 0.056
ESO511-G030	2014	$18.7^{+0.2}_{-0.2}$	$19.2^{+0.5}_{-0.6}$	2.2/99.7	1.02 ± 0.5	0.79 ± 0.39	3656 ± 12	$4.92^{+0.13}_{-0.16}$	$-1.544^{+0.241}_{-0.241}$	-1.113 ± 0.056
ESO578-G09	2014	$19.6^{+2.0}_{-12.8}$	$19.5^{+0.6}_{-0.6}$	2.7/99.9	1.75 ± 0.19	3.39 ± 0.37	5125 ± 14	$9.7^{+0.31}_{-0.31}$	$-1.188^{+0.06}_{-0.06}$	-0.31 ± 0.009
F1041	2013	$16.4^{+0.4}_{-0.0}$	$15.7^{+0.7}_{-1.0}$	2.4/99.8	0.65 ± 0.2	1.04 ± 0.32	3676 ± 886	$4.03^{+0.19}_{-0.27}$	$-1.196^{+0.156}_{-0.161}$	–
HE0003-5023	2014	$2.0^{+8.5}_{-0.4}$	$6.6^{+1.4}_{-1.7}$	3.1/99.9	2.24 ± 0.61	3.62 ± 0.99	3396 ± 0	$1.44^{+0.32}_{-0.38}$	$0.509^{+0.232}_{-0.267}$	–
HE1136-2304	2015	$10.6^{+1.0}_{-1.0}$	$9.1^{+0.5}_{-0.2}$	2.1/99.2	0.19 ± 0.12	0.22 ± 0.14	3544 ± 221	$2.18^{+0.12}_{-0.05}$	$-1.669^{+0.312}_{-0.309}$	-1.417 ± 0.072
HE1136-2304	2016	$20.4^{+1.0}_{-1.0}$	$17.4^{+2.2}_{-3.9}$	1.8/99.4	0.74 ± 0.12	0.86 ± 0.14	3544 ± 221	$4.17^{+0.54}_{-0.96}$	$-1.346^{+0.138}_{-0.215}$	-1.417 ± 0.072
HE1136-2304	2018	$11.0^{+15.6}_{-1.0}$	$11.2^{+4.2}_{-1.8}$	1.5/84.9	0.66 ± 0.12	0.77 ± 0.14	3544 ± 221	$2.69^{+1.03}_{-0.44}$	$-1.038^{+0.346}_{-0.169}$	-1.417 ± 0.072
HE1143-1810	2016	$21.2^{+0.2}_{-1.2}$	$17.5^{+2.5}_{-2.4}$	2.2/99.8	2.87 ± 0.25	5.01 ± 0.44	2143 ± 15	$1.53^{+0.23}_{-0.22}$	$0.674^{+0.135}_{-0.13}$	-1.83 ± 0.231
HE2128-0221	2016	$9.2^{+5.6}_{-5.8}$	$8.3^{+0.7}_{-0.9}$	2.2/99.9	0.59 ± 0.05	2.43 ± 0.21	1660 ± 124	$0.43^{+0.04}_{-0.05}$	$1.311^{+0.088}_{-0.107}$	0.117 ± 0.006
IC4329A	2015	$13.4^{+14.0}_{-0.6}$	$22.7^{+0.8}_{-0.8}$	3.0/100	7.09 ± 0.06	< 2.87	4940 ± 274	$10.69^{+0.38}_{-0.38}$	$-1.369^{+0.031}_{-0.031}$	-1.55 ± 0.153
IRAS01089-47	2013	–	–	1.2/76.8	1.95 ± 0.44	1.55 ± 0.35	1731 ± 124	–	–	0.143 ± 0.072
IRAS09595-07	2013	$61.6^{+12.0}_{-0.4}$	$57.4^{+1.6}_{-1.8}$	1.2/68.5	0.67 ± 0.16	3.03 ± 0.72	2402 ± 18	$6.16^{+0.18}_{-0.2}$	$-0.865^{+0.119}_{-0.12}$	-1.007 ± 0.045
IRAS09595-07	2013	–	–	1.2/68.5	0.67 ± 0.16	3.03 ± 0.72	2402 ± 18	–	–	–
IRAS23226-3843	2013	–	–	2.0/99.7	2.15 ± 0.44	3.96 ± 0.81	–	–	–	1.813 ± 0
MCG+03-47-002	2013	$18.8^{+0.0}_{-0.2}$	$16.8^{+0.4}_{-0.5}$	1.7/96.8	0.28 ± 0.22	0.66 ± 0.52	–	–	–	–

Table G.1 *continued*

Table G.1 *(continued)*

Object	year	$\tau_{\rm peak}$ [days]	$\tau_{\rm cent}$ [days]	$\mathscr{R}_{Re}/\mathscr{C}$ – / %	$f_{5100,\rm obs}$ [mJy]	L_{5100} [10^{43}erg/s]	FWHM [km/s]	$M_{\rm BH}$ [$10^6 M_\odot$]	$log.\dot{\mathscr{M}}$	$log.\dot{\mathscr{M}}_{R_{\rm Fe}}$
MCG-02.12.050	2014	$9.6^{+3.6}_{-0.8}$	$10.8^{+1.3}_{-1.2}$	1.4/86.4	2.31 ± 0.02	< 4.37	5585 ± 782	$6.38^{+0.8}_{-0.73}$	$-0.634^{+0.108}_{-0.1}$	-0.85 ± 0.022
MRK1239	2015	–	–	1.1/79.4	5.51 ± 0.04	< 3.47	1043 ± 358	–	–	0.36 ± 0.003
MRK1347	2014	$21.2^{+1.0}_{-16.8}$	$13.8^{+4.6}_{-1.7}$	1.9/97.4	1.83 ± 0.24	7.41 ± 0.97	1576 ± 540	$0.64^{+0.22}_{-0.08}$	$1.682^{+0.311}_{-0.129}$	0.76 ± 0.001
MRK335	2010	$19.6^{+0.0}_{-0.4}$	$19.0^{+0.4}_{-0.3}$	1.0/57.0	–	–	1611 ± 259	$0.94^{+0.02}_{-0.02}$	–	-1.057 ± 0.036
MRK335	2011	$20.4^{+0.8}_{-10.8}$	$17.5^{+3.9}_{-6.6}$	1.2/72.7	5.19 ± 0.2	4.62 ± 0.18	1611 ± 259	$0.87^{+0.2}_{-0.34}$	$1.11^{+0.199}_{-0.337}$	-1.057 ± 0.036
MRK335	2014	$11.2^{+0.2}_{-5.2}$	$12.0^{+0.9}_{-1.1}$	2.0/99.5	4.49 ± 0.25	3.99 ± 0.22	1611 ± 259	$0.6^{+0.05}_{-0.06}$	$1.343^{+0.072}_{-0.086}$	-1.057 ± 0.036
MRK509	2014	$24.4^{+0.4}_{-1.6}$	$22.9^{+0.8}_{-0.8}$	2.1/99.8	10.29 ± 0.91	17.31 ± 1.53	3451 ± 32	$5.17^{+0.19}_{-0.19}$	$0.421^{+0.053}_{-0.053}$	-1.587 ± 0.114
MRK705	2013	$11.6^{+0.0}_{-0.8}$	$15.5^{+1.0}_{-0.7}$	2.0/95.4	2.43 ± 0.36	3.21 ± 0.48	1919 ± 332	$1.09^{+0.07}_{-0.05}$	$0.677^{+0.093}_{-0.083}$	-0.443 ± 0.009
MRK841	2014	$20.8^{+12.0}_{-1.6}$	$23.8^{+2.5}_{-2.4}$	2.6/99.7	3.28 ± 0.13	6.75 ± 0.27	4645 ± 734	$9.72^{+1.06}_{-1.02}$	$-0.74^{+0.097}_{-0.093}$	-1.797 ± 0.184
NGC1019	2011	$9.2^{+1.6}_{-0.0}$	$9.7^{+2.0}_{-0.8}$	1.5/93.8	0.7 ± 0.32	0.57 ± 0.26	2755 ± 80	$1.41^{+0.3}_{-0.12}$	$-0.677^{+0.289}_{-0.235}$	-0.593 ± 0.014
NGC4726	2013	–	–	1.2/75.0	3.01 ± 0.03	< 3.05	3119 ± 0	–	–	-1.037 ± 0.041
NGC5940	2014	$5.2^{+0.8}_{-0.4}$	$5.9^{+0.8}_{-0.7}$	1.8/97.1	1.26 ± 0.3	2.26 ± 0.54	4033 ± 22	$1.82^{+0.26}_{-0.22}$	$0.002^{+0.168}_{-0.158}$	0.317 ± 0.002
NGC6860	2015	$36.0^{+0.0}_{-3.2}$	$34.7^{+1.0}_{-1.1}$	1.5/93.1	2.0 ± 0.49	0.61 ± 0.15	3668 ± 1016	$9.02^{+0.26}_{-0.29}$	$-2.243^{+0.122}_{-0.123}$	-0.67 ± 0.042
NGC7214	2011	$5.2^{+0.4}_{-0.4}$	$6.9^{+5.2}_{-0.9}$	1.8/97.8	2.74 ± 0.53	2.1 ± 0.41	3662 ± 100	$1.77^{+1.37}_{-0.24}$	$-0.025^{+0.677}_{-0.15}$	3.163 ± 0
NGC7469	2012	$16.0^{+0.0}_{-0.4}$	$9.6^{+3.5}_{-4.8}$	2.1/97.2	9.68 ± 0.96	3.13 ± 0.31	1615 ± 119	$0.48^{+0.18}_{-0.25}$	$1.365^{+0.325}_{-0.444}$	–
NGC7603	2014	$36.8^{+4.0}_{-1.2}$	$35.1^{+1.5}_{-1.3}$	6.8/100	8.12 ± 1.1	9.04 ± 1.22	5778 ± 10	$22.34^{+0.98}_{-0.85}$	$-1.273^{+0.076}_{-0.074}$	0.31 ± 0.002
NGC985	2014	$24.0^{+0.4}_{-0.4}$	$22.2^{+0.7}_{-0.8}$	1.9/98.1	3.73 ± 0.84	10.2 ± 2.3	4675 ± 347	$9.12^{+0.3}_{-0.34}$	$-0.416^{+0.114}_{-0.115}$	-2.1 ± 0.35
PG1149-110	2013	$22.4^{+0.8}_{-6.0}$	$17.3^{+6.2}_{-1.1}$	1.1/65.8	1.4 ± 0.02	< 5.21	3579 ± 700	$4.14^{+1.56}_{-0.28}$	$-0.137^{+0.327}_{-0.058}$	-2.023 ± 0.3
PGC50247	2011	$21.8^{+1.0}_{-1.8}$	$21.6^{+0.9}_{-0.9}$	2.0/99.5	1.02 ± 0.16	0.87 ± 0.14	2377 ± 11	$2.34^{+0.1}_{-0.1}$	$-0.836^{+0.085}_{-0.085}$	-1.573 ± 0.131
PGC50247	2014	$18.4^{+0.4}_{-0.0}$	$20.2^{+0.6}_{-0.4}$	1.7/97.4	1.38 ± 0.12	1.18 ± 0.1	2377 ± 11	$2.19^{+0.07}_{-0.04}$	$-0.581^{+0.05}_{-0.046}$	-1.573 ± 0.131
PGC6498	2013	$24.4^{+0.4}_{-0.0}$	$27.6^{+2.3}_{-3.7}$	1.3/75.1	0.9 ± 0.04	0.45 ± 0.02	3275 ± 770	$5.7^{+0.48}_{-0.78}$	$-2.04^{+0.077}_{-0.121}$	-1.587 ± 0.128
PGC6498	2014	$26.8^{+0.2}_{-2.4}$	$26.0^{+0.3}_{-0.3}$	3.5/100	1.06 ± 0.04	0.53 ± 0.02	3275 ± 770	$5.37^{+0.06}_{-0.06}$	$-1.882^{+0.021}_{-0.021}$	-1.587 ± 0.128
RXSJ062	2013	$20.0^{+0.0}_{-0.4}$	$19.5^{+0.2}_{-1.4}$	1.7/93.0	1.46 ± 0.25	3.23 ± 0.55	1506 ± 30	$0.84^{+0.01}_{-0.06}$	$0.91^{+0.084}_{-0.106}$	-1.98 ± 0.274
RXSJ110	2011	–	–	1.3/85.5	–	–	3849 ± 46	–	–	-1.043 ± 0.37
RXSJ110	2014	–	–	1.2/73.0	–	–	3849 ± 46	–	–	–
RXSJ174	2012	$16.0^{+0.0}_{-0.4}$	$15.4^{+0.6}_{-0.8}$	2.2/99.7	3.63 ± 0.62	2.77 ± 0.47	2222 ± 129	$1.46^{+0.06}_{-0.08}$	$0.328^{+0.09}_{-0.095}$	0.977 ± 0
RXSJ174	2014	$28.4^{+1.2}_{-9.6}$	$20.5^{+1.2}_{-1.2}$	1.9/98.7	3.41 ± 0.29	2.61 ± 0.22	2222 ± 129	$1.94^{+0.12}_{-0.12}$	$0.039^{+0.067}_{-0.067}$	0.977 ± 0
UGC1213	2012	$16.4^{+0.2}_{-0.2}$	$15.0^{+0.5}_{-0.4}$	1.6/97.7	2.05 ± 0.49	1.69 ± 0.4	2693 ± 269	$2.08^{+0.07}_{-0.06}$	$-0.303^{+0.12}_{-0.119}$	–
UM163	2013	$10.0^{+0.8}_{-0.4}$	$10.9^{+0.4}_{-0.5}$	2.3/99.9	1.37 ± 0.2	2.12 ± 0.31	4901 ± 77	$4.97^{+0.19}_{-0.24}$	$-0.911^{+0.079}_{-0.082}$	-0.807 ± 0.051
WPVS007	2012	$10.4^{+0.0}_{-0.4}$	$10.6^{+0.9}_{-1.0}$	2.1/99.4	2.19 ± 0.18	2.56 ± 0.21	1557 ± 163	$0.49^{+0.04}_{-0.05}$	$1.222^{+0.086}_{-0.093}$	4.243 ± 0.002
WPVS48	2013	$17.6^{+0.8}_{-0.0}$	$21.1^{+0.9}_{-1.9}$	2.8/99.8	2.69 ± 0.2	5.88 ± 0.44	1917 ± 24	$1.47^{+0.06}_{-0.14}$	$0.812^{+0.053}_{-0.089}$	-1.66 ± 0.134
WPVS48	2014	$16.4^{+2.4}_{-0.4}$	$18.3^{+0.6}_{-1.3}$	3.8/100	2.69 ± 0.54	5.88 ± 1.18	1917 ± 24	$1.27^{+0.04}_{-0.09}$	$0.936^{+0.102}_{-0.117}$	-0.747 ± 0.018
WPVS48	2018	$19.6^{+6.4}_{-0.8}$	$19.3^{+4.3}_{-0.3}$	2.1/99.2	2.29 ± 0.4	5.0 ± 0.87	1917 ± 24	$1.34^{+0.31}_{-0.02}$	$0.784^{+0.218}_{-0.086}$	-0.747 ± 0.018
WPVS48	avg	$18.9^{+6.4}_{-0.8}$	$18.9^{+2.7}_{-2.7}$	–	2.56 ± 0.7	5.59 ± 1.53	1917 ± 24	$1.31^{+0.19}_{-0.19}$	$0.875^{+0.185}_{-0.185}$	-0.747 ± 0.018

H. COMMENTS ON INDIVIDUAL OBJECTS

Here we elaborate on the idiosyncrasies of the sources in our sample with particular emphasis on the time-lag measurements and host-galaxy subtraction. We compare our results to previously reported measurements, when available.

1. 1H2107-097: Due to its redshift (z=0.02698), the Hα emission line is not fully covered by a single narrowband (NB) filter. Our observations use two NB filters: NB670 and NB680, each covering distinct parts of the Hα line profile. Specifically, the NB670 filter covers the blue wing and a substantial portion of the Hα core and the NB680 band mainly covers the red wing of the line. With no restrictions to the time delay formalism we derived a time delay of $\tau = 12.1^{+3.3}_{-0.6}$ days and $\alpha = 0.54^{+0.04}_{-0.12}$ for the NB670 band and $\tau = 19.3^{+0.6}_{-0.5}$ days, with $\alpha = 0.44^{+0.02}_{-0.02}$ for the NB680 filter. While these results hint at a rotating disk model for the BLR, a more thorough study of the geometry of the Hα line is beyond of the scope of this paper. Therefore, we present an average delay $\tau = 15.7^{+4.2}_{-4.2}$ days for this source. The BV-band FVG reveals a blue trend with a slope of 1.18 ± 0.02, intersecting precisely within the host galaxy's color range. Consequently, we derive host-subtracted flux values, leading to a host-subtracted luminosity of $4.77 \pm 0.57 \times 10^{43}$, erg s^{-1}. In contrast, Boris et al. (2002) conducted a multicolor study, suggesting that in the B band, the Seyfert nucleus contributes only 30% of the total luminosity. This fraction appears notably lower compared to our findings, where the AGN contributes approximately 70% of the total flux.

2. 3C120: The correlation exhibits two peaks, at 55 days and at 80 days, both with $\alpha \sim 0.5$, aligning with the α value derived from $\alpha_{\rm phot}$. For a comprehensive analysis of the same photometric observations conducted by our group, refer to Ramolla et al. (2018). Regarding the Hα line, they reported a delay of $71.2^{+12.4}_{-13.3}$ days, which is consistent with our findings within the measurement uncertainties. 3C 120 has been the subject of numerous reverberation mapping (RM) campaigns. Notably, delays for Hβ from observations conducted between 1989 and 1996 were reported as $38.1^{+21.3}_{-15.3}$ days in Peterson et al. (1998). For the period 2008-2009, Kollatschny et al. (2014) reported delays for various emission lines: $23.9^{+4.6}_{-3.9}$ days for Hγ, $12.0^{+7.5}_{-7.0}$ days for He II, $26.8^{+6.7}_{-7.3}$ days for He I, $27.9^{+7.1}_{-5.9}$ days for Hβ, and $28.5^{+9.0}_{-8.5}$ days for Hα. Additionally, Grier et al. (2012b) provided a delay of $25.9^{+2.3}_{-2.3}$ days for Hβ based on data from 2010-2011. Given the stability of the BV FVG across all observations, we derived host values within our aperture as $B = 2.47 \pm 0.14$ and $V = 5.15 \pm 0.13$ mJy, providing host-subtracted luminosities. For a detailed analysis of the FVG in 3C120, refer to Ramolla et al. (2015).

3. AKN120: The correlation coefficient for $V680$ reveals two peaks: one at 20 days and another at 45 days, both with $\alpha \sim 0.6$. The final centroid delay, derived using our formalism, is $28.1^{+1.4}_{-1.6}$ days, also with $\alpha \sim 0.6$. The peak delay is slightly shorter at $18.6^{+23.0}_{-1.4}$ days, with larger uncertainties reflecting the secondary peak in the correlation. The low value of $R_{\rm e,FR} \sim 0.75$ is primarily due to a 20-day gap in observations and weak features in the light curves. Despite this, we have a high confidence level and include the object in the final analysis, though it approaches a lower quality lag. Previous spectroscopic $H\beta$ campaigns reported delays of $50^{+9.0}_{-12}$ days in 1990 and $36^{+16}_{-9.0}$ days in 1995 Peterson et al. (1998). Haas et al. (2011) conducted a photometric RM campaign in 2010, focusing on Hβ and using the NB filter $OIII$. They initially reported an Hβ delay of 48.0 ± 3.0 days. However, after interpolating missing data points, the delay was revised to $30.2^{+1.0}_{-1.2}$ days. The $H\alpha$ delay from this work appears significantly shorter than the previously reported $H\beta$ delays, but within the uncertainties, the peak delay could be consistent with $\tau_{H\beta} < \tau_{H\alpha}$. The 2018 BV FVG exhibits a tight slope and a blue color, with a slope of 1.07 ± 0.03, consistent with the slopes reported by Winkler (1997).

4. CTSG03_04: The correlation coefficient is broad, spanning from 5 to 25 days, with a peak around 15 days and an average $\alpha \sim 0.5$, which is smaller than the $\alpha_{\rm phot}$ of approximately 0.7. The final reported delay is $t_{\rm cent} = 17.8 \pm 0.9$ days and $t_{\rm peak} = 14.8^{+0.4}_{-1.4}$ days, with a high confidence level. The BR FVG shows a slope of 1.24, indicating a very blue color, consistent with the findings in the color analysis by Boris et al. (2002).

5. ESO141-G55: For the 2013 campaign, the PRM formalism revealed a broad correlation ridge spanning from 2 to 30 days and two regions can be identified: the first region centered around ten days with a $\alpha > 0.6$, and a secondary region extending from almost 15 to 30 days with an $\alpha \sim 0.4$. Applying the formalism without restrictions, we determined a delay of $19.5^{+0.7}_{-0.5}$ days and $\alpha \sim 0.5$, but showing a lot of discrepancies between $\alpha_{\rm cent}$ and $\alpha_{\rm peak}$, due to the broad correlation and the fast increase of α at low delays. Therefore we additionally adjusted the search to focus on delays where $\alpha < 0.6$ and found a delay of $23^{+1.0}_{-0.9}$ days with $\alpha = 0.45^{+0.02}_{-0.02}$. The spectra shows a prominent Hα line with an estimated FWHM of 4980$\pm$578 km/s, therefore $\alpha_{\rm phot} \sim 0.70$ might be taken as an upper limit due to the broad nature of the line. For the 2015 campaign, when analyzing the complete light curve (with a 15-day gap), we report a delay of approximately 24 days. Due to the gap in the light curve, the value for $R_{\rm e,max}$ exceeds unity and therefore then we restrict the delay focusing only in the initial part of the light curve, which reduces the delay slightly with a value of $16.1^{+1.3}_{-1.6}$ days with an α value of 0.39. The averaged delay for both campaign is $19.5^{+1.6}_{-1.8}$ days. The BR FVGs appear stable; in 2013, the BR FVG slope was approximately 1.3, and in 2015 it was around 1.4. While combining both campaigns, the slope decreases slightly to 1.07. Winkler et al. (1992) study reports a BR slope of about 1.16, consistent with our findings. When considering the host color assumption and using the single-epoch FVGs, we derived a host B value of 1.75 ± 0.58 and a host R value of 6.5 ± 0.45. On average, this resulted in an exponent for the host-subtracted SED of $\beta \sim -0.64$, showing the blue character of this AGN. After subtracting the host contribution, the interpolated flux at 5100Å is 11.21 ± 1.11 mJy for 2013 and 7.74 ± 0.83 mJy for 2015, indicating a decrease

in luminosity of nearly 30%. The average luminosoty is 19.52×10^{43}erg/s. Winge et al. (1996) conducted a spectroscopic RM study but encountered challenges in accurately determining the time delay for this.

6. ESO323-G77: The correlation shows a main peak at around 30 days. The time delay determination exhibits a 100% confidence level, but with a low $R_{\rm e,max}$ value (~ 0.5), probably due to the noisy lightcurves, therefore the delay is discarded for further analysis. The BR slope is 0.53 which indicates reddened AGN, and the slope is consistent with previous AGN BR color found in Winkler et al. (1992); Winkler (1997) 0.45, 0.53 indicating that the slope overall didn't changed.

7. ESO374-G25: For a more detailed time lag determination of the 2012 campaing and host-galaxy subtraction see Ramolla (2012). For the 2011 campaing they found $12.5^{+2.0}_{-2.6}$ days, similar than for the 2012 campaing with 11.4 ± 2.7 days by a combination of the SII and NB670 filter, in agreement with our results.

8. ESO399-IG20: There are two possible solutions depending on the value of α. If we restrict α to be greater than 0.5, the main peak occurs at around 20 days. If we allow for smaller values of α, the main peak delay is around 40 days. We argue for the delay at 20 days with a larger α value due to the narrow filter SII, which is narrower and suggests a stronger influence from Hα. An analysis of the photometric data previously presented in Ramolla et al. (2014) reports a delay of $18.7^{+2.5}_{-2.2}$ days, which is in agreement with this study.

9. ESO438-G09: For 2011, we observe a broad correlation coefficient ranging from 5 days to 25 days, with a peak at 15 days. We might distinguish between a shorter delay with a higher α and a longer delay with an α of 0.3. Since $\alpha_{\rm phot}$ is approximately 0.50, we discard the shorter delays but noting that α might be higher for the 2011 epoch since the NB used is the SII filter. The delay found for 2011 is $\tau = 12.2 \pm 0.4$ with $\alpha = 0.29^{+0.02}_{-0.02}$. The 2015 campaign exhibits a distinct peak at 12 days with an alpha of 0.35. The averaged delay for the two epochs is $12.1^{+0.4}_{-0.5}$ days. The B flux shows a decrease of around 20% from 2011 to 2015. For 2015, we found a BR slope of 0.87, which is consistent with the slope found in Winkler et al. (1992). For 2011, the Br_s slope is ~ 1.0, which is also consistent with a stable FVG, as the r_s filter covers shorter wavelengths, resulting in an expected higher slope as BR. Observing the single epoch FVGs, we found a B-host value of 1.12 $\pm$ 0.5 mJy for 2011 and 0.84 ± 0.28 mJy for 2015. Therefore, we assume a B-host value of 1.09 ± 0.53, which is the average between the minimal and maximal values for both epochs. With B_{host} we extrapolate and find a $r_{s,host} = 2.94 \pm 1.47$ mJy and $R_{host} = 3.89 \pm 1.94 mJy$. Finally the f_{5100} host-subtracted flux is 4.1 ± 0.94 mJy for 2011 and 2.81 ± 0.99 for 2015, which translates to a luminosity of 3.77 ± 0.87 and $2.59 \pm 0.91 \times 10^{43}$erg/s, showing a decrease of almost 30% between the two epochs. The average luminosity for both epochs is $3.17 \pm 1.23 \times 10^{43}$erg/s. Although we observed a decrease in the luminosity that is not obvious translated in a shorter delay. This object shows the highest accreting object from R_{Fe}.

10. ESO490-IG26: The Hα line is dominated by narrow components but also shows a broad component. The correlation coefficient shows two possible lag solutions, with peaks at around 15 days and 40 days, both with $\alpha \sim 0.5$. Given that the duration of the light curve is approximately 80 days, the second delay is at the limit of the search range. Therefore, the delay is likely around 15 days. Nevertheless, the delay is excluded from further analysis since the $R_{\rm e,max}$ value is around 0.5, and the confidence level is below 85%. The $Br_{\rm s}$ FVG is red with a slope of 0.60. We are unable to disentangle the host galaxy's contribution from the total flux, so we report an upper limit for the luminosity.

11. ESO511-G030: The light curves show a big gap of observations of around 20 days in both campaigns, being the mean cadence ~4 days for the continuum and ~6 days for the NB band. In 2013 the correlation coefficient shows two main peaks, one at around 17 days with $\alpha \sim 0.6$ and another adjacent at 32 days and $\alpha \sim 0.5$. Running without α restriction we find $\tau_{\rm cent} = 20.6^{+0.6}_{-0.5}$ days and $\alpha = 0.54^{+0.01}_{-0.01}$, which agrees with $\alpha_{\rm phot} \sim 0.5$. For 2014, without restrictions in α we find $\tau = 16.4 \pm 0.4$ days and $\alpha = 0.54^{+0.01}_{-0.01}$, in agreement with the previous campaing. The value for $\alpha_{\rm phot}$ for this campaing is reduced to ~ 0.4 since the NB680 reduces by a factor of 20% but the B and R fluxes remained stable. But this fact is not reflected in the recovered α in the correlation and we are not able to restrict further α value due to the broad nature of the correlation. We report an average delay of $\tau = 18.5^{+0.7}_{-0.64}$ days. The BR FVG slope for 2013 is well defined with 0.70 ± 0.06 showing a slightly red AGN color with $B_{\rm host} = 1.39 \pm 0.28$mJy and $R_{host} = 4.96 \pm 0.41$mJy. On the other hand, the 2014 FVG is not well covered but the 2013-2014 combination yield a slope of 0.61 ± 0.07 with a host value in B of 1.22 ± 0.35 mJy and $R_{\rm host} = 4.35 \pm 0.58$mJy. For 2014 BV yield $B_{\rm host} = 1.65 \pm 0.36$mJy and $V_{host} = 3.43 \pm 0.24$. Since the intersection between the different epochs shows consistent results we average those results and interpolate for the filters V and R to obtain the average host values. We report $B_{\rm host} = 1.42 \pm 0.33$ mJy, $V_{\rm host} = 2.96 \pm 0.70$ mJy and $R_{\rm host} = 4.05 \pm 1.00$ mJy, yielding an interpolate flux f_{5100} of 1.56 ± 0.58mJy and 1.61 ± 0.60 mJy for 2013 and 2014 respectively, which translates to an average luminosity of $1.23 \pm 0.65 \times 10^{43}$erg/s. An X-ray study by Ghosh & Laha (2021) reports an accretion rate of 0.004-0.008 Eddington units. Similarly, our analysis of $\dot{\mathscr{M}}_{R\rm Fe}$ and $\dot{\mathscr{M}}$ also indicates a low level of accretion.

12. ESO549-G49: There is a possible lag solution indicating a delay of around 7 days with $\alpha \sim 0.5$, but the $R_{\rm e,max}$ value is quite low, so this delay is not included in the final results. Additionally, the Hα line is dominated by narrow components,

with the broad component being extremely weak, making the $\alpha \sim 0.5$ value unrealistic for this object. The FVG is poorly constrained.

13. ESO578-G09: The Hα line is well covered by the NB filter and exhibits a very broad component with an FWHM of approximately 5000 km/s. The correlation shows three peaks at around 10, 20, and 30 days, with α values of 0.7, 0.5, and 0.4. Given that $\alpha_{\rm phot} \sim 0.5$, we restrict the α value to around 0.5 and report a centroid delay of $t_{\rm cent} = 19.5 \pm 0.6$ days. The BR FVG is slightly red with a slope of 0.65 but is tight and shows a clear intersection with the host galaxy's color, allowing us to report a host-subtracted luminosity. The host galaxy is edge-on.

14. F1041: There is one possible correlation between 5 and 25 days with $\alpha \sim 0.5$, in agreement with $\alpha_{\rm phot} \sim 0.5$. The H$\alpha$ emission line is well covered by the NB filter and exhibits a strong broad component with $FWHM \sim 3600$ km/s. The FVG is slightly red with a slope of 0.75 for the BR combination. The poor quality of the 6dF spectra around Hβ prevents us from estimating the accretion rate based on $R_{\rm Fe}$.

15. HE0003-5023: The confidence level in the time lag determination is high; however, substantial differences in delays arise depending on the filter used for the continuum. The continuum light curve is particularly noisy at the start of the campaign, which can lead to spurious correlations, such as those observed at very short time lags. Even after removing the noisy data, discrepancies in the lags persist, leading us to exclude this object from further analysis. Additionally, α values vary between 0.7 and 0.3 depending on the filter used. We also lack of spectral data to assess the broadness and covering of the line. Despite these issues, the FVG is well constrained, and we report a host-subtracted luminosity.

16. HE1136-2304: The object is classified as a CL type and has been observed in three different campaigns: 2015, 2016, and 2018. The time delay reported from the 2015 campaign has a high confidence level, with a delay of approximately 10 days, consistent with the value reported by Kollatschny et al. (2018). However, the other campaigns exhibit lower confidence levels due to their shorter duration and are not included in the results for multi-epoch objects. We constructed a multi-epoch FVG and observed a change in the AGN's slope. In the 2018 campaign, the FVG reveals a bluer color, which could indicate a different mechanism within the AGN (see Section). The reverberation mapping spectroscopic study by Zetzl et al. (2018) reports a delay of $15.0^{+4.2}_{-3.8}$ days for the integrated Hα line and $7.5^{+4.6}_{-5.7}$ days for Hβ. Our narrowband (NB) filter only covers the bluer part of the Hα line, so the delays reported are consistent with these findings. For further details on this object, refer to Kollatschny et al. (2018) and Zetzl et al. (2018).

17. HE1143-1810: The Hα emission line is well covered, with a FWHM of approximately 2000 km/s, showing indications of a NLS1 classification, whereas the classification in Véron-Cetty & Véron (2006) lists it as S1.5. The correlation analysis reveals a primary delay between 15 and 20 days with α around 0.5. The BV FVG is well constrained and exhibits a blue characteristic with a slope close to unity. An X-ray study by Ursini et al. (2020) reports an accretion rate of 0.7-0.9 Eddington units, suggesting high accretion activity. However, our analysis of $\dot{\mathscr{M}}_{R\rm Fe}$ indicates low accretion, while $\dot{\mathscr{M}}$ shows moderate accretion.

18. HE2128-0221: The broad component of the Hα line is weak, with an FWHM less than 2000 km/s, and indicating a predominance of narrow lines. The correlation is modest, with $R_{\rm e,max} \sim 0.7$, showing a primary peak around 10 days with $\alpha \sim 0.5$. This value might be overestimated given the nature of the broad component in the spectra. Additionally, there is a secondary peak at 15 days with a lower $\alpha \sim 0.3$, and a potential further delay at 25 days with an even lower α. Due to the low $R_{\rm e,max}$ values at these delays, we report the main peak at approximately 10 days. The FVG is well-constrained and slightly red. This object belongs to the moderate accretors based on the $R_{\rm Fe}$.

19. IC4329A: The correlation coefficient presents two main peaks: one at 15 days with $\alpha \sim 0.5$ and another at 25 days with $\alpha \sim 0.4$. The final centroid delay we report is 23 days, with a peak delay at 14 days. Winge et al. (1996) analyzed spectra from 1992, reporting an upper limit delay of 25 days for Hα, which aligns with our findings. Recently, Bentz et al. (2023) conducted a spectroscopic RM campaign in 2022, finding an Hβ delay ($\tau_{H\beta}$) of $16.3^{+2.6}_{-2.3}$ days, slightly shorter than the centroid Hα delay reported in this work. The BR FVG shows a very red AGN slope of 0.35 ± 0.02, with no possible intersection with the adopted host color. The FVG highlights the extremely red nucleus of this source, which is also identified as an example of an extremely reddened galaxy in Winkler et al. (1992), exhibiting a high range of extinction values (A_V of 2-6 mag). Therefore, the luminosity presented in Table 3 should not be considered an upper limit due to the unknown extinction.

20. IRAS01089-4743: The confidence level in the lag determination is low. While the BR FVG is not well constrained, we present an attempt at host-subtracted luminosity. The spectrum is strongly dominated by narrow lines, with a very weak broad component, as inferred by $\alpha_{\rm phot} \sim 0.3$.

21. IRAS09595-0755: The main correlation coefficient peak does not yield physical values for α, thus no delay is reported. The Hα line, well covered by the NB filter, displays prominent narrow lines alongside a substantial broad component with an FWHM of approximately 2400 km/s. The FVG is notably blue, with a slope of around 1.4 and a tight intersection with the host color. Consequently, we report a host-subtracted luminosity.

22. IRAS23226-3843: From the spectrum, the Hα line is dominated by narrow lines, with the broad component being very weak; hence, we do not report an FWHM value for the Hα line. The weak broad component is also reflected in $\alpha_{\rm phot}$, which is around 0.25. The correlation coefficient shows a peak at approximately 5 days with α around 0.5. There is another peak at 15 days with a smaller α, but the correlation coefficient $R_{\rm e}$ is low, almost 0.7, so we do not report this delay. The FVG is well constrained and shows a red slope of approximately 0.7. Although IRAS23226-3843 is classified as S1, it is known to change its spectral type and is classified as CL. For details on this source, refer to Kollatschny et al. (2020, 2023).

23. MCG+03_47-002: The correlation coefficient indicates a primary delay at around 20 days with an α value of approximately 0.5, which aligns with $\alpha_{\rm phot}$. The spectra do not clearly display the line, so we do not report an FWHM. The BR FVG slope shows a blue trend, but the intersection with the host color is unclear. Consequently, the host-subtracted luminosity for this source is likely overestimated, and the actual luminosity is higher than what is reported in Table 3.

24. MGC-02.12.050: The peak delay is approximately 10 days with $\alpha \sim 0.5$, which is consistent with $\alpha_{\rm phot} \sim 0.43$. The value for $R_{\rm e,max}$ is less than 0.7, and the ratio $R_{\rm e,FR}/R_{\rm e,FP}$ is low. Therefore, we exclude this object from further analysis. The AGN slope appears reddened, but we have limited matched days. The total flux falls within the adopted range for the host-color, so we do not report a host-subtracted luminosity. Instead, we provide an interpolation between the observed fluxes.

25. MRK1239: We couldn't find any significant delay/meaningful value for α. Due to the low variability the FVG is also not well constrained.

26. MRK1347: The Hα emission line is well covered by the NB filter and exhibits prominent narrow lines, with the FWHM for the broad component approximately 1500 km/s. While Véron-Cetty & Véron (2006) classifies it as a S1 galaxy, Cracco et al. (2016) presents it as a NLS1, noting a FWHM of the broad Hβ component of 1614 km/s, similar to the findings of this study. The correlation coefficient shows two peaks: one between 5 and 10 days with $\alpha > 0.6$ and another at 20 days with $\alpha \sim 0.45$. The second peak aligns more closely with $\alpha_{\rm phot}$, which is around 0.5. The FVG shows a slightly red color with a slope of 0.70.

27. MRK335: In the first observational data from 2010, we find 2 peaks, one at 5 days with no meaningful α value and one at 20 days with $\alpha \sim 0.7 - 0.8$, with the result agreeing with $20.5^{+2.0}_{-2.8}$ days reported in Haas et al. (2011). Due to the short duration of the NB light curve, the $R_{e,\rm max}$ value is low, and therefore we do not obtain a high confidence level for this campaign. As a result, we do not include it in the final analysis, but for details on this observing campaign, refer to Haas et al. (2011). For the 2011 campaign, the same pattern occurs: we find a peak at 20 days with $\alpha \sim 0.7$, consistent with the previous campaign. Due to the duration of the campaign, as before, the confidence level is not high. On the other hand, for 2014 the R_e correlation obtained is broad and 3 peaks can be distinguished. One at 5 days with not physical value for α, another at around 15 days with $\alpha \sim$0.6 and at around 20 days with $\alpha \sim 0.5$.

28. MRK509: The correlation coefficient shows a peak at 15 days, but the associated α value exceeds one, which is not feasible. A more likely peak is observed at 25 days with $\alpha \sim 0.6$, and another at 35 days with α between 0.4 and 0.5. Since $\alpha_{\rm phot}$ is approximately 0.75, we favor the 25-day delay. In comparison, the $H\alpha$ delay reported here is $22.9^{+0.8}_{-0.8}$ days, which is notably shorter than the 76.0 ± 7.0 days reported by Peterson et al. (1998) and Peterson et al. (2004), who used much sparser light curves with an average sampling interval of 7 days. The BR FVG slope is approximately 0.90, slightly lower than the 1.2 reported by Winkler et al. (1992); Winkler (1997). Additionally, Boris et al. (2002) found that in MRK 509, the continuum emission from the nucleus contributes nearly 60% to the total flux, which is consistent with the results from the BR FVG.

    More REFs on this object

29. MRK705: The NB filter does not fully covered the broad Hα line, with the blue wing missing, though the $\alpha_{\rm phot}$ is approximately 0.52. The correlation coefficient $R_{\rm e}$ indicates a broad correlation range from 5 to 25 days, with a peak at 11 days. A secondary peak appears around 50 days, but no physically plausible α value can be associated with it.

30. MRK841: The Hα line in Mrk 841 exhibits a very broad component with a FWHM of approximately 4500 km/s. It is well monitored by the NB filter, although the filter does not fully capture the blue and red wings of the line. The correlation coefficient $R_{\rm e}$ reveals two peaks: one around 20 days and another at 30 days, with corresponding α values of 0.5 and 0.4, respectively. These values are somewhat lower than expected based on the broad nature of the line (no $\alpha_{\rm phot}$ available).

Despite this, no other physically plausible solutions for α are evident. The BV FVG analysis shows a well-constrained slope near unity, indicating a typical blue AGN. The $R_{\rm Fe}$ analysis suggests a low accretion rate for this object. Mrk 841 is part of the Lick AGN Monitoring Project (Barth et al. 2015), and a previous study reported an Hβ delay of $11.2^{+4.8}_{-1.9}$ days (U et al. 2022), indicating a Hα to Hβ delay ratio of approximately 2.

31. NGC1019: The $R_{\rm e}$ correlation coefficient exhibits a peak around 10 days, with an α value of approximately 0.75. This α value is reasonable given that the Hα line is monitored with the SII filter, which is narrower and captures more emission line variation. However, since the maximum $R_{\rm e,max}$ value is below 0.7, this result is excluded from the final analysis.

32. NGC4726: The R_e correlation coefficient shows a peak around 15 days, with an α value of approximately 0.7. The $\alpha_{\rm phot}$ value is below 0.3, reflecting the weak nature of the Hα line, as also evident in the 6dF spectrum where no line could be reliably fitted. This delay is discarded due to the low confidence level and the low $R_{\rm e,FR}/R_{\rm e,TP}$ ratio. Additionally, the FVG is not well constrained.

33. NGC5940: The correlation coefficient shows a primary peak at 5 days with an α of approximately 0.6, while $\alpha_{\rm phot}$ is 0.5. The Hα line is well covered by the NB filter and exhibits a broad profile with a FWHM of around 4000 km/s. A previous spectroscopic RM campaign reported an $H\beta$ delay of $5.70^{+0.90}_{-0.82}$ days in Barth et al. (2013), consistent with the delay found in this study. The FVG for the BR filters is around unity and well constrained. The accretion rate derived from $R_{\rm Fe}$ indicates moderate accretion.

34. NGC6860: The correlation coefficient shows a primary peak at around 35 days, but since the $R_{\rm e,FR}$ value is approximately 0.6, we exclude this object from further analysis.

35. NGC7214: The $R_{\rm e}$ correlation coefficient shows a peak around 5 days with an α value of approximately 0.6. The core of the Hα line is well covered by the SII filter, making this value plausible. Despite the peak $R_{\rm e,max}$ being below 0.7, the ratio of $R_{\rm e,FR}/R_{\rm e,TP}$ exceeds 1.6, justifying its inclusion in the final analysis. The FVG is slightly red, with the Br slope around 0.70.

36. NGC7469: Previous spectroscopic reverberation mapping studies have reported an Hβ delay of $4.5^{+0.7}-0.8$ days for the 1996 monitoring year and an Hα delay of $4.7^{+1.6}-1.3$ days, both by Collier et al. (1998), while Peterson et al. (2014) observed an Hβ delay of $10.8^{+3.4}_{-1.3}$ days for the 2010 monitoring year. In this study, the $R_{\rm e}$ correlation exhibits a peak around 15 days, with $R_{\rm e} \approx 0.8$ and a corresponding α value of approximately 0.3. This α value is consistent with the weak broad component observed in the spectra, where the Hα line is primarily dominated by narrow lines. The FVG indicates that the AGN is blue, with a BV slope of 1.27.

37. NGC7603: The Hα line is not completely covered by one single NB filter, and this objects is monitored using two NB filters. The broad component of the line is prominent, with a FWHM of approximately 6000 km/s therefore the $\alpha_{\rm phot}$ is around 0.4. The V-band is assumed as the continuum, since the B filter does not cover the entire observing season. The correlation coefficient reveals a peak at 13 days with α values between 0.4 and 0.5. Additionally, there is a secondary peak around 40 days with an α value of approximately 0.25. Both peaks exhibit high correlation coefficient values, with $R_{\rm e,max} \sim 0.95$. The delay between $VNB670$ and $VNB680$ is $12.6^{+1.0}_{-4.0}$ days and $12.8^{+0.4}_{-0.2}$ days, respectively, with α values of $0.40^{+0.10}_{-0.03}$ and $0.44^{+0.01}_{-0.01}$. When restricting the search to the lower α values, the centroid delays are $35.1^{+1.5}_{-1.3}$ days for $VNB670$ and $35.4^{+0.8}_{-1.1}$ days for $VNB680$. We favor the longer delay because the Hα line is not completely covered, which leads to smaller values for α. Additionally, the longer delay corresponds to a very high correlation coefficient, $R_{\rm e}$, providing a high confidence level. However, we also consider the 13-day delay as a possible alternative. This shorter delay is plausible due to the broad nature of the line, and its high confidence level. Kollatschny et al. (2000) conducted a 20-year observation campaign but was unable to report any delays due to insufficient data sampling. However, they observed asymmetries in the emission lines throughout the campaign, noting that the lines became more asymmetric and exhibited a stronger Balmer decrement when the galaxy was in a lower state. The BR FVG exhibits a blue color with a slope of approximately 1.0, despite having less matched data. Additionally, the accretion rate estimated from $R_{\rm Fe}$ is moderate.

    2014 $42.93^{+3.7}_{-9.0}$ Blex

38. NGC985: The NB filter does not cover the completely the core of the Hα-line. The $R_{\rm e}$ correlation shows a main peak at 24 days with an α of 0.7, which at the first glance appears high due to the coverage of the NB filter. The R_e correlation shows another two correlation peaks at 50 and 60 days with $\alpha \sim 0.4$, but with a very low value for $R_{\rm e}$, $R_{\rm e,max} < 0.6$. Because the broad component of the Hα line is prominent we can argue that the delay at around 24 days shows is representative for the Hα delay. Moreover the $\alpha_{\rm phot}$ is around 0.7, supporting this idea. Monitored as part of the LAMP project (Barth et al. 2015), NGC985 was reported to have an Hβ delay of $7.8^{+10.1}_{-9.8}$ days in (U et al. 2022).

39. PG1149-110: The Hα line is well covered by the filter, with an $\alpha_{\rm phot}$ value of around 0.4. However, the correlation does not produce a clear lag, as the $R_{\rm e}$ values are below 0.5 and the α value approaches 1. Consequently, this delay is excluded from the final analysis. The BV FVG slope is notably blue, with a value of 1.37 ± 0.16.

40. PGC50427: For 2011 observation campaign we obtain a clear correlation at $21.4^{+0.9}_{-0.9}$ days with $\alpha \sim 0.65$. For 2014 we obtain broad correlation from 3 days until 18 days with $\alpha > 0.6$ and another region from 18 until 30 days with $\alpha < 0.6$. Without restriction in α we obtain a delay of $14.2^{+1.6}_{-0.9}$ and $\alpha = 0.74^{+0.04}_{-0.04}$. The $\alpha_{\rm phot}$ of 0.58 for the 2014 campaign sets a limit to the possible α values and since the SII filter is narrower the Hα variation carried within it should be intuitive larger than in the NB670 filter, we set the restriction of $\alpha < 0.6$ and found $\tau = 20.2^{+0.6}_{-0.4}$ and $\alpha = 0.51^{+0.03}_{-0.02}$, being similar to the result in the first campaign. The average delay for both campaigns delay is $17.8^{+1.8}_{-1.3}$ days without any restriction for α, and applying $\alpha < 0.6$ for 2014 is $\tau = 20.8^{+1.1}_{1.0}$ days. The same photometric observations for 2011 and 2014 were analyzed in Pozo Nuñez et al. (2015), where they report $\tau = 20.4^{+0.4}_{-1.0}$ and $\tau = 18.7^{0.6}_{-1.6}$ days for 2011 and 2014 respectively, in agreement with the results reported here with another time delay formalism. Taking into account the intersection for Br and BR we derived an average $B_{\rm host} = 0.62 \pm 0.20$ mJy, extrapolating we find $r_{s,{\rm host}} = 1.67 \pm 0.53$ mJy and $R_{\rm host} = 2.21 \pm 0.70$ mJy. Interpolating the host subtracted fluxes we report $f_{5100} = 1.2 \pm 0.41$ for 2011 and $f_{5100} = 1.42 \pm 0.44$mJy for 2014 with an average luminosity of $1.12 \pm 0.40 \times 10^{43}$erg/s, in agreement with Pozo Nuñez et al. (2015) with $\sim 1.20 \times 10^{43}$erg/s.

41. PGC64989: For the first observation campaign we do not report a reliable delay due to a low confidence level. During the second season, although the B-band didn't fully capture the variability, the R filter did. Thus, we based our delay for the second season on the correlation between R and the NB filter. There's a possibility that the error estimate for the object's luminosity was underestimated. While the individual BR FVGs agree with each other, showing a host component of about 2 mJy in the B band, the combined data indicate that the B host value is halved. Furthermore, the combined data show an AGN color much redder than seen in individual campaigns. The reasons for these differences—whether calibration issues or other factors—are unclear. Therefore, we should interpret the estimated luminosity with caution.

42. RXSJ06225-2317: The broad component of the Hα line is weak, with a FWHM of approximately 1500 km/s observed in the FAST spectrum. The $R_{\rm e}$ correlation shows a clear peak at 20 days with an α value of 0.4, consistent with the $\alpha_{\rm phot}$. The FVG is well constrained.

43. RXJ1103.2-0654: Due to the poor variability of the light curve and unreliable FVG results, no delay or luminosity is reported in the final analysis.

44. RXSJ17414+0348: The Hα line is well covered by the NB670 filter, with $\alpha_{\rm phot}$ around 0.60 for the 2014 campaign. During the 2012 campaign, a peak is observed at 16 days with $\alpha \sim 0.5$. For the 2014 campaign, the correlation coefficient is broader, spanning between 15 and 25 days. The $R_{\rm e}$ value for this campaign exceeds unity due to the long observational gap and lack of overlapping data towards the end; however, the delays are still well-recovered. The FVG is well constrained, and although the matched data for the 2012 campaign is less consistent, the host values align with those from 2014. Consequently, we obtain a host-subtracted luminosity.

45. UGC12138: The SII filter covers well the Hα line, which is dominated by narrow components but also features a strong broad component with a FWHM of approximately 2600 km/s. The correlation coefficient shows a clear peak at 15 days with $\alpha \sim 0.6$, but the $R_{e,FR}$ value is less than 0.7, and therefore is not included in the final analysis. The FVG is well-constrained and indicates a blue nature with a slope of around 1.10.

46. UM163: The broad component is very weak, dominated by narrow lines, with $\alpha_{\rm phot} \sim 0.5$. There is a significant increase in α for the lower delay values, ranging from 0.9 to 0.45. A secondary peak appears at 40 days, but no physical value for α is possible. Therefore, we report the delay despite the high α value. The FVG is well-constrained.

47. WPVS48: We present three observation campaigns. The photometric data for the first two campaigns were previously analyzed in the context of dust RM in Pozo Nuñez et al. (2014) and the BLR together with dust in Sobrino Figaredo et al. (2018). Pozo Nuñez et al. (2014) reports NIR delays of 64 ± 4 and 71 ± 5 days for J and K, respectively. The delays and luminosities remain very stable across all campaigns, with an average $\tau_{\rm cent}$ of 20.3 ± 4.6 days, considering the maximum and minimum values for the three campaigns. The last observation campaign shows a significant gap in the data, causing the correlation coefficient $R_{\rm e}$ to exceed unity and the delay to have larger errors. The FVGs also appear stable; however, the combined BV FVG does not provide a host value. We obtained the host values by combining the individual FVGs, and all are in agreement. The FWHM is less than 2000 km/s. Nevertheless, the accretion rate based on $R_{\rm Fe}$ indicates a low accretion object.

48. WPVS007: The SII filter does not adequately cover the Hα core line, but does include the blue wing. The correlation coefficient is broad, with an $R_{\rm e,max}$ value between 0.6 and 0.7, peaking at 12 days. There is a secondary peak at 25 days, but

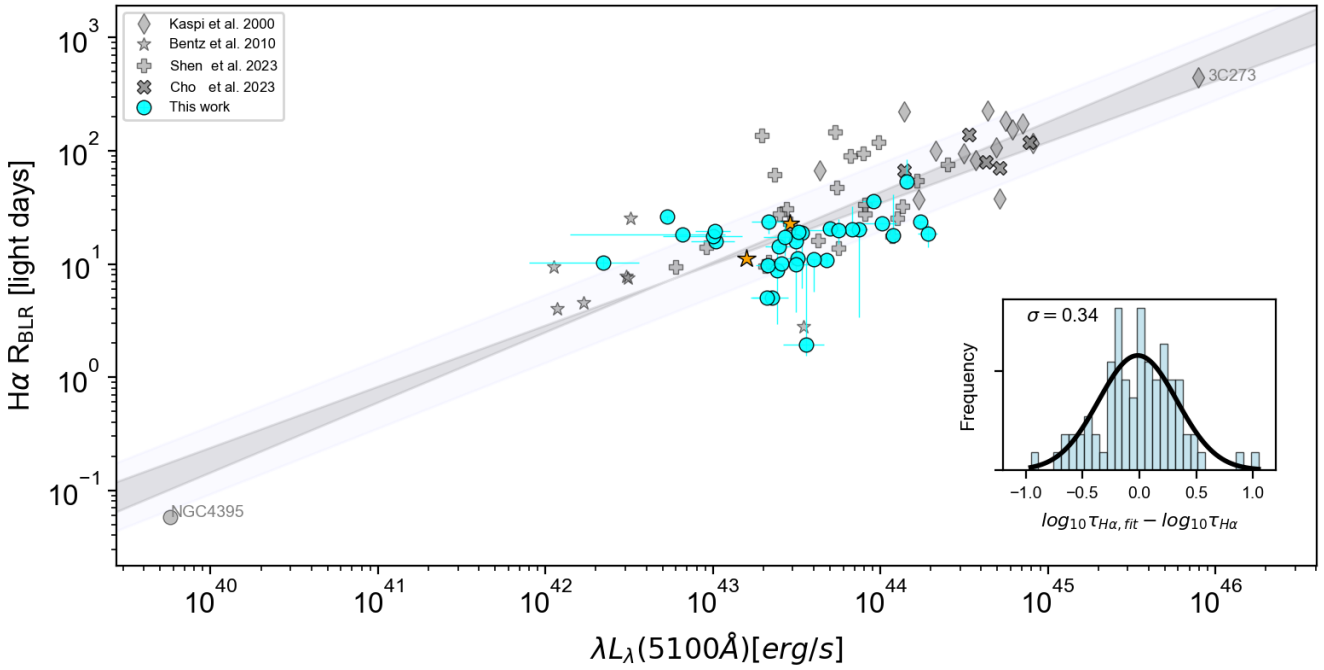

Figure I.1. Same as Figure 11 for peak values.

no corresponding physical α value for this correlation. The high $R_{\rm Fe}$ indicates a high-accreting object. The BV FVG does not suggest a red nucleus, since the AGN slope is high, with a value of 1.08 ± 0.08.

I. RESULTS FOR LAG PEAK VALUES

Scatter slightly larger as for the centroid values with $\sigma = 0.34dex$ (see section 4.4). Restricting the fit to sources in our sample yields $\gamma = 0.16 \pm 0.06$, further restricting to the fit to the 29 most luminous sources in our sample with $\lambda L_\lambda(5100\,\text{Å}) > 1.5 \times 10^{43}\,\text{erg s}^{-1}$ yields a slope $\gamma = 0.49 \pm 0.13$.

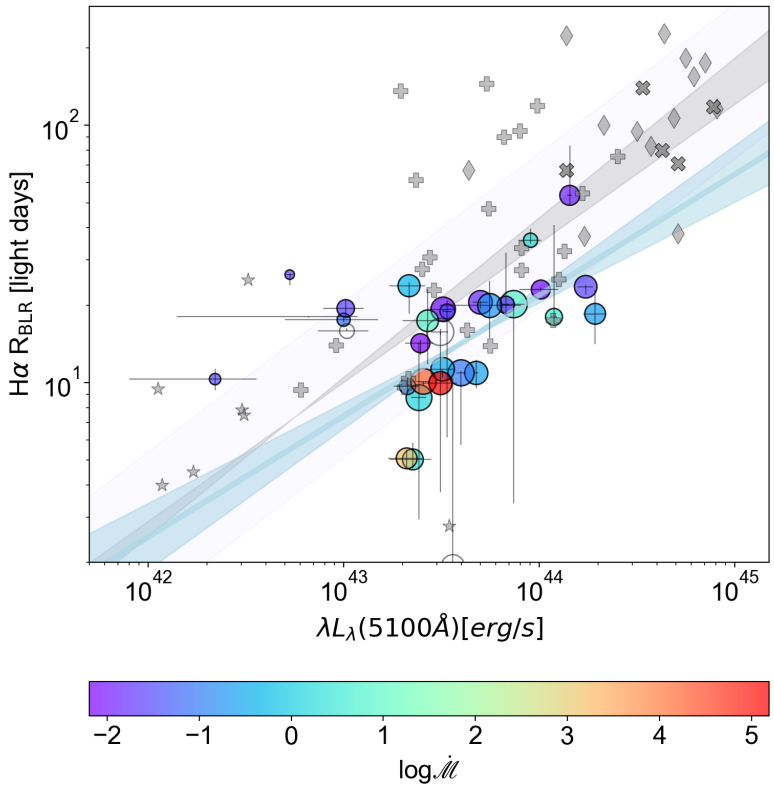

Figure I.2. Same as Figure 13 for peak values.